Dipl. Ing. Heinz Stefan Moisi, BSc.

On the Analysis and Application of a R600 High Temperature Heat Pump

DOCTORAL THESIS

to achieve the university degree of

Doktor der technischen Wissenschaften

submitted to

Graz University of Technology

1. Supervisor

Ao. Univ.-Prof. Dipl.-Ing. Dr. techn. René Rieberer
Institute of Thermal Engineering, Graz University of Technology

2. Supervisor

Prof. Dr.-Ing. Armin Hafner
Department of Energy and Process Engineering, Norwegian University of Science and Technology

Graz, September 2020

AFFIDAVIT

I declare that I have authored this thesis independently, that I have not used other than the declared sources / resources, and that I have explicitly marked all material which has been quoted either literally or by content from the used sources.The text document uploaded to TUGRAZonline is identical to the present doctoral thesis.

Graz, ...

(Signature)

ABSTRACT

Title: On the Analysis and Application of a R600 High Temperature Heat Pump

Author: Heinz Stefan Moisi

1st keyword: natural refrigerant
2nd keyword: experimental analysis
3rd keyword: high temperature heat pump

The project "HotCycle" has been carried out at the Institute of Thermal Engineering (IWT) at the TU Graz under cooperation with Frigopol-Kaelteanlagen GmbH. In the course of this Project, a high temperature heat pump using a modified separating hood compressor with the natural refrigerant *n*-Butane (R600) has been developed and constructed. The heat pump prototype shall provide a supply temperature up to 110 °C in a capacity range of up to 50 kW.

The present thesis describes the development as well as the theoretical and experimental analysis of a high temperature vapour compression heat pump test rig using R600 as refrigerant. A Theoretical analysis of high temperature refrigerants such R600 exhibiting an overhanging two phase region has been conducted regarding the quantity of required superheat based on an isentropic compression to avoid the re-entrance of the compression process into the two phase region (wet compression), causing liquid droplets to form and ultimately compressor damage. A theoretical approach from literature has been refined to provide accurate required superheat characteristics as a function of condensation and evaporation temperature for different high temperature refrigerants, especially R600. Furthermore the effect of the internal isentropic effciency has shown to decrease and shift the superheat maximum to higher evaporation temperatures for a certain condensation temperature.

The heat pump test rig has been developed based on a theoretical study on different cycle configurations obtained from literature. The results have shown that acceptable efficiency results can be obtained using a high pressure receiver and a separate subcooler. Furthermore high degrees of evaporator superheat corresponding to overhanging working fluids shall be decoupled from the heat source to increase evaporation temperature and thus cycle efficiency. The heat pump test rig has been designed accordingly with the possibility to realize two different cycle configurations in terms of superheat preparation. The first configuration states a basic subcritical single stage heat pump cycle. The second configuration utilizes an internal heat exchanger. Furthermore an air cooled separating hood compressor provided by the project partner has been utilized for the first time with R600 and modified with a customary built compressor heat exchanger for suction gas cooling.

A detailed experimental analysis has been carried in order to characterize the compressor and provide performance maps of all investigated cycle configurations. The provision of a supply temperature of 110 °C has been confirmed with source side inlet temperatures in a range from 50 to 80 °C. For the basic cycle, the results have shown a maximum efficiency of 5.7 for source and sink temperature levels of 80/75 °C and 80/110 °C respectively with a

heating capacity of approx. 31 kW. The maximum heating capacity has been obtained to 47 kW for source and sink temperature level of 70/65 °C and 70/100 °C respectively with a COP of approx. 4.5. The application of an internal heat exchanger can improve the heating capacity and efficiency by up to 7.3 % and 6.6 % respectively compared to the basic cycle as a consequence of an increased specific refrigerant heating capacity across the condenser and a decrease of condensation temperature due to an increased desuperheating section inlet temperature. However increased compressor outlet temperatures caused by the IHX can problematic for compressor lubrication. With the investigated high temperature heat pump Carnot and Lorenz efficiencies in a range between 42 % and 53 % and between 21 % and 41 % respectively have been achieved for temperature lifts between 35 and 65 K with a clear correlation to the irreversibility of the compression process.

A simplified semi empirical steady state simulation has been developed based on experimentally obtained compressor efficiency characteristics, modified heat transfer and pressure drop approaches obtained from literature and validated against experimental data. The results of the conducted simulation study has confirmed that increased sink side temperature differences are beneficial for cycle efficiency and heating capacity since subcooling can be harnessed to the greatest extend. Furthermore, in combination with experimental investigations, the simulation results strongly indicate an approximate efficiency optimum at superheat set points equally to the achieved source side temperature difference. Based on the simulation model three different application cases in food industry have been investigated showing a high energy and carbon dioxide reduction potential compared to an natural gas boiler.

In conclusion, the experimental results and experience along with theoretically investigated applications strongly indicate that the presented heat pump concept can be an reliable and efficient alternative to fossil fuel based process heat preparation.

KURZFASSUNG

Titel: Analyse und Anwendung einer R600 Hochtemperatur-Wärmepumpe

Autor: Heinz Stefan Moisi

1. Stichwort: Natürliches Kältemittel
2. Stichwort: Experimentelle Analyse
3. Stichwort: Kompressions-Wärmepumpe

Das Projekt "HotCycle" wurde am Institut für Wärmetechnik (IWT) der TU Graz in Kooperation mit Frigopol-Kälteanlagen GmbH durchgeführt. Im Zuge dieses Projekts wurde eine Hochtemperatur Wärmepumpe unter Verwendung eines modifizierten Trennhaubenkompressors und dem natürlichen Kältemittel n-Butane entwickelt und aufgebaut. Die Randbedingungen für das Wärmepumpenfunktionsmuster umfassen die Bereitstellung einer Nutztemperatur von 110 °C bei einer Heizleistung von bis zu 50 kW.

Die vorliegende Arbeit beschreibt die Entwicklung sowie die theoretische und experimentelle Analyse einer R600 Hochtemperatur-Wärmepumpe. Eine theoretische Analyse der erforderlichen Sauggasüberhitzung zur Vermeidung einer Kondensation während des Kompressionsprozesses für Kältemittel welche ein überhängendes Nassdampfgebiet aufweisen wurde durchgeführt. Bei dieser sogenannten nassen Kompression kann die Ausbildung von Flüssigkeitströpfchen zu Kompressorschäden führen. Dafür wurde ein Näherungsansatz aus der Literatur aufgegriffen und verfeinert, um genaue Kennlinien für die erforderliche Überhitzung als Funktion der Kondensations- und Verdampfungstemperatur für unterschiedliche Hochtemperaturkältemittel, im speziellen aber für R600 abzuleiten. Weiters wurde gezeigt, dass mit sinkendem isentropen Wirkungsgrad das Maximum der erforderlichen Überhitzung sinkt und sich dessen Lage für eine gegebene Kondensationstemperatur zu höheren Verdampfungstemperaturen verschiebt.

Das Wärmepumpenfunktionsmuster wurde auf Basis einer Simulationsstudie mit unterschiedlichen Kreislaufvarianten aus der Literatur durchgeführt. Dabei zeigten die Ergebnisse, dass eine akzeptable Kreislaufeffizienz unter Verwendungen eines Hochdurcksammlers und separaten Unterkühlers möglich ist. Weiters zeigte sich, wenn sehr hohe Sauugasüberhitzungen in Verbindung mit einem überhängenden Kältemittel erforderlich werden, ist es sinnvoll, die Bereitstellung der Überhitzung von der Wärmequelle zu entkoppeln um die Verdampfungstemperatur und somit die Kreislaufeffizienz möglichst hoch zu halten. Das resultierende Wärmepumpenfunktionsmuster wurde entsprechend mit der Möglichkeit zwei Kreislaufkonfigurationen zu untersuchen, konzipiert. Die erste Variante entspricht einem einstufigen unterkritischen Kreisprozess. Die zweite Variante entspricht einem Kreislauf mit internem Wärmetauscher. Zusätzlich wurde eine Adaption des standardmäßig luftgekühlten Trennhaubenkompressors durch einen speziell angefertigten Wärmetauscher auf Sauggaskühlung durchgeführt und erstmalig mit dem Kältemittel R600 verwendet.

Mit dem entwickelten Wärmepumpenfunktionsmuster wurden in weiterer Folge eine detaillierte Kompressorcharakterisierung durchgeführt sowie von Leistungs- und Effizienzkenn-

felder abgeleitet. Die Bereitstellung einer Nutztemperatur von 110 °C konnte für ein Quellentemperaturniveau von 50 bis 80 °C bestätigt werden. Eine maximale Effizienz von 5.7 bei Quellentemperaturen von 80/75 °C und Senkentemperaturen von 80/110 °C konnten bei einer Heizleistung von ca. 31 kW für den Standardprozess erzielt werden. Die maximale Heizleistung mit 47 kW bei einem COP von 4.5 konnte bei Quellen- und Senkentemperaturen von 70/65 °C bzw. 70/100 °C erzielt werden. Die Anwendung des internen Wärmetauschers zeigte eine Erhöhung der Heizleistung und des COP von bis zu 7.3 % bzw. 6.6 %. Die Gründe dafür liegen in einer erhöhten spezifischen Enthalpiedifferenz am Kondensator durch die zusätzliche Sauggasüberhitzung und in einer sinkenden Kondensationstemperatur durch die Erhöhung der treibenden Temperaturdifferenz im Enthitzungsabschnitt des Kondensators. Die steigenden Kompressoreintrittstemperaturen können jedoch problematisch im Hinblick auf das verwendete Kompressoröl sein. Ermittelte Carnot- und Lorenz-Effizienzen zeigten Werte von 42 % bis 53 % bzw. 21 % bis 41 % bei einem Temperaturhub zwischen 35 K und 65 K (d.h. Temperaturdifferenz zwischen Quellenaustritt und Senkenaustritt).

Auf Basis der erhaltenen Kompressorkennlinien sowie modifizierten Wärmeübergangs-vund Druckverlustansätzen aus der Literatur wurde ein einfaches semi-empirisches Simulationsmodel entwickelt und mittels experimenteller Daten validiert. Die damit durchgeführte Simulationsstudie bestätigte die vorteilhafte Auswirkung großer Wärmesenkentemperaturspreizungen auf die Kreislaufeffizienz aufgrund der erhöhten Nutzung der Kältemittelunterkühlung. Weiters weisen, in Kombination mit experimentellen Daten, die erhaltenen Simulationsergebnisse auf ein Maximum hinsichtlich Kreislaufeffizienz für Überhitzungen ident zur der Wärmequellenspreizung hin. Abschließend wurden drei Anwendungsfälle in der Lebensmittelindustrie unter Verwendung des Simulationsmodells betrachtet. Die Ergebnisse zeigten sehr hohes Einsparpotential im Bereich des Energieverbrauchs und der Kohlendioxidemissionen im Vergleich zu einem Erdgas-Dampferzeuger.

Zusammenfassend zeigten die experimentellen Ergebnisse und Erfahrungen in Kombination mit den theoretisch betrachteten Anwendungsgebieten, dass das vorliegende Konzept einer R600 Hochtemperaturwärmepumpe eine verlässliche und effiziente Alternative zur Prozesswärmebereitstellung auf Basis fossiler Brennstoffe darstellen kann.

Preface

The present thesis is the result of the work conducted in the course of the cooperative project "HotCycle" (FFG No.:848892) under the cooperation of TU Graz and Frigopol-Kaelteanlagen GmbH. The project had been funded by the Climate and Energy Fund and carried out within the Austrian Energy Research Program 2015. The following publications and master theses are directly related to the present thesis:

Moisi H., Rieberer R., 2016, Erforderliche Sauggasüberhitzung bei einer R600- Hochtemperatur-Wärmepumpe- Nutzung der Motorabwärme, In Deutscher Klima und Kältetechnischer-Verein (DKV)-Tagung, Kassel, Paper AA II.2

Moisi H., Rieberer R., 2017, Refrigerant Selection and Cycle Development for a High Temperature Vapor Compression Heat Pump, Proc. 12th IEA Heat Pump Conference, Rotterdam, June 2017, ISBN 978-90-9030412-0

Moisi, H., Rieberer, R., Verdnik, M., and Baumhakel, A., 2017, Entwicklung einer R600-Hochtemperatur-Wärmepumpe - Simulation und erste Messungen. In Deutscher Klima und Kältetechnischer-Verein (DKV)-Tagung, Bremen, Paper AA IV.08.

Moisi H., Rieberer R., 2018, Experimental Analysis of a R600 High Temperature Heat Pump, Proc. 13th IIR Gustav Lorentzen Conference, Valencia, 10.18462/iir.gl.2018.1223

Moisi, H., Rieberer, R., and Baumhakel, A., 2018, FFG Nr.: 848892-HotCycle-Kältemittel und Kreislaufdesign für Hochtemperatur-Wärmepumpen kleiner bis mittlerer Leistung mit Trennhaubenkompressor. publizierbarer Endbericht, Österreichische Forschungsförderungsgesellschaft mbH (FFG).

Skreinig, M., 2016, Modellierung, Auslegung und Konstruktion einer Sauggaskühlung für einen Kältemittelkompressor. Master's thesis, Institute of Thermal Engineering, TU Graz.

Verdnik, M., 2017, Inbetriebnahme und messtechnische Analyse einer R600- Hochtemperaturwärmepumpe. Master's thesis, Institute of Thermal Engineering, TU Graz.

First of all I would like to thank Ao. Univ.-Prof. Dipl.-Ing. Dr. techn. René Rieberer for the possibility to carry out the present thesis. His support, patience and constructive remarks have been very much appreciated. Special thanks goes to Dipl. Ing. Manuel Verdnik for his important work in the start up phase of the prototype and all former colleagues at the IWT for the great work environment and support in the workshop. Furthermore I want to thank Ing. Alexander Baumhakel for the perfect cooperation throughout this project. Finally I would like to thank everyone who has not been mentioned and had been directly or indirectly involved in the completion of this present thesis.

Most of all I want to thank my wife Lisa for her infinite patience and of course my parents Erna and Heinrich as well as my sister Gabriela for their support throughout my studying.

Graz, 11.09.2020

Heinz Moisi

CONTENTS

1 INTRODUCTION **1**
1.1 Motivation . . . 1
1.2 Objectives . . . 1
1.3 Structure of the thesis . . . 2

2 STATE-OF-THE-ART **3**
2.1 Definition of a high temperature heat pump . . . 3
2.2 Research on high temperature vapour compression heat pumps . . . 3
2.3 Refrigerants for high temperature applications . . . 7
2.4 Commercial high temperature vapour compression heat pumps . . . 12
2.5 Summary and Differentiation . . . 13

3 FUNDAMENTALS **15**
3.1 Thermodynamics of the vapour compression cycle . . . 15
3.1.1 The Carnot cycle . . . 15
3.1.2 The ideal vapour compression refrigeration/heat pump-cycle . . . 16
3.1.3 The real vapour compression refrigeration/heat pump-cycle . . . 18
3.2 Heat Exchangers in Vapour Compression Cycles . . . 19
3.2.1 General Aspects of Heat Exchangers . . . 20
3.2.2 Evaporator . . . 22
3.2.3 Condenser and Subcooler . . . 25
3.2.4 Internal Heat Exchanger . . . 27
3.3 Compressor . . . 28
3.3.1 The Basic Compression Process . . . 29
3.3.2 Energy Balance and Compressor Efficiency Definitions . . . 31
3.4 Expansion Valve . . . 35
3.5 High Pressure Receiver . . . 37
3.6 Refrigerant *n*-Butane (R600) . . . 38
3.7 Required Superheat . . . 41

4 EXPERIMENTAL SET UP **47**
4.1 Heat Pump Concept and Design . . . 47
4.1.1 Basic Cycle Design Simulations . . . 47
4.1.2 Final Heat Pump Concept and Prototype . . . 52
4.1.3 Design Operation Point . . . 54
4.2 Heat Exchangers . . . 55
4.3 Compressor . . . 59
4.4 Refrigerant Valves . . . 62
4.5 Auxiliary Components . . . 62
4.6 Safety Measures . . . 64
4.7 Source and Sink Hydraulics . . . 65
4.8 Test Rig Control and Data Acquisition . . . 66
4.9 Measurement Equipment . . . 67
4.9.1 Temperature and Pressure . . . 67
4.9.2 Mass and Volume Flow . . . 69
4.9.3 Electrical Compressor Consumption . . . 70

5 EXPERIMENTAL ANALYSIS **71**
5.1 Methodology and Test Matrix . . . 71
5.2 Quality of Experimental Results . . . 72
5.3 Special Operational Behaviour . . . 73
5.3.1 Start Up Phase . . . 74
5.3.2 Superheat Instability . . . 76
5.4 Compressor Characteristics . . . 80
5.4.1 Compression Process and Energy Balance . . . 80
5.4.2 Compressor Efficiencies . . . 84
5.4.3 Characteristics of the Compressor Heat Exchanger . . . 87
5.5 Basic and Superheater Cycle . . . 90
5.5.1 Capacities and Compressor Consumption of the Basic Cycle . . . 91
5.5.2 Efficiency of the Basic Cycle . . . 95
5.5.3 Parameters of the Basic Cycle . . . 97
5.5.4 Influence of the Superheater . . . 100
5.6 Internal Heat Exchanger Cycle . . . 102
5.6.1 Capacities, Compressor Consumption and Efficiency of the IHX Cycle 103
5.6.2 Parameters of the IHX Cycle . . . 106
5.7 Influence of Evaporator Superheat (w/o IHX) . . . 107
5.8 Cycle Comparison and Carnot Efficiency . . . 112
5.9 Additional Remarks . . . 116

6 SIMULATION MODEL **118**
6.1 Basic Methodology and Assumptions . . . 118
6.2 Heat Transfer and Pressure Drop . . . 120
6.2.1 Single Phase Heat Transfer and Pressure Drop . . . 122
6.2.2 Two Phase Heat Transfer and Pressure Drop . . . 126
6.3 Compressor and CHX Parametrisation . . . 129
6.4 Model Validation . . . 132
6.5 Comparison of Parallel- and Counter Flow IHX . . . 134
6.6 Influence of Heat Sink and Source Temperature Difference . . . 136
6.7 Influence of Evaporator Superheat . . . 141
6.8 Optimizing Potential . . . 147
6.9 Concluding Remarks . . . 148

7 HEAT PUMP APPLICATION **150**
7.1 Methodology . . . 150
7.1.1 Natural Gas Steam Boiler . . . 150
7.1.2 R600 High Temperature Heat Pump . . . 151
7.2 Application Cases . . . 151
7.2.1 Food Industry: Evaporation . . . 151
7.2.2 Food Industry: Sterilization of Canned Foods . . . 154
7.2.3 Food Industry: Blanching . . . 157
7.3 Thermodynamic Analysis . . . 159
7.4 Energy Consumption and Emissions . . . 161

8 SUMMARY AND OUTLOOK **164**

LITERATURE **168**

A APPENDIX **177**
A.1 List of Refrigerants 177
A.2 Complementary Heat Exchanger Data 178
A.3 Sensor and Control Signals 183
A.4 Experimental Data 185
A.5 Friction Factors according to Martin (2006) 197
A.6 Validation Results of the Overall Isentropic Efficiency 198

NOMENCLATURE

Symbols

A	area
a	corrugation amplitude, coefficient
b	factor
c	factor
$\dot{C}$	heat capacity rate
$C_{m,V}$	specific molar heat capacity at constant volume
c_p	specific heat at constant pressure
c_q	factor
COP	Coefficient of Performance
d	diameter
E	Energy
f	frequency, factor
G	specific massflow per unit area
h	specific enthalpy
H	height
I	valve opening
IS	inverse slope
K_P	proptional gain
k_{vs}	flow coefficient
KEV	kinetic energy per unit volume
LFL	Lower Flammability Level
$\dot{m}$	mass flow
M	molar mass
m	mass
n	polytropic exponent, number of plates
N	Number
n_p	number of poles
NTU	Number of Transfer Units
Nu	Nusselt Number
p	pressure
P	Power
Pr	Prandtl Number
$\dot{Q}$	heating capacity
q	specific heating capacity, factor
r_q	ratio
Re	Reynolds Number
s	specific entropy, plate thickness
S_m	specific molar entropy
sd	standard deviation
T	temperature in K
t	temperature in °C
U	overall heat transfer coefficient
u	measurement uncertainty
V	volume flow
v	specific volume
$\dot{V}$	volume
V_m	specific molar volume
VHC	volumetric heating capacity
w	specific work, flow velocity
W	work, width
x	vapour quality
y	arbitrary measurement quantity
z	arbitrary derived quantity

Greek letters

α	heat transfer coefficient
β	thermal expansion coefficient
δ	general variation
Δ	difference
η	efficiency
γ	area ratio
λ	efficiency, thermal conductivity
Λ	corrugation wavelentgh
μ	dynamic viscosity
ν	COP ratio
Φ	area enlargement factor
π_p	pressure ratio
ψ	corrugation angle
σ	phase boundary
τ	time
τ_R	reset time
ε	effectiveness
ξ	flow resitance factor
ρ	density

Subscripts and Abbreviations

1, 2, $\hat{3}$,... .	states
amb	ambient
Basic	basic cycle
Bertinat	based on Bertinat (1986)
C	cooling
Ca	Carnot
cf	counter flow
ch	channel
CHX	compressor heat exchanger
clear	clearance
CO_2	carbon dioxide
comp	compressor
cond	condensation
COP	Coefficient of performance
crit	crtitical
D	design
Δp	pressure drop
desup	desuperheating section
diss	dissipation
el	electrical
eq	equivalent
est	estimated
evap	evaporation
exp	experiment
EXV	electronic expansion valve
Fe	stator iron
FI	inverter
fr	friction
H	heating
h	hydraulic
HP	high pressure
HP	heat pump
HT	high temperature
ht	heat transfer
hx	heat exchanger
i	internal, i th component
I, *II*, ...	heat exchanger section
IHX	ihx cycle
imp	impulse
in	inlet
is	isentropic
j	j th component
leak	leakage
Lo	Lorenz
log	logarithmic
Longo	according to **?**
loss	loss
proc	process
prod	product
$\dot{Q}$	heating capacity
*R*600	refrigerant R600
rec	receiver
ref	refrigerant
Reissner	based on Reißner (2015)
req	required
rev	reversible
sat	saturation
set	set point
sf	surface
sink	sink side
source	source side
stat	static
sub	subcooled
sup	superheated
SUP	Superheater cycle
T	temperature in K
t	temperature in °C
th	theoretical
tot	total
trans	transition
$\dot{V}$	volume flow
vap	vapour
vol	volumetric
w	water side
wall	wall
wh	winding head
XV	expansion valve
BPHE	Brazed Plate Heat Exchanger
CHX	Compressor heat exchanger
DCHX	CHX in each stage
DIHX	IHX in each stage
ECO	Economizer
EES	Engineering Equation Solver
EU	European Union
EXV	Electronic Expansion Valve
FFG	Forschungsföderungsgesellschaft
FI	Frequency inverter
FT	Flash tank
GHG	Greenhouse Gas
GWP	Global Warming Potential
HC	Hydro Carbons
HCFO	Hydro Flouro Chloro Olefin
HFC	Hydro Flouro Carbon
HFO	Hydro Flouro Olefin

LP	low pressure
LT	low temperature
$\dot{m}$	mass flow
m	mean value, mechanical
M	momentum
M, EM	Electric drive
max	maximum
min	minimum
nb	normal boiling
NG	Natural gas
op	operation
opt	optimum
out	outlet
ov	overall
p	pressure, plate
P	power
pc	phase change
pf	parallel flow
phx	plate heat exchanger
$port$	heat exchanger ports
pp	pinch point
$prim$	primary

HT-VCHP	High temperature vapour compression heat pump
IC	Intercooler
IHX	internal heat exchanger
IWT	Institute of Thermal Engineering
LI	Liquid injection
LMTD	Logarithmic mean temperature method
LT-HP	Low temperature heat pump
M	Motor
MID	magnetic inductive flow sensor
MSS	Minimum Stable Signal
NBP	Normal Boiling Point
OBP	Ozone Depletion Potential
PID	Proportional-Integral-Derivative
REC	Receiver
SUB	Subcooler
SUP	Superheater
TU	University of Technology
TXV	Thermostatic Expansion Valve
VC-HP	Vapout compression heat pump
VHT-HP	Very high temperature heat pump
VIHX	IHX 3 way valve

1 INTRODUCTION

1.1 Motivation

Global policies and progressive effects of climate change (see e.g. UN, 2015 and IPCC, 2014) require actions to reduce fossil fuel consumption and the corresponding CO_2 emissions. Waste heat recovery states a promising possibility to increase the energy efficiency of thermal processes in industry and can therefore contribute to conquer future challenges in energy demand and greenhouse gas (GHG) emmissions. Considering heat recovering systems, high temperature vapour compression heat pumps can revalue thermal energy at a lower temperature level by means of electrical energy and provide process heat at the required supply temperature. If the generation of the electrical power supplied to the heat pump is entirely based on renewables, a CO_2 neutral process heat supply could be realized. However, using heat pumps for high temperature process heat preparation, distinct working fluids are required in terms of thermophysical properties (e.g. critical pressure and temperature) and environmental aspects (Global Warming Potential, GWP). Especially since the EU directive (EU, 2014) is in effect phasing down HFC refrigerants (hydro flouro carbon), low GWP working fluids for example HFO refrigerants (hydro flouro olefin) and natural refrigerants will become increasingly important for heat pump applications. Thus using such environmentally benign refrigerants can increase the positive effect of heat pumps on fossil fuel consumption and CO_2 emissions.

According to Rieberer et al. (2015) an assumption based on the year 2002 showed that approximately 74 % of the entire energy consumption in Austria‘s industry is represented by thermal energy demand. In Germany for the year 2012, the thermal energy demand resulted to 4960 PJ and makes up approximately 55 % of the total energy consumption (Wolf et al., 2014). Furthermore Wolf et al. (2014) show a heat recovery potential with heat pumps of approximately 437 PJ with a temperature level of up to 100 °C which results in 23 % of the total thermal energy demand in Germany‘s industry in 2012. For Austria, Rieberer et al. (2015) report a similar value with approximately 26 % of the total heat demand or 228 PJ with a temperature level up to 100 °C. Possible applications for high temperature heat pumps can be found in the chemical, food, paper, textile and lumber industry with processes like distillation (100 °C to 160 °C), cooking (70 °C to 120 °C), pasteurization (60 °C to 140 °C) and drying (40 °C to 160 °C) (see Wolf et al., 2014, Wolf, 2017).

The present work focuses on the theoretical and experimental analysis of a high temperature vapour compression heat pump using the natural refrigerant *n*-butane (R600) as working fluid for heat supply temperatures up to 110 °C in a capacity range up to 50 kW. The aim is to give insight on and a detailed analysis of the operation and key aspects of a high temperature heat pump using a hydrocarbon as working fluid (HC) for future application in process heat preparation in order to exploit the above stated waste heat potential and improve energy efficiency in the manufacturing industry.

1.2 Objectives

The main objective is given by the experimental analysis in terms of performance and operation behaviour of a high temperature heat pump using R600 as a refrigerant. In the course of this thesis a high temperature heat pump test rig has been designed. The construction of the heat pump prototype has been carried out by the project partner Frigopol Kaelteanlagen GmbH. Performance maps regarding the Coefficient of Performance (COP), heating capacity

as well as compression end temperatures, compressor efficiencies etc. for variable operating conditions shall characterise the heat pump prototype. Based on the obtained data, a simulation model can be parameterised and validated. The validated simulation model enables to investigate the performance of the heat pump under varying boundary conditions and can therefore show optimizing potential, design and operating recommendations and further possibilities of application. Furthermore potential application cases shall be outlined and technological boundary conditions (e.g. COP) shall be investigated for the selected application cases and compared to conventional systems for thermal energy supply (most commonly gas boilers).

1.3 Structure of the thesis

The present thesis is divided into four main parts:

1. *Chapters 2 and 3*: The first part consists of a comprehensive review of the state of the art in terms of high temperature heat pumps followed by the physical and thermodynamical basics of the heat pump cycle, it's components (e.g. heat exchangers, compressor), working fluid and control characteristics .

2. *Chapters 4 and 5*: Constituting the second part, a detailed description of the experimental set up in terms of test rig structure, measurement equipment, methodology and uncertainty estimation is given followed by the discussion of experimental results considering different operational behaviour, steady state performance maps and the influence of different parameters on heat pump operation.

3. *Chapters 6 and 7*: Within the third part, a simulation model of the heat pump test rig is described regarding components, methodology, parametrization and validation as well as simulation results in terms of cycle optimization potential are discussed. Based on the simulation model different application cases for the R600 high temperature heat pump obtained from literature are investigated thermodynamically with a brief outlook on CO_2 reduction potential.

4. *Chapter 8*: The fourth and final part constitutes a summary and conclusion of the obtained results and closes with an outlook on improvement potential of the introduced R600 high temperature heat pump.

2 STATE-OF-THE-ART

Research and development on high temperature vapour compression heat pumps (HT-VCHP) has increased significantly in the last years. This chapter shall give insight to the current state of the art in terms of research, utilized and promising refrigerants as well as a brief overview on already commercially available high temperature heat pumps.

2.1 Definition of a high temperature heat pump

Essentially, the application of heat pumps is devided into two sectors. The first field of application is the building sector providing space heating and hot water. The second, very wide field, is the industrial use of heat pumps recovering waste heat for process heat supply. As stated by several authors (e.g. Reißner, 2015; Wolf, 2017), the supply temperature threshold of residential heat pumps lies at 60 °C. Wolf (2017) described heat pumps with supply temperatures up to 60 °C as "low temperature heat pumps" (LT-HP). Reißner (2015) for example, defines high temperature heat pumps (HT-HP) starting at 70 °C supply temperature while Arpagaus (2018) classifies high temperature heat pumps within supply temperatures 80 °C and 100 °C. A further distinction has been made into "very high temperature heat pumps" (VHT-HP) by Arpagaus (2018) for supply temperatures starting with 100 °C and by Wolf (2017) starting with 120 °C. In the present thesis the threshold for high temperature heat pumps has been selected to be 80 °C, a further distinction into very high temperature heat pumps is not maintained. Besides vapour compression heat pumps (VC-HP) alternative concepts such as absorption-compression heat pumps, so called hybrid heat pumps, (Hannl, 2015) , thermo-acoustic heat pumps (e.g Yang et al., 2014) and rotational heat pumps (Adler and Mauthner, 2017) are investigated and partially commercially available in the context of industrial/high temperature application. However, since the investigated high temperature heat pump of the present thesis is of the vapour compression type, the focus in the entire work lies on vapour compression heat pumps.

2.2 Research on high temperature vapour compression heat pumps

The past and current research on high temperature heat pumps covers a wide variety of cycle configurations and refrigerants. An early theoretical work on high temperature heat pumps using natural refrigerants has been carried out by Tamura et al. (1997), describing a cascade cycle with screw compressor and expander using working fluids ammonia (R717) in the first and water (R718) in the second stage. The boundary conditions state a temperature lift between an evaporation temperature in the first stage of 40 °C and the condensation temperature of second stage with 180 °C. The results showed a COP_H of 2.97 assuming an isentropic compression and expansion. More recently different cycle configurations in connection with high temperature vapour compression heat pumps had been investigated by Cao et al. (2014). Within their study, six different subcritical heat pump cycles, including for example the conventional single stage vapour compression cycle, a two stage cycle with cooling the hot gas of the first stage compressor and economizer cycles using heat exchanger and flash tank respectively, has been investigated by means of simulation. The refrigerant R152a has been selected with given evaporation temperatures ranging between 25 and 35 °C and condensation temperatures between 98 and 108 °C. The economizer cycle using an flash tank showed the best performance in terms of COP_H among the examined cycle configurations with absolute values of 3.6 to 4.2 for temperature lifts between condensation and evaporation of approx. 70 °C to 60 °C. Kondou and Koyama (2015) investigated numerically four complex cycle configurations using up to three heat pumps in series and

cascade layouts with refrigerants R717, R365mfc, R1234ze(E) and R1234ze(Z). The operation mode ranged from subcritical for the low temperature stages to transcritical for the high temperature stages. Supply temperatures of 160 °C and a source inlet temperature of 80 °C have been assumed. The best performance in terms of COP_H has been achieved using a so called "multiple stage extraction cycle" with the refrigerant R1234ze(Z). A further theoretical study on high temperature heat pumps especially considering the natural refrigerants ammonia (R717), carbon dioxide (R744), propane (R290) and isobutane (R600a) has been carried out by Sarkar et al. (2007). Subcritical and transcritical single stage cycles have been investigated for heat source temperatures of 20 and 60 °C and supply temperatures of 100, 150 and 200 °C considering very large temperature differences between 70 and 170 K on the heat sink side. Besides optimum discharge pressures for the transcritical cycles (e.g. CO_2), the influence of a high degree of subcooling has been examined for the subcritical cycles (e.g. ammonia). Under the given boundary conditions the results showed, that the propane based heat pump provides the highest COP_H of up to 4.17 for heat supply temperatures of 100 (subcritical) and 150 °C (transcritical). Ammonia performed best in a subcritical cycle for supply temperatures of 200 °C with the major drawback of very high compressor discharge temperatures of up to 400 °C and condensation pressures up to 11 300 kPa.

Besides theoretical work carried out, experimental studies are increasingly published in the field of high temperature vapour compression heat pumps. Bobelin and Bourig (2012) presented experimental results of a high temperature heat pump using scroll compressors in a subcritical single stage cycle for a heating capacity up to 200 kW in an evaporation and condensation temperature range of 35 °C to 60 °C and 80 °C to 138 °C, respectively (see Figure 2.1a). The COP_H for example has been reported to be in between 4 and 5, for an evaporation temperature of 60 °C and a condensation temperature of approx. 110 °C using the not closer specified refrigerant ECO3 (a blend with R245fa according to Reißner, 2015).

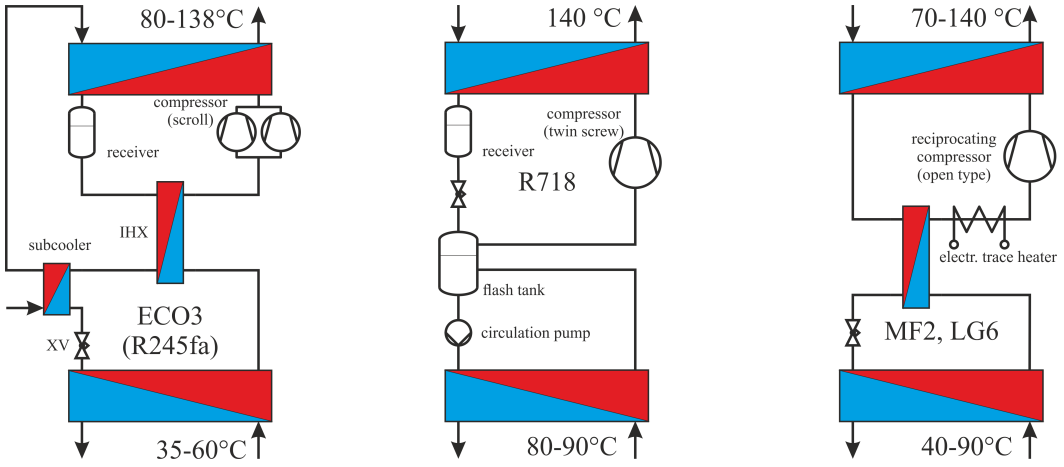

(a) Bobelin and Bourig (2012) (b) Chamoun et al. (2014) (c) Reißner (2015)

Figure 2.1: Simplified heat pump cycle layouts investigated by the respective authors providing supply temperatures of up to 140 °C

Water as a refrigerant for condensation temperatures up to 140 °C has been investigated theoretically and experimentally in a subcritical single stage heat pump cycle using a newly developed twin screw compressor by Chamoun et al. (2014) (see Figure 2.1b). The main focus of this study however, has been laid on modeling and validation of a transient heat pump model based on the heat pump prototype. While no experimental data of heating capacity nor COP have been presented in this paper, simulation results showed a heating

capacity up to 390 kW for a heat source inlet temperature of 94 °C and a supply temperature of approx. 121 °C. A calculated COP_H of 5 has been reported for a source inlet temperature of 95 °C and a condensation temperature of 145 °C. A lab scale prototype (heating capacity of approx. 10 kW) of a single stage high temperature heat pump utilizing an internal heat exchanger has been investigated by Reißner (2015) (see Figure 2.1c). The prototype has been operated with refrigerants MF2 and LG6 for evaporation temperatures ranging from 40 to 90 °C and condensation temperatures from 70 to 140 °C. Unfortunately the refrigerants cannot be closer specified due to confidentiality reasons. However Reißner (2015) stated that MF2 and LG6 are non toxic, non flammable and exhibit a Global Warming Potential (GWP) of 1. The cycle efficiency has varied for a temperature lift between evaporation and condensation of 30 K between approx. 3.5 to 6 for LG6 and between 5.5 to 6 for MF2. For a temperature lift of 60 K the COP_H ranges from approx. 2.5 to 3.1 and from approx. 2.9 to 3.2. A similar study has been conducted by Noack (2016) considering a lab scale high temperature heat pump, experimentally investigating a single stage cycle layout without internal heat exchanger and utilizing a suction gas cooled reciprocating compressor (see Figure 2.2a). However, the utilized refrigerant is not specified. The heating capacity of the prototype results in approx. 10 kW for an evaporation temperature of 80 °C and a condensation temperature of 120 °C. The COP_H in this operation point has been reported to be 4.5. The maximum presented condensation temperature resulted in 142 °C. Considering the hydro flouro olefin (HFO) refrigerant R1336mzz(Z), experimental studies have been carried out by Helminger et al. (2016) and Nilsson et al. (2017). Helminger et al. (2016) experimentally investigated the application of R1336mzz(Z) in a lab scale test rig of a single stage heat pump cycle utilizing an internal heat exchanger (see Figure 2.2b). For an evaporation temperature of 65 °C and a condensation temperature of 100 °C a heating capacity of 12 kW can be realised. The experimental tests have been conducted, by varying the evaporation temperature in a range between 30 and 90 °C in addition to a varying condensation temperature from 75 to 160 °C. The test rig consisted mainly of standard components and reached a COP_H of approx. 2.7 at a heat source inlet temperature of 97.3 °C and a supply temperature of 156.3 °C. The work of Nilsson et al. (2017) examines again a single stage cycle configuration using an internal heat exchanger as well as a special developed water cooled piston compressor based on expander technology for organic rankine cycles (see Figure 2.2c). The prototype delivered a heating capacity of 33 kW for a heat source inlet temperature of 95 °C and a heat supply temperature of 140 °C reaching a COP_H of 4. This heat pump, the so called "Heat Booster" is already commercially available, offered by the Norwegian Company Viking Heat Engines (see also section 2.4). Very recently, Arpagaus et al. (2018a) presented theoretical and first experimental results of a lab scale high temperature heat pump using the hydro flouro chloro olefin (HCFO) R1233zd(E) as refrigerant (see Figure 2.2d). Besides theoretical studies dealing with the investigation of different refrigerants (i.e. R365mfc, R245fa, R1234ze(Z), etc.) in regards to optimum COP in dependence on condensation temperature and temperature lift, the developed heat pump has been tested for heat source inlet temperatures between 40 and 80 °C and heat sink outlet temperatures ranging from 70 to 150 °C. The temperature differences on the source and sink side have been set to 3 and 5 K, respectively. The cycle layout has been again a single staged heat pump using an internal heat exchanger as well as a suction gas cooled reciprocating compressor. A heating capacity of approx. 5.1 kW and a COP_H of 2.4 has been reported for a source inlet temperature of 60 °C and a source outlet temperature of 110 °C. A maximum supply temperature of 151 °C has been achieved with the investigated test rig.

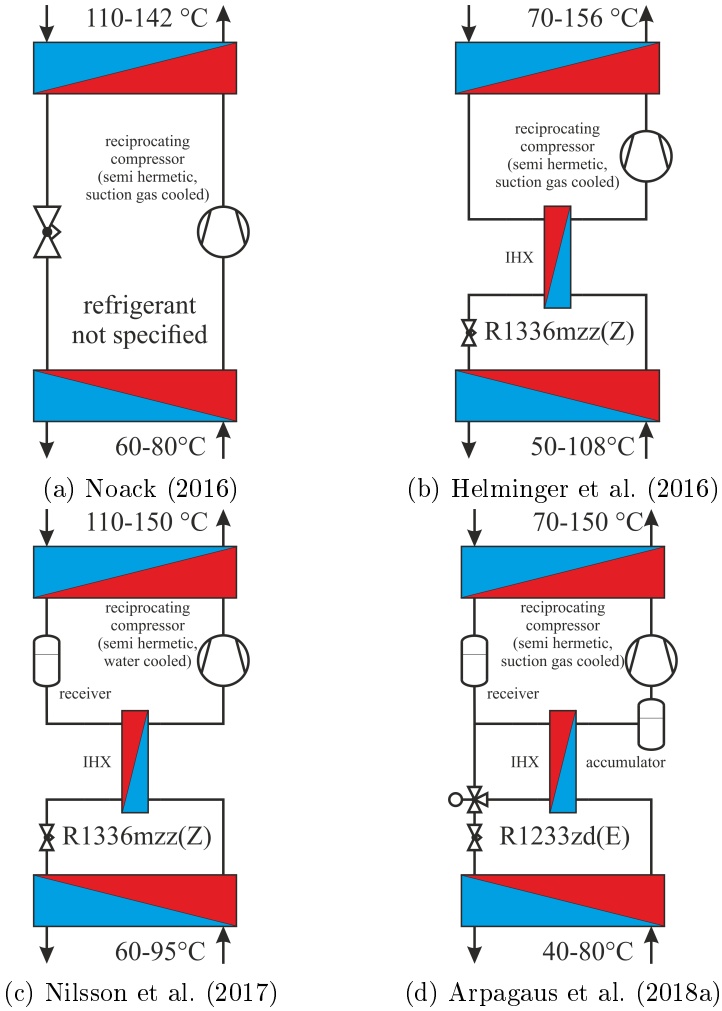

(a) Noack (2016) (b) Helminger et al. (2016)

(c) Nilsson et al. (2017) (d) Arpagaus et al. (2018a)

Figure 2.2: Simplified heat pump cycle layouts investigated by the respective authors using mainly HFO refrigerants

In terms of hydrocarbons (HC) based high temperature heat pumps, Wemmers et al. (2017), Drexler-Schmid et al. (2017) and Bamigbetan et al. (2018b) and carried out experimental studies. Wemmers et al. (2017) tested a 160 kW pilot scale industrial heat pump in a Dutch papermill using R600 (n-Butane) as refrigerant (see Figure 2.3a). The heat pump delivers low pressure steam at 50 kPa gauge (approx. 111 °C) to 240 kPa gauge (approx. 138 °C) from waste heat with 60 °C. A single stage cycle is used, where the steam generation takes place in the condenser, the suction gas superheat is realized with an internal heat exchanger and a subsequently arranged subcooler provides hot process water decoupled from the steam generation to increase the overall efficiency. A combined COP_H (process water and steam generation) of 4.2 has been reported for an evaporation temperature of approx. 55 °C and a steam pressure of 240 kPa gauge. The application of an ejector for expansion work recovery in a n-Butane (R600) based high temperature heat pump has been investigated in the Austrian research project "High Butane 2.0" by Drexler-Schmid et al. (2017) (see Figure 2.3b). The heat pump test rig achieved a heating capacity of approx. 35 kW at a heat source inlet temperature of approx. 60 °C and a heat sink outlet temperature of approx. 124 °C. As expected, the ejector has increased the suction pressure for the compressor by approx. 25 % in the described operation point. However in comparison to experimental results without ejector, no positive effect of the pressure lift on COP_H has been observed. In fact, even a decrease in cycle efficiency resulted. The COP_H for the standard cycle and the above described operation point resulted in 2.5 while the ejector cycle reached only 2.35. The

reason for the efficiency deterioration is yet unclear, however the authors suspect the cause in refrigerant mass migration and/or an unfavorable compressor operation point due to the suction pressure increase.

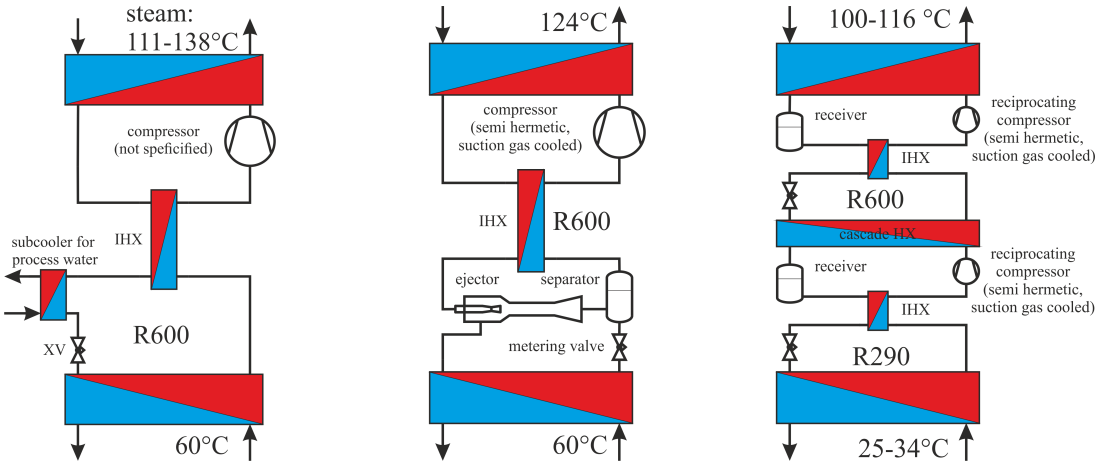

(a) Wemmers et al. (2017) (b) Drexler-Schmid et al. (2017) (c) Bamigbetan et al. (2018b)

Figure 2.3: Simplified heat pump cycle layouts investigated by the respective authors using HC refrigerants

A recent publication regarding high temperature heat pumps with hydrocarbons has been conducted by Bamigbetan et al. (2018b) (see also Bamigbetan et al., 2019a and Bamigbetan et al., 2019b). On the contrary to the other mentioned authors, Bamigbetan et al. (2018b) investigated a cascade cycle utilizing Propane (R290) in the first stage and n-Butane (R600) in the second stage (see Figure 2.3c). In every stage an internal heat heat exchanger is used for suction gas superheating. The utilized suction gas cooled reciprocating compressor has been modified to sustain suction gas temperatures of up to 80 °C. The prototype has been tested for source inlet temperatures in a range from 25 to 34 °C and sink outlet temperatures ranging from 100 to 116 °C with an average temperature lift of approx. 80 K and a rated heating capacity of approx. 20 kW. The efficiency for the heating purpose only, ranged between 2 and 2.5 while a combined COP for heating and cooling varied from 3.1 to 4 with a maximum achieved supply temperature of approx. 116 °C.

2.3 Refrigerants for high temperature applications

Refrigerant selection is an integral part of the development process for any heat pump. The determination of basic characteristics of refrigerants such as critical data (pressure, temperature) in combination with the thermodynamic cycle (e.g. sub/trans/supercritical) are basically determined by the required source and sink temperature levels as well as their temperature glide. Based on the temperature boundary conditions as well on the selected thermodynamic cycle, the final selection requires further criteria regarding thermodynamic properties, environmental and legal aspects, technological boundaries and safety issues. The following enumeration sums up the most important selection criteria in four categories and comments briefly the single aspects. The list of criteria is mainly based on Reißner (2015), Arpagaus et al. (2018b), Bamigbetan et al. (2018a) and Moisi and Rieberer (2017), the comments are including own interpretations and additions.

a) *Thermodynamic properties:*

- **Thermodynamic cycle**: As stated above the selected heat pump cycle, is strongly dependent on the temperature level of the heat sink and especially on the desired heat

sink temperature difference. A high heat sink temperature glide might be more in favour for a trans- or supercritical cycle (e.g. CO_2 based heat pumps), however, high gas cooler pressures might be problematic in terms of available compressor technology. Subcritical cycles then require a corresponding high critical temperature in order to meet the desired supply temperatures. As already mentioned in connection with the thermodynamic cycle, appropriate critical conditions are required to realise the desired heat pump cycle and sink temperature levels. Considering a subcritical single stage cycle for a certain set of evaporation and condensation temperature, the theoretical COP exhibits a steady increase for refrigerants with increasing critical temperatures (Bertinat, 1986). Low critical pressures are of course favorable for material strength and thus wall dimensions, considering compressors and piping.

- **Theoretical COP and volumetric heating capacity (VHC):** Naturally, a high theoretical COP is desired for any heat pump application. The VHC states a measure of the required compressors size. A high VHC requires smaller equipment for the same heating capacity and vice versa. The VHC decreases for refrigerants with increasing normal boiling point (Bertinat, 1986). The volumetric heating capacity can be calculated according as the product of the density at compression inlet ($rho_{comp,in}$) and the specific heating capacity at the selected condensation pressure (q_H, see Section 3.1.2) following Equation 2.1 (compare to Falkner, 2018).

$$VHC = \rho_{comp,in} \cdot q_h \tag{2.1}$$

- **Pressure ratio:** The pressure ratio has a significant influence on compressor efficiencies. The volumetric efficiency (λ_{vol}) decreases nearly linear with an increasing pressure ratio (Section 5.4). The compressor's total isentropic efficiency ($\eta_{is,tot}$) exhibits usually a maximum at a certain pressure ratio (Section 5.4).
- **Normal boiling point (NBP):** The normal boiling point constitutes the saturation temperature of a substance at atmospheric pressure (e.g. 101.3 kPa). The NBP is especially of interest in connection with heat pumps down times. If the NBP lies above ambient temperature (approx. 25 °C), a saturation pressure below atmosphere occurs due to cooling down and could lead to infiltration of air into the heat pump cycle, which decreases cycle efficiency and capacity.
- **Heat transfer properties and pressure drop:** Clearly, high heat transfer coefficients reduce necessary heat transfer areas and in combination with low pressure drops allows the use of more compact components

b) *Environmental and legal aspects:*

- **Ozone Depletion Potential (ODP):** With the Montreal Protocol (UNEP, 1989), working fluids exhibiting an ODP > 0 are phased out with 1.January 1989. Refrigerants affected by this regulation are basically all chloride containing refrigerants such as the chloroflourocarbons (CFCs) R11, R12, R113 and R114 as well as hydrochloroflourocarbons (HCFCs) like R21, R123 and R141b. However, refrigerants like R1233zd(E) or 1224yd(Z) do exhibit very low ODP values (0.00034 and 0.00012 respectively) and are currently commercially available (see Arpagaus, 2018). As further stated by Arpagaus (2018) the low ODP is a results of very short atmospheric lifetimes with 40.4 and 21 days for R1233zd(E) and R1224yd(Z) respectively.
- **Global Warming Potential (GWP):** The GWP has been found increasingly important since the F-Gas regulation (EU, 2014) has been into effect since April 2014, phasing

down refrigerants with high GPW (>150). With the Kigali amendment (UNEP, 2016) to the Montreal protocol the production, trade and use of certain HFC refrigerants (e.g. R245fa, R365mfc, R134a, etc.) will be significantly restricted starting with 1.January 2019. Hence recently, low GWP refrigerants such as natural working fluids (NH_3, CO_2, hydrocarbons (HC)) and hydroflouroolefins (HFOs) are stepping in the spotlight of refrigerant selection.

c) *Technological boundaries:*

- **Maximum compressor pressure:** As stated above the high pressure level is of importance for compressor selection. The current maximum pressure level for commercially available reciprocating refrigerant compressors and standard refrigerants (e.g. R134a, R410a, R290) lies around 2800 to 4200 kPa. Ammonia compressors are available up to 6000 kPa while CO_2 compressors can be found up to 16 000 kPa.
- **Maximum compressor discharge temperature:** The compressor discharge temperature is a critical aspect for lubricant stability and viscosity and is especially important for high temperature applications. Excess compressor discharge temperatures might decrease the lubricant viscosity to a critical level where compressor lubrication becomes insufficient or even decompose the compressor lubricant.
- **Refrigerant stability:** The refrigerant itself has to be chemically stable in the desired field of operation.
- **Miscibility of refrigerant and lubricant:** The miscibility of refrigerant and lubricant affect thermophysical properties, heat transfer and pressure drop (e.g. Shen and Groll, 2005a and Shen and Groll, 2005b). If the lubricant is strongly diluted by refrigerant, viscosity might not be sufficient in order to maintain appropriate compressor lubrication (Hughes et al., 1980). Miscibility gaps at certain operating conditions might cause lubricant accumulation in different cycle components (e.g. evaporator).
- **Compressor suction temperature:** The limitation of the compressor suction temperature concerns mainly suction gas cooled compressors. Excess suction gas temperatures increase the motor coil temperature which is supposed to be cooled by the refrigerant. In order to maintain the same heat flux, the coil temperature has to increase for high suction gas temperatures at steady state conditions assuming nearly constant heat transfer coefficients. In the worst case, the coil temperature reaches the maximum allowed value.
- **Availability:** The refrigerant has to be commercially available, at least if a commercial product is aimed for.
- **Material compatibility:** Corrosion effects have to be avoided in order to maintain long service life, safety and high cycle efficiency. Therefore compatibilities with sealing and piping materials are essential in refrigerant selection and heat pump development.

d) *Safety:*

- **Flammability and Toxicity:** The flammability of refrigerants becomes increasingly important since low GWP refrigerants like HFOs (some of them are mildly flammable e.g. R1234yf and R1234ze(Z), safety Group: A2L, see for example Mikielewicz and Wajs, 2019) and hydrocarbons (highly flammable, safety group: A3) are stepping into the focus not only in high temperature heat pumps. While toxicity is commonly related to Ammonia (mildly flammable and toxic, safety group: B2L), also R245fa which is currently used in commercial high temperature heat pumps (see Section 2.4) is classified as toxic (safety group: B1). Flammability and toxicity of a refrigerant require

certain safety measures (e.g. ventilation), limits the refrigerant charge and influences the possible installation site of a heat pump (see EN378, 2016 and Corberán et al., 2008).

Considering these aspects, amongst others, leads to a variety of possible refrigerants for high temperature vapour compression applications. Bamigbetan et al. (2018a) theoretically investigated a selection of potential high temperature working fluids including CFCs and HCFCs (e.g. R113, R114, R141b, etc.), HFCs (e.g. R245fa, R365mfc, etc.), HCFOs (e.g. R1233zd(E)) and HFOs (e.g. R1234ze(Z), R1336mzz(Z)) as well as natural refrigerants (e.g. R718, R717, R600, R600a, etc.) for supply temperatures up to 125 °C. Based on a subcritical single stage heat pump simulation model with a heating capacity of 20 kW, above mentioned refrigerant properties such as GWP, suction gas temperature, compressor discharge temperature, COP and refrigerant charge have been analysed. The authors concluded that the list of potential high temperature working fluids narrows down to natural refrigerants, HCFOs (R1233zd(E)) and HFOs (R1336mzz(Z)) for future applications in high temperature heat pumps due to legal regulations (see above). Furthermore R600 and R1233zd(E) are stated to be the most promising among the investigated working fluids. R600 due to its wide application range and R1233zd(E) due to a high cycle efficiency. Arpagaus et al. (2018b) carried out a theoretical analysis in terms of COP, VHC and pressure ratio of potential refrigerants investigating a subcritical single stage cycle using an internal heat exchanger. The temperature lift between evaporation and condensation temperature has been kept constant at 70 K while the condensation temperature has been varied. The underlying refrigerant cycle is based on an IHX configuration using an internal isentropic efficiency ($\eta_{is,i}$) of 0.7 and subcooling of 5 K (compare to Chapter 3). The theoretical COP has been calculated analogously to Section 3.1.2. The volumetric heating capacity has been calculated according to 2.1. The results of the study in terms of theoretical COP (left) and VHC (right) are depicted in Figure 2.4. Furthermore the critical temperature of the different working fluids is indicated by dots. Due to a high critical temperature and thus a higher phase change enthalpy, the azeotropic HFC SES36 (blend with R365mfc, according to Arpagaus et al. (2018b)) exhibits the highest efficiency followed by the HC R601 (Pentane) for condensation temperatures between 130 and 160 °C. R600 (n-Butane) for example performs last in terms of COP.

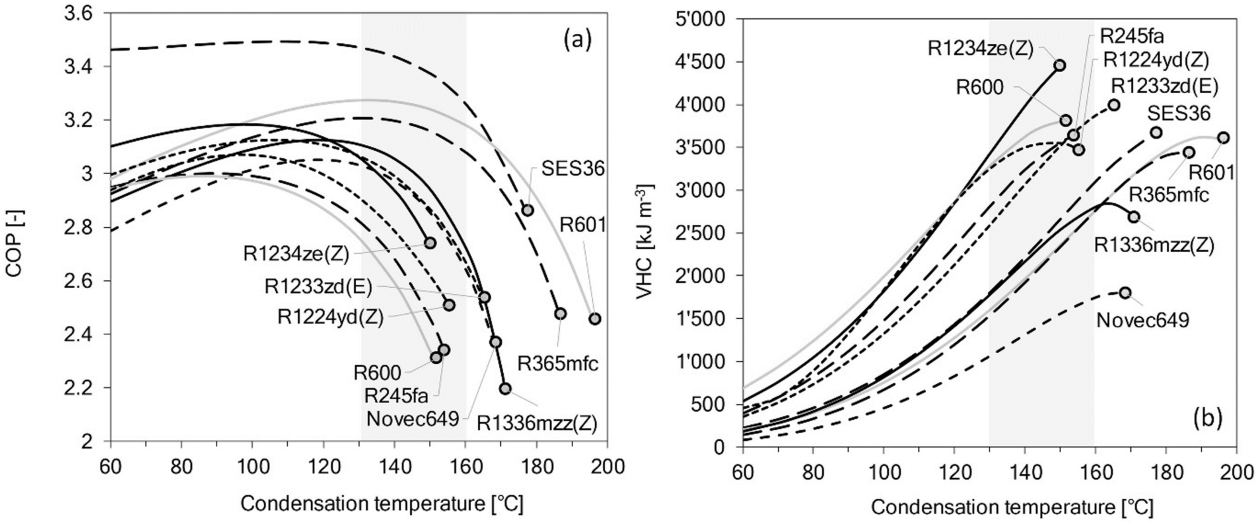

Figure 2.4: Theoretical results of an IHX cycle with $\eta_{is,i} = 0.7$ and 5 K subcool for potential high temperature refrigerants in terms of COP (right) and VHC (left) as a function of the condensation temperature for a temperature lift of 70 K (Arpagaus et al., 2018b, modified)

Considering the volumetric heating capacity (VHC), the HFO refrigerant R1234ze(Z) displays the highest values followed by R600 (n-Butane) until the critical temperature is reached. In a similar way, Reißner (2015) conducted simulations considering refrigerants in sub-, trans- and supercritical single stage heat pump processes with internal heat exchanger. However the temperature lift has been set to 50 K and the internal isentropic efficiency to 0.8. The results obtained by Reißner (2015) for a theoretical COP (left) and VHC (right) are depicted in Figure 2.5. The COP decreases for each working fluid reaching the transcritical process (transition from full to dashed line) which is in accordance to the results by Arpagaus et al. (2018b). Regarding the VHC, an increasing trend with the condensation temperature can be observed since the temperature lift is held constant, the suction gas density increase stronger than the phase change enthalpy decreases until the condensation comes in the vicinity of the critical temperature. Beyond the critical temperature, pressure and temperature become independent. Therefore a COP optimizing algorithm has been applied by Reißner (2015) to find the optimum high pressure. In the considered condensation temperature range, the hydrocarbon Cyclopentane exhibits the best performance regarding the theoretical COP but falls behind considering the volumetric heating capacity. The same behaviour, however in the other direction, can be observed for the HFO R1234yf, with the lowest COP among the investigated fluids, performing best in terms of VHC. This fundamental trade off between COP and the volumetric heating capacity in vapour compression cycles has been reported by e.g. Domanski et al. (2014).

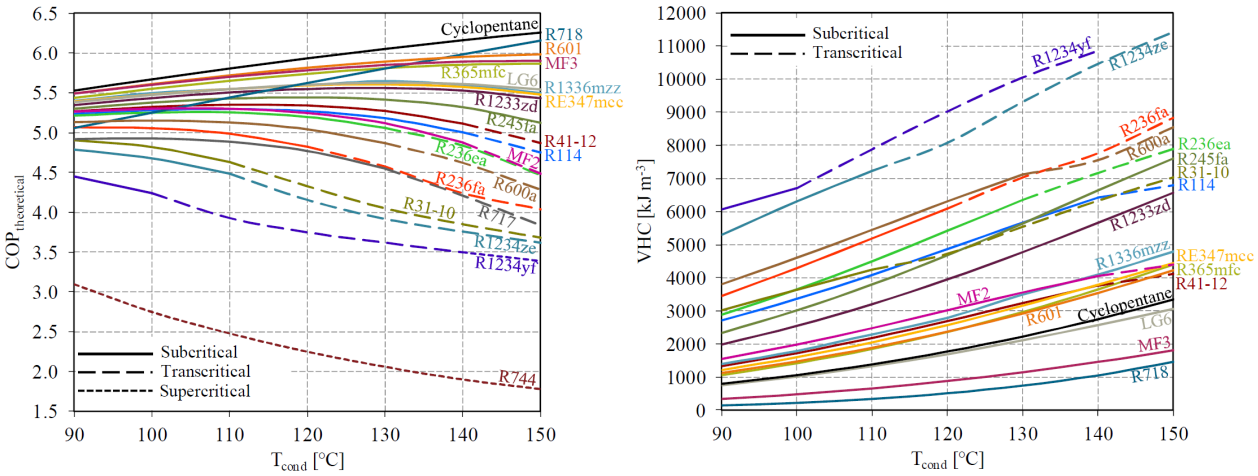

Figure 2.5: Theoretical results of an IHX cycle with $\eta_{is,i} = 0.8$ and 5 K subcool in terms of COP (right) and VHC (left) as a function of the condensation temperature for a temprature lift of 50 K obtained from Reißner (2015)

The trade off between COP and VHC is a good example for the difficulties in selecting suitable high temperature refrigerants. Based on the findings of the reviewed papers the current state of the art in terms of high temperature refrigerants includes working fluids of all chemical families like the synthetic CFCs, HCFCs, HCFOs, HFO and natural refrigerants. Furthermore, blending refrigerants increase the possibilities to a wide variety of potential high temperature working fluids. The qualification for a certain application however, is restricted by the above mentioned criteria of thermodynamic properties, environmental and legal aspects, technological restrictions and safety issues.

2.4 Commercial high temperature vapour compression heat pumps

In contradiction to the current research activities, commercial high temperature heat pumps can mainly be found with heating capacities above 50 kW. The company Ochsner Energietechnik (Ochsner, 2018), for example, offers single stage and cascade heat pumps utilizing screw compressors for supply temperatures up to 130 °C and a heating capacity in a range from 170 kW to 1.5 MW. The utilized refrigerants are R134a for the first stage and the not closer specified ÖKO1 (contains R245fa according to Arpagaus et al., 2018b) and ÖKO2 (GWP=1, according to Ochsner, 2018). The british company Star Refrigeration (Star, 2016) offers the ammonia based "Neat Pump" for supply temperatures of up to 90 °C and a heating capacity in between 380 kW and 6 MW. In terms of R744 (CO_2), Engie (2018) provides the high temperature heat pump "thermeco2" (previously offered by Dürr, see Figure 2.6) for supply temperatures up to 110 °C and a heating capacity from 50 kW up to 1.1 MW. As already mentioned above, the norwegian company Viking Heat Engines has introduced the so called "Heat Booster". Heating capacities up to 200 kW and supply temperatures of up to 150 °C using the refrigerant R1336mzz(Z) can be realised. The comprehensive study by Arpagaus et al. (2018b) has classified the commercially available (as in 2018) high temperature vapour compression heat pumps by supply temperature, heating capacity and compressor type (see Figure 2.6).

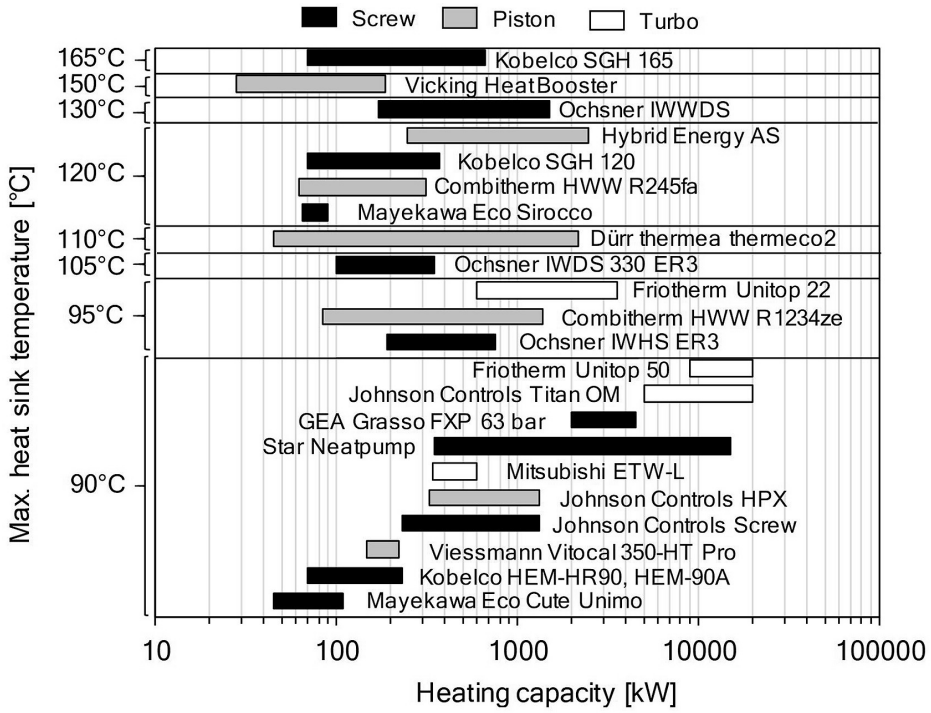

Figure 2.6: Commercially available high temperature heat pumps classified by maximum supply temperature, heating capacity and compressor type (Arpagaus et al., 2018b)

According to Arpagaus et al. (2018b), the high temperature heat pump by Japanese company Kobelco reaches the highest supply temperatures of 165 °C by providing low pressure steam of 120 °C with a vapour compression cycle using R245fa and a subsequent mechanical vapour recompression (MVR) to achieve 165 °C. CO_2 heat pumps by Mayekawa can provide supply temperatures up to 120 °C. Figure 2.6 includes the absorbtion-compression (hybrid) heat pump by the Norwegian company Hybrid Energy using ammonia and water as refrigerants for providing supply temperatures up to 120 °C. Natural refrigerants in commercial

high temperature heat pumps are almost exclusively R717 (Ammonia) and R744 for supply temperatures up to 90 and 120 °C (i.e. GEA Grasso, Johnson Controls and Thermeco2, Mayekawa respectively). Furthermore the synthetic refrigerant R245fa is widely used in commercial heat pumps (e.g. Ochsner, Combitherm, Kobelco) Regarding cycle configurations single stage heat pumps are commonly utilized (e.g. Kobelco, Viking, GEA Grasso, Star Refrigeration, Combitherm) but also cascade and economizer systems are applied (Ochsner and Friotherm respectively).

2.5 Summary and Differentiation

The current state of the art in terms of high temperature vapour compression heat pumps regarding research activities, refrigerants and commercially available heat pumps has been outlined in the previous sections. Theoretical and experimental studies have been carried and proved that supply temperatures up to 160 °C can be achieved in a single stage vapour compression heat pump with currently available equipment using the HFO R1336mzz(Z) (Nilsson et al., 2017; Helminger et al., 2016). In research, mainly lab scale prototypes (<15 kW) are investigated utilizing a variety of compressor technologies such as scroll (Bobelin and Bourig, 2012), suction gas cooled (e.g. Bamigbetan et al., 2018b; Drexler-Schmid et al., 2017; Arpagaus et al., 2018a; Noack, 2016) and open type (Reißner, 2015) reciprocating compressors as well as screw compressors (Chamoun et al., 2014). In almost every case, a single stage cycle with internal heat exchanger with slight variations in component order, has been the configuration of choice (see Section 2.2). Regarding refrigerants the research focus has been set on "future proof" low GWP working fluids due to the increasingly restrictive legal situation (see section 2.3). Furthermore not closer specified refrigerants have been investigated (e.g. Reißner, 2015). Another family of refrigerants which has been analysed regarding high temperature heat pumps, are natural working fluids like water (R718) and n-Butane (R600). Three publications have been found regarding experimental studies on R600 high temperature heat pumps. Besides simulation and economic considerations, Drexler-Schmid et al. (2017) have been focused on the functionality and performance of the ejector compared to a standard single stage cycle. Due to problems in operation, experimental results for one operation point have been obtained and published. The pilot scale R600 high temperature heat pump by Wemmers et al. (2017) proved experimentally the supply of low pressure steam with approx. 138 °C with a single stage cycle and published COP data for five different steam pressures (50, 80, 120, 200 and 240 kPa gauge) at a constant evaporation temperature of approx. 55 °C. The study by Bamigbetan et al. (2018b) gives detailed experimental results on a R290/R600 cascade system in terms of compressor efficiencies, compressor discharge temperatures and COP in dependence of heat sink outlet temperatures.

As discussed in section 2.4, commercially available high temperature heat pumps (as in 2018) cover heating capacities in a range from 50 kW to 20 MW and can provide up to 165 °C. Refrigerants used above for supply temperatures 100 °C are basically R245fa, R1336mzz(Z) and CO_2. The single stage heat pump cycle states the most common cycle configuration applied.

In the course of this project, the masterthesis of Verdnik (2017) contributed significantly to the start up phase of the prototype and provided first experimental results. The present thesis extends the work of Verdnik (2017) by providing a detailed experimental and theoretical analysis, on different heat pump cycle configurations (Basic, IHX), operational boundary conditions and application cases. An investigation of a single stage R600 heat pump providing a supply temperature of up to 110 °C as conducted within this thesis could not, to the best knowledge of the author, be found in open literature (as in 2020). Furthermore, the

application and experimental analysis of a customary designed heat exchanger in order to facilitate suction gas cooling with a separating hood compressor states a novelty compared to the currently used directly cooled (refrigerant is in direct contact with the compressor motor coils) semi hermetic compressor technology.

3 FUNDAMENTALS

3.1 Thermodynamics of the vapour compression cycle

3.1.1 The Carnot cycle

Based on experience, the second law of thermodynamics describes the basic principles of transforming mechanical energy (work) into thermal energy (heat). The postulate of the second law based on Clausius is expressed by the following statement (Fermi, 1956, p. 30):

"A transformation whose only final result is to transfer heat from a body at a given temperature to a body at a higher temperature is impossible"

A basic heat pump process thus seems to violate the second law of thermodynamics by absorbing heat at a certain temperature T_C and rejecting heat at higher temperature T_H. However, the final result in this case is not solely the described transfer of heat but also the application of mechanical work (w) in order to realize such a process (Bosnjakovic, 1998). A reversible heat pump or refrigeration process can then be described by the well known Carnot cycle. The underlying changes of state are depicted in Figure 3.1 in a T/s diagram.

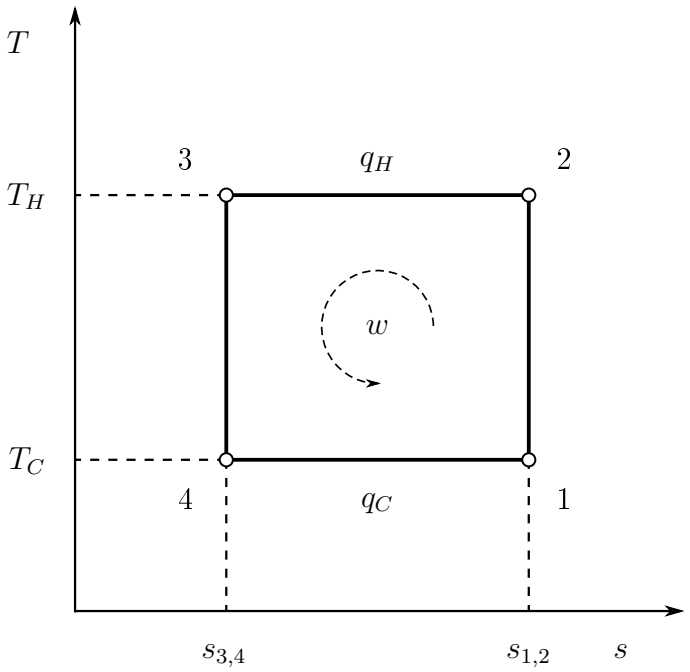

Figure 3.1: T/s diagram of a Carnot cycle

In order to realize the increase in exergy of heat (corresponding to an increase of temperature), the Carnot cycle has to be performed counter clockwise and consists of the following changes of state and their idealisations (Fermi, 1956; Feynman et al., 2007):

- isentropic compression (states 1 to 2): An ideal fluid undergoes a reversible compression without friction losses and heat transfer to the surrounding
- isothermal heat rejection at T_H (states 2 to 3): The heat sink is considered of infinite size, therefore the temperature T_H remains constant during the heat rejection
- isentropic expansion (states 3 to 4): An ideal fluid undergoes a reversible expansion without friction losses and heat transfer

- isothermal heat absorption at T_C (states 4 to 1):The heat source is considered of infinite size, therefore the temperature T_C remains constant during the heat absorption.

The Carnot cycle provides a scale for the improvement potential of real heat pump cycles and yet shows the ultimate limit which cannot be reached in real applications. However, it makes different cycle configurations and realized plants comparable. The main performance indicator in this regard is the Coefficient of Performance (COP). Therefore the Coefficient of Performance of the Carnot (COP_{Ca}) cycle shall be briefly derived and discussed. Applying the first law of thermodynamics to the above described cycle (see Figure 3.1), Equation 3.1 holds the connection between thermal energy (q) and work (w).

$$q_C - q_H + w = 0 \tag{3.1}$$

The change of the specific entropy (ds) can further be written with equation 3.2 as the the variation of the reversible heat (δq_{rev}) divided by the temperature T at which the heat is transferred (see e.g. Bosnjakovic, 1998; Baehr and Kabelac, 2006).

$$ds = \frac{\delta q_{rev}}{T} \tag{3.2}$$

The COP for heating purposes (index H) considering any heat pump cycle can be formulated with equation 3.3 as the ratio between the specific heating capacity (q_H) and the required compression work (w).

$$COP_H = \frac{q_H}{w} \tag{3.3}$$

Combining equations 3.1, 3.2 and 3.3 and keeping in mind that all changes of state are reversible, the well known relation for the efficiency of the Carnot heat pump cycle ($COP_{Ca,H}$) can be established as follows.

$$COP_{Ca,H} = \frac{q_H}{q_H - q_C} = \frac{T_H \cdot \Delta s}{(T_H - T_C) \cdot \Delta s} = \frac{T_H}{T_H - T_C} \tag{3.4}$$

Equation 3.4 shows the fundamental connection between temperature lift and the cycle efficiency. Considering high temperature heat pumps, large temperature lifts might be required, however are not favourable regarding cycle efficiency. Therefore it is necessary to keep the temperature lift as small as possible for the given boundary conditions.

3.1.2 The ideal vapour compression refrigeration/heat pump-cycle

As stated above the Carnot cycle constitutes the ideal refrigeration/heat pump cycle using an ideal working fluid. A practical heat pump process requires some modification in order to be technical feasible. First of all, working fluids of different kinds are utilized in refrigeration/heat pump cycle showing real fluid behaviour (e.g. see Section 3.6). Transport properties of these fluids are dependent on the thermodynamic state and in case of mixtures also on the composition. In a vapour compression cycle considering a real fluid, phase changes of the refrigerant occur during operation. At the heat source, the absorption of thermal energy is facilitated by evaporation of the refrigerant. In the heat sink the heat is rejected mainly by condensation. Since pressure and temperature are not independent in the vapour/liquid equilibrium the high and low pressure are determined by the heat source and sink temperatures. Thus starting the thermodynamic cycle at the saturated vapour line of an arbitrary refrigerant, an isentropic compression leads to a superheated state at the end

of the compression (states 1 to 2is, Figure 3.2). The refrigerant is then assumed to be cooled down following an isobaric change of state until the saturated vapour line is reached and is assumed to subsequently condensate until the saturated liquid state is attained (states 2is to 4, Figure 3.2). In contradiction to the Carnot process, the expansion work is not recovered in the ideal vapour compression cycle, since the potential of the recoverable expansion work is strongly dependent on refrigerant properties and the operation point of the heat pump (see e.g. Lawrence and Elbel, 2019). Expansion devices such as turbines, expander and ejectors can be complex and in cases, expensive components (see e.g. Murthy et al., 2019; Elbel and Lawrence, 2016). Therefore the cost versus benefit issue of such devices has to be considered. As a practical alternative, an expansion valve represented by an isenthalpic change of state is considered (states 4 to 5, Figure 3.2). Finally, the refrigerant expands into the two phase region and is subsequently evaporated until the initial state is attained again (states 5 to 1, Figure 3.2).

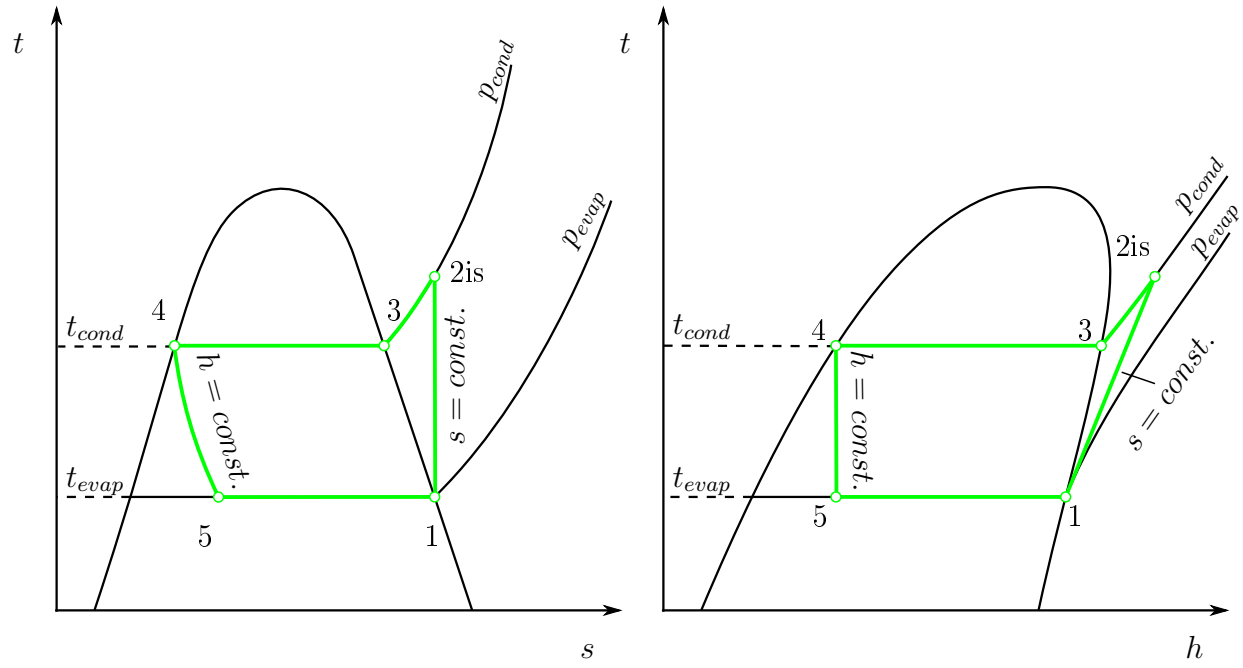

Figure 3.2: t/s and t/h diagram (left and right respectively) of an ideal vapour compression cycle (Perkins/Evans-Cycle) with real working fluid

The specific heating capacity (q_H) of the ideal cycle can be expressed by the enthalpy difference across the condenser (see Figure 3.2) by applying the first law of thermodynamics for a steady state, open system (Equation 3.5).

$$q_H = h_{2,is} - h_4 \tag{3.5}$$

The theoretical isentropic compression work (w_{is}) can be determined analogous and thus Equation 3.6 yields the following relation.

$$w_{is} = h_{2,is} - h_1 \tag{3.6}$$

Taking the general expression for the heat pump cycle efficiency of Equation 3.3 combined with Equations 3.5 and 3.6 yields the efficiency of the ideal vapour compression cycle ($COP_{H,th}$, Equation 3.7).

$$COP_{H,th} = \frac{q_H}{w_{is}} = \frac{h_{2,is} - h_4}{h_{2,is} - h_1} \tag{3.7}$$

The efficiency of the ideal vapour compression cycle is still a function of the temperature lift, however in contrast to the Carnot cycle, also a function of the refrigerant (see Domanski et al., 2014). An important consequence of this fact is, that different operating conditions require different refrigerants in order to yield the highest efficiency (compare to Section 2.3).

3.1.3 The real vapour compression refrigeration/heat pump-cycle

As discussed before, the Carnot and the ideal refrigeration cycle are a purely thermodynamic point of view which shows the ultimate thermodynamic limit of a heat pump. When it comes to the realization of a heat pump, certain components such as heat exchangers, valves, pipes and compressors are required, which cannot be considered ideal. In order to increase the refrigerant pressure, a compressor is required (e.g. reciprocating compressor). Since the real compression process is whether adiabatic, nor frictionless, a true reversible change of state cannot be realized. Therefore a polytropic compression will be the result as depicted in Figure 3.3 (see also Section 3.3). Furthermore pressure drops will arise at the inlet and outlet valves of the compressor (Maurer, 2016). In terms of heat transfer at the source and sink several aspects have to be considered. In order to exchange heat between two working fluids (i.e refrigerant and source/sink medium) without mixing them or bringing them into direct contact, heat exchangers (e.g. plate heat exchangers) of a finite area and a certain geometry have to be applied. Since the area of the heat exchanger is finite and the heat transfer coefficient is limited based on flow rate, thermodynamic state (e.g. temperature, pressure, phase, concentration, etc.), fluid and structure material properties as well as geometry (see Sections 3.2.2 and 3.2.3) a certain temperature difference remains between sink or source fluid and the refrigerant which causes an increase of the temperature lift of the heat pump cycle. This temperature difference states the minimum temperature difference (pinch point temperature difference) in the considered heat exchanger. The location where this pinch point occurs is dependent on the temperature characteristics of the heat sink and source as well as of the refrigerant and thus dependent on the thermal capacity flow of each medium (see Sections 3.2.2 and 3.2.3). The single and two phase flow also causes pressure drops in heat exchangers, piping and auxiliary components such as refrigerant receivers and oil separators (see also Sections 3.5 and 4.5). Heat losses to the ambient of components are an additional deviation from the ideal heat pump, especially interesting in high temperature applications. High pressure liquid receivers or low pressure accumulators are required in a heat pump cycle to balance the refrigerant mass in different cycle components for varying operation points (see Section 3.5). Compressors, depending on the type (piston, screw, scroll, etc.), are more or less sensitive to liquid droplets in the suction gas. Therefore a sufficient superheat of the suction gas has to be maintained in order to avoid the compression of incompressible liquid causing so called "liquid slugging" and thus compressor damage. In an ideal cycle, saturated liquid at the outlet of the condenser is assumed. Without a liquid receiver, however, this state is difficult to achieve since the outlet state is determined by heat transfer, refrigerant charge, flow rate and temperature characteristics of both, refrigerant and sink medium. The result is a certain degree of subcool which can be beneficial due to the increase of enthalpy difference across the condenser. However it also can be counter productive at low heat sink temperature differences (or a constant temperature, e.g. evaporation) by increasing the condensation temperature (see Sections 3.2.3). Considering most of these aspects a real heat pump cycle along with the hydraulic layout is depicted in Figure 3.3.

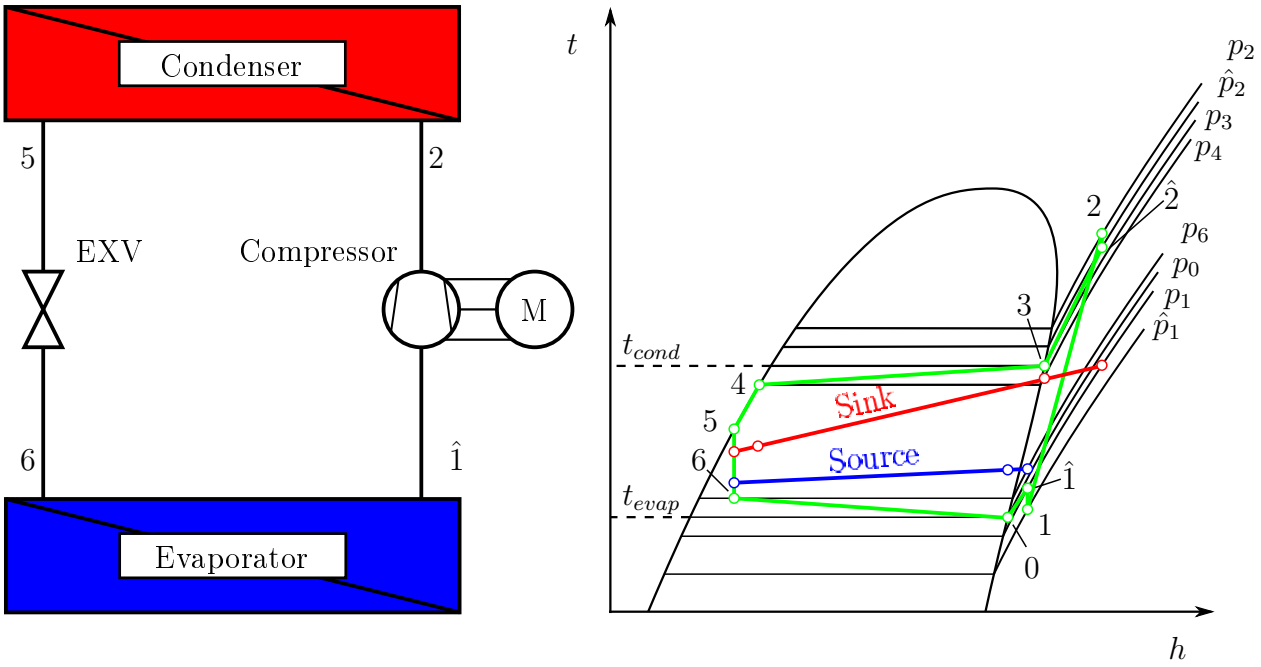

Figure 3.3: Hydraulic layout (left) and t/h diagram (right) of a real single stage vapour compression cycle

The consequence of the discussed irreversibilities is of course a reduced cycle efficiency. The COP thus is not longer solely a function of the refrigerant and the temperature lift, but also dependent, for instance on component geometry, ambient conditions, transport properties and flow patterns. The efficiency of a real vapour compression heat pump cycle ($COP_{w,H}$) can thus be expressed by Equation 3.8 as the ratio of heating capacity transferred to the heat sink ($\dot{Q}_{w,H}$) and the total electrical consumption of the compressor ($P_{el,comp}$).

$$COP_H = \frac{\dot{Q}_{w,H}}{P_{comp,el}} \tag{3.8}$$

How the heating capacity and the electrical consumption of the compressor is defined as well as the thermodynamics behind them will be discussed in Sections 3.2.3 and 3.3 respectively.

3.2 Heat Exchangers in Vapour Compression Cycles

As stated above, via heat exchangers in vapour compression cycles the refrigerant absorbs heat from a source and rejects it to a heat sink. Furthermore so called internal heat exchangers can be used to transfer heat from the high pressure side of the vapour compression cycle to the low pressure side in order to increase efficiency and/or provide sufficient superheat at the compressor inlet. During the heat transfer, the different media such as the refrigerant and source or sink fluids undergo different changes of state and/or temperature. A thermodynamic description of those changes is required to design and analyse the heat pump process as well as to set up an appropriate simulation model and shall therefore be discussed in the following sections. Many types of heat exchangers exist for example "shell and tube" or compact heat exchangers of the brazed plate type (BPHE). Furthermore different types of flow arrangements such as counter, cross or parallel flow with all their advantages and disadvantages can be distinguished. A comprehensive source of information on different heat exchanger types and their design is provided by Shah and Sekulic (2003) for example. However, the focus of this section shall lie on thermodynamic basics to describe heat exchangers in regard to the experimental analysis of Chapter 5 and the simulation model of Chapter 6.

3.2.1 General Aspects of Heat Exchangers

As Baehr and Kabelac (2006) state, a heat exchanger is an apparatus in which heat is transferred from a fluid stream with a higher temperature to a fluid stream with a lower temperature separated by some kind of structure or wall. Figure 3.4 shows the schematic of a counterflow heat exchanger with the corresponding idealized $t/\dot{Q}$ diagram ($\dot{Q}/\dot{Q}_{hx}$ describes the fraction of the heat transferred at the current temperature difference and total transferred heat across the heat exchanger).

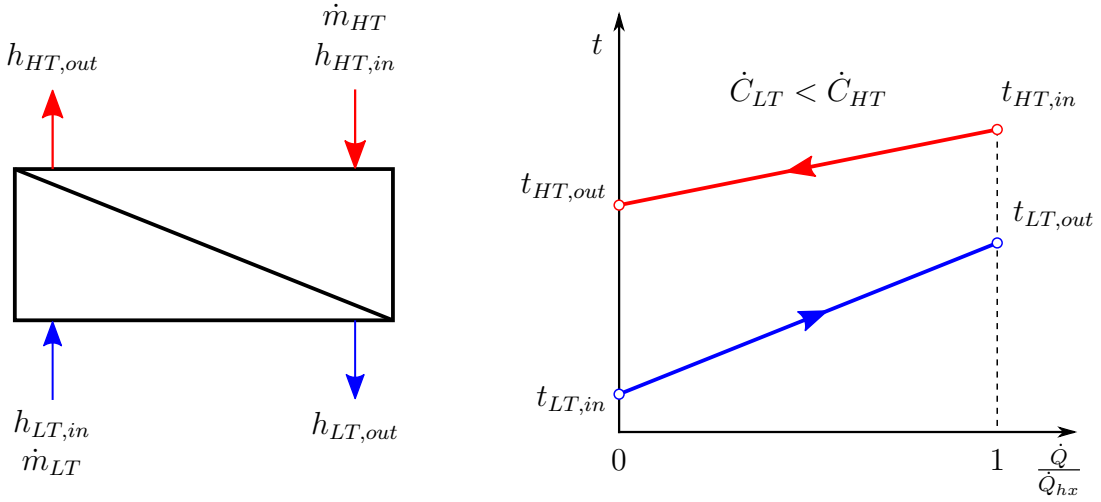

Figure 3.4: Schematic of a counter flow heat exchanger (left) and corresponding t/Q diagram (right)

The most basic thermodynamic description of a heat exchangers states the energy transferred across each fluids system boundaries. For an open steady system which does not perform any form of work, according to Figure 3.4, the energy balances can be written as the product of the respective mass flow ($\dot{m}_i$) and the enthalpy (h_i) difference across the heat exchanger.

$$\dot{Q}_{HT} = \dot{m}_{HT} \cdot (h_{HT,in} - h_{HT,out}) \tag{3.9}$$

$$\dot{Q}_{LT} = \dot{m}_{LT} \cdot (h_{LT,out} - h_{LT,in}) \tag{3.10}$$

With indexes HT referring to the fluid of higher temperature and LT to the fluid of lower temperature. Finally, neglecting heat losses, the energy balance across the entire heat exchanger leads to the combination of Equations 3.9 and 3.10.

$$\dot{m}_{HT} \cdot (h_{HT,in} - h_{HT,out}) = \dot{m}_{LT} \cdot (h_{LT,in} - h_{LT,out}) \tag{3.11}$$

If the fluid streams undergo a change of state in the single phase region and pressure changes are neglected, the enthalpy differences can be expressed by the specific heat at constant pressure c_p and the temperature difference of the considered fluid stream. Equation 3.11 therefore converts into Equation 3.12.

$$\dot{m}_{HT} \cdot c_{p,HT} \cdot (t_{HT,in} - t_{HT,out}) = \dot{m}_{LT} \cdot c_{p,LT} \cdot (t_{LT,in} - t_{LT,out}) \tag{3.12}$$

In general the specific heat capacity for pure fluids is a function of pressure and temperature. In the liquid phase however the pressure dependency can mostly be neglected (Kleiber and Joh, 2006). For a change of state in the gaseous phase the pressure dependency might be considered. A very common and simplified way to account for the temperature dependency

is to use the average temperature between inlet and outlet as given in Equation 3.13 (see also Gnielinski, 2006 or Baehr and Stephan, 2010).

$$\bar{c}_{p,i}(t_m) = f\left(\frac{t_{in} + t_{out}}{2}\right) \tag{3.13}$$

According to Bergman et al. (2011) the heat transferred in a heat exchanger $\dot{Q}_{hx}$ can be described as a function of a overall heat transfer coefficient U_{hx}, the effective area A_{hx} of the heat exchanger and a certain temperature difference ΔT_m given by Equation 3.14 .

$$\dot{Q}_{hx} = U_{hx} \cdot A_{hx} \cdot \Delta T_{m,j} \tag{3.14}$$

While the considered temperature difference $\Delta T_{m,j}$ can either be defined locally with an assumed constant heat transfer coefficients since temperature differences change across the flow path as depicted in Figure 3.4 or overall values might be considered since they are easier accessible for heat exchanger analysis. The "Logarithmic Mean Temperature Method" (LMTD) constitutes a prominent approach to define an overall mean temperature difference along the heat exchanger flow path. The LMTD has been derived for counter and parallel flow heat exchangers by many authors for example Shah and Sekulic (2003), Bergman et al. (2011) or Baehr and Stephan (2010). A very important aspect of the LMTD-Method and of its derivation is the assumption of a constant overall heat transfer coefficient and a constant specific heat capacity along the heat exchanger flow path. Equation 3.15 describes the logarithmic mean temperature difference $\Delta T_{m,log}$ as given below for the counterflow case (cf) referring to Figure 3.4.

$$\Delta T_{m,i} = \Delta T_{m,log,cf} = \frac{(t_{HT,in} - t_{LT,out}) - (t_{HT,out} - t_{LT,in})}{\ln \frac{(t_{HT,in} - t_{LT,out})}{(t_{HT,out} - t_{LT,in})}} \tag{3.15}$$

The temperature change of each flow stream is strongly dependent on the so called heat capacity rates $\dot{C}_i$ as depicted in Figure 3.5 (see e.g. Bergman et al., 2011).

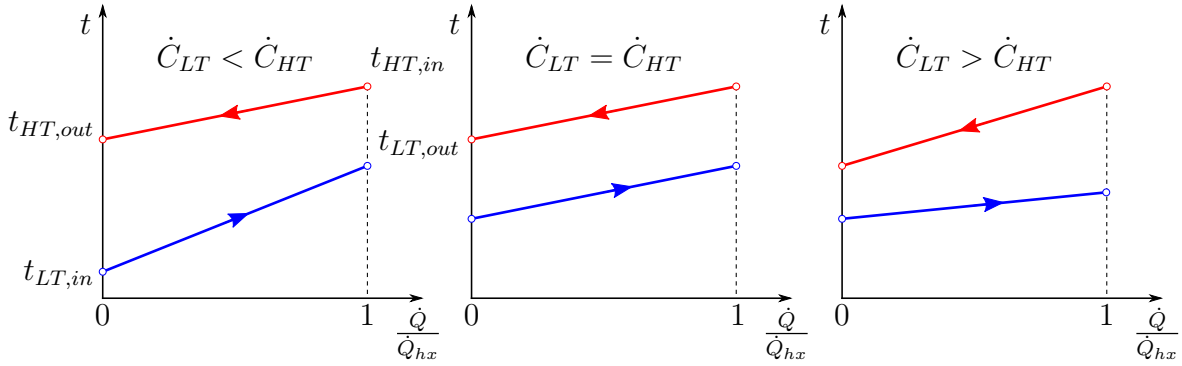

Figure 3.5: Temperature characteristics as a function of transferred heat flux for a counter flow heat exchanger in three different cases of heat capacity rates (based on Bergman et al., 2011)

Equation 3.16 shows the heat capacity rate $\dot{C}_j$ as the product of massflow $(\dot{m}_j)$ and specific heat at constant pressure $(c_{p,j})$ where the index j can be replaced by the considered flow stream.

$$\dot{C}_j = \dot{m}_j \cdot c_{p,j} \tag{3.16}$$

In the case of identical heat capacity rates of each fluid stream the temperature difference remains constant along the heat exchanger at least theoretically. In reality however, changing

fluid properties and heat transfer coefficients are responsible for variant temperature differences along the heat exchanger. In the present work the above outlined LMTD-Method has been used to analyze the utilized heat exchangers in the heat pump test rig based on the acquired experimental data. In this particular case all input variables such as massflow, fluid properties and temperatures are at disposal to calculate either an overall heat transfer coefficient ($U_{hx,j}$) or the product $U_{hx,i} \cdot A_{hx,j}$ for different heat exchanger sections (e.g. subcooler or condenser respectively, see Chapter 6). For the simulations described in Section 6 the well known "Effectiveness/NTU-Method" (ε/NTU) has been utilized to model the appliedjeat exchangers. The basic premise of this approach is to define a maximum transferable capacity $\dot{Q}_{hx,max}$ of the considered heat exchanger. According to Shah and Sekulic (2003) and Bergman et al. (2011) this maximum heat flux is connected via a factor called "effectiveness" (ε) to the actual heat flux $\dot{Q}_{hx}$ transferred by the heat exchanger as given by Equation 3.17.

$$\dot{Q}_{hx} = \varepsilon \cdot \dot{Q}_{hx,max} \tag{3.17}$$

The theoretically maximum achievable capacity can be the defined as the product of the lower heat capacity rate of both fluid streams ($\dot{C}_{min}$) and the assumption of the outlet temperature of the lower capacity rate side reaching the inlet temperature of the higher capacity rate side in a counterflow heat exchanger, this assumption corresponds to a heat exchanger of infinite size. Equation 3.18 shows the relationship.

$$\dot{Q}_{hx,max} = \dot{C}_{min} \cdot (t_{HT,in} - t_{LT,in}) \tag{3.18}$$

As also shown by many authors (e.g. Baehr and Stephan, 2010) the effectiveness ε for any type of heat exchanger (e.g. counter-, parallel-, crossflow) can be written with Equation 3.19 as a function of the so called Number of Transfer Units (NTU) and the ratio between the heat capacity rates of both fluid streams.

$$\varepsilon = f\left(NTU, \frac{\dot{C}_{min}}{\dot{C}_{max}}\right) \tag{3.19}$$

With NTU defined by Equation 3.20 as the ratio between the product of the overall heat transfer coefficient and heat exchanger area and the respective heat capacity rate.

$$NTU = \frac{U_{hx,j} \cdot A_{hx,j}}{\dot{C}_j} \tag{3.20}$$

The main assumptions of constant specific heat capacities and a constant overall heat transfer coefficient with this approach are identical to the LMTD-Method.The functional relationship of Equation 3.19 will be described in the following sections for each heat exchanger utilized in the investigated refrigeration cycle. Finally, the ε/NTU approach has been utilized for describing these heat exchangers in the simulation model discussed in Chapter 6. The advantages of this method are the easy implementation and the increased calculation stability with the chosen simulation software (see Chapter 6) in contradiction to the LMTD-Method described above.

3.2.2 Evaporator

In a vapour compression heat pump, heat is absorbed due to evaporation constituting the heat source of the system. This absorption takes place in a heat exchanger commonly

known as evaporator. A basic ideal evaporation process of a pure refrigerant can be considered isothermal with pressure and temperature interdependent in the two phase region. The heat transfer fluid however can undergo a temperature change if single phase heat transfer is assumed. Furthermore a counter flow arrangement shall be considered. The corresponding temperature characteristics of both fluids as a function of the transferred heat flux ($\dot{Q}_{evap}$) is depicted in Figure 3.6. In reality, pressure drops, changes in thermophysical properties with temperature and pressure as well as changing heat transfer coefficients alter the temperature characteristic . Furthermore, in many cases, so called dry expansion systems are realized, resulting in a certain degree of superheat at the outlet on the refrigerant side (see Sections 3.1.3 and 3.4) which is consequently decreasing the overall heat transfer coefficient since a section of the evaporator is occupied by refrigerant in the vapour phase displaying significantly lower heat transfer coefficients (compare to Section 6). Figure 3.6 shows on the left, a schematic of a counter flow evaporator with inlet and outlet states in accordance to Figure 3.3 in Section 3.1.3. The corresponding $t/\dot{Q}$ diagram is illustrated on the right side of Figure 3.6.

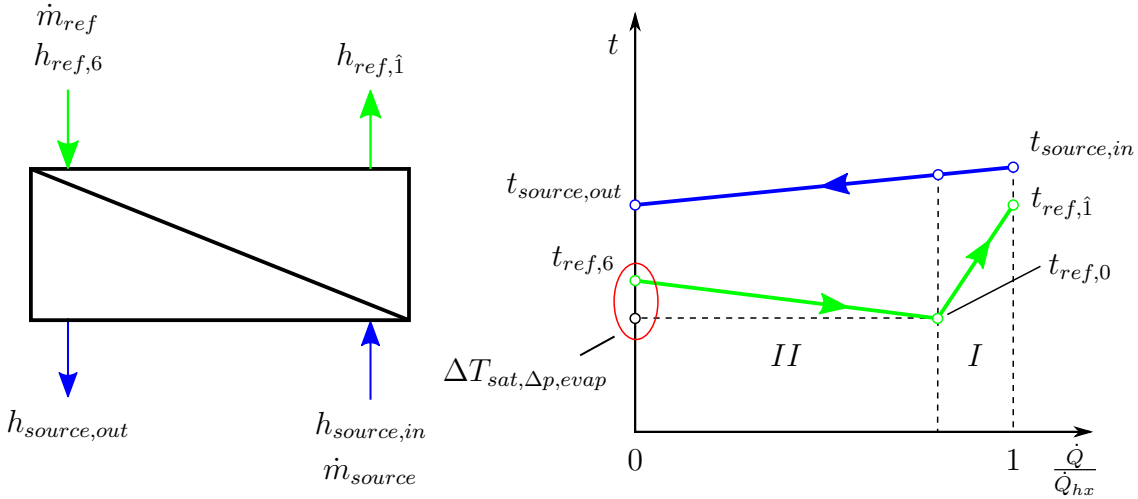

Figure 3.6: Schematic of a counter flow evaporator (left) and corresponding $t/\dot{Q}$ diagram (right) considering the pressure drop induced temperature change during evaporation

Note that the pressure drop in the evaporation section (II) induces a temperature change ($\Delta T_{sat,\Delta p,evap}$) which can be calculated as the difference of the evaporator inlet temperature $t_{ref,6}$ and the temperature of saturated vapor $t_{ref,0}$ following Equation 3.21. Since the saturation pressure or temperature ($p_{sat,ref,0}$) are in many cases very difficult to obtain experimentally and the pressure at the outlet of evaporator is more readily available, the pressure of the evaporator outlet is selected to determine the saturation temperature ($t_{evap} = t_{ref,0} \coloneqq t_{sat}(p_{ref,\hat{1}})$).

$$\Delta T_{sat,\Delta p,evap} = t_{ref,6} - t_{ref,0} \tag{3.21}$$

Theoretically, during evaporation, the specific heat of a pure fluid results to infinity and thus the heat capacity rate, since no temperature change occurs during supply of thermal energy (if the pressure drop is neglected).

As discussed in Section 3.2.1, NTU is a function of the effectiveness ε and the heat capacity rate $\dot{C}$ (see Equation 3.16). In case of a phase change of one flow stream with neglected pressure drops, the NTU characteristic simplifies to Equation 3.22 and is solely a function of the single phase flow stream regardless of the flow arrangement (see Bergman et al., 2011;

Baehr and Stephan, 2010; Shah and Sekulic, 2003).

$$NTU_{evap,II} = -\ln(1 - \varepsilon_{evap,II}) \tag{3.22}$$

Since the ε/NTU method is based on the assumption of constant heat capacity rate accross the heat exchanger, an evaporator with a superheating section has to be considered differently. Each heat exchanger section has to be modeled as a single heat exchanger connected in series (compare to Baehr and Stephan, 2010). Thus the superheating section assumed in a counterflow arrangement yields Equation 3.23 (Bergman et al., 2011) in terms of the ε/NTU method.

$$NTU_{evap,I} = \frac{1}{\frac{\dot{C}_{min,evap,I}}{\dot{C}_{max,evap,I}} - 1} \cdot \ln\left(\frac{\varepsilon_{evap,I} - 1}{\varepsilon_{evap,I} \cdot \frac{\dot{C}_{min,evap,I}}{\dot{C}_{max,evap,I}} - 1}\right) \tag{3.23}$$

The degree of superheat has a strong influence on the evaporation pressure and thus on cycle efficiency. A high degree of superheat shifts the pinch point temperature (lowest temperature difference across the heat exchanger) difference to the source side inlet of the heat exchanger in contradiction to a complete evaporation without superheat, presumably the source temperature difference remains constant. The result is a decreased evaporator heating capacity due to a decreased temperature difference in the evaporation section in combination with a significantly decreased available heat exchanger area. As a consequence the evaporation temperature decreases along with the pressure and thus the refrigerant massflow determining suction gas density. Figure 3.7 shows the comparison of temperature characteristics in an evaporator with and without superheat.

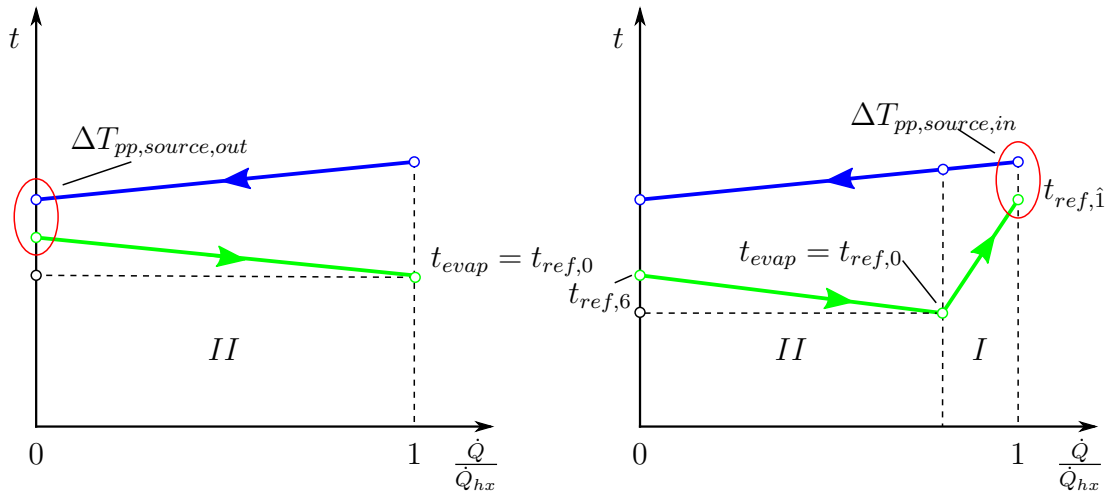

Figure 3.7: Evaporator temperature characteristics without (left) and with refrigerant superheat

The degree of (suction gas) superheat in an evaporator can then be described by Equation 3.24 as the difference between the temperature at the evaporator outlet ($t_{ref,\hat{1}}$, see Figure 3.3 and 3.6) and the saturation temperature at the pressure of the evaporator outlet ($t_{sat,ref,\hat{1}} = t_{sat}(p_{ref,\hat{1}})$)

$$\Delta T_{sup,ref,\hat{1}} = t_{ref,\hat{1}} - t_{sat,ref,\hat{1}} \tag{3.24}$$

The pinch point temperature differences can be found as the difference between source side inlet ($t_{source,in}$) and refrigerant outlet temperature ($t_{ref,\hat{1}}$) and between source side outlet ($t_{source,out}$) and refrigerant side inlet ($t_{ref,6}$), respectively, following Equations 3.25 and 3.26.

$$\Delta T_{pp,source,in} = t_{source,in} - t_{ref,\hat{1}} \tag{3.25}$$

$$\Delta T_{pp,source,out} = t_{source,out} - t_{ref,6} \tag{3.26}$$

A consequence of the reduced evaporation pressure due to superheat is the increased pressure ratio which causes a reduced volumetric, has an effect on compressor efficiency, increases specific compressor work and hence increasing compressor consumption (see Section 3.3). An important conclusion of these statements is, that at a given source temperature difference (ΔT_{source}) a certain threshold of superheat exists where a transition of the pinch point temperature difference from the source side inlet ($\Delta T_{pp,source,in}$) to the source side outlet ($\Delta T_{pp,source,out}$) of the evaporator occurs if the superheat is progressively reduced. A common premise in heat pump technology is, to choose the superheat as low as possible in order to use the given heat exchanger area most effectively (compare to Maurer, 2016). In combination with the lowest possible heat source temperature difference (ideally $\Delta T_{source} = 0\,\mathrm{K}$ e.g. during phase change) the highest possible evaporation pressure and thus cycle efficiency can be achieved. However, a degree of superheat below this approximate value has almost no influence on evaporator capacity, evaporation pressure/temperature and thus cycle efficiency. Therefore a minimum degree of superheat can be determined for each source side temperature difference which will be discussed based on experimental data and simulations in Chapters 5 and 6 respectively. This is especially of interest if superheat control stability becomes an issue which will be discussed in Section 3.4. Additionally, the combination of source side temperature difference and the degree of superheat becomes important if a certain degree of superheat is required in order to avoid a so called wet compression which will be described in Section 3.7.

3.2.3 Condenser and Subcooler

In subcritical vapour compression heat pump cycles, heat is rejected on the high pressure side via a so called condenser. A condenser can be divided into three sections which are depicted schematically in Figure 3.8. In the first section, the so called desuperheating section, hot gas leaving the compressor is cooled down by the heat transfer fluid of the heat sink until the saturated vapour curve is reached (State $\hat{2}$ to 3). Subsequently to the desuperheating, a condensation of the refrigerant takes place until the saturated liquid is reached if a complete condensation is assumed (State 3 to 4). The thermodynamic state at the end of the condensing section is strongly dependent on the temperature characteristics of the heat sink and capacity determining factors like heat exchanger area and heat transfer coefficients.

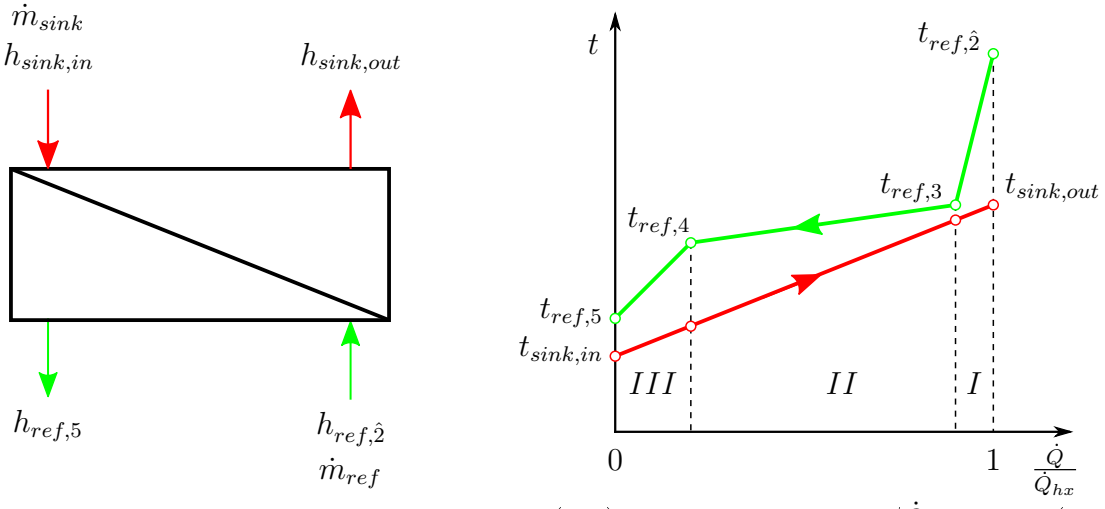

Figure 3.8: Schematic of a counter flow condenser (left) and corresponding $t/\dot{Q}$ diagram (right) considering the pressure drop induced temperature change during condensation

Thus a saturated liquid state at the outlet of the condenser is very difficult to maintain without a receiver. As a consequence either an incomplete condensation with vapour qualities (x, for definition see Section 3.5) above zero or a subcooled state (State 5) can occur. In order to describe the heat exchanger in terms of the ε/NTU-Method an analoguos approach to the evaporator can be used. The three sections of the condenser, desuperheating (I), condensation (II) and subcooling (III) can again be considered as three separate heat exchangers in series connection applying the ε/NTU approach for each section. Hence the desuperheating and subcooling section can be modeled according to Equation 3.22 as a counter flow heat exchanger. The condensing section can then be described analogous to Equation 3.21 with the assumption of an infinite specific heat and neglecting the pressure drop induced temperature difference (neglected to fit the theoretical approach). One possibility to ensure a saturated liquid state at the outlet of the condenser over a wide range of operation is provided by the use of a high pressure receiver (see Section 3.5). A subsequent heat exchanger called subcooler (SUB) can be utilized to increase the useful enthalpy difference on the refrigerant side by subcooling the saturated liquid leaving the receiver. Figure 3.9 depicts the temperature characteristics with condensation pressure drop neglected and the corresponding condenser layout utilizing a high pressure receiver (REC) with (left) and without subsequent subcooler (SUB). Pottker and Hrnjak (2015) and Pitarch et al. (2018) have shown theoretically and experimentally that a trade off between an increase of enthalpy difference and hence heating capacity due to the subcooled outlet state and an increase in condensation temperature exists as indicated in Figure 3.9. The increase of the condensation temperature is a result of a decreased temperature difference at the condensation section inlet and additionally of a decreased heat transfer coefficient due to the heat exchanger area occupied by liquid refrigerant as Pottker and Hrnjak (2015) stated, if the configuration consists only of a single condenser (see Figure 3.8). The reason for condensation temperature increase in the case of a receiver/subcooler combination (3.9) can be found in an increased heat sink inlet temperature of the condenser due to the heat absorption in the subcooler as stated by Pitarch et al. (2018).

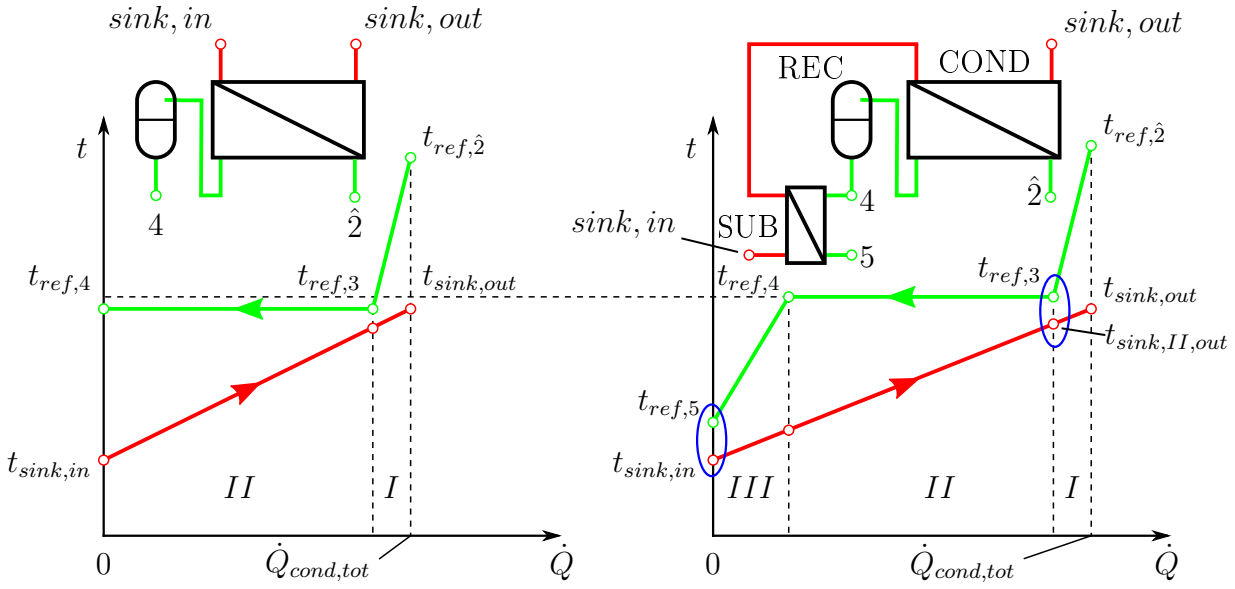

Figure 3.9: Temperature characteristic and corresponding layout of a condenser (COND) using a high pressure receiver (REC) without (left) and with subcooler (SUB, right)

The investigations of Pitarch et al. (2018), Pitarch et al. (2017a) and Pitarch et al. (2017b)

showed furthermore that the optimum degree of subcooling ($\Delta T_{sub,opt}$) is mainly dependent on the sink side temperature difference (approximated, more precisely it is the temperature difference $t_{cond} - t_{sink,in}$) and the pinch point temperature difference ($\Delta T_{pp,sink}$) because of the finite heat exchanger area. It can be estimated with Equation 3.27.

$$\Delta T_{sub,opt} \approx t_{ref,3} - t_{sink,in} - \Delta T_{pp,sink} \tag{3.27}$$

Prerequisite for Equation 3.27 is that the pinch point temperature difference $\Delta T_{pp,sink}$ is assumed to be identical at the sink side inlet and the condensing section outlet (marked blue in Figure 3.9) as defined by Equation 3.28.

$$\Delta T_{pp,sink} = t_{ref,5} - t_{sink,in} = t_{ref,3} - t_{sink,II,out} \tag{3.28}$$

Since the enthalpy of condensation decreases with increasing condensation temperature, the utilization of subcooling with the receiver/subcooler configuration can improve heating capacity and thus cycle efficiency. The influence of the heat sink temperature difference in connection with the degree of subcooling, will be discussed in Chapter 6.

3.2.4 Internal Heat Exchanger

The internal heat exchanger (IHX) transfers heat from the high pressure side to the suction side of the compressor. The refrigerant is therefore subcooled ($\Delta T_{sub,IHX}$) if a saturated liquid state is assumed at the condenser outlet (states 4 to 4′, Figure 3.10). On the low temperature side of the IHX, the refrigerant is superheated ($\Delta T_{sup,IHX}$) before it enters the compressor suction inlet (states 1 to 1′). The IHX configuration in a vapour compression cycle (left) as well as a corresponding t/h diagram (right) is depicted in Figure 3.10. The dashed lines indicate the IHX cycle with in the t/h diagram, the full lines represent the ideal vapour compression cycle of Section 3.1.2 for comparison.

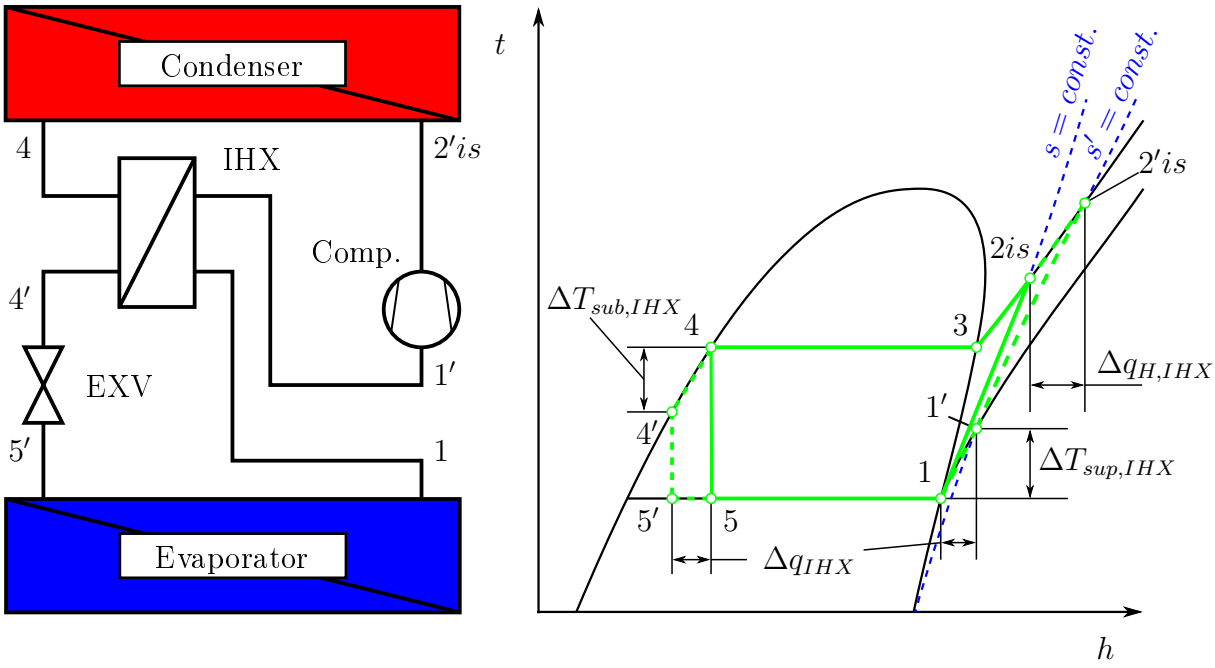

Figure 3.10: Layout (left) and simplified t/h diagram (right) of the ideal vapour compression cycle (full) and the ideal vapour compression cycle with internal heat exchanger (dashed)

Main reasons why such a heat exchanger has been applied in the past are for example, to ensure a certain degree of superheat at the compressor inlet to avoid compressor damage

due liquid droplets (compressor oil dilution, valve damage) and/or to provide a liquid or subcooled state at the inlet of the expansion device (see Domanski et al., 1994). Furthermore, regarding the refrigeration application, Domanski et al. (1994) investigated theoretically the influence of an IHX on the cycle efficiency based on the ideal vapour compression cycle described in Section 3.1.2. The results have shown that the improvement potential in terms of COP (in refrigerating case) are strongly depending on operating conditions and fluid properties and thus refrigerant. However even a negative effect of the IHX on cycle efficiency can occur. The reason can be found in taking a look on the refrigerant cycle in the t/h diagram of Figure 3.10. Due to the subcooling (state 4 to 4′) the enthalpy difference is increased in the evaporator (Δq_{IHX}). For the heat pump case, the resulting superheat at compressor inlet increases the enthalpy difference in the desuperheating section ($\Delta q_{H,IHX}$) which increases the total heating capacity in the condenser. However since the gradient of the isentropes as indicated in Figure 3.10 becomes lower with increasing enthalpy of the compressor inlet state (state 1′), the required compression work (w'_{is}) increases. The cycle efficiency of the IHX cycle can then be expressed with Equation 3.29 (compare to Equation 3.7)

$$COP'_{H,th} = \frac{q_H + \Delta q_{H,IHX}}{w'_{is}} = \frac{h'_{ref,2,is} - h_{ref,4}}{h'_{ref,2,is} - h'_{ref,1}} \tag{3.29}$$

Obviously, the IHX has a positive effect on cycle efficiency based on the ideal vapour compression cycle if Equation 3.30 holds true.

$$\frac{COP'_{H,th}}{COP_{H,th}} > 1 \tag{3.30}$$

However, as already stated in parts by Domanski et al. (1994) and Maurer (2016), the improvement potential in real applications depends on further influences. The additional pressure drop on the suction side of the compressor increases the pressure ratio hence decreasing the compressor's volumetric and isentropic efficiency as well as additionally increasing compression work (compare to Section 3.3 and Chapter 5). The pressure drop decreases the suction gas density and thus decreasing the refrigerant massflow. Furthermore the temperature increase of the refrigerant due to superheating, lowers the suction gas density which as well decreases the refrigerant massflow. Finally the increased compressor outlet temperature can be critical regarding a degradation of the compressor lubricant, especially in high temperature applications. One advantage of the IHX might not be considered in the first place if standard heat pump applications are considered. In high temperature heat pump applications, refrigerants with a so called "overhanging" 2 phase region are increasingly applied (e.g. R245fa) and require a certain degree of superheat in order to avoid a compression entering the two phase region (so called "wet compression"). The internal heat exchanger can provide the necessary superheat decoupled from the heat source which can be advantageous in terms of cycle efficiency. This aspect will be discussed in detail in Section 3.7. Regarding the mathematical description for the simulation models of Chapter 6, the energy balance and the ε/NTU relations as outlined in Sections 3.2.1 and 3.2.2 can be applied analogously.

3.3 Compressor

In the present work, an inverter driven semi hermetic separating hood compressor of the reciprocating type (see Chapter 4) is utilized in the heat pump test rig. Hence the following basics are briefly discussing important definitions and thermodynamic analysis based on that compressor type in order to understand the modeling approach and results of Chapters 5 and 6.

3.3.1 The Basic Compression Process

The basic thermodynamic change of state of the refrigerant in a compressor can be illustrated in a p/V diagram (indicator diagram) as depicted in Figure 3.11. Starting the compression process with the piston closely after bottom dead center, the refrigerant is compressed from state 1 to state $\hat{2}$. The pressure $p_{ref,\hat{2}}$ in top dead center of the compressor has to be higher than the pressure in the in the hot gas line $p_{ref,2}$ (approx. condensation pressure) in order to open the discharge valves. Due to a cylinder clearance (V_2), remaining refrigerant is expanded until state $\hat{1}$ is reached again below the suction line pressure $p_{ref,1}$ causing the suction valves to open drawing refrigerant into the cylinder, completing the working cycle. In general, the change of state during compression and re-expansion can be approximated by a polytropic due to dissipation and heat exchange across the cylinder walls (see Eifler et al., 2009).

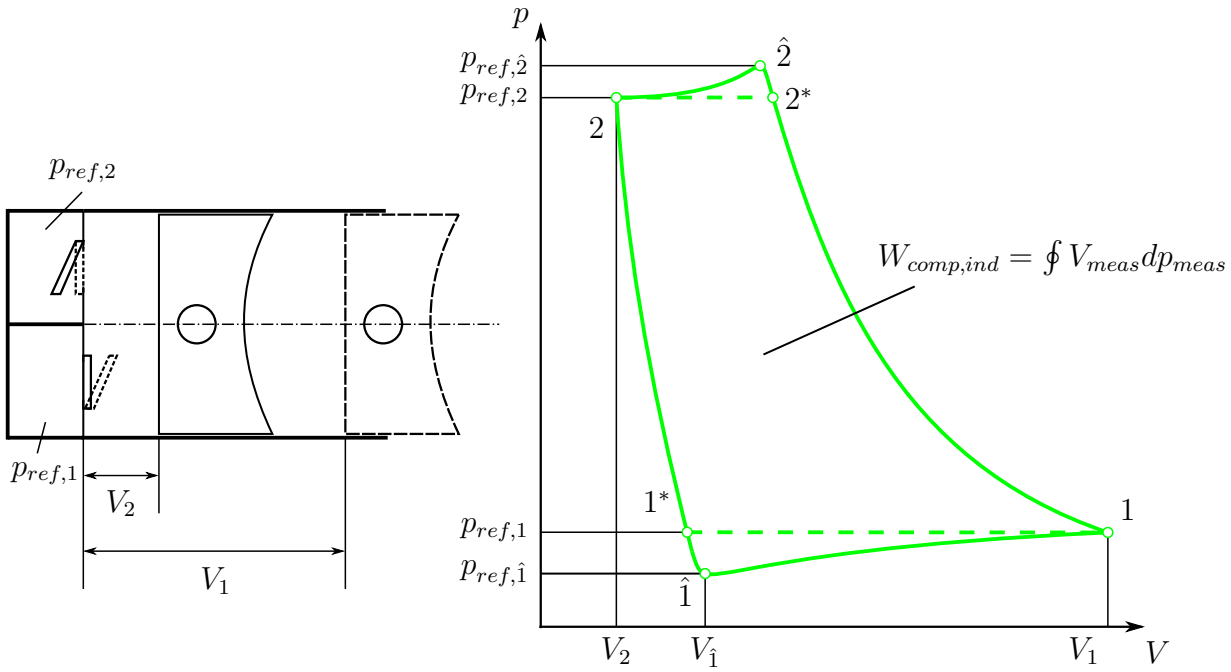

Figure 3.11: Schematical single cylinder compressor (left) and corresponding p/V diagram (right) of the compression working cycle based on Maurer (2016) and Eifler et al. (2009)

The resulting work $W_{comp,id}$ performed by the piston on the per working cycle has been derived for example by Eifler et al. (2009) based on an ideal compressor (reversible changes of state) and can be generally described by Equation 3.31 as the ring integral of the Volume V along the pressure characteristic (dp) analogously to the area enclosed by the changes of state of the real process given in Figure 3.11. The ring integral and thus the total ideal compressor work can be determined by the sum of work for each change of state during the compression process.

$$W_{comp,id} = \oint_V V \, dp = \sum W_j \tag{3.31}$$

Based on the simplifying assumption of isobaric charging and discharging processes, as indicated in Figure 3.11, the compressor work may be written with Equation 3.32 as the sum of compression work $W_{1,2^*}$, discharging work $W_{2^*,2}$, the work of re-expansion due to the

compressor clearance $W_{2,1^*}$ and finally the discharge work $W_{1^*,1}$.

$$W_{comp,id} = \underbrace{-\int_{1}^{2^*} p\,dV}_{W_{1,2^*}} + \underbrace{p_{ref,2} \cdot (V_{2^*} - V_2)}_{W_{2^*,2}} \underbrace{-\int_{2}^{1^*} p\,dV}_{W_{2,1^*}} \underbrace{- p_{ref,1} \cdot (V_1 - V_{1^*})}_{W_{1^*,1}} \tag{3.32}$$

If the p/V diagram (indicator diagram) is determined experimentally by the transient measurement of the pressure (p_{meas}) in the cylinder connected to the corresponding volume determined as a function of the crank angle and the crank drive geometry (as indicated in Figure 3.11), the indicated work $W_{comp,ind}$ can be determined analogously with Equation 3.33 and includes irreversibilities of the compression process (see Hölz et al., 2007 and Eifler et al., 2009). However, as stated by Eifler et al. (2009) a true thermodynamic description cannot be given by the indicator diagram since changes of the cylinder mass due to leakage occur and effect the cylinder pressure.

$$W_{comp,ind} = \oint_{V} V_{meas}\,dp_{meas} \tag{3.33}$$

Finally, Stouffs et al. (2001) has related the technical work of an thermodynamical open steady state flow process ($w_{comp,t}$) neglecting potential and kinetic energy (see Stephan et al., 2013), to the indicated work as given in Equation 3.34 (see also Section 3.3.2).

$$m_{ref,cyl} \cdot w_{comp,t,1,2^*} = m_{ref,cyl} \cdot \int_{p_{ref,1}}^{p_{ref,2}} v\,dp + q_{diss} \approx W_{comp,ind} \tag{3.34}$$

With $m_{ref,cyl}$ describing the representative refrigerant mass in the cylinder and q_{diss} as the dissipated energy due to friction effects, pressure and velocity distributions. Since the compression/expansion process is difficult to describe in real applications, the change of state (e.g. 1 to $\hat{2}$) can be approximated by a polytropic approach following Equation 3.35 (see Bosnjakovic, 1998 and Baehr and Kabelac, 2006).

$$p \cdot v^n = const. \tag{3.35}$$

With v describing the specific volume of the fluid. Furthermore Bosnjakovic (1998) and Baehr and Kabelac (2006) derived the compression/expansion work based on the polytropic change of with the prerequisite of a constant polytropic exponent (n). This approach is also valid for real gases since no restrictions have been made in the course of the derivation. Equation 3.36 describes the specific compression work $w_{1,2^*}$ based on a polytropic change of state.

$$w_{1,2^*} = \int_{1}^{2*} v\,dp = \frac{n}{n-1} \cdot p_{ref,1} \cdot v_{ref,1} \left[\left(\frac{p_{ref,2}}{p_{ref,1}} \right)^{\frac{n-1}{n}} - 1 \right] \tag{3.36}$$

If start and end state of the compression are obtained by measurement as described in Chapter 5, an average constant polytropic coefficient can be calculated by rearranging Equation 3.35 to 3.37 (see Baehr and Kabelac, 2006).

$$n = -\frac{\ln\left(\frac{p_{ref,2}}{p_{ref,1}}\right)}{\ln\left(\frac{v_{ref,2}}{v_{ref,1}}\right)} \tag{3.37}$$

However, as discussed by Eifler et al. (2009), the polytropic exponent n varies during the compression process itself. In the first phase of the compression, the refrigerant absorbs heat from the cylinder walls until the temperature of the gaseous refrigerant rises above the wall temperature. In the second phase, due to this increase of temperature, the heat is transported to the surrounding, cooling the refrigerant. This change of state might even reach the end point of a virtual isentropic compression, which would lead to an internal isentropic efficiency ($\eta_{is,i}$) of the compressor of 1. The definition of the internal internal isentropic efficiency and others are discussed in the following section.

3.3.2 Energy Balance and Compressor Efficiency Definitions

Thermodynamically, the compressor unit, which shall include the compressor itself, an electric drive (M) and an frequency inverter (FI) for capacity control can be considered as a steady state open system. Several system boundaries can be drawn in order to define losses in different sections of the compressor unit and thus defining different efficiency parameters. A schematic of the compressor unit including system boundaries and corresponding heat and exergy fluxes is illustrated in Figure 3.12, left.

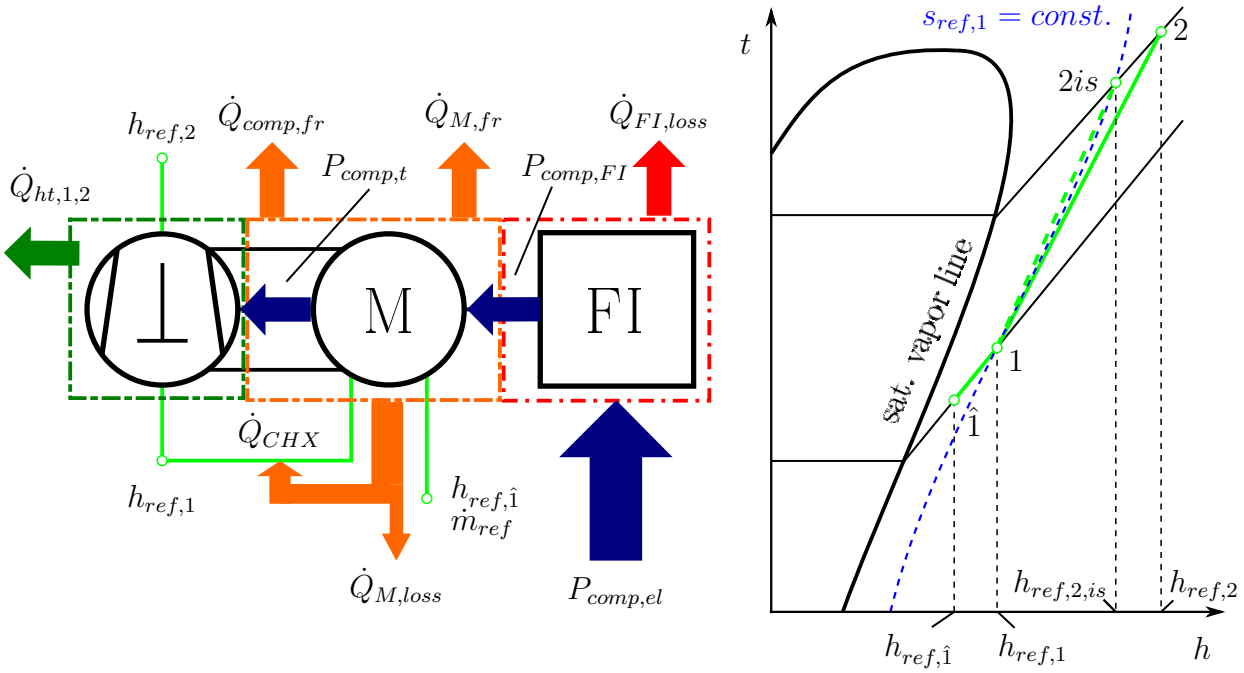

Figure 3.12: Schematic compressor unit and corresponding energy fluxes (left) and t/h diagram of the idealized change of state during the compression (based on the inlet and outlet states of the compressor)

Applying the first law of thermodynamics across the entire compressor unit, the total electrical compressor consumption $P_{comp,el}$ can be determined by the sum of entering and exiting enthalpy fluxes ($\dot{m}_{ref} \cdot h_{ref,j}$) and the sum of losses denoted by $\dot{Q}_{comp,loss}$ as described by Equation 3.38.

$$P_{comp,el} = \dot{m}_{ref} \cdot (h_{ref,2} - h_{ref,1}) + \underbrace{\dot{m}_{ref} \cdot \left(h_{ref,1} - \hat{h}_{ref,1}\right)}_{\dot{Q}_{CHX}} + \dot{Q}_{comp,loss} \tag{3.38}$$

The enthalpy fluxes entering and exiting the compressor heat exchanger (CHX, see Chapter 4) are treated separately with $\dot{Q}_{CHX}$ denoting the heat transferred from the electric drive to

the refrigerant, increasing the suction gas enthalpy from state $\hat{1}$ to 1. As discussed in Moisi and Rieberer (2016), motor heat losses based on electro-magnetic effects ($\dot{Q}_{M,el,loss,tot}$) are mainly caused by ohmic losses of the copper coils, hysteresis, stray as well as eddy current losses of the stators iron core. A part of the electrical caused heat losses of the drive however, leaves the system unused ($\dot{Q}_{M,loss}$) as indicated in Figure 3.12 due conduction within the compressor structure and ultimately convection to the surrounding. If the red and orange system boundaries of Figure 3.12 are considered, further losses can be determined in connection with the compressor drive. Additionally to the electro-magnetic losses of the motor, friction losses of moving parts such as bearings ($\dot{Q}_{M,fr}$) as well as losses of the frequency inverter ($\dot{Q}_{FI,loss}$) can be addressed. With compressor friction losses caused by, for example, crankshaft and bearings ($\dot{Q}_{comp,fr}$) and the losses during the compression process itself due to heat transfer through the cylinder walls ($\dot{Q}_{ht,1,2}$, see Equation 3.41), the total losses of the compressor unit can finally be described by Equation 3.39. Partially the heat losses are transferred to the refrigerant effecting the refrigerant enthalpy and compression work (see Equation 3.41). The described heat losses shall therefore only consider the remaining fraction transferred to the ambient since dissipated heat transferred to the refrigerant is generally not accessible for analysis.

$$\dot{Q}_{comp,loss} = \dot{Q}_{FI,loss} + \underbrace{\dot{Q}_{M,fr} + \dot{Q}_{M,loss} + \dot{Q}_{comp,fr}}_{\dot{Q}_{M,tot}} + \dot{Q}_{ht,1,2} \tag{3.39}$$

The prediction of the total compressor consumption prior to an experimental analysis would require a complex and detailed model in order to cover all aspects mentioned above. Especially electro-magnetic losses are difficult to determine analytically and are often times approximated semi empirically or simulated by finite element methods (see Moisi and Rieberer, 2016). Thus the well known efficiency approach has been selected to describe the compressor unit within the simulation model and for the experimental analysis. This approach is based on experimentally easy accessible quantities such as the inlet and outlet states of the compressor, refrigerant mass flow and the total electrical consumption. The starting point of this approach is an isentropic compression process as depicted in Figure 3.12,right. Simplifying Equation 3.38 for a reversible adiabatic open system yields the required isentropic mechanical power $P_{comp,is}$ as the product of refrigerant mass flow and enthalpy difference.

$$P_{comp,is} = \dot{m}_{ref} \cdot (h_{ref,2,is} - h_{ref,1}) \tag{3.40}$$

Considering the green system boundary in Figure 3.12, which shall enclose solely the gaseous refrigerant occupied volume from right before and after the charge and discharge valves, the energy balance shall have a slightly different starting point in order to explain the following efficiency definition. As proposed by Baehr and Kabelac (2006), the general energy balance for an open steady system in specific values regarding states given in Figure 3.12 right, connects the specific compression work $w_{1,2}$ (see Section 3.3.1, Equation 3.36), friction/dissipation within the gas $q_{diss,1,2}$ and the heat transfer across the cylinder walls $q_{ht,1,2}$ to the enthalpy change of the refrigerant as given in Equation 3.41.

$$\underbrace{\overbrace{\int_1^2 v\,dp}^{w_{1,2}} + q_{diss,1,2}}_{w_{comp,t,1,2}} - q_{ht,1,2} = h_{ref,2} - h_{ref,1} \tag{3.41}$$

The specific process losses $q_{comp,proc,loss}$ (see Equation 3.39) can then be described with Equation 3.50

$$\frac{\dot{Q}_{comp,proc,loss}}{\dot{m}_{ref}} = q_{comp,proc,loss} = q_{diss,1,2} - q_{ht,1,2} \tag{3.42}$$

The left side of Equation 3.41 can be considered as the required effort to increase the enthalpy of the gaseous refrigerant from state 1 to state 2 in a non adiabatic, irreversible compressor. As stated by Hannl (2015), the left side of Equation 3.41 can be denoted as "work induced on the refrigerant" $w_{comp,ref,i}$ since the system boundary includes only the gaseous refrigerant. Based on this assumption the so called "internal" isentropic efficiency $\eta_{is,i}$ can be defined by combining Equations 3.40 and 3.41 yielding the following relation.

$$\eta_{is,i} = \frac{P_{comp,is}}{P_{comp,ref,i}} = \frac{w_{comp,is}}{w_{comp,ref,i}} = \frac{\dot{m}_{ref} \cdot (h_{ref,2,is} - h_{ref,1})}{\dot{m}_{ref} \cdot (h_{ref,2} - h_{ref,1})} \tag{3.43}$$

Hence Equation 3.43 accounts for all effects which cause a deviation from an isentropic compression process. The internal isentropic efficiency can then be obtained experimentally by using the inlet and outlet states of the compressor as described in Chapter 5. An analogous approach can be utilized in order to account for all other irreversibilities and heat losses given in Equation 3.38 and illustrated in Figure 3.12. Considering the friction of mechanical parts as well as the motor losses which correspond to the orange system boundary, a "mechanical" efficiency η_m can be defined as the ratio between the power induced on the refrigerant of Equation 3.43 and the power supplied by the frequency inverter to the compressor motor $P_{comp,FI}$.

$$\eta_m = \frac{P_{comp,ref,i}}{P_{comp,FI}} = \frac{\dot{m}_{ref} \cdot (h_{ref,2} - h_{ref,1})}{P_{comp,FI}} \tag{3.44}$$

The inverter power can be obtained experimentally as output by the inverter itself (see Chapters 4 and 5). At this point, it is important to note that the heat absorbed by the refrigerant ($\dot{Q}_{CHX}$) in the compressor heat exchanger increasing the enthalpy from state $\hat{1}$ to 1 is not considered as benefit in Equation 3.44 thus the mechanical efficiency is related to the enthalpy difference $\Delta h_{ref,1,2}$ and not $\Delta h_{ref,\hat{1},2}$ (see Figure 3.12). In commonly applied semi hermetic suction gas cooled compressors, the refrigerant state between compressor suction chamber and motor cooling outlet is most likely not accessible compared to the present case (see Section 4.3). This would require to consider the compressor as a black box with an inlet state before the compressor motor and the compressor outlet state (states $\hat{1}$ and 2 respectively, see Figure 3.12). Based on the same approach described above, a combined change of state of superheat and compression has to be treated like a single compression process between state $\hat{1}$ and state 2. As a consequence the isentropic efficiency decreases due to the "artificially" increased compression enthalpy difference ($\Delta h_{ref,1,2} + q_{CHX}$) and simultaneously the mechanical efficiency increases because of the same reason. Considering the measured total compressor consumption as identical to both efficiency approaches the black box approach would result in a lower overall isentropic efficiency due to a lower isentropic compression work based on inlet state $\hat{1}$ because of the divergent behaviour of isentropes with increasing enthalpy. Therefore the separate analysis of the compression process has been found to be the more useful to discuss the major influences and furthermore to be more appropriate describing the compression process for the simulation model. Although the recovered motor waste heat has not been accounted for as a benefit in the efficiency considerations, ultimately it is considered in the heating capacity of the heat pump and thus in

the COP due to the increase in compressor outlet enthalpy which contributes to the heating capacity.

The last energy related efficiency η_{FI} connects the FI power to the total electrical consumption of the compressor and accounts for heat losses of the inverter (red system boundary). Equation 3.45 yields the FI efficiency with both quantities obtainable from experiment.

$$\eta_{FI} = \frac{P_{comp,FI}}{P_{comp,el}} \tag{3.45}$$

Finally, Equations 3.43, 3.44 and 3.45 can be combined to yield the overall isentropic efficiency describing all energy related losses and irreversibilities.

$$\eta_{is,ov} = \eta_{is,i} \cdot \eta_m \cdot \eta_{FI} \tag{3.46}$$

In addition to the above mentioned "energy related" efficiencies another aspect has to be considered. In real compressor applications, the actual mass flow ($\dot{m}_{ref}$) is lower than the theoretically possible mass flow ($\dot{m}_{ref,th}$). The ratio between the actual and theoretical mass flow is denoted as volumetric efficiency (λ_{vol}) and can be defined, according to Eifler et al. (2009), with Equation 3.47.

$$\lambda_{vol} = \frac{\dot{m}_{ref}}{\dot{m}_{ref,th}} \tag{3.47}$$

The theoretical mass flow can be obtained from Equation 3.49 by considering the compressor frequency f_{comp} (the slip has been neglected), the number of pole pairs of the compressor motor n_p, the suction gas density $\rho_{ref,1}$ and the geometric swept volume of the compressor V_{comp}.

$$\dot{m}_{ref,th} = \frac{f_{comp}}{n_p} \cdot \rho_{ref,1} \cdot V_{comp} \tag{3.48}$$

As stated by Maurer (2016) and Eifler et al. (2009), the volumetric efficiency is a combination of several effects such as the re-expansion due to the compressor clearance (λ_{clear}), pressure drops of the suction valve ($\lambda_{\Delta p}$) as well as heat absorption in the suction chamber (λ_T) causing a decrease of suction gas density and finally leakage effects (λ_{leak}). The volumetric efficiency can then be written with Equation 3.49 (see Maurer, 2016).

$$\lambda_{vol} = \lambda_{clear} \cdot \lambda_{\Delta p} \cdot \lambda_T \cdot \lambda_{leak} \tag{3.49}$$

A detailed description of the different influences on the volumetric efficiency has not been carried out during the course of this thesis. However the characteristics of the compressor volumetric efficiency has been determined experimentally based on Equation 3.47 and described in Chapter 5. With all the efficiencies and energy balances defined, the total electrical consumption of the compressor can be finally calculated with Equation 3.50.

$$P_{comp,el} = \lambda_{vol} \cdot \frac{f_{comp}}{n_p} \cdot \rho_{ref,1} \cdot V_{comp} \cdot \frac{(h_{ref,2,is} - h_{ref,1})}{\eta_{is,i} \cdot \eta_m \cdot \eta_{FI}} \tag{3.50}$$

This semi empirical compressor model has been parametrized based on experimental data and utilized for the cycle simulations described in Chapter 6.

3.4 Expansion Valve

Considering Carnot's cycle as discussed in Section 3.1.1 an expansion process following the heat rejection is required in order to absorb heat at a low temperature level. Theoretically this expansion work can be recovered by using expanders, turbines or ejectors. However since such devices are often times complex, costly and efficiencies are limited, simple expansion valves are commonly utilized in vapour compression heat pumps and refrigeration applications. Nevertheless ejectors are increasingly utilized in R744 (CO_2) commercial refrigeration applications (Hafner et al., 2014) and have been investigated regarding a R600 high temperature heat pump by Drexler-Schmid et al. (2017) as discussed in Chapter 2. In this present investigation the focus lies on standard expansion valves as utilized in the test rig (see Chapter 5). Thermodynamically, the flow process, respectively the change of state across the expansion valve, can be considered isenthalpic as outlined for example by Bosnjakovic (1998), based on the assumption of negligible heat losses and constant flow velocities at the inlet and outlet. Thus the thermodynamic description of an expansion valve follows Equation 3.51.

$$dh_{XV} = 0 \tag{3.51}$$

In dry expansion applications, the expansion valve controls the superheat at the outlet of the evaporator. Basically two standard solutions of expansion valves have been established in heat pump and refrigeration applications. The first type constitutes the so called Thermostatic Expansion Valve (TXV). In its simplest form, the TXV consists of a membrane with the evaporation pressure acting on one side and the pressure of a secondary fluid on the other (see e.g. Eames et al., 2014 or Mithraratne et al., 2000). The secondary fluid (or charge) is contained in a so called bulb and connected via a tube to the volume on the secondary side of the membrane. The bulb is applied on the suction line sensing the temperature of the evaporator outlet.

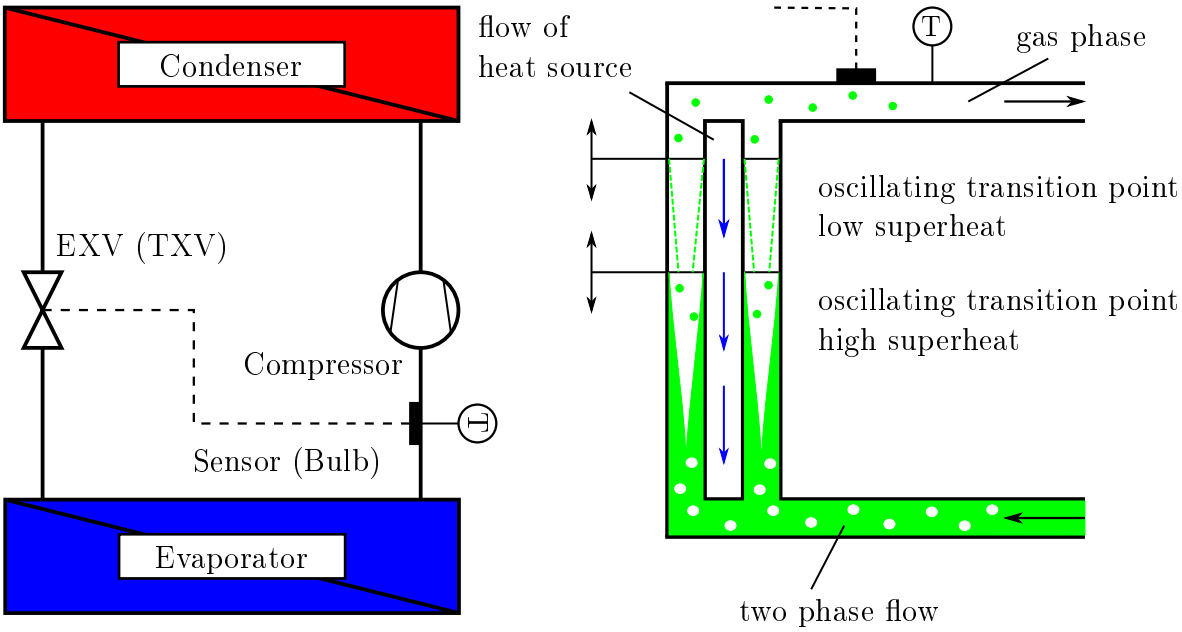

Figure 3.13: Schematic installation of the expansion valve control (left) and simplified illustration of the theory behind the hunting problem for a plate evaporator (right)

If the outlet temperature increases, due to an decrease in evaporator capacity (e.g. decrease in compressor speed), the pressure of the TXV charge increases above the evaporation pres-

sure corresponding to it's pressure/temperature characteristic and thus opening the expansion valve. A static superheat can be adjusted via spring loading the push rod of the TXV. The second expansion valve type is simply electronically controlled, with a solenoid steadily varying the valve opening and thus determining the refrigerant superheat (other drives might be considered such as stepper motors). The Electronic Expansion Valve (EXV) is controlled with a PI or PID controller (Proportional-Integral-Derivative) using the superheat signal obtained by measuring pressure and temperature at the outlet of the evaporator and calculating the corresponding saturation temperature (see Equation 3.23 and Figure 3.13). After the appropriate PID parameters are determined basically any superheat can be adjusted. However, as already mentioned in Section 3.2.2, below a certain superheat threshold, the expansion valve operation becomes increasingly unstable for both, EXV and TXV, causing the so called "hunting" problem (see e.g. Mithraratne and Wijeysundera, 2002). The "hunting" problem describes the periodical opening and closing of the expansion valve (see 3.14) due to an unstable superheat signal received from the temperature sensor (EXV) or bulb (TXV) (see Liang et al., 2010). The transition point of two phase and single phase flow within an evaporator shifts towards the evaporator outlet and thus towards the temperature sensor or bulb which provides the signal for the expansion valve control as schematically depicted in Figure 3.13, right. As reported by Wedekind and Stoecker (1968) and Wedekind (1971), this transition point is randomly fluctuating even in steady operation along the flow path. A more recent study by Huang et al. (2019) presenting optical investigations also connected an alternating flow pattern change at the outlet of an EXV with changing cooling capacity to refrigerant cycle instabilities. These fluctuations and additionally liquid droplets which might be dragged along the flow path (especially at high mass flows and thus evaporator capacities), can reach the temperature sensor, especially at a low degree of superheat when the transition point is close to the sensor as indicated in Figure 3.13 for a plate evaporator. The liquid refrigerant at saturation temperature is detected by the sensor or bulb resulting in sudden drop of the superheat signal forcing the expansion valve to close.

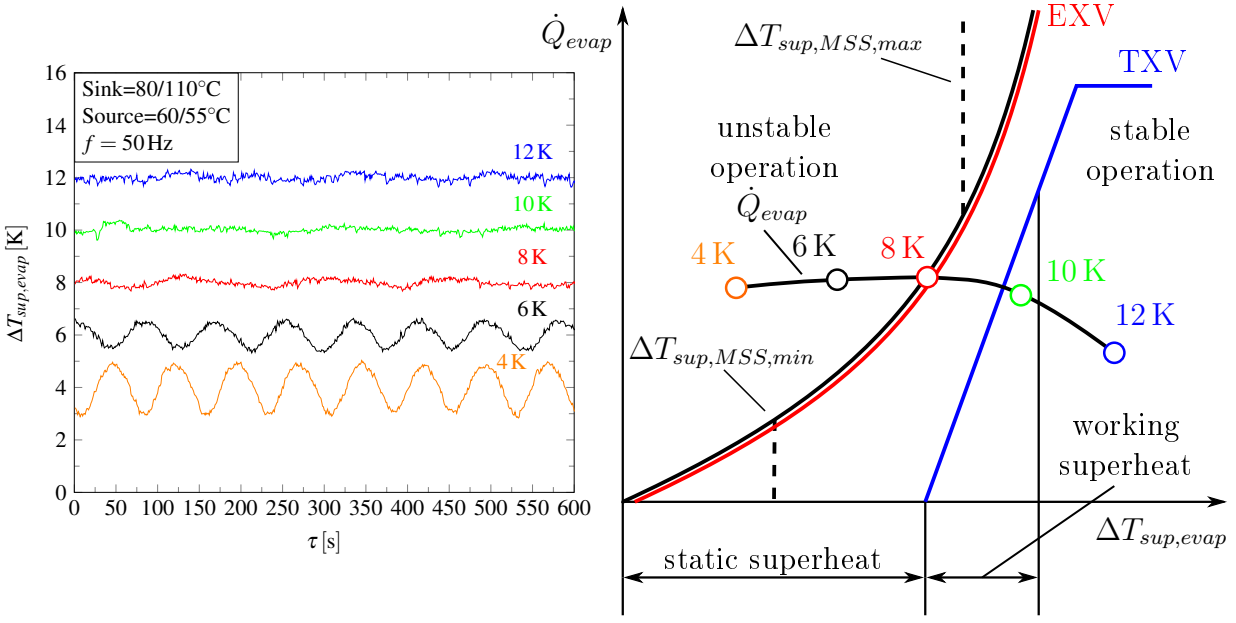

Figure 3.14: Experimental data of the superheat signal for a certain operation point and different superheat setpoints (left, see Chapter 5) and theoretical characteristic of the Minimum Stable Superheat (MSS-Theory) as a function of evaporator capacity including EXV/TXV operation characteristics and the evaporator capacity characteristic (right, own modification based on Maurer, 2016; Chen et al., 2008; Huang et al., 2019)

The superheat increases again until the set value is reached, however the transition point is to close the evaporator outlet and the same process starts again with the next liquid droplets reaching the sensor causing the expansion valve to "hunt" the superheat signal. Figure 3.14 left, shows experimental results of the superheat signal as a function of time for different superheat set points obtained with the investigated test rig for a certain operation point (see also Chapter 5). The increasing instability of the expansion valve operation with decreasing superheat can be clearly observed. The operation instability can be considered therefore more as an evaporator characteristic than a problem of the control loop or controller parametrization. Hence evaporator geometry, heat flux, heat transfer, flow velocity etc. might have a significant influence on the superheat threshold when unstable expansion valve operation starts. As reported by Chen et al. (2008), Huelle (1972) proposed firstly the so called "Minimum Stable Superheat Theory" (MSS-Theory) which describes the minimum stable superheat as a function of the evaporator capacity as depicted in Figure 3.14, right. The primary literature source however of Huelle (1972) has not been at disposal for the present thesis, therefore information from secondary sources have been utilized (e.g. Maurer, 2016; Chen et al., 2002b; Chen et al., 2008; Liang et al., 2010). The monotonic MSS line depicted in Figure 3.14, divides the operating behaviour of an evaporator into a stable and unstable region. The experimental operation points are indicated on the evaporator capacity characteristic (see Chapter 5). If the operating characteristic of a TXV crosses the MSS line, process instability occurs. EXVs can operate very close to the MSS line allowing the lowest possible degree of superheat in terms instability (see Figure 3.14) and thus increase cycle efficiency (compare to Section 3.2.2). The experimental investigations of Chen et al. (2002b) and Chen et al. (2008) confirmed the existence of the MSS line for TXV and EXV controlled systems. However Chen et al. (2008) proposed a modified MSS line based on experimental data indicating a lower and upper limit of the minimum stable superheat as depicted in Figure 3.14 ($\Delta T_{sup,MSS,min}$ and$\Delta T_{sup,MSS,max}$). As discussed in Section 3.2.2, low degrees of superheat are desired in terms cycle efficiency however restricted by the above described inherent characteristics of the vapour compression cycle. The influence of superheat on cycle efficiency and aspects of stability regarding the investigated R600 high temperature heat pump are discussed experimentally and simulation based in Chapters 5 and 6, respectively.

3.5 High Pressure Receiver

A high pressure receiver constitutes a volume containing refrigerant commonly located at the outlet of the condenser. With changing operation points, the refrigerant mass distribution within the heat pump changes depending on the density hence pressure and temperature, the heat exchanger and piping volume. The purpose of the high pressure receiver is to balance the mass migration ensuring in any considered operation point the apporpriate amount of refrigerant in the respective components (Rajapaksha and Suen, 2004). Within the operating range of the heat pump a liquid refrigerant level shall always remain in the receiver volume to ensure a liquid state at the inlet of the expansion valve. Thermodynamically the high pressure receiver determines the outlet quality of the condenser ($x_{ref,4}$, see Figure 3.15) considering a steady state operation, neglecting pressure drops and heat losses. The quality of the refrigerant is described by Equation 3.52 as the ratio between vapour ($\dot{m}_{ref,vap}$) and total refrigerant massflow ($\dot{m}_{ref}$).

$$x_{ref} = \frac{\dot{m}_{ref,vap}}{\dot{m}_{ref}} = \frac{\dot{m}_{ref,vap}}{\dot{m}_{ref,vap} + \dot{m}_{ref,liq}} \tag{3.52}$$

With a certain liquid level the refrigerant quality within the receiver can be be determined utilizing Equation 3.52 for a closed volume based on the volume of each phase ($V_{rec,vap}$,

$V_{rec,liq}$) and the density of saturated vapor and liquid ($\rho_{ref,sat,vap}$, $\rho_{ref,sat,liq}$) as illustrated in Figure 3.15.

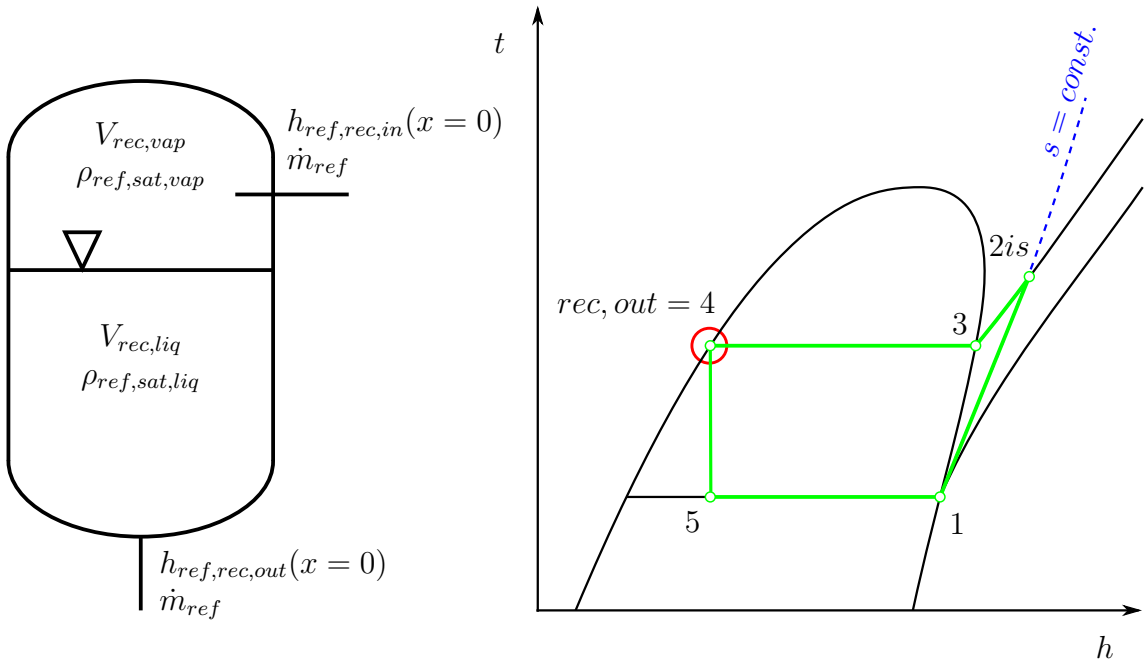

Figure 3.15: Simplified layout of a high pressure receiver with enthalpy fluxes and the corresponding t/h diagram of an ideal heat pump cycle, receiver position indicated with a red circle

Applying the first law of thermodynamics according to Figure 3.15 for a steady state open system and neglecting a heat transfer across the system boundary, Equation 3.53 yields the following relationship.

$$\dot{m}_{ref} \cdot h_{ref,rec,in} = \dot{m}_{ref} \cdot h_{ref,rec,out} \tag{3.53}$$

Since the outlet enthalpy ($h_{ref,rec,out}$) corresponds to a saturated liquid state, the inlet enthalpy must be identical according to Equation 3.53 implying an inlet vapour quality $x_{ref,rec,in}$ of zero (saturated liquid) as long as the receiver displays a distinct liquid level. The saturated liquid enters either a subcooler further decreasing the temperature or enters directly the expansion valve.

3.6 Refrigerant *n*-Butane (R600)

As already outlined in Chapter 2, different criteria apply for the selection of a suitable refrigerant. These criteria can be of the technical type such as high and low pressure limits of the compressor, environmental reasons concerning Global Warming Potential (GWP) and Ozone Depletion Potential (ODP) and thermophysical properties like critical temperature and pressure. The applied selection criteria for the present case are summarized in Table 3.1 and have been described in Moisi and Rieberer (2017).

Table 3.1: Refrigerant Selection Criteria (Moisi and Rieberer, 2017)

No.:	Characteristic	Criterion
1	Critical temperature	$t_{ref,crit} > 120\,°C$
2	Vapor pressure at 20 °C	$> 101.3\,kPa$
3	Ozone depletion potential (ODP)	0
4	Global warming potential (GWP)	< 150
5	Commercially available	yes
6	Listed in Standard EN378 (EN378, 2016)	yes
7	Threshold of high pressure	$p_{HP} \leq 2800\,kPa$
8	Threshold of low pressure	$500\,kPa \geq p_{LP} \leq 1900\,kPa$

The main criterion for the refrigerant is the critical temperature $t_{ref,crit}$ if only, like in this case, a subcritical heat pump process is considered. Therefore the threshold of the critical temperature has been set to 120 °C in order to fulfill the desired outlet temperature of 110 °C. Another aspect is the vapor pressure of the refrigerant at ambient temperature (approx. 20 °C), which is important to stay above ambient pressure in order to avoid air infiltration into the refrigerant circuit at down times of the system. Since the Montreal Protocol (UNEP, 1989) an ODP of zero is mandatory. Furthermore the Kigali amendment (UNEP, 2016) to the Montreal Protocol aims for phasing out refrigerants with a high GWP, therefore a limit of 150 has been considered (see also Calm, 2008). In order to find a certifiable heat pump concept according to EN378 (2016), the refrigerant must be commercially available and listed in the mentioned standard. Finally the considered compressor limits the high and low pressure to 2800 kPa and 1900 kPa respectively (see Chapter 4). The selection criteria had been applied to the working fluid data base of the Engineering Equation Solver Software (F-Chart, 2016) and additionally the HFO-Refrigerant R1336mzz-Z, which has not been available in the utilized software version. The entire list of investigated refrigerants can be found in Appendix A.1. Finally, based upon the criteria of Table 3.1, the hydrocarbon refrigerant *n*-Butane (R600) has been selected for the high temperature heat pump test rig. The detailed selection process has been described in Moisi and Rieberer (2017) and shall not be discussed at this point, instead some characteristics of R600 are summarized. The refrigerant *n*-Butane (R600) is a flammable non-toxic hydrocarbon (safety classification according to EN378 (2016): A3) from the group of alkanes. As an isomer of the more commonly used Isobutane (R600a), properties of R600 are very similar (Palm, 2008). As summarized by Palm (2008), Granryd (2001) and Harby (2017), the compatibility of hydrocarbon refrigerants shows no restrictions in terms of typical construction materials, however, sealing material such as EPDM, natural rubbers and silicon rubbers should be avoided. Furthermore, hydrocarbons show a high solubility in mineral oil which can be critical in terms of lubricant viscosity (Palm, 2008). With a critical temperature of 152 °C and a Normal Boiling Point of −0.53 °C, R600 fits perfectly the selection criteria of Table 3.1. Furthermore R600 shows GWP and ODP values of 3 and zero respectively. An overview on main properties of R600 can be obtained from Table 3.2.

Table 3.2: Overview on main properties of n-Butane

Property	Symbol	Value	Source
Chemical formula	-	$CH_3CH_2CH_2CH_3$	EN378 (2016)
Safety classification	-	A3	EN378 (2016)
Molar mass	M_{R600}	58.12 g/mol	F-Chart (2016)
Critical temperature	$t_{ref,crit}$	152 °C	F-Chart (2016)
Critical pressure	$p_{ref,crit}$	3796 kPa	F-Chart (2016)
Normal boiling point	$t_{ref,nb}$	−0.53 °C	F-Chart (2016)
Density at 25 °C/101.3 kPa	$\rho_{ref,amb}$	2.45 kg/m^3	EN378 (2016)
Lower Flammability Level	LFL	0.048 kg/m^3	EN378 (2016)
Global Warming Potential	GWP	3	EN378 (2016)
Ozone Depletion Potential	ODP	0	EN378 (2016)

Besides the main properties discussed above, the saturation pressure and temperature characteristic is a very important aspect in terms of refrigerant selection. In the beginning of development process, heat source and sink temperature boundary conditions are the starting point for heat pump equipment design. The resulting pressure levels and ratios are essential for compressor selection, piping and heat exchanger design. Considering the investigated test rig the pressure boundary conditions have been discussed above (see Table 3.1). In this regard, Figure 3.16 left, shows the p/t- characteristic of R600 compared to different refrigerants. A very strong difference in terms of saturation pressure/temperature for example can be observed between R600 and R717 (Ammonia). If Ammonia would have been selected for a supply temperature of 110 °C a high pressure level exceeding 5000 kPa would have been the result, which requires an above standard compressor technology (current standard approx. 3200 kPa). The high pressure level for R600 results in approx. 1800 kPa. R245fa shows a similar saturation characteristic as R600 while for R600a the pressure lies above at identical temperatures and exhibits a lower critical temperature and pressure. The HCFO R1233zd(E) would require the lowest high pressure level with approximately 1250 kPa to meet the temperature boundary condition of 110 °C.

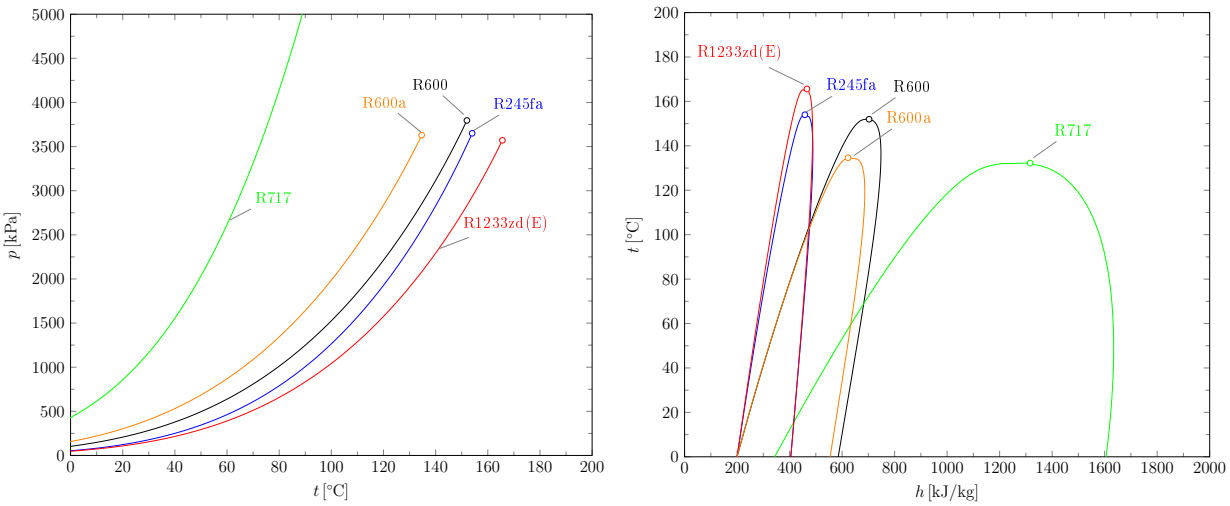

Figure 3.16: Comparison of saturation characteristics (left) and two phase regions in a t/h diagram (right) for refrigerants R600, R717, R245fa, R1233zd(E) and R600a, property data obtained from REFPROP v. 9.1 (Lemmon et al., 2013)

Regarding phase change enthalpy (Δh_{pc}), R600 lies between R717 and R245fa as depicted in Figure 3.16 right. R600a exhibits a slightly smaller two phase region than R600 resulting in a lower phase change enthalpy. A low phase change enthalpy indicates a higher refrigerant mass flow for a given heating capacity which in combination with the suction gas density influences the compressor size (see Chapter 2, volumetric heating capacity). Furthermore the shape of the two phase region can have a significant effect on heat pump operation. As depicted in Figure 3.16 the slope of saturated vapour line appears rather different between R600 and R717. For R600, isentropic characteristics can cross the saturated vapour line leading to a so called "wet compression" as already mentioned in Section 3.2.2. R717 however does not exhibit this behaviour which is a consequence of shape of the two phase region. This aspect has been considered as a central point for the test rig design and operation of the present thesis and shall be discussed in detail in Section 3.7.

3.7 Required Superheat

In high temperature heat pump applications, suitable refrigerants often times exhibit a so called "overhanging" two phase region. The term "overhanging" particularly describes the shape of the saturation lines in a t/s diagram as depicted for example in Figure 3.17 for R600 compared to the "bell" shaped phase boundary of R717.

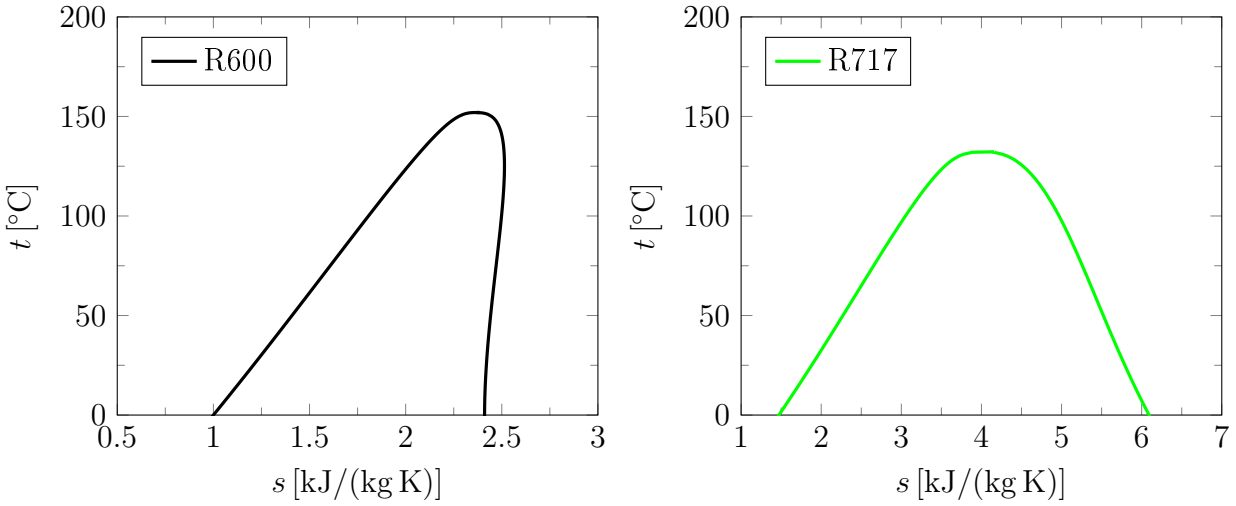

Figure 3.17: Overhanging shape of the two phase region of R600 (left) compared to the "bell shaped" phase boundary of R717 (right), property data based on Lemmon et al. (2013)

Morrison (1994) theoretically investigated the reason for working fluids exhibiting a certain form of saturation boundary and concluded that with increasing molecule complexity, working fluids are more likely to display, as described by (Morrison, 1994, p.503), a *"re-entrant vapour phase $T-S$ diagram"*. The starting point of Morrison (1994) investigation is the total differential of the molar entropy regarding temperature and molar volume ($S_m(T, V_m)$), leading to change of entropy with respect to the temperature at the saturation boundary (σ). In combination with the Maxwell relation $(\partial S_m/\partial V_m)_T = (\partial p/\partial T)_V$ (p denotes pressure) and the partial differential of the entropy with respect to temperature at constant volume $(\partial S_m/\partial T)_V = C_{m,V}/T$ (see Baehr and Kabelac, 2006) the phase boundary in a temperature/entropy diagram can be described by Equation 3.54.

$$\left.\frac{dS_m}{dT}\right|_\sigma = \left[\frac{1}{T}\cdot C_{m,V} + \left(\frac{\partial p}{\partial T}\right)_V \left.\frac{dV_m}{dT}\right|_\sigma\right] \tag{3.54}$$

Morrison (1994) has qualitatively analysed both terms on the right hand side of Equation 3.54. The first term $C_{m,V}/T$ is always positive as a result of the second law of thermodynamics (see Baehr and Kabelac, 2006). Typically the pressure increases with temperature at constant volume thus $(\partial p/\partial T)_V$ is positive. The change of the volume on the saturated vapour boundary with respect to temperature is negative resulting in a negative product. Hence the absolute values of the first and the second term determine whether the saturated vapour boundary is in parts overhanging (positive inverse slope, $dS_m/dT > 0$), bell shaped (negative inverse slope, $dS_m/dT < 0$) or even isentropic ($dS_m/dT = 0$) (see also Reißner, 2015). As furthermore stated by Morrison (1994) that the second term is similar from fluid to fluid, the dominant factor for the likeliness of overhanging two phase region is the specific isochoric heat capacity. Since in many cases, with increasing molar mass and thus molecule complexity, $C_{m,V}$ increases, the more likely an overhanging saturation boundary manifests. Based on property data, Reißner (2015) correlated the specific molar isochoric heat capacity of natural refrigerants (e.g. R601, Cyclopentane, R718, R717), HFO's (e.g. R1234ze, R1234yf), HFC's (e.g. R245fa, R236fa, R236ea) and not closer defined experimental refrigerants (MF2, MF3, LG6), confirming this statement. Furthermore Reißner (2015) has used a simplified approach to calculate the inverse slope ($IS \approx dS_m/dT$) for a set of synthetic high temperature working fluids and a saturation temperature of 80 °C, showing a linear correlation with increasing $C_{m,V}$ which agrees with the statements of Morrison (1994). Figure 3.18 depicts different compression processes in a t/s diagram of R600 underlying the determination of the required superheat $\Delta T_{req,sup}$ including a wet compression (red). The consequence of the overhanging phase boundary is the possibility of refrigerant condensation during compression ("wet compression", see Figure 3.18) which can lead to compressor damage.

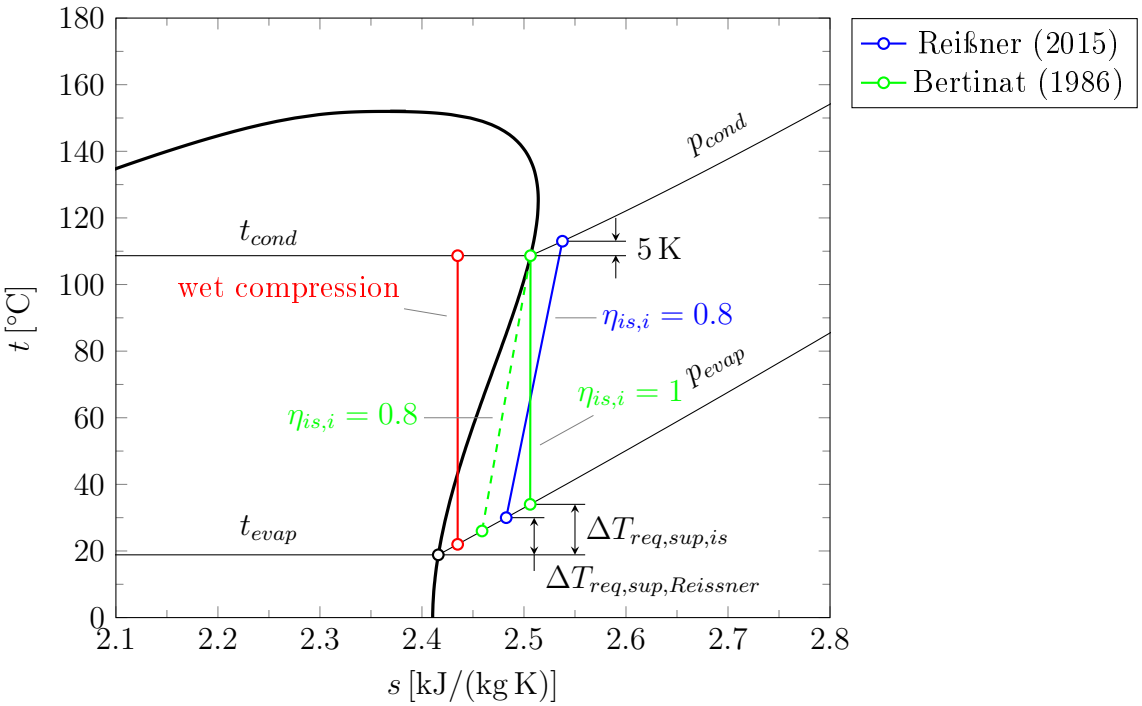

Figure 3.18: Definition of a wet compression (red) and the required superheat based on Reißner (2015) (blue) and Bertinat (1986) (green) in a t/s diagram for R600 based on property data of Lemmon et al. (2013)

Increased compressor heat losses could enhance the possibility of wet compression. A suffi-

cient suction gas superheat can avoid entering the two phase region during the compression process. This required degree of superheat is highly dependent on the evaporation and condensation temperature as well as on the refrigerant itself. A basic approach to calculate the required superheat has been suggested by Bertinat (1986), using an isentropic change of state with a end point on saturated vapour line for a certain condensation temperature t_{cond} and the starting point on the isobaric curve corresponding to a certain evaporation temperature t_{evap} (green full line, Figure 3.18). Hence, the calculation of the required superheat for a certain operation point supported by a fluid property data base (e.g. Lemmon et al., 2013 or F-Chart, 2016) follows Equations 3.55 to 3.59 corresponding to Figure 3.18 (see also Moisi and Rieberer, 2016).

$$s_{ref,2} = f\left(t_{cond}, x = 1\right) \tag{3.55}$$

$$s_{ref,1} = s_{ref,2} \tag{3.56}$$

$$p_{evap} = f\left(t_{evap}, x = 1\right) \tag{3.57}$$

$$t_{ref,1} = f\left(p_{evap}, s_{ref,1}\right) \tag{3.58}$$

$$\Delta T_{req,sup} = t_{ref,1} - t_{evap} \tag{3.59}$$

Reißner (2015) for example, has defined the required superheat ($\Delta T_{req,sup,Reissner}$, blue in Figure 3.18) by considering a compression process with an internal isentropic efficiency of 0.8 (see Equation 3.43) and a temperature difference of 5 K between compression end temperature and condensation temperature (t_{cond}). With this approach, Reißner (2015) accounts for a more realistic compression process, however, simultaneously implies a certain behaviour which might not be generally valid. In contradiction to the present methodology (Equations 3.55 to 3.59) and the approach of Reißner (2015), Bertinat (1986) derived analytically the required superheat ($\Delta T_{req,sup,Bertinat}$) based on an isentropic change of state (see Figure 3.18). From a combination of the Maxwell relation and the Clausius-Clapeyron Equation (see e.g. Bosnjakovic, 1998) as well as $T \cdot ds = c_p \cdot dT$ on an isobaric, Equation 3.60 yields the required superheat as a function of the isobaric thermal expansion coefficient β, the difference in specific volume between saturated vapour and liquid $(v'' - v')$, the specific heat at constant pressure c_p, the phase change enthalpy Δh_{pc} and the temperature T. σ again denotes the phase boundary and p denotes the state point on the isobaric (p_{evap}).

$$\Delta T_{req,sup,Bertinat} = \int_{T_{evap}}^{T_{cond}} \left(\frac{T}{c_p}\right)_p \left(\frac{c_p}{T}\right)_\sigma \left|1 - \left[\frac{\beta \cdot \Delta h_{pc} \cdot v''}{c_p \cdot (v'' - v')}\right]_\sigma\right| dT_\sigma \tag{3.60}$$

Since the Equation 3.60 is complex to solve, Bertinat (1986) simplified the relation using mid point values and stating that the first two terms in the integrand cancel each other out. This yields to Equation 3.61, providing a simple relation to approximate the required superheat for a certain refrigerant and operation point. The property quantities are evaluated at the saturated vapour curve (σ) with the arithmetic mean of condensation and evaporation temperature.

$$\Delta \bar{T}_{req,sup,Bertinat} \approx \left|1 - \left[\frac{\bar{\beta} \cdot \Delta \bar{h}_{pc} \cdot \bar{v''}}{\bar{c_p} \cdot (\bar{v''} - \bar{v'})}\right]_\sigma\right| \cdot (T_{cond} - T_{evap}) \tag{3.61}$$

The evaluation of the required superheat provided by Reißner (2015) and Bertinat (1986) only comprises a certain operation point for different refrigerants. Therefore a parameter variation has been carried out, utilizing all three approaches for comparison and to evaluate the superheat characteristic for R600 in the entire field of operation. Figure 3.19 shows the

obtained results for the present approach (black full line), Equation 3.61 (red dashed line) and the approach of Reißner (2015) (blue dashed and dotted line).

The results of the present approach utilizing property functions (black full line) shows steady characteristics of the required superheat increasing with increasing temperature lift and exhibiting a distinct maximum at the saturation temperature where the entropy on the saturated vapor curve has a minimum (for R600 approx. 0 °C, compare to Figure 3.17). The maximum values are ranging between 7 K and 17.6 K for a condensation temperature of 60 °C and 120 °C respectively. For example an evaporation temperature of 50 °C and a condensation temperature of 110 °C yields a required superheat of approx. 11 K. Equation 3.61 derived by Bertinat (1986) (dashed red line) shows a similar behaviour as the more accurate property function approach and displays very good agreement in a certain evaporation temperature range, however the distinct maximum cannot be reproduced. The deviation starts approximately at 30 % to 50 % of the respective temperature lift increasing with increasing condensation temperature. This is very likely a consequence of the mean property values used in Equation 3.61. An evaluation of Equation 3.60 however, is suspected to follow exactly the property function results. The function of Reißner (2015) (blue dashed and dotted line) exhibits basically a similar form with the maximum shifted to an evaporation temperature of approx. 45 °C and significantly lower superheat values as a consequence of an internal isentropic efficiency of 0.8. It can be observed that 5 K of discharge superheat remains when the evaporation temperature approaches the condensation temperature.

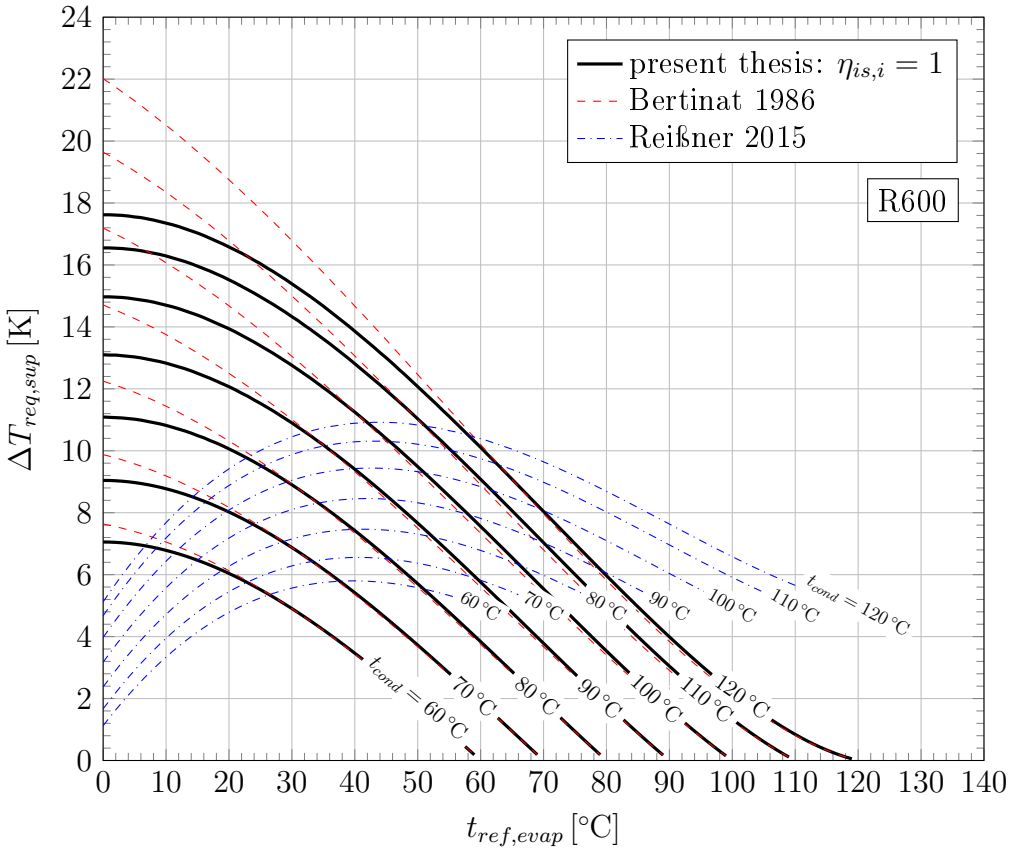

Figure 3.19: Required superheat characteristics for R600 as a function of the evaporation temperature with the condensation temperature as a parameter using Equations 3.55 to 3.59 for an isentropic change of state (black full line) and the modifications by Reißner (2015) as well as Equation 3.61 derived by Bertinat (1986), property data are based on F-Chart (2016)

Although the maximum values of Reißner (2015) are lower, the absolute value of the re-

quired superheat results higher than the property function approach for decreasing temperature lifts (intersection of black and blue line for a certain condensation temperature) which is consequence of the imposed discharge superheat of 5 K. As an example, for a condensation temperature of 60 °C and 120 °C, this intersection point lies at approx. 25 °C and 60 °C respectively. The influence of a non isentropic compression, i.e. an internal isentropic efficiency lower than 1, on the required superheat results is depicted in Figure 3.20 for refrigerants R600 (left), R1336mzz-Z and R245fa (right) for a condensation temperature of 110 °C. As already discussed above, a decreasing isentropic efficiency shifts the maximum towards higher evaporation temperatures and lowers the absolute values. The shift of the maximum is a consequence of a non linear increase of entropy difference with increasing temperature lift which defines the state point $s_{ref,1}$ and thus the resulting superheat (see Figure 3.20). The shape of the superheat characteristics is basically the same for different refrigerants and a function of the form of the saturated vapour curve.

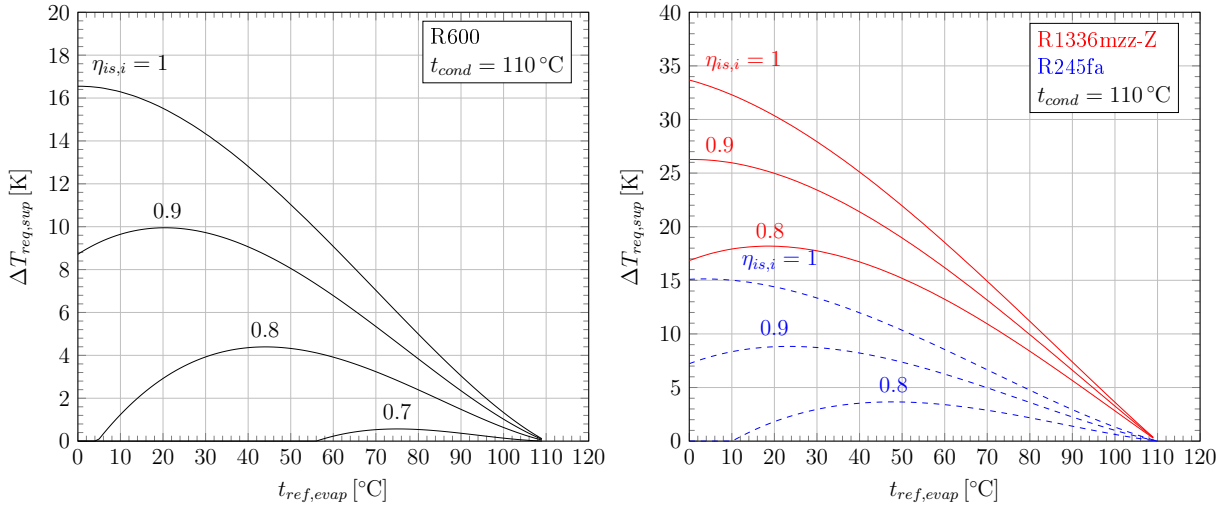

Figure 3.20: Comparison of the required superheat characteristics for R600, R1336mzz-Z and R245fa, depending on the internal isentropic efficiency and a condensation temperature of 110 °C

Hence characteristic superheat curves can be found for each refrigerant exhibiting an overhanging phase boundary. The higher the slope of the saturated vapour curve the higher degree of superheat is theoretically necessary. Due to the assumption of a isentropic change of state the resulting curves can be considered more as a refrigerant property, in contradiction to Reißner (2015), where already process parameters are anticipated (e.g. discharge temperature). Figure 3.21 depicts the comparison of different high temperature working fluids in terms of required superheat based on the isentropic approach for a condensation temperature of 110 °C. It can be observed, that for example, R1336mzz-Z and Neopentane would theoretically require a superheat of approx. 25 K compared to R600 with 13 K at an evaporation temperature of 40 °C .

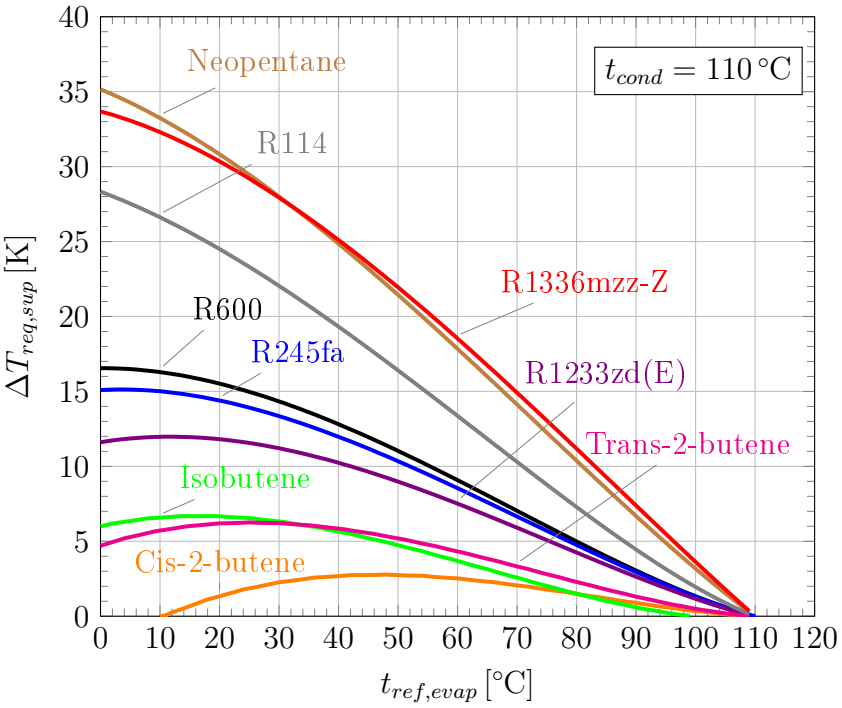

Figure 3.21: Comparison of superheat characteristics for different high temperature working fluids based on the isentropic approach and a condensation temperature of 110 °C

In reality, the compression process does not follow a isentropic characteristic since heat transfer to and from the gaseous refrigerant defines the change of state. As already discussed in Section 3.3, high heat transfer rate from the refrigerant to the ambient might result in high internal isentropic efficiencies close to one, increasing the risk of a compression entering the two phase region. This might be the especially the case for high temperature heat pumps due to the increased temperature level. Hence it is most likely that different values of superheat are necessary in real applications because of compressor irreversibilities to keep a safe distance from the 2 phase region.

Especially critical is the heat pump start up phase which will be discussed in Section 5.3.1, where cylinder and compressor housing require a certain amount of time to heat up to operation temperature which causes high heat transfer rates from the refrigerant to the cylinder walls. Hence a quasi isentropic or even cooled compression can be the result increasing the possibility of a wet compression.

Realizing a high suction gas superheat within the evaporator will decrease the evaporation temperature and therefore the heat pump efficiency. Hence measures have to be taken in order to avoid high values of superheat in the evaporator e.g. by means of an internal heat exchanger (see Chapter 5), the use of suction gas cooled compressors (see Chapter 4) or other external heat sources. Therefore the preparation of suction gas superheat is essential for the design and the control strategy of high temperature heat pumps using overhanging working fluids.

4 EXPERIMENTAL SET UP

The design and measurement concept as well as components of the heat pump prototype shall be described in the following sections. Especially for the heat pump concept and design (see Section 4.1) information has been provided in publications Moisi and Rieberer (2017), Moisi et al. (2018) and in parts in Moisi et al. (2017) and Moisi and Rieberer (2018). Furthermore, Verdnik (2017) has given a detailed description on the heat pump prototype, components and measurement concept (compare e.g. to Sections 4.2, 4.4 or 4.5). Skreinig (2016) and Moisi and Rieberer (2016) have provided information on the design and construction of the compressor heat exchanger (CHX) described in Section 4.3.

4.1 Heat Pump Concept and Design

The high temperature application of vapour compression heat pumps has to face different technological challenges. High temperature lifts have a significant effect on cycle efficiency as shown by the Carnot Cycle in Sections 3.1.1 and 5.8. High condensation temperatures resulting in high compression end temperatures can lead to lubricant related problems in terms of insufficient viscosity or oil degradation and decomposition (see Section 2.3 and 4.3). Furthermore, as outlined in Section 3.7, many refrigerants considered for subcritical high temperature application exhibit an overhanging two phase region which can lead, under certain process circumstances, to refrigerant condensation during compression ("wet compression"). This effect can cause liquid droplets to form and ultimately compressor damage. In order to avoid a wet compression, sufficient suction gas superheat depending on the temperature lift and refrigerant and internal isentropic efficiency of the compressor has to be considered. However a high suction gas superheat provided in the evaporator can lead to a decrease in evaporation temperature an thus cycle efficiency (see Section 3.2.2).

4.1.1 Basic Cycle Design Simulations

The basic question in the design process has been, how to address those challenges technologically but also considering complexity, component availability and reliability. As a result two key aspects have been considered to be the basis for the cycle design. The first aspect addresses cycle modifications in order to increases cycle efficiency and heating capacity. The second aspect has considered the provision of sufficient suction gas superheat for the use with overhanging working fluids such as R600. In this regard simplified design simulations have been conducted as described in Moisi and Rieberer (2017) and Moisi et al. (2018). The simulations have been carried in the software package Engineering Equation Solver (EES) v.9.901 (F-Chart, 2016) (see also Chapter 3).

The following passages, formatted in *italic* have been taken identically from Moisi and Rieberer (2017), only references and variable names have been adapted and complemented:

The simulation study has been carried out in two steps. The first step has been a set of design simulations in order to determine compressor swept volume and heat transmission coefficients ($U \cdot A$) of the condenser and evaporator for a basic single and a 2 stage heat pump cycle in a design point of operation. For the heat exchanger design, a pinch point temperature difference of 4 K *has been assumed. The second step has been the application of the obtained parameters to the different cycle configurations. For the simulation, heat losses as well as pressure drops due to fluid friction have been neglected. The compressor efficiency has been modeled as a function of the pressure ratio and obtained from manufacturer data*

(see Moisi et al., 2017 or Moisi et al., 2018). *The same method has been applied to the compressors volumetric efficiency (λ_{vol}). The heat exchangers have been modeled with the obtained UA-values from the design simulations. Furthermore only steady state simulations have been conducted. The refrigerant is R600. The pressure ratios in the first and second stage of the 2 stage cycles have been assumed to be identical. The design parameters and boundary conditions are given in* Table 4.1. *Therein, the overall isentropic efficiency ($\eta_{is,ov}$) is defined as the ratio between compressor power with isentropic compression and the actual electrical consumption of the compressor* (see Section 3.3.2).

The design simulation boundary conditions in Table 4.1 are taking the project premises such as the heating capacity of 50 kW and a supply temperature of 110 °C into account (see Chapter 1). Furthermore, with the required superheat at the compressor inlet of 18.5 K the overhanging nature of R600 is considered according to Section 3.7.

Table 4.1: Parameters and boundary conditions for the design simulations (Moisi and Rieberer, 2017, modified)

Refrigerant	R600
Design heating capacity ($\dot{Q}_{w,H,D}$)	50 kW
Design pinch point ($\Delta T_{pp,D}$)	4 K
Design heat sink temperatures ($t_{sink,in,D}/t_{sink,out,D}$)	80 °C/110 °C
Design heat source temperatures ($t_{source,in,D}/t_{source,out,D}$)	60 °C/50 °C
Overall isentropic efficiency ($\eta_{is,ov}$)	0.3 to 0.56
Volumetric efficiency (λ_{vol})	0.8 to 0.9
Superheat at compressor inlet for R600 ($\Delta T_{req,sup}$)	18.5 K
Subcool at expansion valve inlet (ΔT_{sub})	5 K

The investigated cycle configurations are mainly based on Cao et al. (2014) and include the most common heat pump cycle layouts. However since the suction gas superheat is a critical parameter for overhanging working fluids and has a main influence on heat pump efficiency (compare to Section 3.7)*, different sources of superheat preparation have been investigated. The six main cycle configurations are depicted in* Figure 4.1. *The basic single stage cycle (1) displays the conventional heat pump cycle and serves as basis for further comparison. The advantages of the 2 stage cycle (2) are the reduced compressor power because of the staged compression. The liquid injection (3, LI) should decrease compressor outlet temperatures and slightly increase condenser massflow and thus heating capacity. Furthermore compressor power should be decreased by staged compression. The economizer configurations (4, ECO_w_FT and 5, ECO_w_IHX) increase the condenser massflow and provide a multi stage compression. The intercooler provides (6, IC) again a staged compression as well as lower compressor outlet temperatures.All main cycle configurations of* Figure 4.1 *had been extended with an internal heat exchanger (IHX) and a suction gas heat exchanger (CHX) for the cycle simulations. The CHX has been modeled basically as a separate heat source providing the suction gas superheat independently from the heat pump heat source* (compare to Chapter 6). *In this case the CHX is assumed to be a suction gas cooled compressor motor* (see Section 4.3). Figure 4.2 *illustrates the different superheat configurations exemplary for the basic cycle*

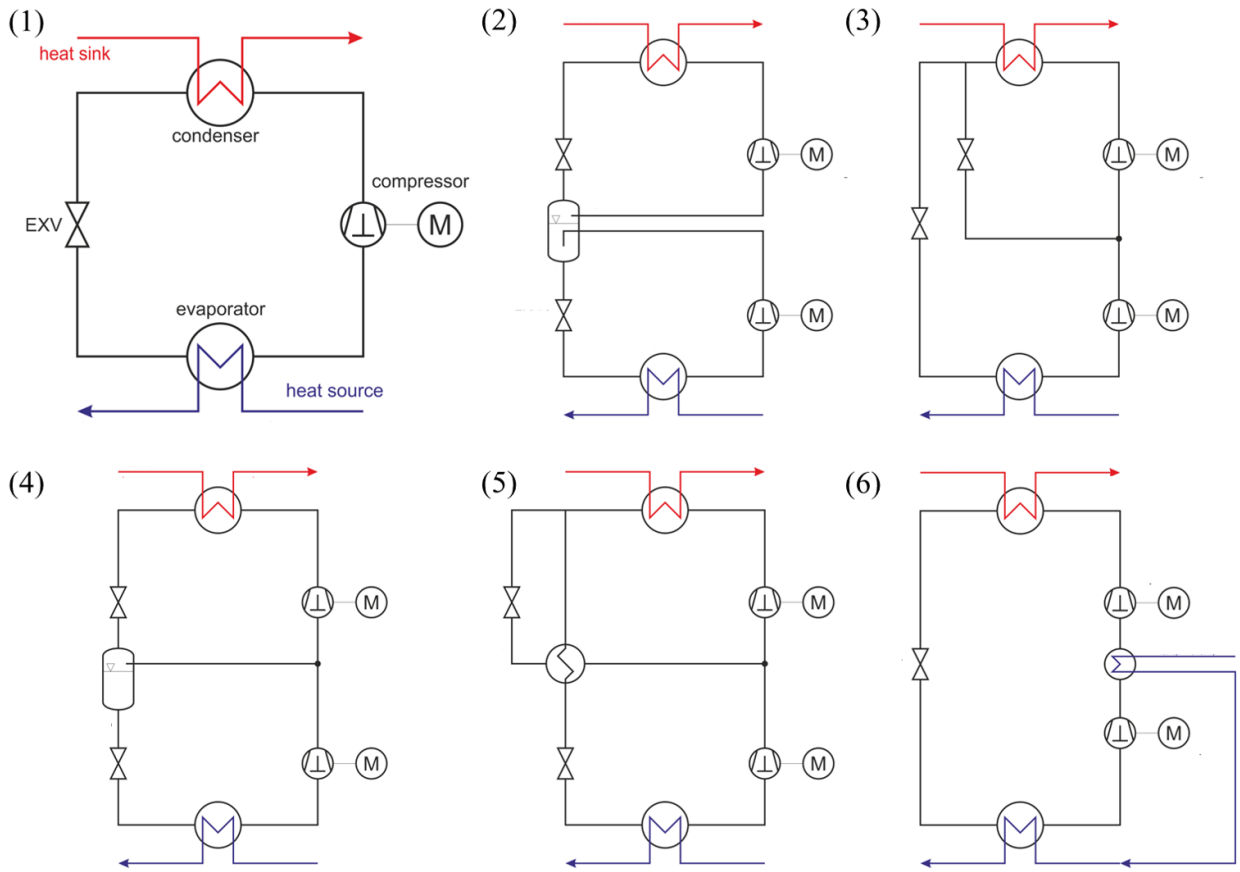

Figure 4.1: Main group of cycle configurations for the design simulation study based on Cao et al. (2014) , (1) basic, (2) 2 stage, (3) liquid injection (LI), (4) economizer with flash tank (ECO_FT), (5) economizer with heat exchanger (ECO_HX), (6) intercooler (IC) (based on Moisi and Rieberer, 2017, modified)

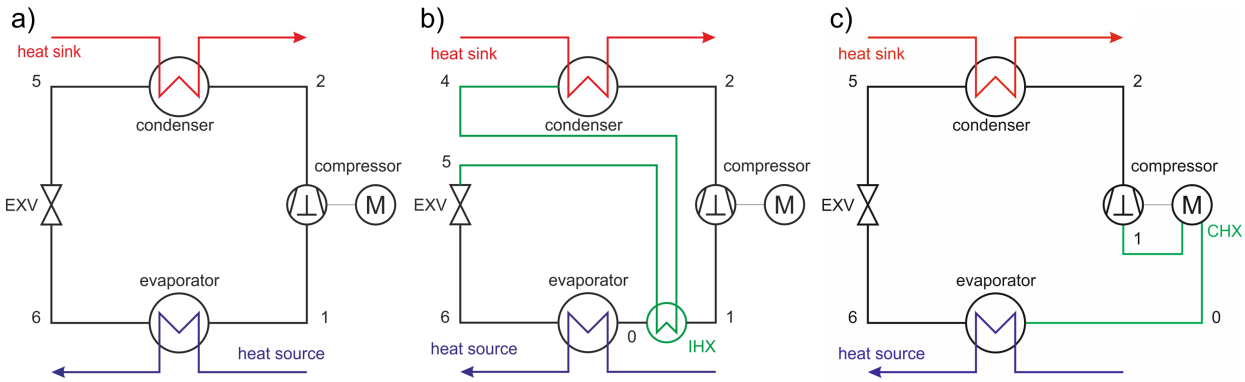

Figure 4.2: Different cycle configurations in terms of suction gas superheat preparation, a) basic, b) internal heat exchanger (IHX), c) suction gas cooled compressor (CHX) (based on Moisi and Rieberer, 2017, modified)

The combination of cycle layouts from Figure 4.1 and 4.2 *results in 20 variations of heat pump cycles. That means that there is a basic concept* (Figure 4.2a), *a concept with internal heat exchanger* (4.2b, IHX) *and a concept with suction gas heat exchanger* (Figure 4.2c, CHX). *The 2 stage cycle* (Figure 4.1; 2) *represents a special case. Since the refrigerant*

state in the flash tank is assumed to be saturated, a sufficient superheat has to be ensured in order to avoid a wet compression in the second compressor stage. Therefore it is necessary to utilize either an internal heat exchanger (DIHX=Double IHX) or a suction gas heat exchanger (DCHX=Double CHX) in the second stage. Both possibilities have been investigated. The same could be true for the remaining 2 stage concepts like the liquid injection or the ECO_FT. In real applications however, an appropriate superheated state at compressor inlet of the second stage has to be maintained by the intermediate pressure by the EXV of the second stage. In the case of the intercooler the heat exchanger design has to be considered regarding sufficient superheat. The results for the heating capacity ($\dot{Q}_{w,H}$, left) *and the efficiency* ($COP_{w,H}$, right) *for two operation points and the refrigerant R600 are displayed in* Figure 4.3. *It can be observed that the heating capacity for the design point* (Figure 4.3, green bars) *of both Basic and 2_stage cycle, results in* 50 kW *corresponding to the design boundary conditions. The influence of the IHX and CHX can be clearly observed for the heating capacity and the efficiency. Since the high required superheat has not been entirely provided in the evaporator, the evaporation temperature can increase, hence the suction gas density increases and therefore the heating capacity (Basic, Basic_IHX, Basic_CHX for example). The Basic_CHX cycle already shows an improvement of approx.* 11 % *in terms of COP and* 27 % *in heating capacity compared to the basic configuration. The efficiency increases with increasing evaporation temperature, although the refrigerant mass flow increases but the pressure ratio decreases* (compare to Chapter 5). *Hence the increase of compressor power is lower than the increase of heating capacity.*

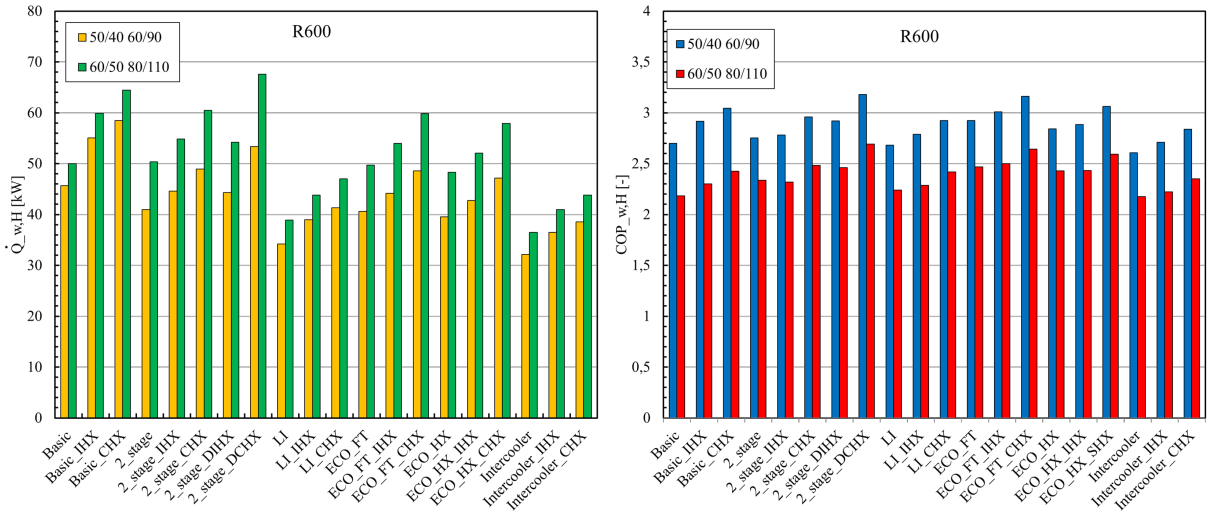

Figure 4.3: Simulation results for heating capacity ($\dot{Q}_{w,H}$, left) and $COP_{w,H}$ (right) for different cycle configurations and operation points a) heat source 50/40 °C, heat sink 60/90 °C; b) heat source 60/50 °C, heat sink 80/110 °C) (based on Moisi and Rieberer, 2017, modified)

The best performance is shown by the 2 stage cycle with CHX in both stages (2_stage_DCHX) for each operation point. For the design point (green and red bars), the heating capacity increases by approx. 34 % *and for the* $COP_{w,H}$ *by approx.* 24 % *compared to the basic cycle. The absolute efficiencies however are rather low with a maximum of 2.7 for the design point (80 /110 °C) and the assumed compressor efficiencies. The economizer cycle with CHX and flash tank (ECO_FT_CHX) shows a similar COP improvement of approx.* 21 %, *but a lower improvement in the heating capacity by approx.* 20 % *compared to the basic cycle. This indicates a higher absolute compressor power demand compared to 2_stage_DCHX.*

In terms of performance the 2 stage cycle with DCHX should be selected for the heat pump prototype. However the higher system complexity in terms of hydraulics, components and control is increasing the investment costs significantly compared to the basic cycle. Another aspect is, if the 2_stage_DCHX is compared with the Basic_CHX cycle, the advantage decreases significantly with a remaining improvement for the heating capacity of 4 % *and in terms of COP of* 11 %*. Therefore a final investigation of a basic cycle using IHX has been carried out. Based on the statements of* Section 3.4*, the heat source temperature difference should be kept as small as possible to increase the evaporation temperature. Furthermore the increase of subcooling can increase the heating capacity if the source side temperature lift is high. Hence the source side temperatures have been changed to* 60 °C *(inlet) and* 55 °C *(outlet) and the useable subcooling to* 25 K*. The results showed a* $COP_{w,H}$ *of 3.4 due to these measures and the application of an IHX, for sink temperatures of* 80 °C *(inlet) and* 110 °C *(outlet) as well as condenser/evaporator pinch points of* 4 K*. Therefore the single stage with additional superheat preparation (IHX, CHX) and an extended use of refrigerant subcooling has been considered as final prototype cycle for the further development of the R600-HTHP because of the more simple system and acceptable efficiency values.*

In conclusion, based on the simplified design simulation described in Moisi and Rieberer (2017) and above, the single stage basic cycle with suction gas superheat decoupled from the heat source to the largest extend (by means of IHX and CHX) and utilizing an increased degree of subcooling (see also Section 3.2.3) has been found to be good compromise in terms of cycle complexity, efficiency and heating capacity and has therefore been selected for the high temperature heat pump test rig described in the following section.

4.1.2 Final Heat Pump Concept and Prototype

The design of the final heat pump test rig has been based on the cycle simulations outlined in the previous section. Since suction gas superheat in combination with overhanging working fluids has been a main task in the development process, two different cycle configurations have been realised within the final high temperature heat pump test rig (Basic and IHX configuration). The test rig constitutes a single stage heat pump as depicted schematically in Figure 4.4 using an adapted suction gas cooled frequency controlled separating hood compressor (see Section 4.3) for refrigerant compression, a condenser for refrigerant liquefaction, a high pressure receiver for refrigerant storage and a subcooler for further subcooling. Downstream of the subcooler an internal heat exchanger is located in parallel flow arrangement and can be hydraulically shut off by respective valves. An EXV provides the expansion from high pressure level to evaporation pressure and serves as superheat control actuator. The two phase refrigerant is fully evaporated and superheated in the evaporator. In the case when the IHX is not used, valves V5,V6,V8 and V9 are closed by manually operated shut off valves (Basic configuration). Additionally, in the Basic configuration the heat exchanger area of the evaporator can be extended by an extra heat exchanger denoted as superheater.

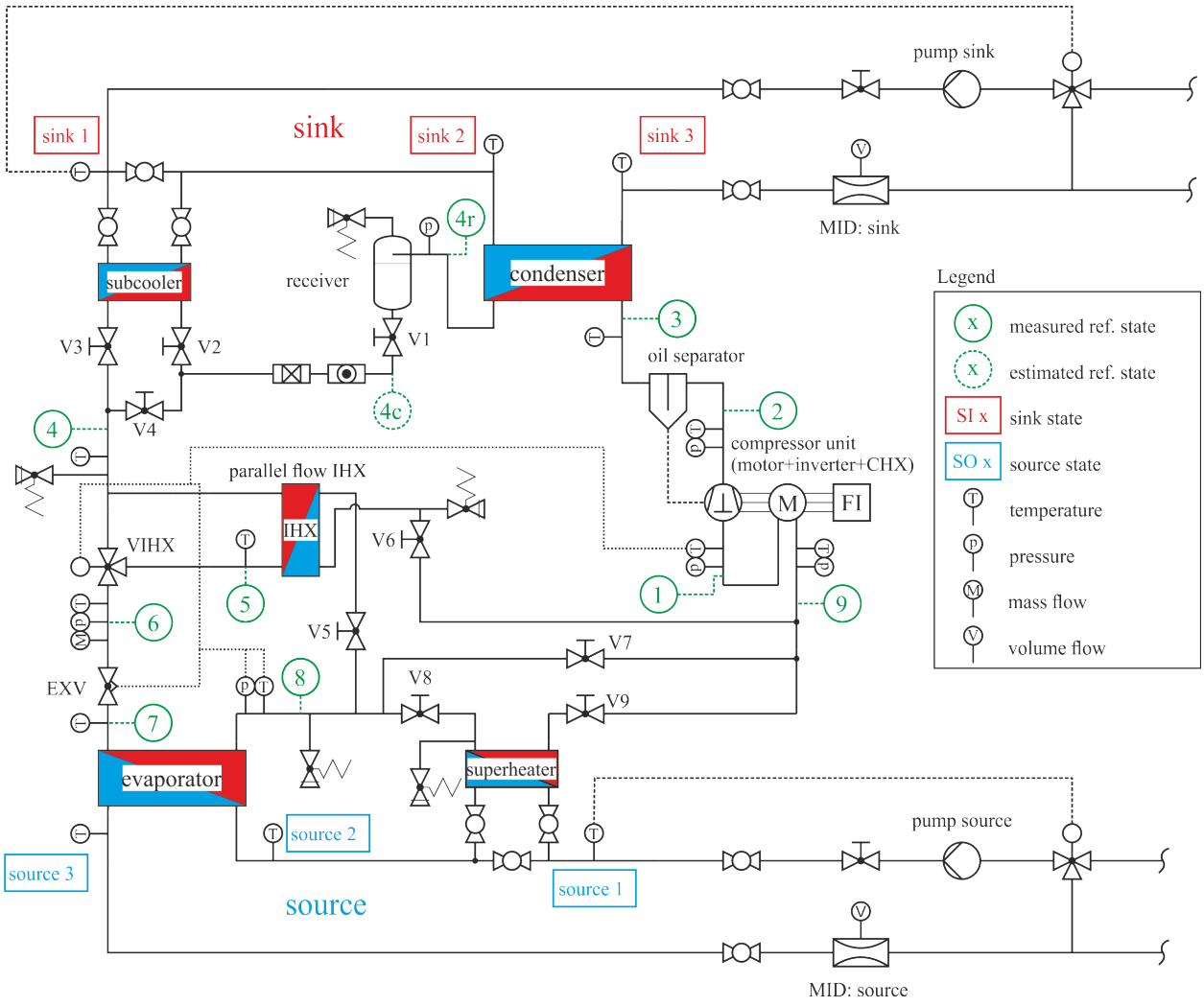

Figure 4.4: Realized hydraulic layout of the R600 high temperature heat pump test rig including sensor positions and source and sink hydraulics

The internal heat exchanger, transfers heat from the high pressure side to the suction side further superheating the refrigerant as outlined in Chapter 3. In this cycle configuration,

valve V7, V8 and V9 are closed. The solenoid three way valve VIHX is set to 100 % in order to direct the refrigerant mass flow entirely across the IHX. Figure 4.4 illustrates further the defined sensor positions of pressure, temperature, volume flow and mass flow with the corresponding refrigerant states marked by green circles. The defined measurement concept provides the possibility to derive heat pump performance indicators such as COP and heating capacity and the derivation of state diagrams for a detailed cycle analysis and comparison, as carried out in Chapter 5. The heat pump test rig further includes source and sink hydraulics to provide the necessary boundary conditions for different operation points as also indicated in Figure 4.4 (see Section 4.7). An oil separator in the discharge line shall ensure the oil return and appropriate oil level in the compressor (see Section 4.5). Pressure relief valves are utilized at certain locations to avoid an inadmissible pressure increase if shutoff valves are remain unintentionally closed or other operation errors occur. The high temperature heat pump prototype has been constructed by the project partner Frigopol Kälteanlagen GmbH (Frigopol, 2020a) and is enclosed in a ventilated housing. Figure 4.5 shows the entire test rig located in the laboratory of the Institute of Thermal Engineering at TU Graz including the heat pump prototype (right) and the source and sink hydraulics behind the control stand (left).

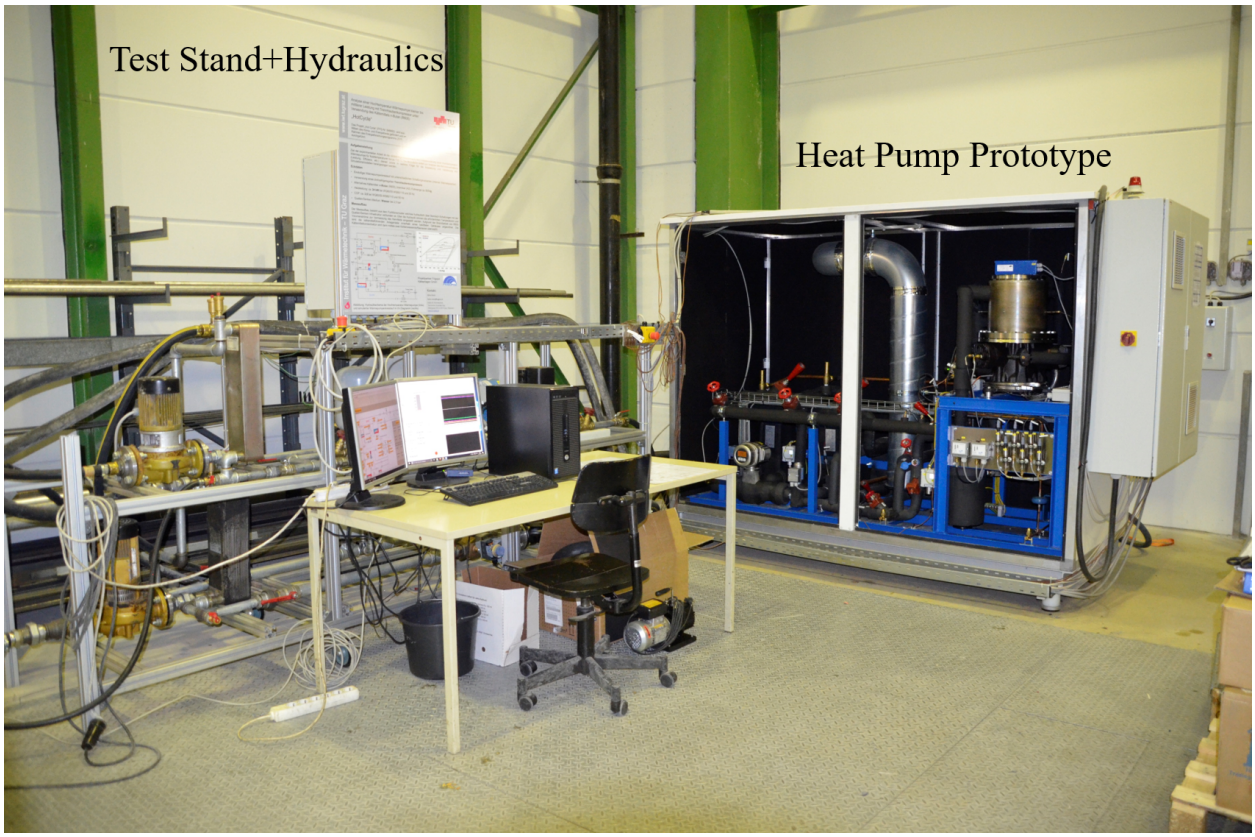

Figure 4.5: R600 high temperature heat pump test rig including source and sink hydraulics located in the laboratory of the Institute of Thermal Engineering (IWT) at TU Graz (as in 2018)

Figure 4.6 shows a more detailed look on the heat pump prototype, depicting the compressor including CHX and the condenser. The remaining heat exchangers are located in the background and are therefore not clearly visible but described in detail in Section 4.2. Furthermore the suction and discharge lines are indicated as well as the high pressure receiver in the right bottom area of the test rig. Since R600 exhibits strong flammability (compare to Section 3.6) the heat pump has to be encapsulated within a ventilated housing. The

duct system is indicated in Figure 4.6 and the safety measures will be outlined in Section 4.6. Furthermore the Coriolis massflow sensor can be recognized in the left bottom area implemented in the high liquid pressure line at the outlet of the VIHX (compare to Figure 4.4)

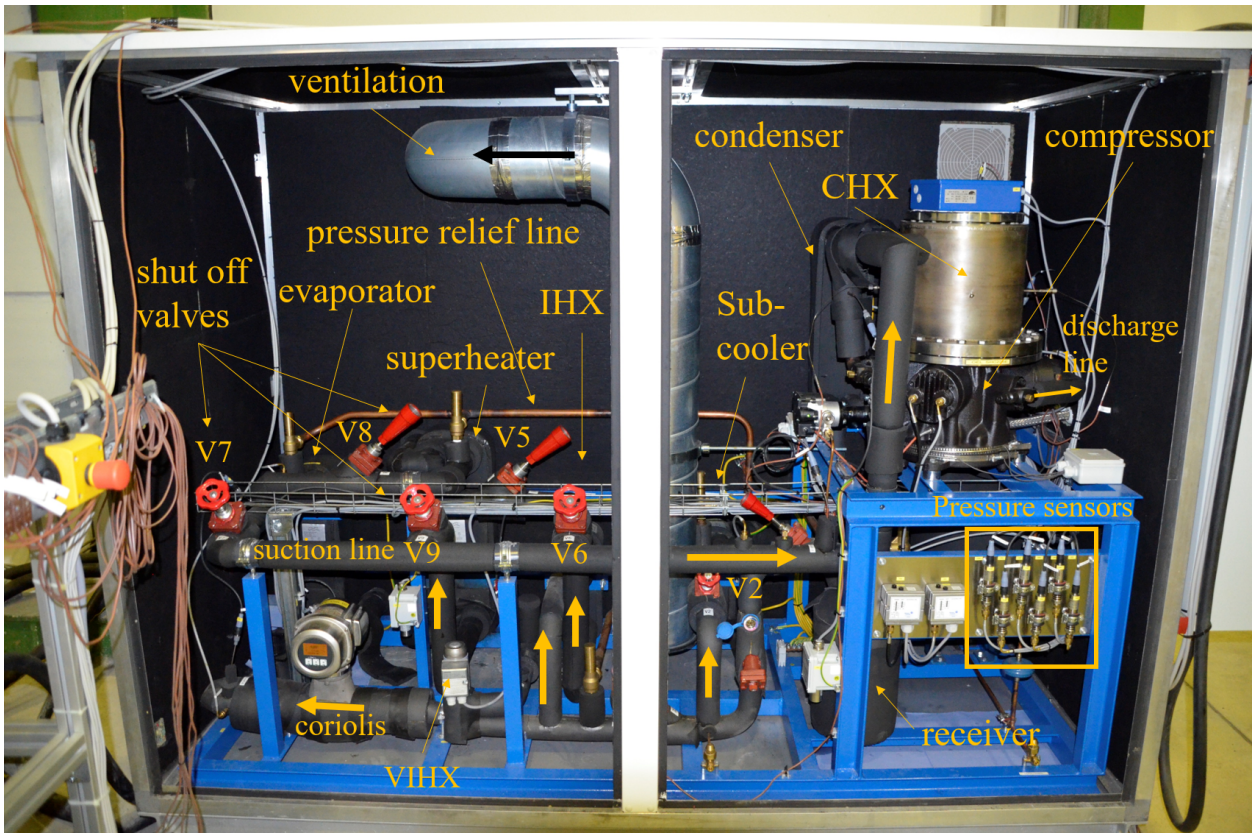

Figure 4.6: Front view of the R600 high temperature heat pump prototype with open housing, indicated flow directions and components

Main components of the test rig as well as the measurement equipment are discussed in Sections 4.2, 4.3, 4.4, 4.5 and 4.9. The design operation point is outlined in the following section.

4.1.3 Design Operation Point

The design operation point has been derived from the simplified cycle simulations described in Section 4.1.1. Based on the insight to provide an acceptable efficiency by decreasing the evaporator superheat for a given heat source temperature difference and utilizing a subcooler in order to increase the specific heating capacity (compare to Section 3.2.3). Considering the project goals of providing a supply temperature of 110 °C using a separating hood compressor from the project partner in a heating capacity range of up to 50 kW the design operation point for the component dimensioning has been defined as given in Table 4.2. The design calculations have been again carried out with the EES software package v. 9.901 using energy balances, compressor efficiency and consumptions relations as described in Chapter 3 (see also Moisi et al., 2018).

Table 4.2: Design operation point for component dimensioning

Refrigerant	R600	
Source/sink medium	Water	
Pinch point temperature difference (evap. and cond.)	ΔT_{pp}	4 K
heat sink temperatures	$t_{sink,in}/t_{sink,out}$	80 °C/110 °C
heat source temperatures	$t_{source,in}/t_{source,out}$	60 °C/55 °C
Evaporator superheat	$\Delta T_{sup,evap}$	2 K
IHX superheat	$\Delta T_{sup,IHX}$	10 K
CHX superheat	$\Delta T_{sup,CHX}$	5 K
Subcool at subcooler outlet	ΔT_{sub}	25 K
Compressor frequency	f	75 Hz
Swept volume	$\dot{V}$	$\approx 45\,\mathrm{m^3/h}$
heating capacity (result)	$\dot{Q}_{w,H}$	40.8 kW
Coefficient of performance (result)	$\dot{C}OP_{w,H}$	3.4

The obtained refrigerant, source and sink states as well as massflow rates have served as input quantities for heat exchanger, EXV and hydraulics sizing. Piping and EXV dimensioning has been carried out by Frigopol using manufacturer design tools based on the input data from the design simulations. Similarly the input data has been provided to the heat exchanger manufacturer for the selection of the respective components (see Section 4.2). The heating capacity is a result of the largest available separating hood compressor in the product range of the project partner Frigopol (see Section 4.3). Furthermore this compressor has not been tested with n-Butane (R600) before, hence efficiency characteristics have had to be utilized based on standard ammonia application of the compressor (see Moisi et al., 2018).

4.2 Heat Exchangers

In the intended capacity range, brazed plate heat exchangers offer a compact and inexpensive heat transfer possibility and have therefore been selected throughout, for all heat transfer purposes except the CHX. As outlined above, the heat exchanger sizing and selection has been carried out by the manufacturer Alfa Laval (AlfaLaval, 2020) based on the provided input data. As an example the evaporator model obtained from AlfaLaval (2016a) and the corresponding built in situation in the heat pump test rig is depicted in Figure 4.7. Figure 4.7 furthermore displays the EXV location, source and refrigerant flow directions as well as the pressure and temperature measurement positions of refrigerant states 6, 7 and 8 (EXV inlet, outlet and evaporator outlet respectively, compare to Figure 4.4). The subcooled refrigerant enters the EXV at state 6 and is subsequently expanded reaching state 7 before entering the evaporator. The refrigerant leaves the evaporator normally in a superheated state 8.

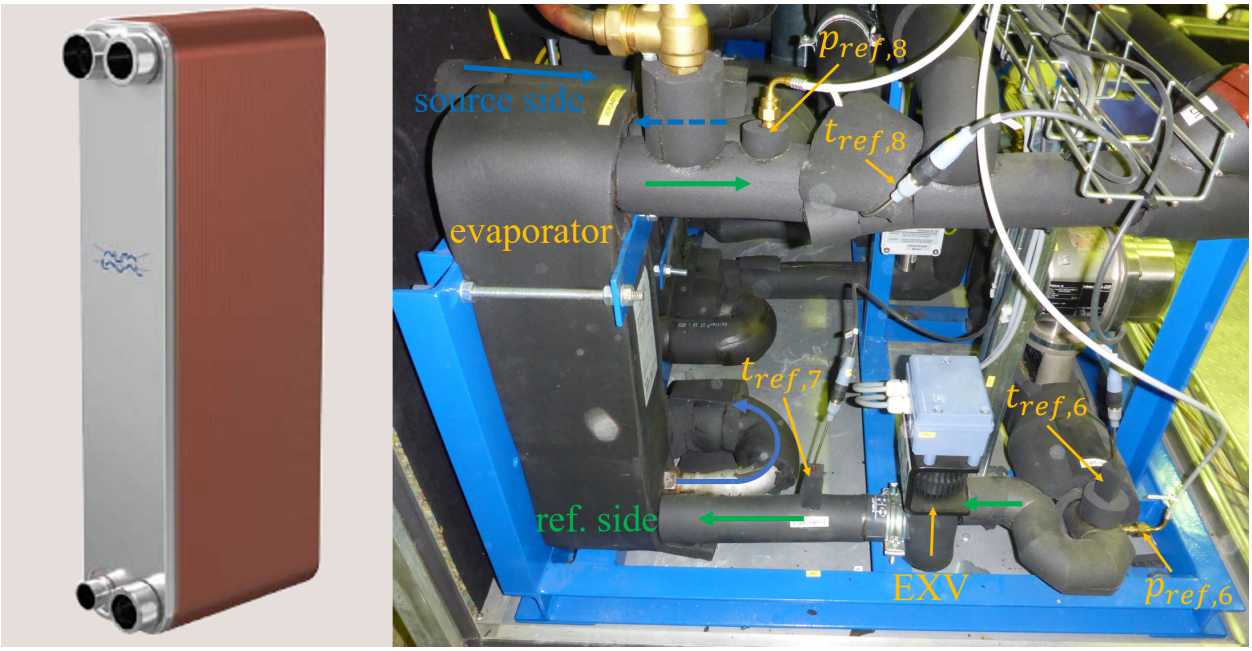

Figure 4.7: Evaporator type (left, AlfaLaval, 2016a) and built in situation of the evaporator including sensor position

The realized flow arrangement of the evaporator, superheater and IHX is depicted in Figure 4.8. The refrigerant flow is indicated by green arrows, the source flow follows blue arrows. Depending on the shut off valve position the refrigerant leaving the evaporator enters the superheater (V8=open) or the internal heat exchanger (V5=open). Further indicated is the above described parallel flow configuration of the IHX with both flow streams (HP/LP=high/low pressure side) entering the heat exchanger on the same side.

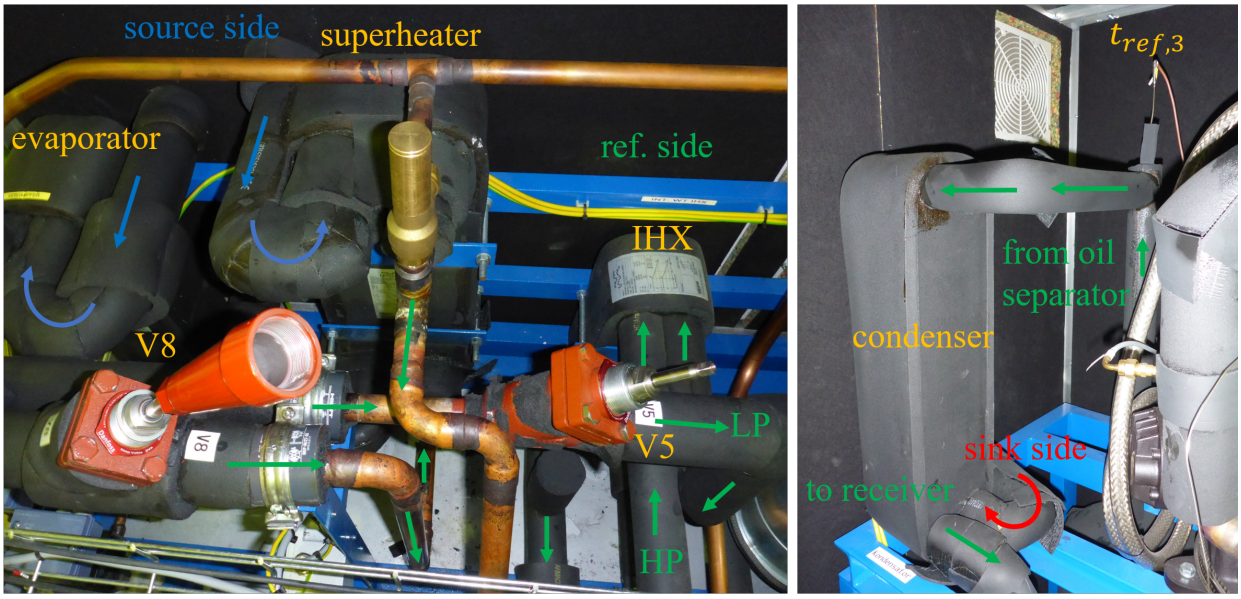

Figure 4.8: Realized flow arrangement of evaporator, superheater and IHX (left) as well as of the condenser (right)

The condenser arrangement is depicted in Figure 4.8 on the right showing the gaseous refrigerant from the oil separator entering the condenser (state 3) and leaving towards the liquid

receiver. The sink medium leaves the subcooler (compare to Figure 4.5) and enters the condenser on the bottom. Table 4.3 summarizes the model and design data of the implemented heat exchangers obtained from the manufacturer (see also Verdnik, 2017). The design data is based on the design operation point simulations outlined in Section 4.1.3. The basic geometry, heat transfer area, pressure drop and heat transfer data have been obtained from the technical specification and offer documents provided by AlfaLaval (2016b). The information presented in Table 4.3 has been utilized for the determination of heat transfer coefficients and geometry parameters as decribed in Chapter 6. Table 4.3 is complemented by data given in Appendix A.2 containing geometry and heat exchanger parameters such as number of plates and corrugation angle further required to determine heat transfer correlations.

Table 4.3: Design data of utilized brazed plate heat exchanger for the high temperature heat pump prototype obtained from AlfaLaval (2016b)

Description		Symbol	Unit	Evaporator	Condenser	Subcooler	Superheater	IHX
Manufacturer		-	-	Alfa Laval	Alfa Laval	Alfa Laval	Alfa Laval	Alfa Laval
Model		-	-	AC-70X-40M	CB62-40AH-F	CB30-14H	CB110-20L	CB30-30L-F
Design heat transfer area		$A_{phx,ht,D}$	[m^2]	1.94	2.3	0.35	2.02	0.81
Design heat transmission coefficient		$U_{hx,D}$	[kW/(m^2 K)]	5.04	2.417	2.357	0.247	0.225
Design Capacity		$\dot{Q}_{hx,D}$	[kW]	30.95	31.59	9.427	1.638	2.495
Flow direction		-	-	counter	counter	counter	counter	counter
Length		L_{hx}	[m]	0.127	0.141	0.069	0.139	0.106
Width		W_{hx}	[m]	0.111	0.113	0.113	0.191	0.113
Height		H_{hx}	[m]	0.526	0.529	0.313	0.616	0.313
HT	Medium	-	-	Water	R600	R600	Water	R600
	massflow	$\dot{m}_{HT}$	[kg/s]	1.483	0.119	0.119	1.104	0.119
	Inlet temp.	$t_{HT,in}$	[°C]	60	122.2	111.3	60	86.3
	Outlet temp.	$t_{HT,out}$	[°C]	55	111.3	86.3	59.6	79.3
	Pressure drop	$\Delta p_{hx,HT}$	[kPa]	37.6	3.84	3.24	3.7	0.21
LT	Medium	-	-	R600	Water	Water	R600	R600
	massflow	$\dot{m}_{LT}$	[kg/s]	0.1216	0.3232	0.3232	0.09246	0.119
	Inlet temp.	$t_{LT,in}$	[°C]	51.7	110	87	45	53
	Outlet temp.	$t_{LT,out}$	[°C]	53	87	80	56	65.7
	Pressure drop	$\Delta p_{hx,LT}$	[kPa]	78.2	2.62	8.76	1.38	4.96

4.3 Compressor

The heat pump prototype is equipped with a reciprocating inverter driven separating hood compressor which has been provided by the project partner Frigopol. The so called separating hood consists of stainless steel sheet metal and encloses the rotor of the compressor in order to separate all refrigerant carrying parts from the stator and thus the surrounding (see also Figure 4.11). In combination with highly flammable refrigerants such as R600, the separating hood allows compressor motor maintenance without opening the refrigerant circuit. In the standard configuration this compressor is air cooled and utilized mainly in combination with classic refrigerants such as ammonia (R717) and R134a (Frigopol, 2020b). In order to utilize the compressor waste heat and provide suction gas superheat decoupled from the heat source a special compressor heat exchanger (CHX) has been designed. The separating hood compressor can be considered semi hermetic and is depicted in Figure 4.9 in the standard air cooled (left) and the modified suction gas cooled version (CHX) .

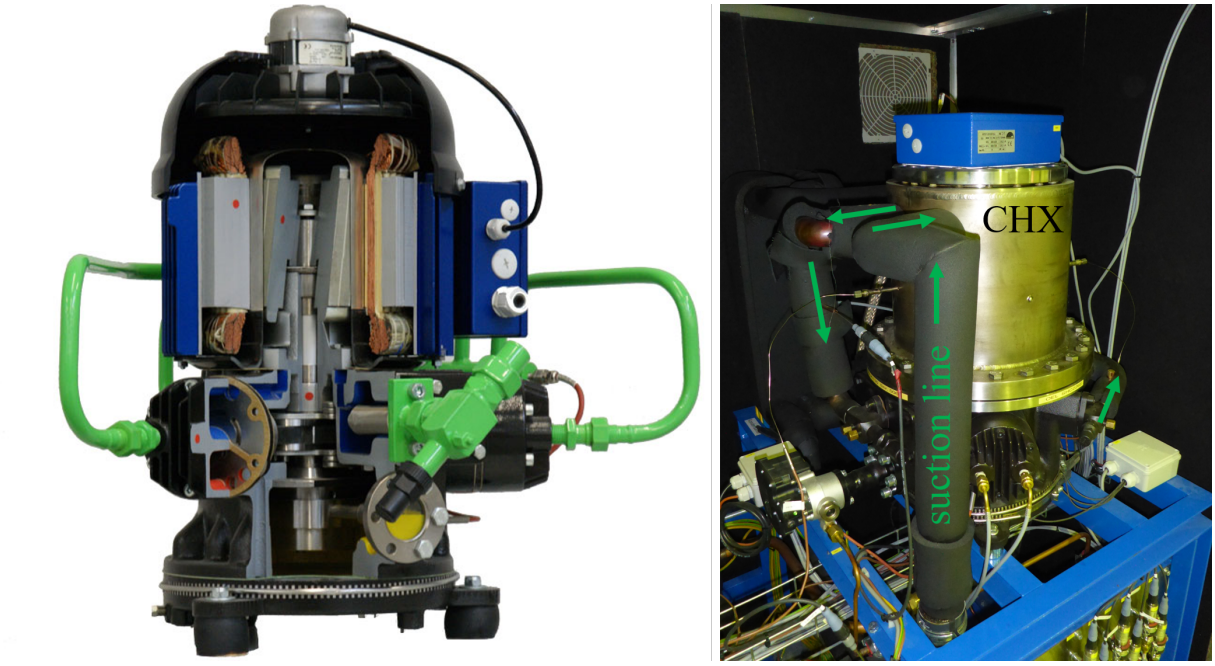

Figure 4.9: Standard air cooled separating hood compressor (Frigopol, 2020a, left) and the modified suction gas cooled configuration utilized for the heat pump prototype (right)

The basic compressor data is given in Table 4.4. The compressor speed can be controlled with a frequency inverter from the manufacturer ABB (ABB, 2016). The maximum high pressure is limited to 28 bar and the low pressure has to remain between 0.5 and 19 bar. For compressor lubrication the synthetic polyalphaolefin (PAO) Mobil-SHC-226E has been utilized with basic data summarized in Table 4.5 obtained from Mobil (2018). Investigations on required superheat for overhanging working fluids presented in Section 3.7 and cycle design simulations outlined in Section 4.1.1 have shown that decoupling of superheat from the heat source can improve efficiency. Furthermore the redirection of the compressor motor waste heat to the refrigerant can improve cycle efficiency. Therefore, the standard air cooled separating hood compressor has been adapted to a suction gas cooled design with the CHX prototype. The CHX prototype consists of two coaxial pipes forming an annular gap flow channel with a height of 10 mm. The annular flow channel is devided into 10 passes by separating walls resulting a meandering flow of the refrigerant along the circumference of the CHX as depicted in Figure 4.10.

Table 4.4: Basic compressor data obtained from Moisi and Rieberer (2016) and Verdnik (2017)

Basic Type	Frigopol 30L-DLRX-13
Frequency range	35-75 Hz
Swept volume at 1450 min^{-1}	29.94 m^3/h
Max. high pressure	28 bar
Low pressure range	0.5 to 19 bar
Nominal electrical power	9.6 kW
Number of cylinders	3
Motor type	asynchronous, 400 V, 3 phase, cage induction
Number of poles	2
Synchronous speed range	1050 to 2250 min^{-1}
Frequency inverter (FI)	ABB ACH580-01

Table 4.5: Basic data of compressor lubricant obtained from Mobil (2018)

ISO Viscosity Grade	68
Viscosity Index	136
Viscosity at 40 °C	69 $\mathrm{mm/s}^2$
Viscosity at 100 °C	10 $\mathrm{mm/s}^2$
Pour point	−50 °C
Flash point	266 °C
Density at 15 °C	0.83 $\mathrm{kg/dm}^3$

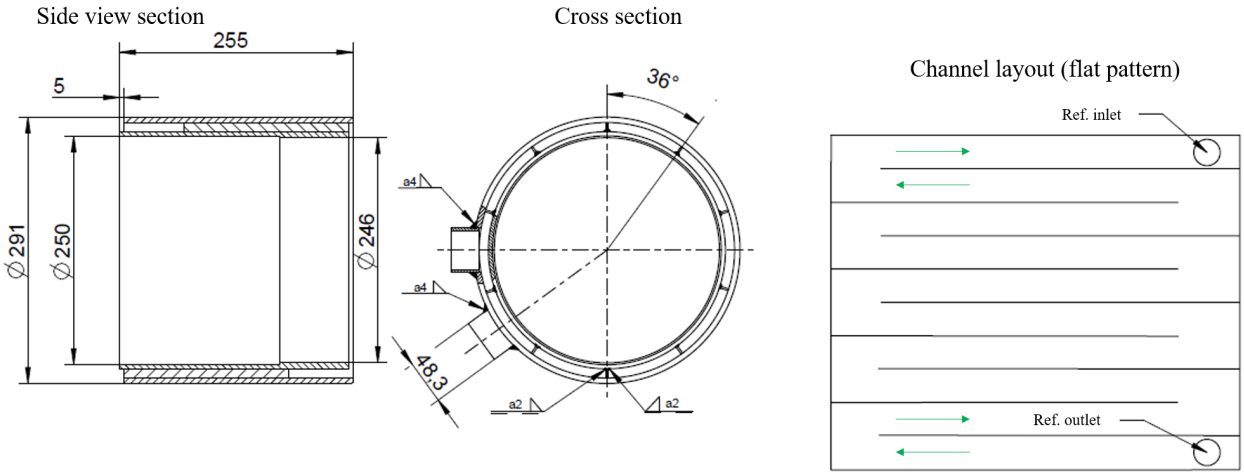

Figure 4.10: Construction drawing of the CHX flow channel arrangement (based on Skreinig, 2016, modified)

The stator of the compressor motor is pressed into the heat exchanger under a thermal joining procedure and then connected to the compressor via a flange as illustrated in Figure 4.11. The basic CHX design has been carried out by Skreinig (2016) with additional constructive adaptions by Frigopol for piping connections and sensor application. It has been executed as a stainless steel welding construction.

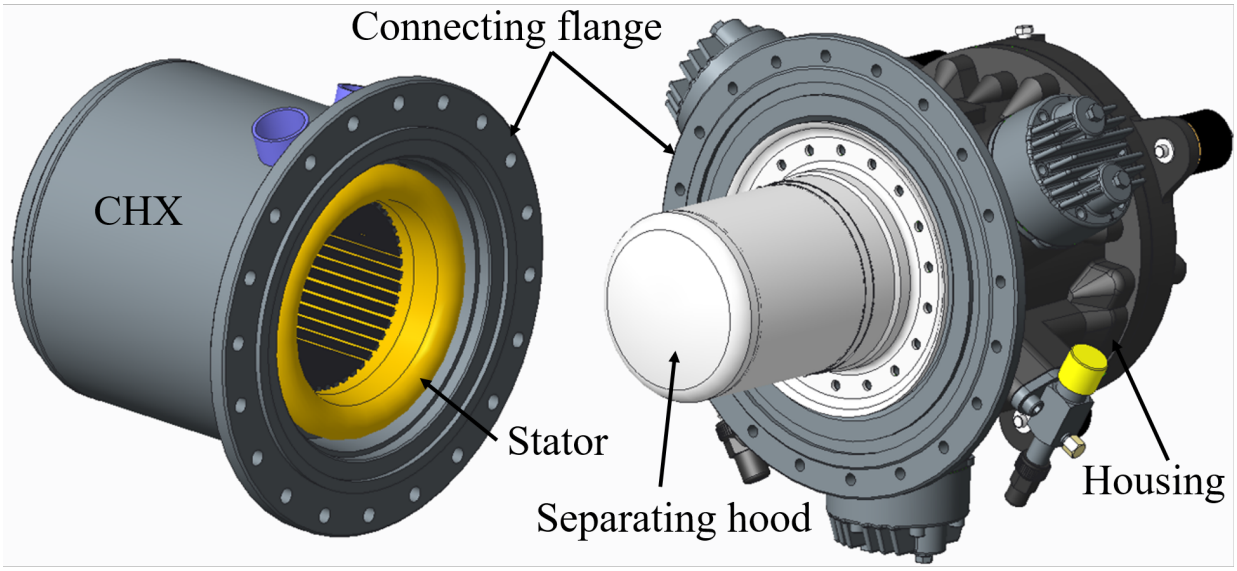

Figure 4.11: CAD drawing of CHX assembly and compressor (based on Skreinig, 2016, modified)

As a consequence of the novel compressor cooling and the first application with n-Butane as refrigerant, the compressor drive has been equipped with temperature sensors to support the characterization of the compressor heat exchanger and to monitor the winding head temperature ($t_{EM,wh}$) throughout the experimental testing phase. For the winding head temperature a PT1000 temperature sensor as been implemented by the compressor manufacturer. Additionally the iron core surface temperature ($t_{Fe,sf,j}$) at the interface of CHX and stator iron core has been of interest for the present study. Two thermocouple Type K temperature sensors with a diameter of 1 mm have been applied on opposite locations on the CHX circumference approximately at the center height of the iron core . The sensor locations are schematically indicated Figure 4.12 along with the built in situation at the test rig (additionally indicated is the refrigerant temperature at the suction chamber inlet $t_{ref,1}$).

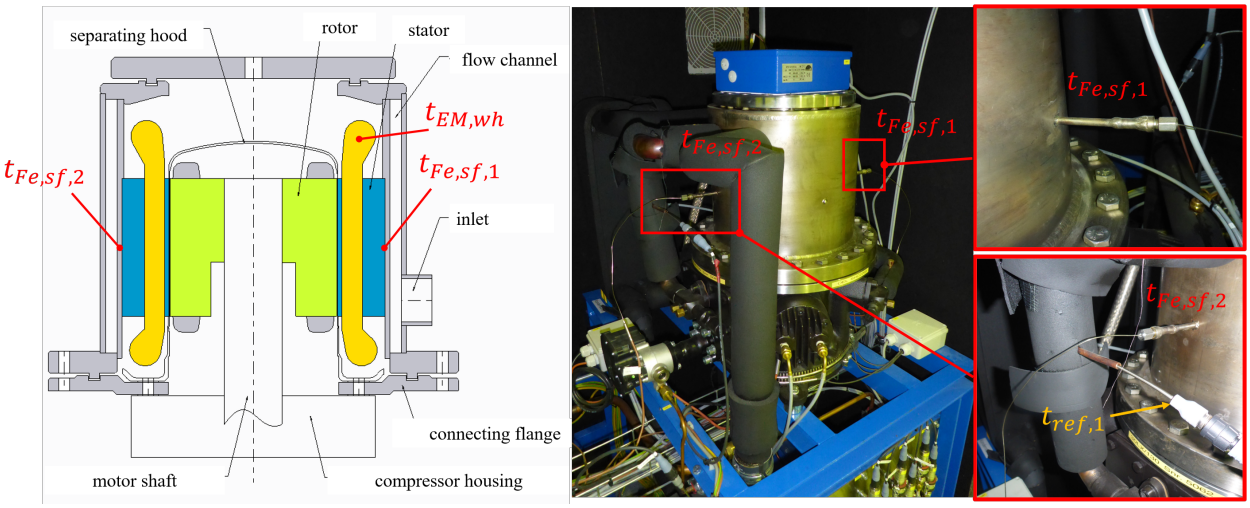

Figure 4.12: Schematic compressor drive temperature sensor positions and test rig built in situation of iron core surface temperature sensors

The maximum allowed winding head temperature has been specified by the compressor manufacturer with approx. 180 °C. Experimental results concerning compressor drive temperatures are discussed in Chapter 5.

4.4 Refrigerant Valves

Two groups of actively operated valves are utilized within the high temperature heat pump. The first group contains the solenoid operated and hermetically sealed refrigerant valves such as the expansion valve (EXV) and the 3 way valve controlling the internal heat exchanger flow (VIHX). Both valves have been dimensioned by the project partner using manufacturer design tools and the input data from the design simulations (see Section 4.1.3). The EXV exhibits a proportional operating characteristic and a normally closed position at stand still. The IHX path is closed for VIHX valve at down times of the test rig. Table 4.6 summarizes the basic data and appearance of the initial and replacement EXV as well as the VIHX (compare to Verdnik, 2017).

Table 4.6: Basic design data and appearance of the EXV and VIHX obtained from Verdnik (2017), Siemens (2015a) and Siemens (2010)

Description	replacement EXV	VIHX (3 way)
Manufacturer	Siemens	Siemens
Type	MVL661.15-1.0	M3FK15LX
Nominal diameter	DN15	DN15
k_{vs}-value	1 m^3/h	3 m^3/h
Signal	4 to 20 mA	4 to 20 mA
Positioning time	<1 s	approx. 1 s
Appearance		

The second group contains the manually operated shut off valves to realize different cycle configurations manufactured by Danfoss (Danfoss, 2010). Corresponding to the gaseous and liquid refrigerant state, the nominal dimension DN25 (V5,V6,V7,V8,V9) and DN20 (V1,V2,V3,V4) have been selected respectively (see Figures 4.4 and 4.6). The shut off valves are of the SVA type and applicable for R600, pressure up to 40 bar and a temperature range from −50 to 150 °C (see Danfoss, 2010).

4.5 Auxiliary Components

Under auxiliary components, the liquid receiver, oil separator and oil level regulator are summarized. The utilized liquid receiver type FMP 7.1+SV(M28/M28) has been obtained from manufacturer Frigomec and holds a volume of 7.1 l (Frigomec, 2012). The pressure threshold lies at 28 bar in a temperature range between −10 and 120 °C (see Frigomec, 2012). The oil separator OS-42 FY and filter F-10L has been obtained from the manufacturer ESK Schultze (ESK, 2017). The oil separator holds a volume of 18.5 l with an initial oil filling of

approx. 600 g. The maximum allowed pressure lies at 31 bar in a temperature range of −10 to 140 °C (ESK, 2017). The oil level in the compressor is monitored by an oil level regulator, type INT280-130 from the manufacturer Kriwan (Kriwan, 2017). The oil level is optically sensed in a sight glass. Is the oil level below a certain threshold during operation the oil level regulator valve opens and compressor lubricant can return from the oil separator at high pressure to the compressor low pressure side. Figure 4.13 illustrates the built in situation of the described auxiliary components.

Figure 4.13: Test rig built in situation and component details of oil level regulator, liquid receiver and oil separator

Further auxiliary components such as sight glass and refrigerant filter as indicated in Figure 4.13 are standard components commonly used in heat pump technology and are not discussed in detail.

4.6 Safety Measures

The application of highly flammable refrigerants such R600 requires a certain set of safety measures to avoid the formation of a explosive refrigerant air mixture. A guideline in this regard can be found in the standard EN378 (2016) (see also Corberán et al., 2008). As mentioned above, the heat pump prototype is located in a ventilated housing (see also Figure 4.5). The refrigerant concentration within the housing is measured by two gas detectors located approximately 250 mm above ground since R600 has a higher density than air (see Chapter 3). The detectors are connected to a safety control unit. In an event of refrigerant leakage, the safety control unit shuts off the power supply of the entire test rig and sets off an visual and acoustic signal if a refrigerant concentration of 20 % of the lower flammability level (LFL) of R600 is reached (see also Chapter 3). Simultaneously the safety ventilation system will be set in effect to transport the refrigerant air mixture outdoors (see Figure 4.14 on the right). The gas detectors and the control unit remain in operation. The acoustic and visual signal stops if the concentration decreases below 5 % of the LFL, the test rig however remains disconnected from the power supply until the alarm has been confirmed via a safety button. The detectors have been of the type ExDetector HC 150 from the manufacturer Bieler+Lang (Bieler+Lang, 2010). For the safety control unit the GMC 8022 of Bieler+Lang has been utilized (Bieler+Lang, 2003). Figure 4.14 shows the different safety measures combined in the high temperature heat pump test rig.

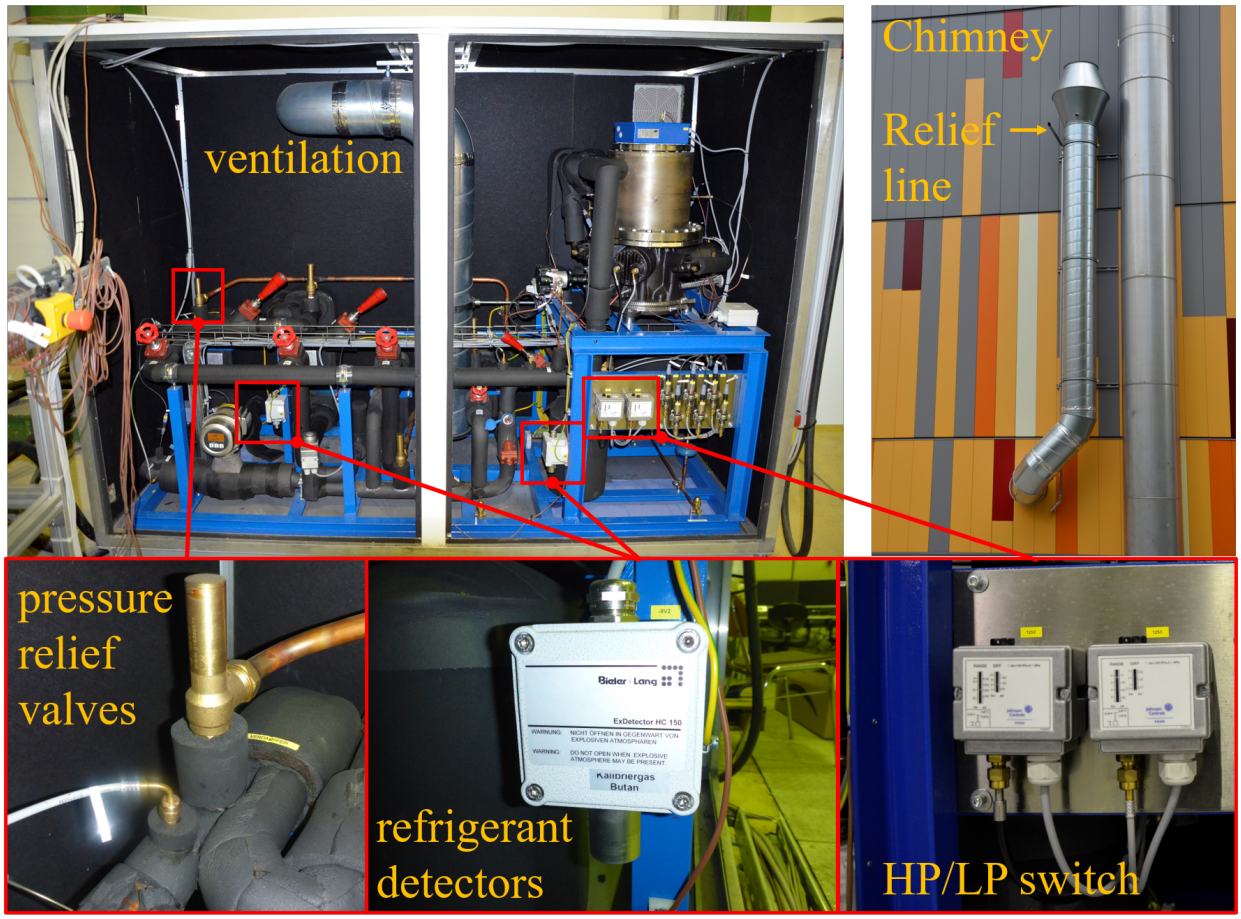

Figure 4.14: Safety measures of the high temperature test rig (compare to Verdnik (2017))

In addition to the flammability based safety measures, standard precautions such as pressure relief valves and high and low pressure switches (HP/LP) have been implemented as indicated

in Figure 4.14. The pressure relief valves open at 24 bar, releasing the refrigerant via a relief line to the outdoors (see Figure 4.14). Furthermore the compressor motor thermal safety disconnects the compressor power supply at a winding head temperature of 180 °C (see Section 4.3).

4.7 Source and Sink Hydraulics

The source and sink hydraulics have been realized as admix circuits in order to control the inlet temperature of the evaporator and subcooler respectively as depicted in Figure 4.15 (see also Figure 4.4). Both circuits have been designed identically with PI controlled 3 way valves and frequency controlled centrifugal pumps to provide the required inlet temperature and the desired flow rate. The flow rate can additionally be adjusted using metering valves in the supply lines. The source and sink hydraulics are connected via heat exchangers to the heat source and sink infrastructure of the IWT as indicated in Figure 4.15. Both supply and return lines can be connected by opening ball valves in order to preheat both circuits before heat pump start up. It has been possible to adjust a fixed bypass using bypass metering valves in both circuits however this option has never been used throughout testing. The different cycle configurations can be realized by operating the respective ball valves. Two expansion vessels ensure a constant absolute system pressure of approximately 250 kPa. The volume flow is determined by magnetic inductive flow meters (MID) located in the return lines of the respective circuits (see Section 4.9).

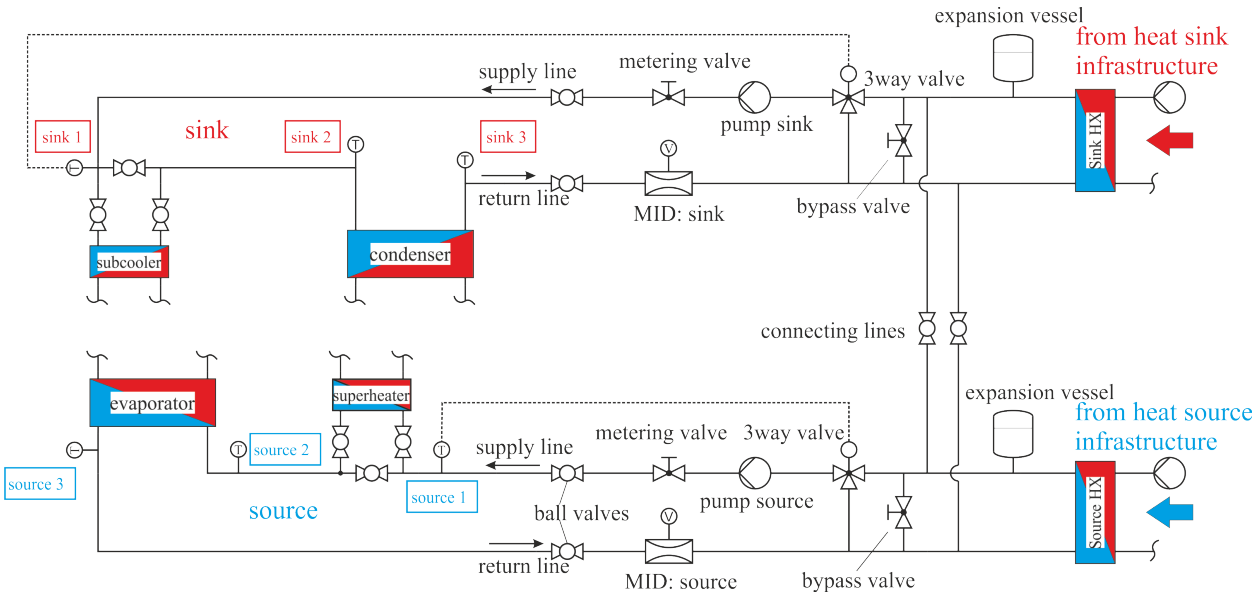

Figure 4.15: Layout of the source and sink hydraulics

Table 4.7 summarizes the main parameter and components of the source and sink hydraulics. The control parameters (K_p and τ_R) for the mixing valves have been derived by Verdnik (2017).

Table 4.7: Main parameter and components of source and sink hydraulics

Parameter	Source	Sink	Literature
Mixing valve	VXG44.40-25	VXG44.20-6.3	Siemens (2015b)
Valve motor	SAS61.33	SAS61.33	Siemens (2016)
Pump	Grundfos TPE/2-40-120	Grundfos TPE 25-90/2	Grundfos (2016)
Proportional gain (K_P)	0.5 %/K	−0.5 %/K	Verdnik (2017)
Reset time (τ_R)	0.1 min	0.2 min	Verdnik (2017)
Temperature range	50 to 80 °C	50 to 110 °C	-
Max. flow rate	approx. 1.6 dm^3/s	approx. 0.47 dm^3/s	-
Nominal diameter	DN50	DN25	-

The mixing valves exhibit a linear flow characteristic. The basic input quantity for the mixing valves are the desired inlet temperatures of the subcooler and evaporator respectively (sink 1 and source 1 in Figure 4.15). However, depending on the cycle configuration the input signal can be switched to the appropriate temperature (e.g. source 2 for the Superheater configuration). The flow rate has been adjusted manually by changing the pump speed and operating the metering valves accordingly to the desired source and sink temperature difference across the condenser (+subcooler) and evaporator (see Chapter 5).

4.8 Test Rig Control and Data Acquisition

The heat pump control and data acquisition software has been realized within a LabVIEW 2015 SP1 environment (NI, 2020a). As corresponding hardware a cRio 9074 rack from National Instruments (NI, 2020b) with the required input and output modules for control and data acquisition has been selected. Table 4.8 summarizes briefly the module configuration obtained from Verdnik (2017) (modified and translated). A complete list of input and output signals can be found in Appendix A.3.

Table 4.8: Module configuration of the test rig data acquisition system obtained from Verdnik (2017) (modified and translated)

Module	Model	Type	Configuration
1	NI 9375	Digital In/Out	16 Inputs (24 V DC), 16 Outputs (6 to 30 V)
2	NI 9208	Analog In	16 Inputs (±21.5 mA), 24 bit
3	NI 9265	Analog Out	4 Outputs (4 to 20 mA), 16 bit
4	NI 9263	Analog Out	4 Outputs (±10 V), 16 bit
5	NI 9201	Analog In	8 Inputs (±10 V), 12 bit
6	NI 9217	RTD	4 Inputs, temp. dependent resistances, 24 bit
7	NI 9217	RTD	4 Inputs, temp. dependent resistances, 24 bit
8	NI 9213	Thermocouple	16 Inputs for thermocouple

The main actuators controlled by the developed control environment are the superheat control realized with the EXV, the compressor speed and the source and sink inlet temperatures. The superheat control is carried out with a simple PI (proportional-integral) controller obtained from LabVIEW library software components. Depending on the cycle configuration it has been possible to switch the superheat input value calculated from sensor position 8 (Basic and IHX) to sensor position 9 (SUP) (see Figure 4.4). The superheat value has then

been calculated as outlined in Chapter 3. The proportional gain (K_P) and the reset time (τ_R) for the EXV is given in Table 4.9.

Table 4.9: Utilized PI parameters corresponding to the respective EXV size

Parameter	Unit	Value
Proportional gain (K_P)	[%/K]	0.8
Reset time (τ_R)	[min]	0.7

The compressor speed is manually controlled by providing an analog current signal to the frequency inverter proportional to the compressor frequency. The source and sink inlet temperatures are controlled by 3 way valves utilizing again a PI controller similar to the EXV (see Section 4.7).

4.9 Measurement Equipment

An overview on the different measurement equipment, its specification and built in situation regarding temperature, pressure, mass and volume flow as well as electrical consumption shall be given in the following subsections. The schematic position of all sensor locations can be found in Figures 4.4 and 4.15. An entire list of all measured quantities with corresponding sensors can be obtained from Appendix A.3.

4.9.1 Temperature and Pressure

In order to minimize the possibility of leakage, temperature sensors within the refrigerant circuit have been implemented by copper pipes soldered into the piping system as depicted in Figure 4.16 exemplary for sensor locations 6 and 9 (photographs taken during maintenance). Therefore the temperature sensors are only indirectly in contact with the refrigerant. As sensor type, mainly PT100 according to DIN EN 60751 Class A with a diameter of 3 mm and a length of 150 mm have been utilized to determine the refrigerant temperatures (PMR, 2016, compare to Appendix A.3).

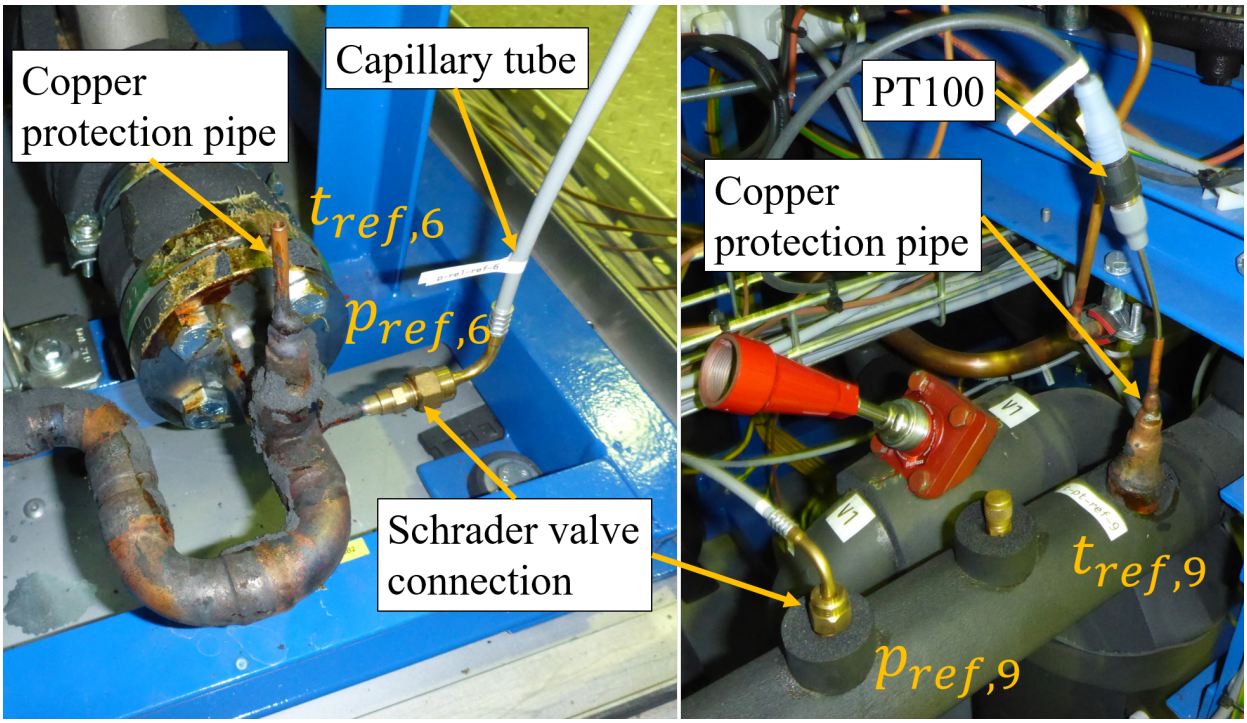

Figure 4.16: Realized refrigerant temperature and pressure sensor application exemplary for sensor position 6 (left) and 9 (right)

The pressure sensors have been applied using Schrader valves and capillary tubes as illustrated in Figure 4.16. The pressure sensors are all collected on a console and connected to the other end of the capillary tubes (see Figure 4.6). The refrigerant pressure is measured relatively to the ambient. The absolute refrigerant pressure is then calculated in combination with the absolute pressure measured of the ambient air within the test rig housing. The pressure sensors are of the strain gauge principle with specifications summarized in Table 4.10.

Table 4.10: Pressure sensor specification PMR (2016)

Medium	Model	Type	Range	Error
R600	PIT-C	relative	0 to 40 bar	$\leq 0.2\,\%$ FS
Air	PIT-C	absolute	750 to 1250 mbar	$\leq 0.3\,\%$ FS

The source and sink temperature sensors are in direct contact with the heat transfer medium using cutting ring screw connections as depicted in Figure 4.17 for the source side and in detail for the sink inlet temperature with sensor annotations indicated. All sink and source temperature sensors are realized as Type T thermocouples Class 1 with a length of 150 mm and a diameter of 3 mm PMR (2016).

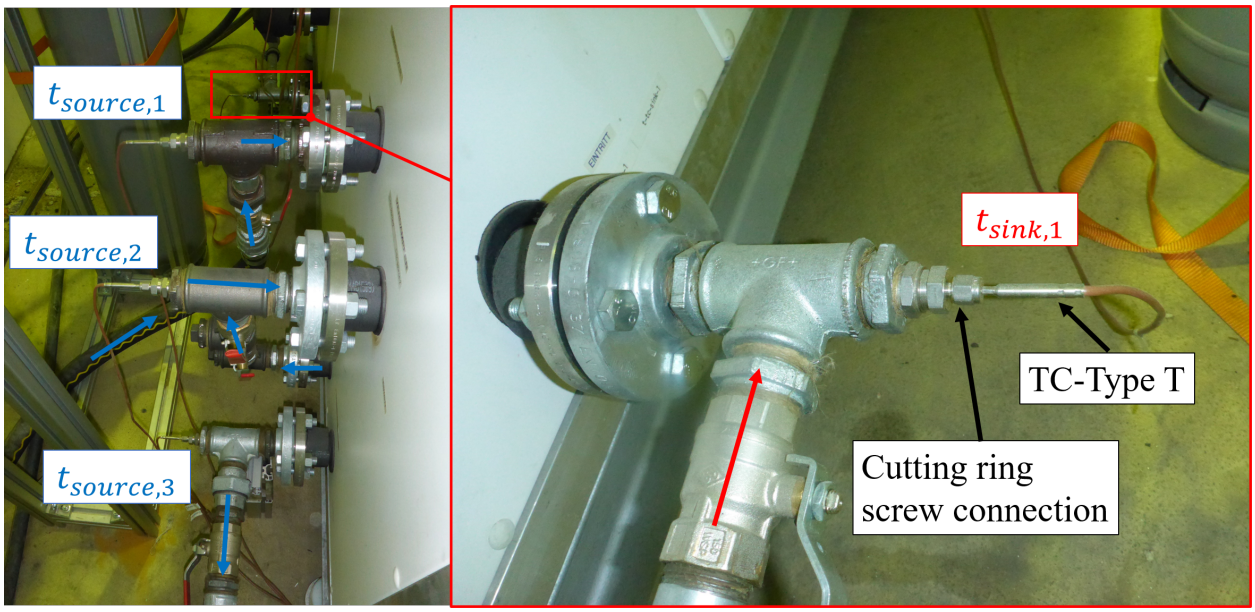

Figure 4.17: Realized source temperature sensor application (left) and detailed built in situation exemplary for the sink inlet temperature (sink,1) (right)

4.9.2 Mass and Volume Flow

The refrigerant massflow has been directly measured using a coriolis massflow sensor located between the EXV and VIHX (see also Figures 4.4 and 4.5). Source and sink volume flow has been determined utilizing magnetic inductive (MID) flow meters located in the return lines of the respective hydraulic circuit. Figure 4.18 shows the test rig built in situation for the coriolis (left) and the MID sensor in the sink hydraulics (right) (see also Figure 4.5 and Section 4.7 respectively).

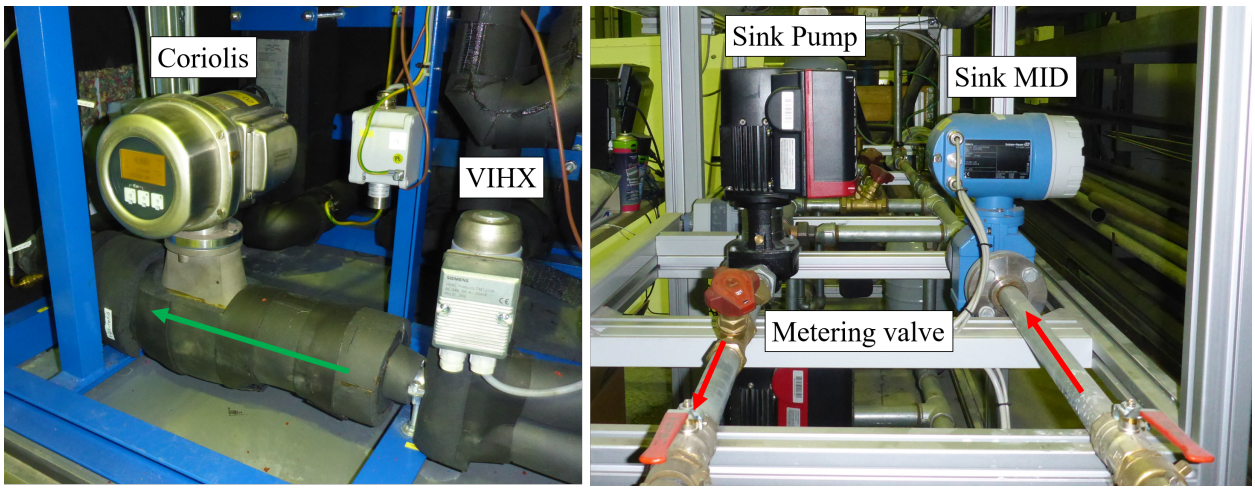

Figure 4.18: Built in situation of the coriolis refrigerant massflow sensor (left) and the sink MID volume flow sensor (right)

An overview on flow sensor specification is given in Table 4.11

Table 4.11: Overview on test rig flow sensor specification

	Ref. Circuit	Source	Sink
Medium	R600	Water	Water
Type	Corilolis	MID	MID
Manucaturer	Endress+Hauser	Endress+Hauser	Endress+Hauser
Model	Proline Promass 83F	Proline Promag 50P	Proline Promag 50P
Range	0 to 2 kg/s	0 to 4 dm^3/s	0 to 2 dm^3/s
Nom. diamenter	DN15	DN25	DN25
Literature	E+H (2016b)	E+H (2016a)	E+H (2016a)

4.9.3 Electrical Compressor Consumption

The total electrical compressor energy consumption ($W_{comp,el}$) is simply measured by an electric energy meter (counter) of the type ELTAKO DSZ12D-3x65 (1000 Impulse per kW h, ELTAKO, 2020). The impulse counter is located before the frequency inverter considering the the total energy consumption of the FI/compressor unit as schematically depicted in Figure 4.19 (compare to Figure 3.12). Please note that the CHX inlet state denotation has changed in Figure 4.19 from $\hat{1}$ to 9, corresponding to the experimental set up depicted in Figure 4.4.

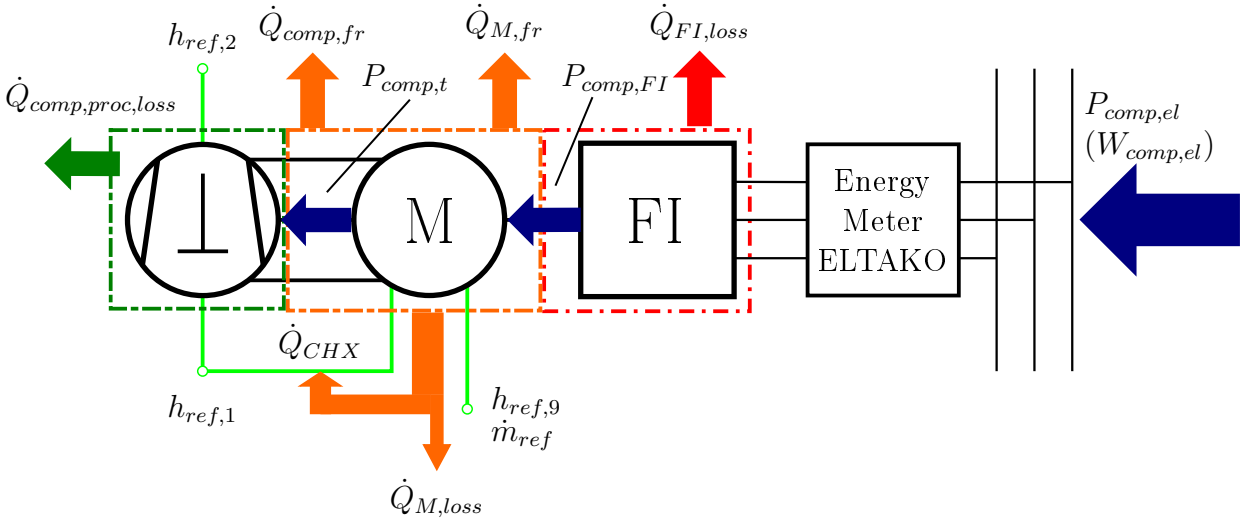

Figure 4.19: Schematic position of the utilized energy meter

The total electrical compressor consumption $P_{comp,el}$ (in W, see also Equation 3.38 and 3.50) can then be calculated using the absolute number of impulses (N_{imp} in 3600 W s) and the time interval ($\Delta\tau$ in s) at two consecutive points in time (τ and $\tau + \Delta\tau$) following Equation 4.1.

$$P_{comp,el}(\tau + \Delta\tau) = \frac{[N_{imp}(\tau + \Delta\tau) - N_{imp}(\tau)]}{\Delta\tau} \tag{4.1}$$

The digital signal of the energy meter has been read in by the test rig control software and recorded by an implemented counter. The power output of the frequency inverter $P_{comp,FI}$ (see also Equation 3.44 and 3.45) has been obtained from the inverter itself as analog current signal. Both signals and their module assignment can be found in Appendix A.3.

5 EXPERIMENTAL ANALYSIS

The main focus of the experimental analysis has been the detailed performance evaluation of the single stage R600 high temperature heat pump test rig with different cycle configurations. In this regard performance maps of different parameters shall elucidate the system behavior for different operation points. Especially the efficiency and heat capacity of the different cycle configurations have been of interest since there is still only a small amount of data available in literature (see for example Verdnik, 2017, Wemmers et al., 2017, Moisi et al., 2017, Moisi and Rieberer, 2018). The use of state diagrams (t/h) supports a detailed cycle analysis. A further, very interesting point represents the characterization of the utilized separating hood compressor with the newly developed compressor heat exchanger (CHX) regarding efficiency, pressure drop and heat transfer. Special operational behaviour such as the heat pump start up phase as well superheat instability have been investigated. The obtained experimental data have finally been used to parametrize the simulation model described in Chapter 6.

5.1 Methodology and Test Matrix

The developed test rig provides the possibility to investigate three main cycle configurations with focus on superheat preparation (Basic, SUP and IHX, see also Chapter 4). Therefore a test matrix has been defined in order to enable the creation of performance maps regarding different parameters. These performance maps are based on experimental data of steady state operation points. The compressor frequency, the source inlet temperature and the temperature difference ($t_{source,in}$, ΔT_{source}) along the evaporator as well as the sink inlet temperature and the temperature difference ($t_{sink,in}$, ΔT_{sink}) along the condenser (and subcooler) have served as input parameters for the test rig control. Furthermore a superheat set point has been been provided as input parameter for the EXV control (see Section 5.3.2). Temperature differences on the source and sink side have been adjusted manually by changing the corresponding pump speed and operating respective metering valve (see Chapter 4). After the system reached a steady state, the operation point has been recorded for at least 20 min if not declared otherwise. The field of operation ranges for source side inlet temperatures from 50 °C to 80 °C and sink outlet (supply) temperatures from 80 °C to 110 °C. With 35 Hz, 50 Hz and 75 Hz (approx. 20.9 m^3/h, 29.9 m^3/h and 44.9 m^3/h respectively), three different compressor frequencies have been applied for each cycle configuration. The main boundary conditions and test matrix can be obtained from Table 5.1. In total, 298 operation points have been recorded, including repeated tests and tests with only minor changes. The raw data on which the performance and parameter maps presented in Sections 5.5 and 5.6 (in total 88 operation points) are based on, can be found in Appendix A.4. Additionally, the degree of superheat for certain operation points have been investigated as well as the dynamic start up behaviour. The resulting refrigerant charge for the test rig has been determined experimentally. As a starting point an refrigerant charge of 8.3 kg has been selected. However in high load points a distinct increase in condensation pressure and correspondingly a subcooling has occurred already in the condenser indicating a flooded receiver. As a consequence the refrigerant charge has been reduced to 7.7 kg. All operation map results in Sections 5.5,5.6,5.7 and 5.8 are therefore based on a refrigerant charge of 7.7 kg.

Table 5.1: Main boundary conditions and test matrix (based on Moisi and Rieberer, 2017, modified)

Boundary Conditions		Test Matrix			
Refrigerant	R600	$t_{sink,in}$	$t_{sink,out}$	$t_{source,in}$	$t_{source,out}$
Sink medium	water (250 kPa)	°C	°C	°C	°C
Source medium	water (250 kPa)	50	80	50	45
Recording interval	$\geq$ 20 min	60	90		
Configurations	CHX, SUP, IHX	70	100		
Frequency	35 Hz, 50 Hz, 75 Hz	80	110		
Sink temp. diff	30 K	-	-	60	55
Source temp. diff.	5 K	60	90		
		70	100		
		80	110		
		-	-	70	65
		-	-		
		70	100		
		80	110		
		-	-	80	75
		-	-		
		-	-		
		80	110		

The, in the following sections discussed condensation temperature t_{cond} has been calculated based on the pressure at the compressor outlet (state 2, compare to Figure 4.4) since it is the last pressure sensor upstream of the condenser inlet (see also Section 3.2.3 for the defined location of t_{cond}). The evaporation temperature has then been calculated on the basis of the pressure at state 8 (compare to Figure 4.4) since the it is the first pressure sensor downstream of the evaporator outlet (see also Section 3.2.2 for the used definition of t_{evap}). The saturation pressure in state 7 (compare to Figure 4.4) is calculated with the measured temperature $t_{ref,7}$ (compare to Figure 4.4) and the appropriate refrigerant properties. For the entirety of the presented experimental results and in correspondence with Figure 4.4, the following assignment of condensation and evaporation temperature as well as the pressure value at state 7 is valid.

$$t_{cond} \coloneqq t''_{ref,3}(p_{ref,2})$$

$$t_{evap} \coloneqq t''_{ref,7}(p_{ref,8})$$

$$p_{ref,7} = p_{sat}(t_{ref,7})$$

The general quality of the obtained experimental results is discussed briefly in the following section.

5.2 Quality of Experimental Results

Any experimental result is afflicted with uncertainties influenced by sensor type, installation and signal conversion processes. The uncertainties for the, in Chapter 4 described, measurement principles and the derived quantities (e.g. heating capacity) have been estimated

based on the concept of Gaussian error propagation using the software package EES v.9.901 (F-Chart, 2016). The Pt100 and thermocouple Type-T temperature sensors have been calibrated using a process thermostat resulting in a maximum measurement deviation of ±0.1 K and ±0.25 K respectively (see Verdnik, 2017). The deviation of the volume flow, mass flow and pressure have been derived on basis of manufacturer data in combination with conversion errors of the data acquisition modules as described in detail by Verdnik (2017). The resulting measurement deviations for each measurement principle considering the entirety of recorded experimental data are given in Table 5.2

Table 5.2: Minimum and maximum values of the estimated measurement deviation for each principle and the entirety of recorded experimental data based on the approach by Verdnik (2017)

	temperature	pressure	volume flow	mass flow	electrical power
	$u_{tot,t}$	$u_{tot,p}$	$u_{tot,\dot{V}}$	$u_{tot,\dot{m}}$	$u_{tot,P}$
	K	kPa	dm^3/h	kg/h	W
min.	± 0.1	± 0.51	± 9.7	± 1.3	± 13
max.	± 0.25	± 14.1	± 44.4	± 3.2	± 72

Furthermore the empirical standard deviation sd_y of the recording period has been included into the measurement deviation of each quantity to account for the variation in time or in other words, the steadyness of the observed operation points. This yields a total deviation $u_{tot,y}$ for each measurement principle (y) as a combination of the estimated measurement deviation $u_{m,y}$ and the standard deviation sd_y based on Gaussian error propagation following Equation 5.1. This approach is an interpretation of a methodology provided by BIPM (2008) for uncertainty estimation, where empirical and non empirical uncertainties are treated identically as uncorrelated non sytematic deviations. In the present case, the timely variations of a quantity over the recorded period in a steady state operation point, have been treated as uncorrelated repeated observations.

$$u_{tot,y} = \sqrt{u_{m,y}^2 + sd_y^2} \tag{5.1}$$

The total deviation of a derived quantity $u_{tot,z}$ can then be found with Equation 5.2 by using again the approach of Gaussian error propagation (see e.g. Hoffmann, 2015) and the total deviation of the corresponding measurement principles of Equation 5.2.

$$u_{tot,z} = \sqrt{\sum_{j=1}^{N} \left[\frac{\partial f}{\partial y_j} \cdot u_{tot,y,j} \right]^2} \tag{5.2}$$

The error margins given in the following discussion of experimental results are either based on Equation 5.1 if the quantity is a directly measured (e.g. temperature) or on Equation 5.2 if a derived quantity is considered (e.g. heating capacity) and thus including the standard deviation of the recorded interval.

5.3 Special Operational Behaviour

Two superheat related issues have been of special concern during the experimental analysis of the R600 heat pump test rig. As already discussed in Chapter 3 the degree of superheat at compressor inlet is an important control quantity regarding efficiency, cycle stability and

equally important, to avoid compressor damage due to liquid suction or wet compression. Specifically of interest in terms of wet compression is the start up phase while superheat stability considerably influences the cycle efficiency.

5.3.1 Start Up Phase

The start up phase of a high temperature heat pump using an overhanging working fluid such as R600 can be critical in terms of wet compression since test rig components, especially the compressor, need to heat up significantly above ambient temperature. The cast iron housing of the compressor and the customary built CHX (see Section 4.3) are representing high thermal capacities which, depending on the required electrical power (or compressor speed), can result in rather long heat up periods implying an extended operation period where wet compression can occur. In the start up phase, refrigerant flows from the outlet of evaporator with certain degree of superheat to the inlet of the CHX. The CHX and the compressor motor are still at a lower temperature, causing the refrigerant to cool down before entering the suction chamber of the compressor. If the superheat is sufficiently high at the CHX inlet, the refrigerant is still in a superheated state at the suction chamber inlet. Due to the low temperature of the cylinder walls, heat transfer is increased during the compression process leading to quasi isentropic change of state or even to a change of state with an entropy decrease if only the end points are considered (compare to Sections 3.3 and 3.7). In combination with a low degree of superheat the cooled compression process is likely to enter the two phase region causing liquid droplets to form, which can damage the compressor. As an example for a start up process with a compressor speed of 35 Hz and a cycle configuration without subcooler (see Chapter 4), Figure 5.1 shows the transient experimental results for a compressor outlet temperature $t_{ref,2}$, condensation temperature $t_{cond} = t''_{ref,3}$ (see Section 5.5), evaporation temperature $t_{evap} = t''_{ref,7}$ (see also Section 5.5), superheat before CHX inlet $\Delta T_{sup,ref,9}$, superheat at the inlet of the compressor $\Delta T_{sup,ref,1}$ (see Section 3.2.2 and 4.3) as well as the EXV setting I_{EXV}. Furthermore sink and source temperatures are depicted. It has to be noted that the presented case does not represent a true "cold start". The provided transient data has been recorded shortly after the compressor start with component temperatures (e.g. compressor, CHX) close to their initial values. In general, before heat pump start up, it has been found appropriate to preheat the source and sink medium to the vicinity of the desired temperature levels. This can be observed in Figure 5.1 at $\tau = 0\,\mathrm{s}$ where the initial source and sink inlet temperatures (dash-dotted) are around 50 °C. The pressure levels in the condenser and evaporator at stand still rise accordingly to the sink and sources temperatures. The heat pump has been started with a constant EXV opening of 20 % (gray line) until $\tau = 50\,\mathrm{s}$, switching to the PI control with a superheat set point of $\Delta T_{sup,ref,9,set} = 30\,\mathrm{K}$ (the green line shows the actual superheat signal $\Delta T_{sup,ref,9}$) until approximately 280 s. From this time the superheat set point has been successively reduced reaching a value 8 K at 1200 s which additionally results in a stepwise increase of the evaporation temperature (blue solid line). As discussed above, the critical phase in terms of wet compression will be in the beginning when component temperatures are still low. A sequence of t/h diagrams depicted in Figure 5.2 corresponding to the transient data in Figure 5.1 shall elucidate this problem. Figure 5.2a shows the t/h diagram after 100 s. It can be observed that state 6 is still subcooled although no subcooler is utilized, which is a consequence of cold piping and components between the high pressure receiver and sensor position 6 (compare to Chapter 4.1.2, Figure 4.4). Furthermore mass migration is still ongoing in this early start up phase, the high pressure receiver and the piping towards the EXV are located at the lowest point in the system where liquid refrigerant accumulates during downtimes.

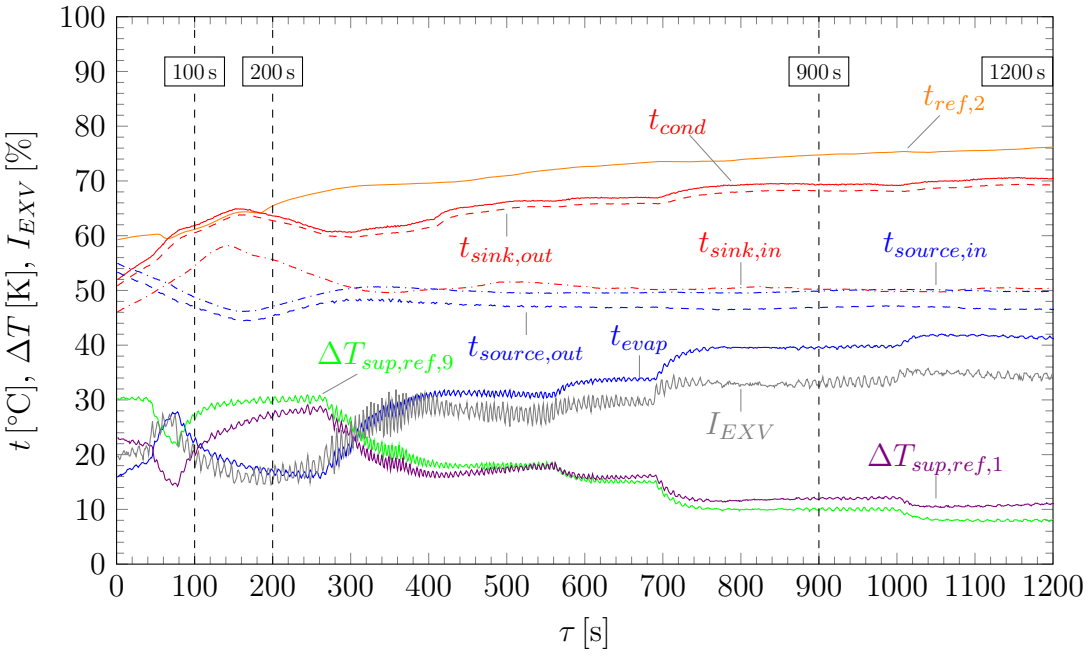

Figure 5.1: Transient data of temperatures, superheat and EXV setting during the start up phase of the heat pump test rig, for a compressor frequency of 35 Hz, in this case no subcooler has been utilized.

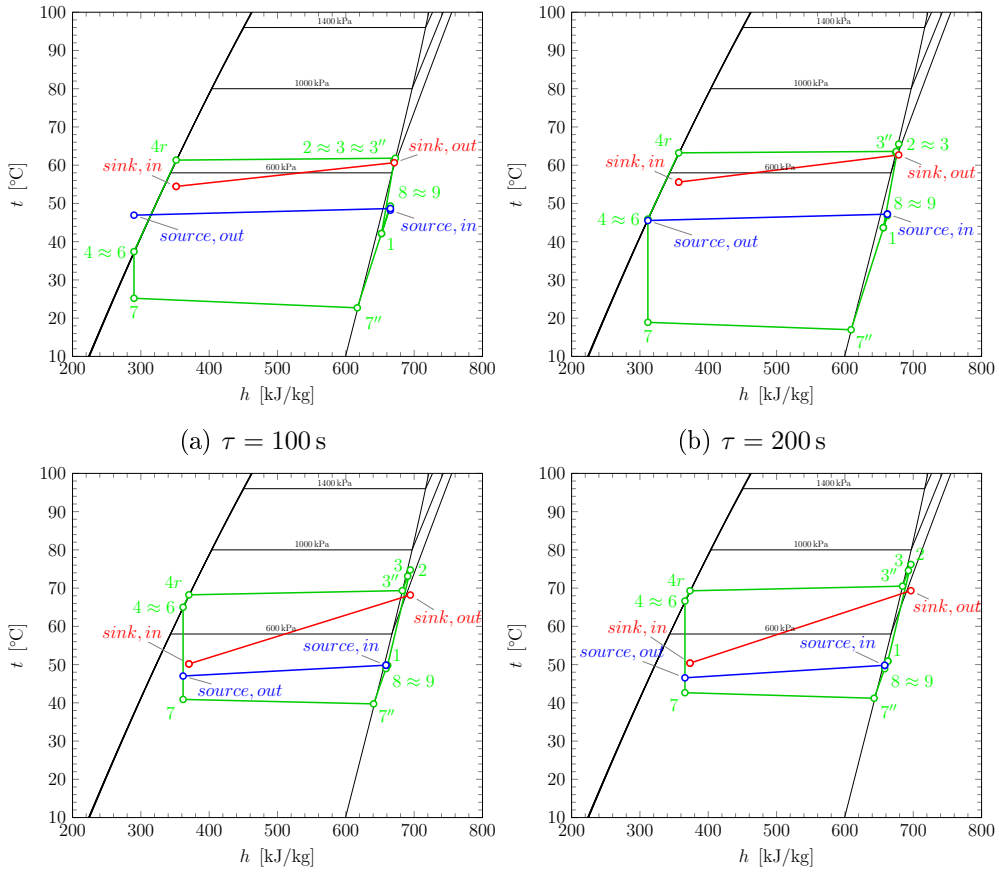

(a) $\tau = 100\,\mathrm{s}$ (b) $\tau = 200\,\mathrm{s}$

(c) $\tau = 900\,\mathrm{s}$ (d) $\tau = 1200\,\mathrm{s}$

Figure 5.2: Sequence of cycle states in a t/h diagram during start up for operation points at 100 s, 100 s, 900 s, 1200 s corresponding to Figure 5.1

Additionally, the high degree of superheat at state 9 results in a low evaporation pressure and thus suction gas density, leading to a reduced refrigerant mass in the evaporator. The superheat in state 1 is reduced from approx. 25 K ($\Delta T_{sup,ref,9}$) to 20 K due to the still "cold" thermal mass of the CHX and the compressor motor. The compressor outlet temperature $t_{ref,2}$ equals the condensation temperature which is an indication of a wet compression in this operation point. However it has to be noted that this can only be interpreted as an indication. Two aspects have to be taken into account in this regard. The first point is, that the enthalpy in state 2 has been calculated based on pressure and temperature measurement. If a two phase state occurs, pressure and temperature are interdependent and the state cannot not be completely defined without additional information. Therefore, the compressor outlet state cannot be depicted in the t/h diagram correctly. As a result, state 2 is assumed to lie directly on the phase boundary which can be observed in 5.2a. The second aspect is the sensor position which is located outside of the compressor in the hot gas line (approximately a 200 mm distance, compare to Chapter 4, Figure 4.4). Heat losses between the compressor and the sensor position might also influence the result. Figure 5.2b shows a similar cycle state at 200 s, but the subcooling is reduced due to mass migration and increasing system temperature. The compressor outlet temperature has slightly increased above condensation temperature indicating that the outlet state of the refrigerant is superheated. The superheat at the compressor inlet ($\Delta T_{sup,ref,1}$) is still lower than the superheat at state 9 due to an insufficient heat transfer from the compressor motor, but the difference between state 9 and 1 decreases. After the start up phase, the heat pump approaches steady operation. As depicted in Figures 5.2c and 5.2d at 900 s and 1200 s respectively, the degree of subcool has been strongly decreased as a consequence of a decreased superheat and hence an increased suction gas density. Nevertheless, still a small amount of subcool remains (approx. 3 K) although the subcooler is not utilized which indicates a slightly overcharged system for this operation point and cycle configuration. The compression process has developed a distinctly higher compressor outlet temperature. Thus a dry compression process can be assumed. The superheat (state 1) due to the compressor motor heat losses has increased above the evaporator superheat as depicted in Figures 5.1 and 5.2d indicating that the compressor motor temperature has increased sufficiently to heat up the suction gas. The described case stands as an example of the start up behaviour of any cycle configuration which has been investigated during experimental testing. In the first phase the compression outlet temperature equals the condensation temperature although a high degree of superheat at the CHX inlet has been set. The evaporator superheat is decreased significantly by the cold CHX which is further counter productive in terms of wet compression. The practical experimental work showed that the combination of a high evaporator superheat as described above with a higher compressor frequency increasing the absolute value of motor heat losses and furthermore decreasing the time during the compression process for heat transfer from the suction gas to the cylinder wall (see Eifler et al., 2009) can significantly shorten the critical start up phase of the compression process. However, despite the presented experimental data indicating a wet compression in the start up phase, liquid slugging or hammering could not been observed acoustically. Furthermore an inspection of one cylinder head has been carried out at the end of the experimental tests showing no obvious signs of damage in this regard. Therefore further investigations considering the start up phase using overhanging working fluids states an interesting future topic.

5.3.2 Superheat Instability

Probable reasons for superheat and thus control instability have been described in Chapter 3.4 with the common explanation for the instability phenomenon based on evaporator

characteristics rather than to be considered a control problem. As already outlined in Chapters 3 and theoretically and experimentally investigated in Chapters 5 and 6, the degree of superheat can influence the COP of a heat pump significantly. A common approach aims to minimize the evaporator superheat to the lowest possible value in order to maintain a high driving temperature difference in the superheating section and utilize a high fraction of evaporator area with a high two phase heat transfer at the same time ensuring that no liquid refrigerant enters the compressor. The minimum stable superheat would then describe the lower limit of possible superheat set points. In the course of the experimental testing, especially during the heat pump test rig start up phase, unstable superheat behaviour has been observed by Verdnik (2017). In his masterthesis, Verdnik (2017) has investigated different approaches in terms of control strategies and parameter in order to reduce superheat instability. For instance, an increase of the proportional gain and the reset time for a quicker control reaction could not improve superheat stability. The findings of Verdnik (2017) support the theory regarding superheat stability to be more an evaporator characteristic as discussed in Chapter 3 than a control problem. In order to gain more insight on the influence of the evaporator configuration and to determine a "minimum" stable superheat set point for the performance analysis, a variation of the superheat set point has been carried out for a circuit configuration with and without superheater. As a starting point, it is important to describe the evaporator, superheater and sensor configuration in more detail. Figure 5.3 shows a schematic sketch of the low pressure part of the test rig including sensor positions 8 and 9 (see Chapter 4). In the "evaporator only" case (blue arrows), when valves V8 and V9 are closed, the superheated vapour simply leaves the evaporator and passes sensor position 8 followed by sensor position 9 and subsequently enters the CHX (see Figures 4.4 and 4.7). The distance from the evaporator outlet to sensor 8 is approx. 0.25 m and for sensor 9 with approx. 2 m rather long with valves, bends and junctions in between. Is the superheater active (red arrows), valve V7 is closed, valves V8 and V9 are open, the refrigerant passes through the evaporator, the connection piping and finally through the superheater before reaching the sensor position 9 and the compressor. On the right side of Figure 5.3, a simplified $t/\dot{Q}$ diagram depicts the temperature characteristics of the refrigerant (green) and the source medium (blue) of the superheater configuration. Depending on the EXV set point, the superheat is distributed between the evaporator and the superheater (states 8 and 9).

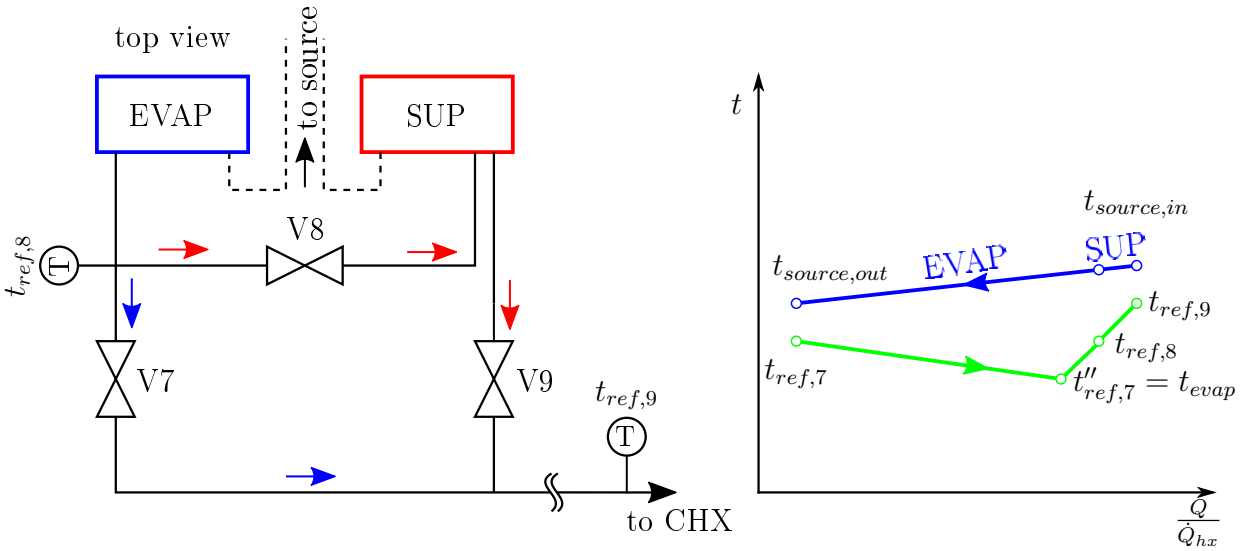

Figure 5.3: Schematic sketch of the built in situation of evaporator, superheater and sensor positions 8 and 9 (left) and the corresponding $t/\dot{Q}$ diagram for the superheater configuration

The results over a period of 10 min for the superheat set point variation with source tem-

peratures of 60/55 °C, sink temperatures of 80/110 °C and a compressor speed of 50 Hz and the basic evaporator configuration i.e without superheater is displayed in Figure 5.4. The superheat calculated at position 8 ($\Delta T_{sup,ref,8}$) and 9 are represented by dashed and solid lines respectively. Both superheat values have been determined analogously to Equation 3.24 using the respective pressure values. The superheat calculated at position 9 has been selected as control variable. Figure 5.4 shows the increasing superheat instability with decreasing superheat set point. The superheat signal remains stable from 12 K to 8 K with $\Delta T_{sup,ref,8}$ and $\Delta T_{sup,ref,9}$ exhibiting identical results in this range.

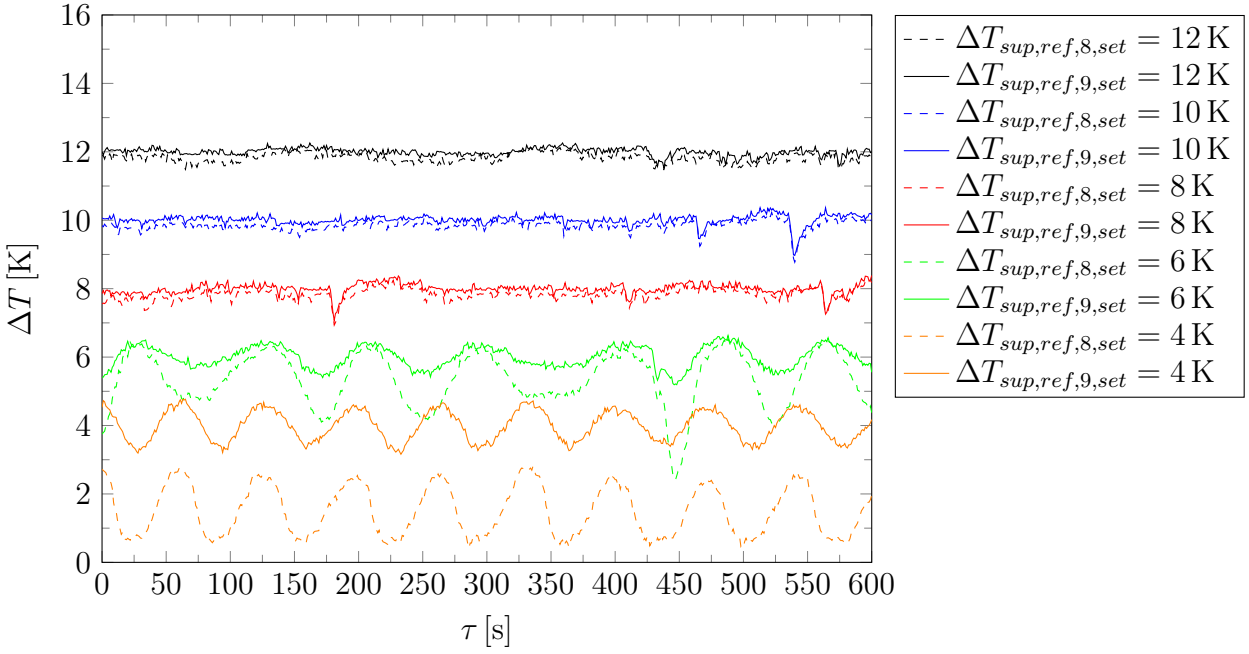

Figure 5.4: Superheat signals of sensor position 8 (evaporator outlet, dashed line) and 9 (CHX inlet, solid line) for different superheat set points and the control sensor location 9 for 50 Hz, source temperatures 60/55 °C, sink temperatures of 80/110 °C, without superheater

A distinct instability starts at a superheat of 6 K (precisely, first signs of instability have been observed at a superheat of 7 K). At this point, $\Delta T_{sup,ref,8}$ falls below $\Delta T_{sup,ref,9}$ especially in periods of an opening EXV. This indicates, that the transition point between two phase and superheated flow (see Chapter 3) moves towards evaporator outlet and thus sensor position 8. As discussed in Section 3.4, the transition point might oscillate in steady evaporator operation. This can cause, in an otherwise superheated vapour flow, saturated liquid or vapour to be dragged along or dispersed. However the liquid and vapour phase are not yet in thermal equilibrium, otherwise the main flow (at measured temperature) would not exhibit a degree of superheat of approx. 6 K. The lower outlet temperature sensed at position 8 can then be interpreted as a mean temperature between the saturated liquid and the superheat vapour flow. In this regard the pipe inner diameter of 25 mm in combination with a sensing length of the Pt100 sensor of approx. 15 mm, and a rectangular alignment to the refrigerant flow might have also an influence on the final value of $t_{ref,8}$. In cases where the expansion valve closes due to the decreasing superheat signal, $\Delta T_{sup,ref,8}$ reaches the value $\Delta T_{sup,ref,9}$ which indicates that the distance of the transition point to sensor 8 has sufficiently increased again. However the superheat set point lies within a range, where transition point fluctuations or oscillations can cause again a sudden decrease of superheat forcing the EXV to react. With a set point of 4 K the described effect is amplified due to a transition point even closer to sensor 8. Interestingly, the values $\Delta T_{sup,ref,9}$ and thus $t_{ref,9}$ are basically higher

than $\Delta T_{sup,ref,8}$ below the stable superheat threshold although no additional heat source is located in between (in the evaporator only case). One possible explanation might be the rather long distance from evaporator outlet to sensor position 9. Along this flow path heat can be exchanged between the superheated main flow, piping and valves leading to a partial evaporation of liquid fractions until position 9 is reached. Remaining liquid refrigerant which is still not in thermal equilibrium with the superheat main flow reaches sensor 9 and causing the superheat to decrease. The temperature at position 9 however, is higher since less saturated refrigerant reaches sensor 9. A similar behaviour can be observed for the same operation point and an active superheater (see Figure 5.3) as depicted in Figure 5.5. In this configuration, the transition point from two phase to superheated vapour shifts into the superheater with a decreasing superheat setpoint. Starting with 12 K, the transition point remains in the evaporator resulting in a superheat of 11 K at position 8. With a setpoint of 8 K the transition point has already been shifted into the superheater with superheat at position 8 nearly zero which indicates a two phase state at this location. An interesting difference can be observed in contradiction to the above described case. The starting point of a distinct superheat instability can be found at lower degrees of superheat (lower than 6 K) which is a consequence of the heat exchanger series arrangement. However a slight onset of instability can already be observed at 6 K.

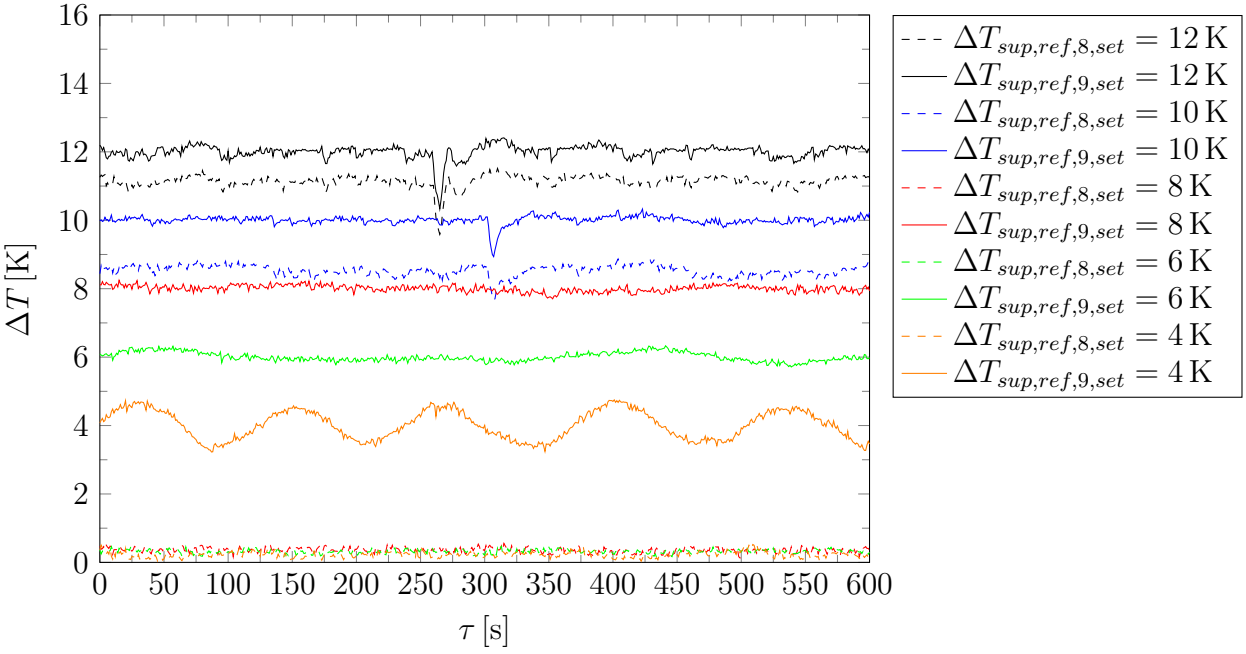

Figure 5.5: Superheat signals of sensor position 8 (evaporator outlet, dashed line) and 9 (CHX inlet, solid line) for different superheat set points and the control sensor location 9 for 50 Hz, source temperatures 60/55 °C, sink temperatures of 80/110 °C, with superheater

The above discussed experimental results regarding superheat instability have been interpreted based on MSS-Theory as oultined in Section 3.4. However since a detailed analysis of superheat stability has not been the focus of the present thesis, the experimental possibilities in this regard were limited to the above presented analysis. The complex two phase flow and heat transfer behaviour causing the control instability deduced above, could not have been verified experimentally and shall therefore be considered cautiously. Nevertheless qualitative statements regarding the influences on superheat stability can be made. The different onset and frequency of the instability for the two investigated heat exchanger configurations in combination with the work of Verdnik (2017) where different control strategies have been

analyzed, is a strong indication that the instability problem states a heat exchanger/heat transfer characteristic. Furthermore the control sensor position has a high influence on the instability which can be observed in Figure 5.4, where a in parts random behaviour is exhibited by $\Delta T_{sup,ref,8}$ at a superheat set point of 6 K. Additionally experimental experience showed, that a use of sensor 8 as control input has made the system more prone to instability due to the close location to the evaporator outlet, increasing the minimum stable superheat in some tests to 10 K as discussed for example in Moisi and Rieberer (2018). In contradiction to the MSS-Theory however, only a weak connection between evaporator capacity and superheat stability has been observed. By tendency, the superheat signal has exhibited a more stable characteristic with decreasing evaporator temperature or compressor speed however in a very limited range. As a result of the experimental experience, a superheat set point of 8 K in combination with the control sensor position 9, has been found to provide a sufficiently stable (comparable to Figure 5.4) heat pump operation. Therefore a superheat set point $\Delta T_{sup,ref,set,9}$ of 8 K has been used throughout the experimental performance analysis of the heat pump test rig described in this Chapter.

5.4 Compressor Characteristics

The characterisation of the utilized separating hood compressor in combination with R600 as refrigerant and a high temperature application has been of special interest in the course of this thesis. Furthermore an experimental analysis of the newly designed compressor heat exchanger prototype (CHX, see Section 4.3) in terms of pressure drop, transferred heat and motor cooling ability has been carried out. While Verdnik (2017) already presented first experimental results regarding compressor efficiencies and CHX characteristics, the data basis has been broadened and a detailed analysis of the obtained experimental data shall be provided in the following sections. Based on the gathered results, efficiency characteristics have been derived for the semi empirical simulation model.

5.4.1 Compression Process and Energy Balance

In order to analyze the compression process some assumptions and simplifications have to be made since not all relevant quantities have been determined experimentally. If the specific energy balance described in Section 3.3 (see Equation 3.41) is considered, quantities such as heat of dissipation ($q_{diss,1,2}$) or the heat flux across cyclinder walls ($q_{ht,1,2}$) are difficult to determine. In contradiction to the enthalpy difference between the compressor inlet (state 1) and outlet (state 2) which are more accessible. Knowing the inlet and outlet state however provides the possibility to determine a mean polytropic exponent $\bar{n}$ according to Equation 3.37. The compression work $w_{1,2}$ can then be approximated using Equation 3.36, neglecting the charge, discharge and re-expansion work. The relation between the ratio of the specific volume at the compressor inlet ($v_{ref,1}$) and oultet ($v_{ref,2}$) and the pressure ratio ($\pi_p = p_{ref,2}/p_{ref,1}$) based on the experimental data is depicted in Figure 5.6 corresponding to left ordinate (red). The calculated polytropic exponents (green) show a fairly constant dependency on the pressure ratio. The reason for the scattering of the results are mainly the compressor frequency and the evaporation temperature both defining the refrigerant flow inside the compressor and simultaneously the mean temperature level. A more detailed analysis has shown that with increasing compressor speed and evaporation temperature, n increases. For a certain source inlet temperature which corresponds to a certain range of evaporation temperatures (depending on superheat set point and source temperature difference) the polytropic exponent decreases slightly with the pressure ratio. In order to approximate the relation between specific volume and pressure ratio, a mean polytropic exponent

$\bar{n}$ in combination with the polytropic relation of Equation 3.37 has been found suitable since it displays good agreement with experimental data as shown in Figure 5.6 (dashed red line). The relation between specific volume and pressure ratio displays a nearly linear dependency due to a polytropic exponent close to one ($\bar{n} = 0.9754$). A closer look on Equation 3.40 reveals that the specific compression work must be identical to the specific enthalpy difference of an isentropic change of state if no dissipation and heat transfer takes place (compare Equation 3.43 and 3.41). Indeed a comparison between the isentropic enthalpy difference based on pressure and temperature measurement and the use of fluid property functions (F-Chart, 2016) and the polytropic approach depicted in Figure 5.6 confirms this statement. Since the specific compression work $w_{1,2}$ has been calculated based on state point 2 (compare to Section 5.5) and not on the isentropic state point 2is, this results might be misleading. However the main influence on $w_{1,2}$ if Equation 3.36 is considered, are the pressure ratio and the suction volume $v_{ref,1}$. The pressure for the determination of the isentropic state 2is and state 2 are considered identical and the difference of the specific volume between state 2is and state 2 is rather small (maximum 7 % decrease based on state 2). Hence the influence of the different state points regarding the calculation of the isentropic enthalpy difference (i.e. $\Delta h_{ref,is,1,2}$) and the specific compression work is negligible.

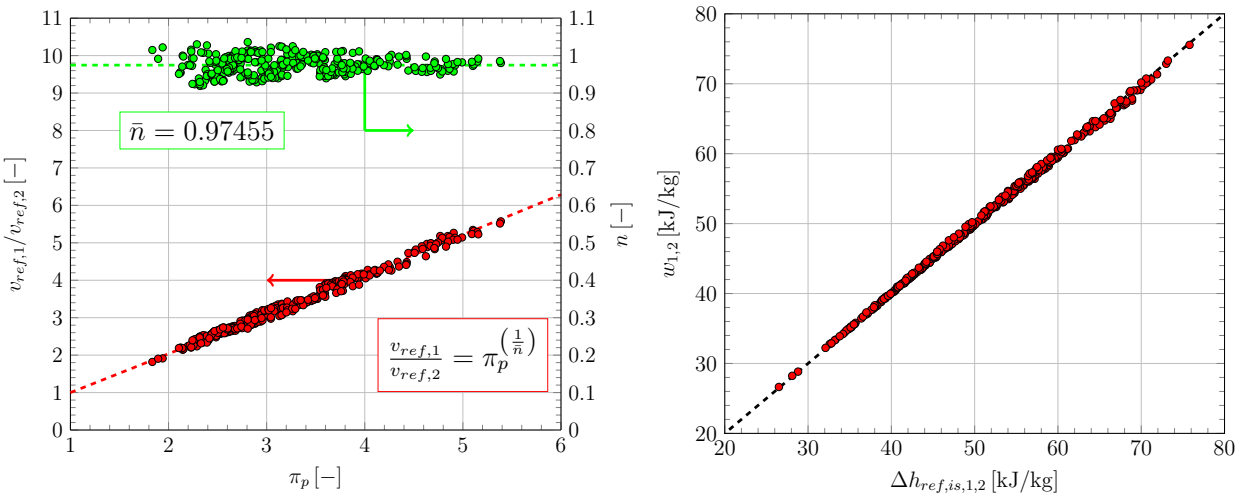

Figure 5.6: The relation between the ratio of the specific volume at compressor inlet ($v_{ref,1}$) and outlet ($v_{ref,2}$) and the pressure ratio (π_p) based on experimental data (red, left ordinate) with the resulting polytropic exponent (n) calculated with Equation 3.37 for all experimental operation points (green, right ordinate) and the comparison of isentropic enthalpy difference $\Delta h_{ref,is,1,2}$ and calculated specific compression work $w_{1,2}$ (right)

The specific compression work($w_{1,2}$) has been evaluated according to Equation 3.36 with the corresponding polytropic exponent for each operation point. A comparison to the experimentally determined enthalpy differences ($\Delta h_{ref,1,2}$) for 35 Hz, 50 Hz and 75 Hz is depicted in Figure 5.7. The characteristic of the specific compression work shows a clear dependency on the pressure ratio which is of course a consequence of Equation 3.36. An influence of the compressor speed via the polytropic exponent on the compression work can not be observed. In contradiction, the experimentally obtained specific enthalpy difference $\Delta h_{ref,1,2}$ increases with increasing compressor speed. Therefore the main influence on the compression process besides the pressure ratio can be found in compressor speed as depicted in Figure 5.7. An explanation for the observed behaviour can be found in increasing dissipation processes due to increased flow velocity through valves, channels and into the cylinder. Furthermore, the increasing compressor speed may increase the heat transfer coefficient within the cylin-

der, however the available time for the heat transfer from the gas to the cylinder wall is significantly reduced.

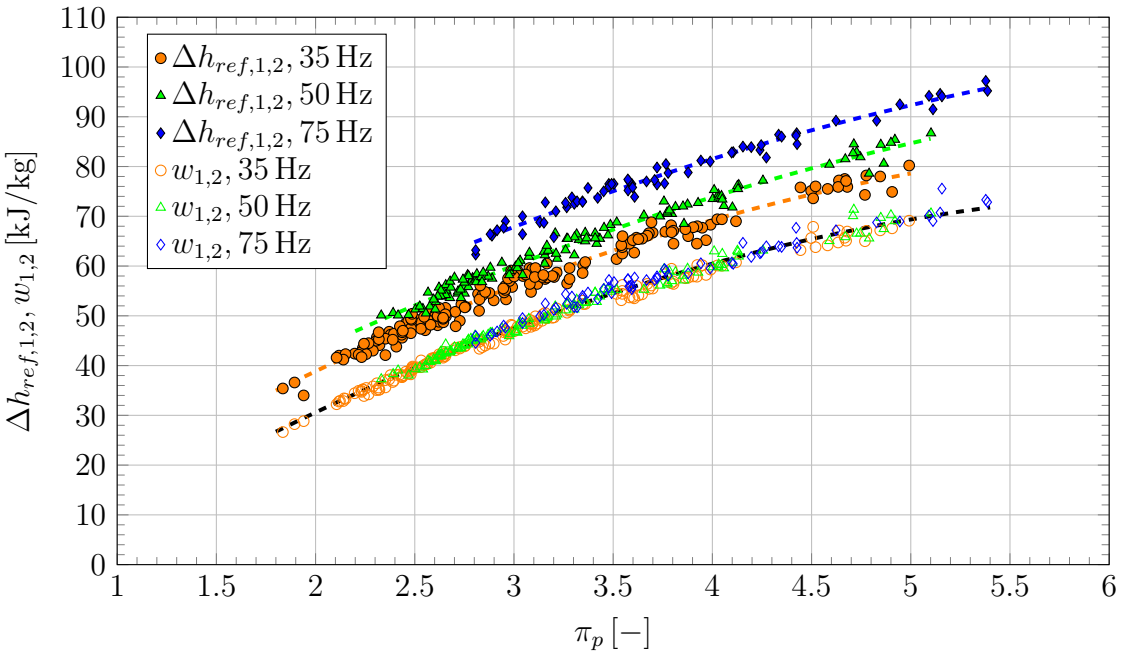

Figure 5.7: Comparison of compression enthalpy difference $\Delta h_{ref,1,2}$ for different compressor frequencies and the estimated compression work based on a polytropic change of state $w_{1,2}$

The compressor energy balance discussed in Section 3.3.2 (see Equation 3.38) can be illustrated using the above derived specific compression work ($\approx$ isentropic work) and the enthalpy difference multiplied by the refrigerant massflow ($P_{comp,is}$ and $P_{comp,ref,i}$ respectively), the electrical power output of the frequency inverter ($P_{comp,FI}$) and finally the total electrical consumption of the compressor ($P_{comp,el}$). Figure 5.8 shows, for example, the total compressor consumption as a function of the pressure ratio for a source inlet temperature of 50 °C and a compressor frequency of 50 Hz. The compressor consumption increases with the evaporation temperature (represented by the source inlet temperature) and thus suction gas density and, as described above, increases with the pressure ratio, which states the main influence on compression work. The difference between the total compressor consumption and the electrical power applied to compressor is defined by losses of the frequency inverter ($\dot{Q}_{FI,loss}$, red and orange marks, see Equation 3.41). The depicted experimental results also include the heat transferred from the compressor motor to the refrigerant ($P_{comp,ref,i}+\dot{Q}_{CHX}$, violet marks, see Equations 3.38 and 3.41). The induced power on the refrigerant $P_{comp,ref,i}$ (green marks, Equation 3.41) is based on the enthalpy difference of compressor inlet and outlet. The isentropic compressor consumption remains, as the frictionless and adiabatic effort to increase the pressure of the refrigerant (blue marks, see Equation 3.40). The horizontal scattering of the experimental data is a result of different evaporation temperature corresponding to the same source inlet set point due to different cycle configurations (Basic, SUP, IHX, see Sections 4.1.2, 5.5 and 5.6) and superheat set points in combination with the source side temperature difference. Although a higher evaporation temperature for a certain condensation temperature decreases the pressure ratio, the increase in suction gas density compensates the expected decrease in compressor consumption. Based on the obtained results, mechanical friction, motor heat losses can be determined as the difference between $P_{comp,FI}$ and $P_{comp,ref,i}+\dot{Q}_{CHX}$ as indicated in Figure 5.8 ($\dot{Q}_{M,tot}$, compare to Section 3.3.2).

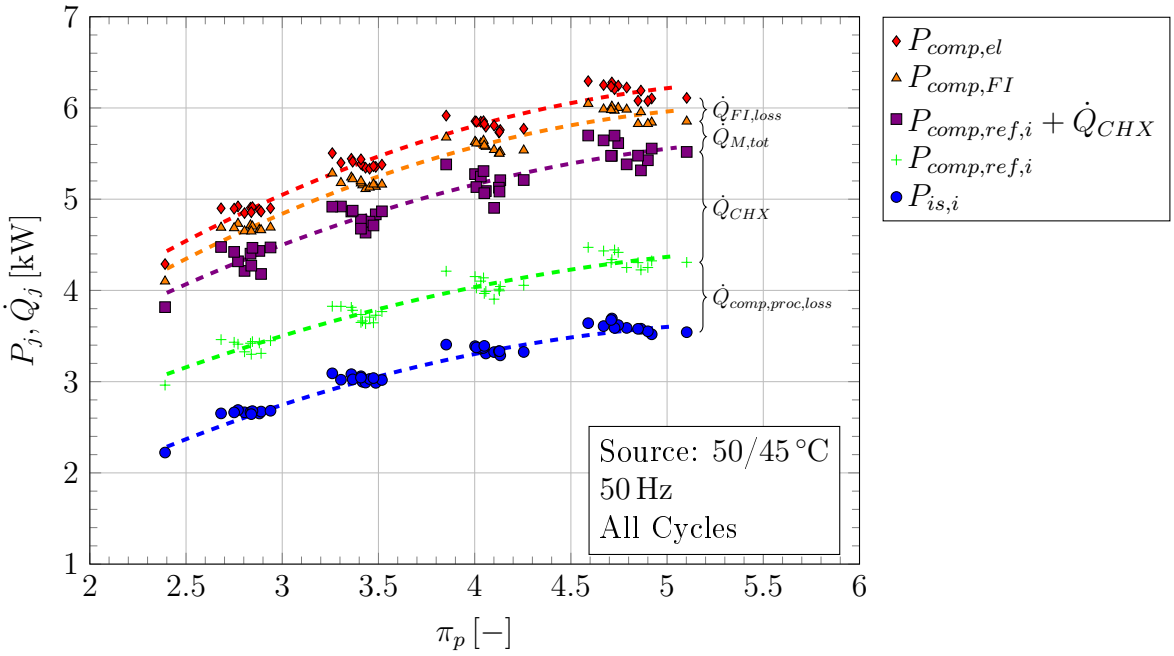

Figure 5.8: Characteristics of compressor consumption and loss distribution based on a source inlet temperature of 50 °C and compressor speed of 50 Hz

An overview on compressor losses for the entire investigated operation map (see Section 5.1) and the basic cycle configuration (no SUP, no IHX, see Section 5.5) is given in Figure 5.9. It stands out that the results for a compressor speed of 75 Hz and a source inlet temperature of 80 °C are missing. In this case the cooling ability of the CHX is not sufficient and thus the winding head temperature of the stator coil has increased to a critical value in the vicinity of 180 °C (see Section 5.4.2). Therefore this operation point could not have been observed experimentally.

As displayed in Figure 5.9 the total compressor consumption increases with increasing evaporation temperature, frequency, and as discussed above, with the pressure ratio. The compressor process losses (green, see Equations 3.41 and 3.50) can be found between approx. 0.5 kW and 2.7 kW which states the major part of the compressor irreversibilities. The, via CHX, recovered compressor motor waste heat (violet) states the second largest fraction of compressor energy ranging from ca. 0.7 kW to 1.7 kW. The mechanical losses $\dot{Q}_{M,tot}$ based on the combination of Equations 3.38, 3.39 and 3.41 (orange) show an outstanding behaviour in cases of a source inlet temperatures of 60 °C for all three compressor frequencies. These operation points do either not exhibit any or very low additional mechanical heat losses in contradiction to all other operation points. The reason, however is yet unclear. It is probably a consequence of the order how the tests have been carried out. After the first set of source temperatures has been recorded, the second set has been started with a high condensation temperature level. In the successively investigated operation points of lower temperature levels, the rather massive compressor motor and CHX might not have reached entirely a steady state. Furthermore measurement uncertainties have of course an influence on the result of $\dot{Q}_{M,tot}$. For comparison, the maximum total uncertainty defined by Equation 5.1 of $\dot{Q}_{CHX}$ results in approximately ±80 W, the maximum total uncertainty of the FI output $P_{comp,FI}$ for example holds a value of approx. ±160 W which in combination can lead to the observed values of $\dot{Q}_{M,tot}$. Nevertheless, the remaining results indicate that mechanical losses in a range between 0.2 kW and 1.1 kW occur throughout the investigated operation

map. The remaining fraction are heat losses of the frequency inverter (red) with values up to 0.4 kW.

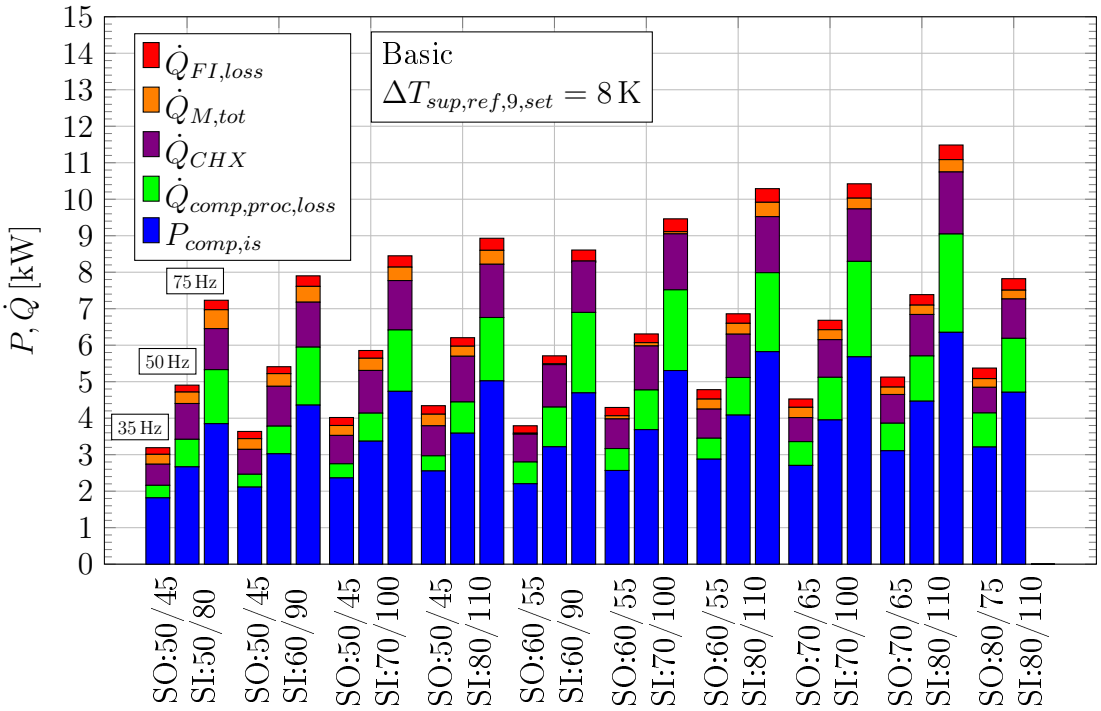

Figure 5.9: Composition of the compressor energy fractions for the investigated operation map

The analysis carried out above has shown the detailed distribution of the compressor energy fluxes with the main fractions identified as dissipation including heat transfer losses ($\dot{Q}_{comp,proc,loss}$) and the motor waste heat ($\dot{Q}_{CHX}$) making up to approx. 25 % and 20 % respectively of the total electrical compressor consumption . The dominant influence on dissipation losses has been found to be the compressor frequency and thus flow conditions within the compressor. A closer look on the compressor heat exchanger and it's characteristics will be made in Section 5.4.3. The resulting compressor efficiencies based on the given compressor analysis shall be briefly discussed in the following section.

5.4.2 Compressor Efficiencies

Efficiency definitions are a common methodology to characterize a heat pump compressor and can be utilized as simulation model inputs. The characterization of the utilized separating hood compressor has been of special interest throughout the experimental work, since it has not been applied in either, high temperature applications nor with the refrigerant R600. Furthermore the replacement of the air cooled housing by the compressor heat exchanger provides the possibility to enable compressor motor cooling and redirect a part of the waste into the heat pump process. The main efficiency definitions which are necessary to fully describe the compressor have been already discussed in Section 3.3. Figure 5.10 summarizes the derived efficiency parameters as a function of the pressure ratio and the compressor frequency including the internal isentropic efficiency (Equation 3.43), mechanical efficiency (Equation 3.44), the inverter and volumetric efficiency (3.45 and Equation 3.47, respectively), and finally the overall isentropic efficiency of the compressor (Equation 3.46). Basically the results follow well known compressor characteristics which are discussed for example in Maurer (2016) or Bach et al. (1966). The internal isentropic efficiency increases with pressure ratio and decreases significantly as outlined in Section 5.4.1 with the compressor frequency

and thus piston speed. The results show values in a range from approx. 0.7 to 0.93 (see Figure 5.10a). In contradiction, the mechanical efficiency following Equation 3.44 decreases with increasing pressure ratio and increases with compressor frequency which appears counter intuitive since mechanical losses are often times connected with velocity (compressor speed). At this point it has to be noted that the fraction of recovered compressor waste heat is not included as a benefit in this definition as already discussed in Section 3.3. A closer look on the ratio of the sum of internal compressor power $P_{comp,i}$ and the recovered waste heat $\dot{Q}_{CHX}$ and the inverter $P_{comp,FI}$ has revealed that the fraction of remaining losses ($\dot{Q}_{M,tot}$, see Figure 5.9) is nearly constant with pressure ratio and compressor frequency. The fraction of process losses however increases and becomes the dominant factor at higher compressor speed. The resulting mechanical efficiency lies within 0.6 and 0.8 (see Figure 5.10b).

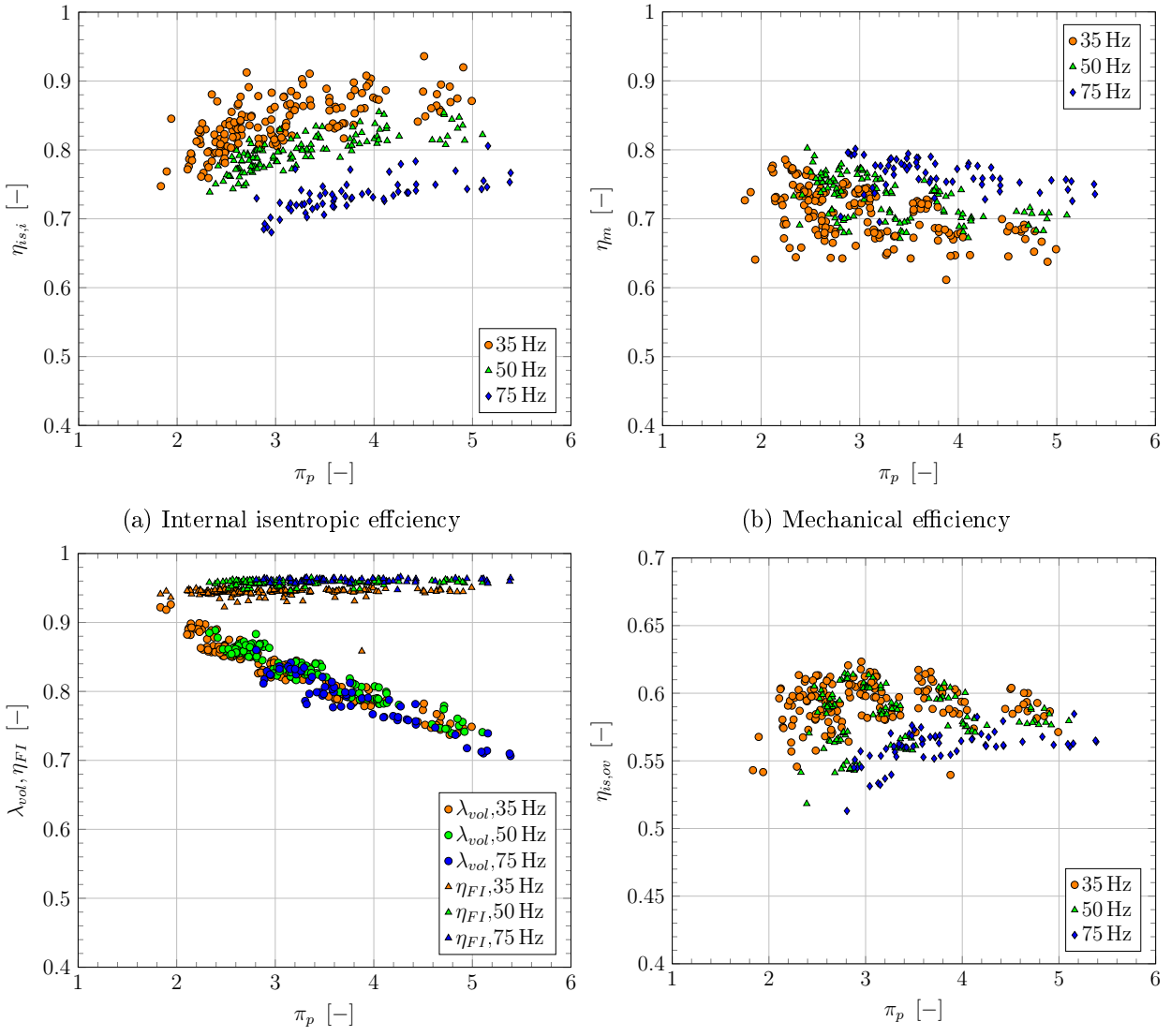

(a) Internal isentropic effciency

(b) Mechanical efficiency

(c) Volumetric and frequency inverter efficiency

(d) Overall isentropic efficiency

Figure 5.10: Overview on compressor efficiencies as function of pressure ratio and compressor speed based on the entire set of experimental data

The inverter frequency shows a nearly constant value of approximately 0.95 throughout all experimental tests. The volumetric efficiency exhibits the well known linear correlation with the pressure ratio and ranges in between 0.92 and 0.7 decreasing with increasing pressure ratio since leakage increases due to a higher pressure difference. Interestingly the inverter efficiency

and the volumetric efficiency are nearly independent of the compressor speed (see Figure 5.10c). The overall isentropic efficiency of the compressor exhibits a similar behaviour as the internal isentropic efficiency being the dominant factor. The overall isentropic efficiency increases with increasing pressure ratio reaching a certain maximum which is dependent on compressor frequency. The values are lying between 0.51 and approx. 0.62 (see Figure 5.10d, please note the different ordinate scaling). Taking a look at the above presented overview, the scattering of the experimental data especially for the mechanical efficiency which reflects also in the overall isentropic efficiency, indicates a further quantity influencing the results. As depicted in Figure 5.11 the mechanical efficiency increases with increasing evaporation temperature which is also reflected in the overall isentropic efficiency. It can be observed that the results for 35 Hz and 50 Hz are steadily increasing while for 75 Hz the data points reach a plateau. In the right diagram of Figure 5.11 the overall isentropic efficiency increases with increasing evaporation temperature can be observed for frequencies of 35 Hz and 50 Hz but not clearly for 75 Hz.

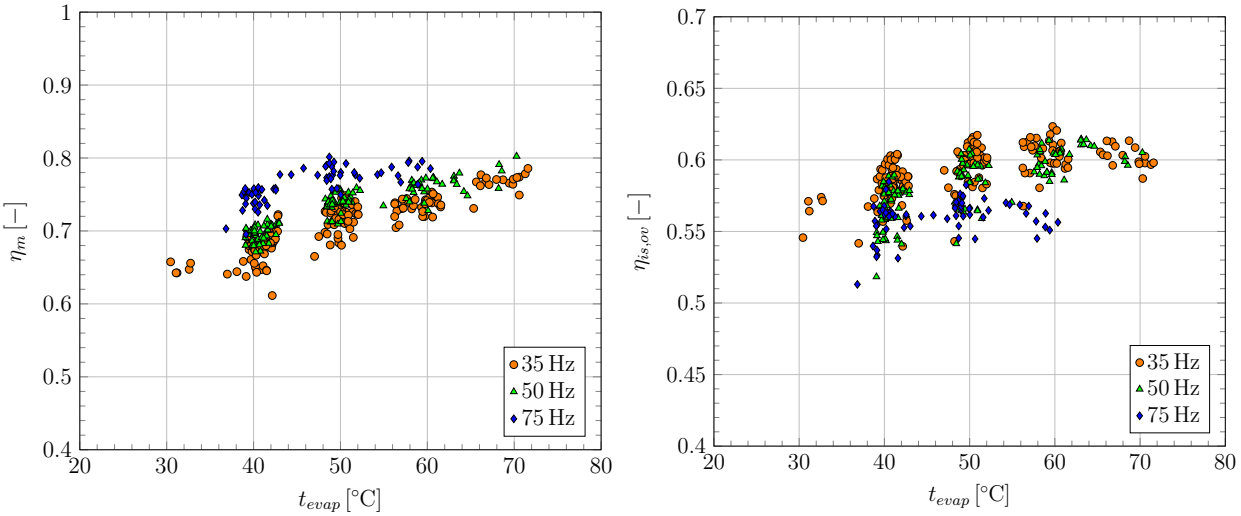

Figure 5.11: Influence of evaporation temperature on mechanical and overall isentropic efficiency with the compressor frequency as parameter

The increase of the mechanical efficiency with evaporation temperature, frequency and thus massflow is closely correlated to the ratio between recovered compressor motor waste heat and the inverter output which decreases with increasing refrigerant massflow (see Section 5.4.3). Since the additional motor losses ($\dot{Q}_{M,tot}$) are nearly independent of the pressure ratio and frequency as discussed above, the main influence on the mechanical efficiency is indeed the heat transfer from the compressor motor to the suction gas. With a decreasing effectiveness of the compressor cooling the mechanical and thus overall isentropic efficiency increases. However in terms of compressor speed and pressure ratio, the process losses are the dominant factor. It has again to be noted that the utilized efficiency definitions do not include the recovered waste heat as a benefit. This is because of the separation of compressor suction gas cooling and the actual compression process due to the CHX prototype (see Sections 3.3.2, 4.3). Therefore the separate analysis of the compression process has been found to be the more useful to discuss the major influences and furthermore to be more appropriate describing the compression process for the simulation model.

5.4.3 Characteristics of the Compressor Heat Exchanger

The experimental analysis of the custom built compressor heat exchanger has been of large interest within the present thesis since no practical experience has been at disposal in advance. Besides theoretical assumptions such as the basic design carried out by Skreinig (2016) and a detailed thermal network model presented by Moisi and Rieberer (2016) (see also Section 4.3) no data regarding motor waste heat recovery, the resulting superheat and most importantly the winding head temperatures of the stator has been available. Furthermore the suction gas pressure drop due to the CHX states a critical quantity regarding cycle efficiency. In terms of absolute recovered motor waste heat ($\dot{Q}_{CHX}$), values in a range between 0.34 kW and approx. 1.7 kW arise for a compressor speed of 35 Hz and 75 Hz, respectively, as depicted in Figure 5.12,left as a function of condensation temperature. The recovered heat exhibits an increasing tendency if all recorded operation points are considered and follows a similar characteristic as the compressor power (see Figure 5.8). Regarding the evaporation temperature, the recovered waste heat decreases slightly with increasing evaporation temperature for frequencies 35 and 50 Hz however displays a strong increasing characteristic for 75 Hz as depicted in Figure 5.12 on the right. The main influence however is again the compressor frequency. With an increasing compressor frequency, the total compressor consumption increases and thus motor waste heat.

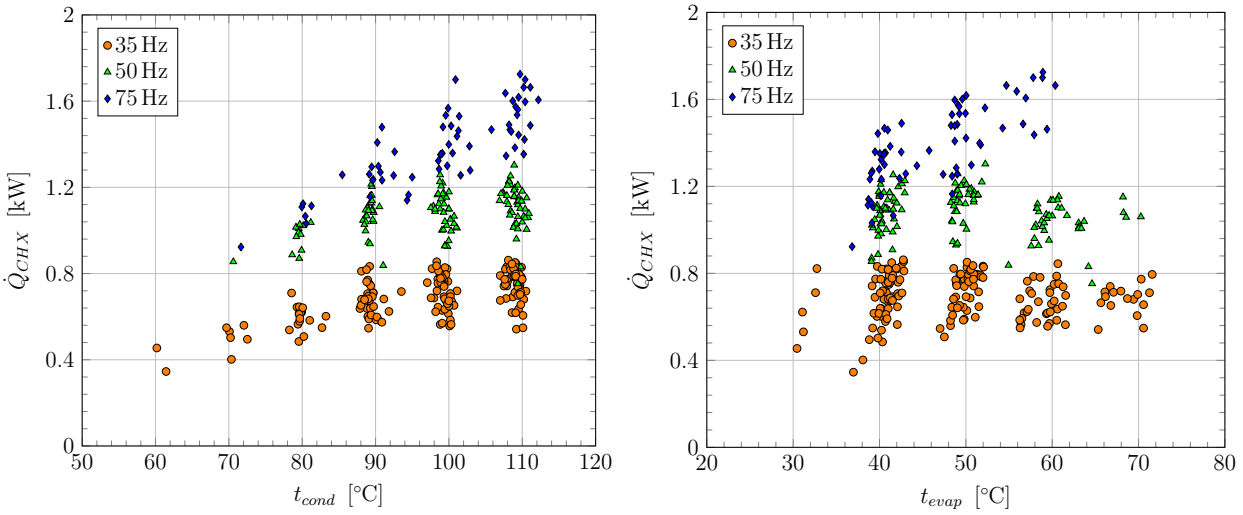

Figure 5.12: Absolute value of the recovered motor waste heat as a function of the condensation temperature (left), the evaporation temperature (right) for different compressor frequencies

While the compressor frequency determines the volume flow of the compressor, the increasing suction gas density results in an increasing refrigerant massflow and in turn again in a higher compressor consumption. The increasing massflow enhances the refrigerant side heat transfer, which however is not the limiting factor in the overall heat transfer coefficient since the transferred heat is actually slightly decreasing with increasing evaporation temperature and thus massflow at least for frequencies 35 an 50 Hz. This might be a consequence of a higher temperature level determined by an increased evaporation temperature causing a rise in CHX heat losses to the surrounding across the outer cylinder shell (see Section 4.3). As mentioned above, a different behaviour however can be observed for the highest considered compressor speed. The increasing CHX heat tranfer closely correlates to the winding head temperature ($t_{EM,wh}$, see Section 4.3) and it's difference to the evaporation temperature in cases of 75 Hz which can be observed in Figure 5.13. Furthermore the CHX

entry temperature ($t_{ref,9}$, see Section 4.1.2) and the stator iron core surface temperature ($t_{sf,Fe,1}$, see Section 4.3) are given for comparison. The overall temperature of the compressor drive increases with increasing entry/ evaporation temperature level. While results for 35 and 50 Hz follow the same trend as the CHX entry temperature, the motor temperature for 75 Hz increases strongly as a result of the limited CHX area and heat transfer coefficient. The high compressor power in the 75 Hz case in combination with the given heat transfer and heat exchanger area, requires an equilibrium at a higher temperature level. The resulting temperature differences between the winding head and the evaporation temperature as depicted in Figure 5.13 reflect this behaviour. The winding head temperatures are ranging between approx. 70 and 160 °C. It might have been noticed that winding head temperatures in an evaporation temperature range of up to 70 °C and a compressor speed of 75 Hz (source inlet 80 °C) are missing. In these high load cases the winding head threshold of 180 °C has been approached several times resulting in one safety shut off event. As a consequence these operation points have been omitted for safety reasons.

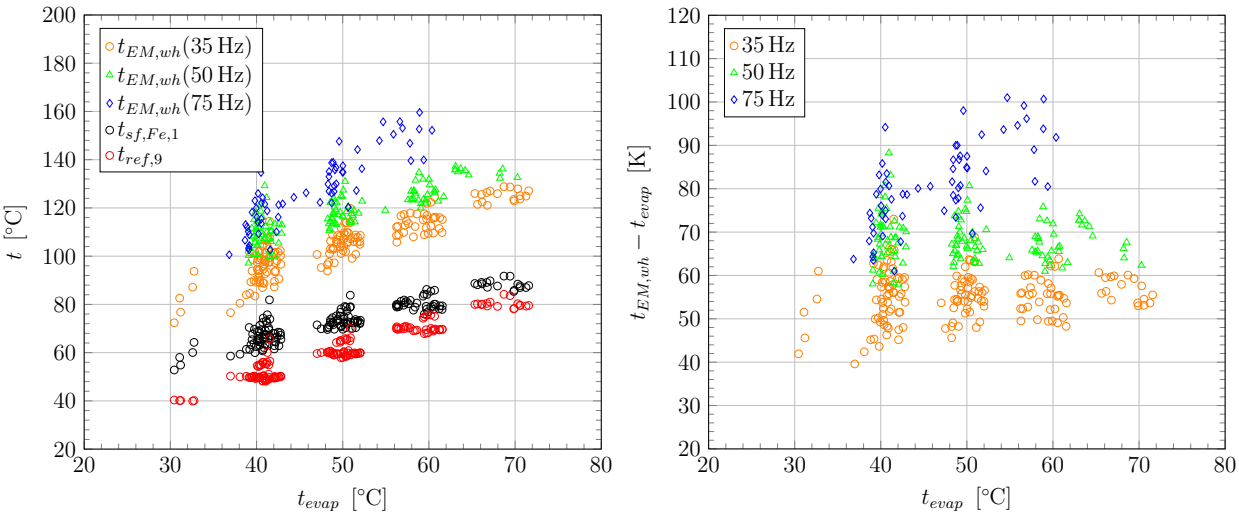

Figure 5.13: Winding head, surface temperature of the stator iron core and CHX entry temperature (left), temperature difference between winding head and evaporation temperature (right) as a function of the evaporation temperature and compressor frequency

The absolute values of the recovered waste heat increases, however the fraction of recovered waste heat compared to the inverter output decreases significantly with increasing evaporation temperature and compressor frequency which supports the statements from above. The combination of evaporation temperature and compressor speed is represented by the resulting refrigerant massflow. At high compressor loads represented by a higher refrigerant massflow and the given heat exchanger, CHX channel arrangement and heat transfer coefficient the recoverable heat is limited. In comparison to the mechanical efficiency defined above a clear correlation can be observed. While the fraction of recoverable waste ($\dot{Q}_{CHX}/P_{comp,FI}$) decreases from 0.24 to 0.14 the mechanical efficiency increases significantly from approx. 0.6 to 0.8 with increasing refrigerant massflow as displayed in Figure 5.14. Due to the additionally installed CHX, an additional pressure drop arises on the compressor suction side which can significantly influence the cycle efficiency. With increasing pressure drop the pressure ratio increases. As a result, the volumetric efficiency decreases however the overall compressor efficiency might increase depending on the compressor frequency (see Figure 5.10).

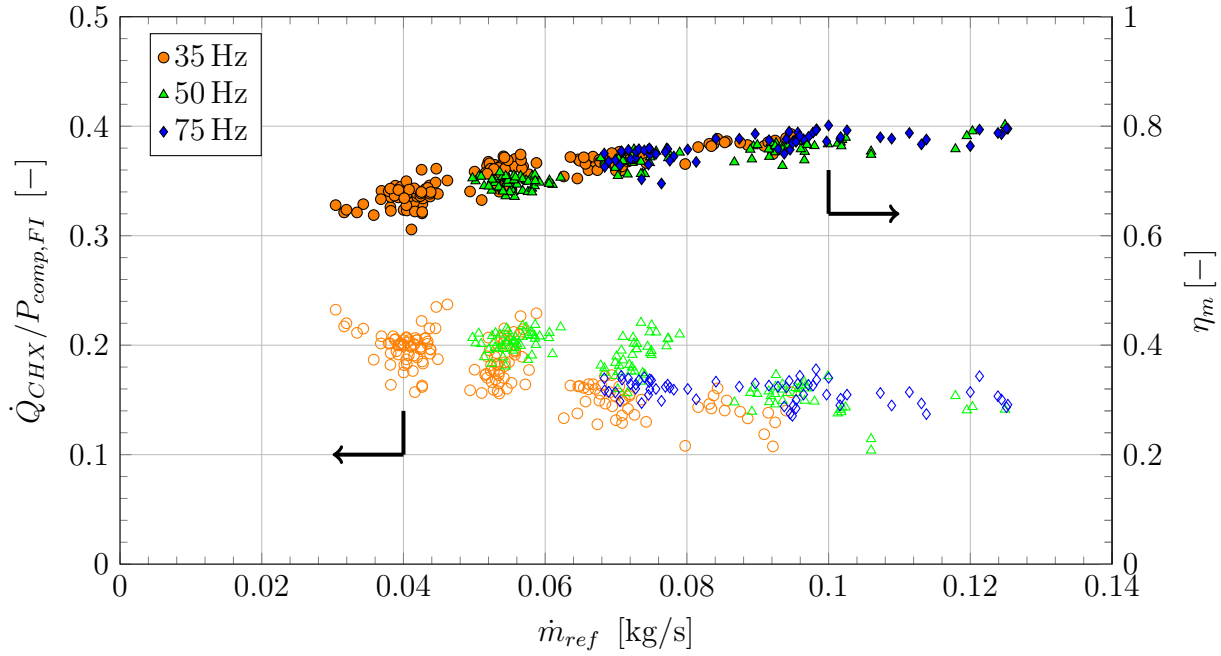

Figure 5.14: Comparison between the ratio of recovered waste heat and inverter output and the mechanical efficiency as a function of the refrigerant massflow

Due to the constant channel geometry the flow velocity remains nearly constant for a certain compressor frequency. As a consequence, only the change in density has an effect on the CHX pressure drop. Figure 5.15 shows the CHX pressure drop calculated based on measured $p_{ref,9}$ and $p_{ref,1}$ (see Section 4.1.2) as a function of the refrigerant massflow with the compressor speed as parameter. With increasing suction gas density and thus massflow the pressure drop increases nearly linear. With increasing compressor speed this characteristic is shifted to higher pressure drops due to the increasing volume flow. The total pressure drop of the installed CHX can be significant and range from approx. 5 to 68 kPa. Experimental results regarding the pressure drop have also been presented by Verdnik (2017).

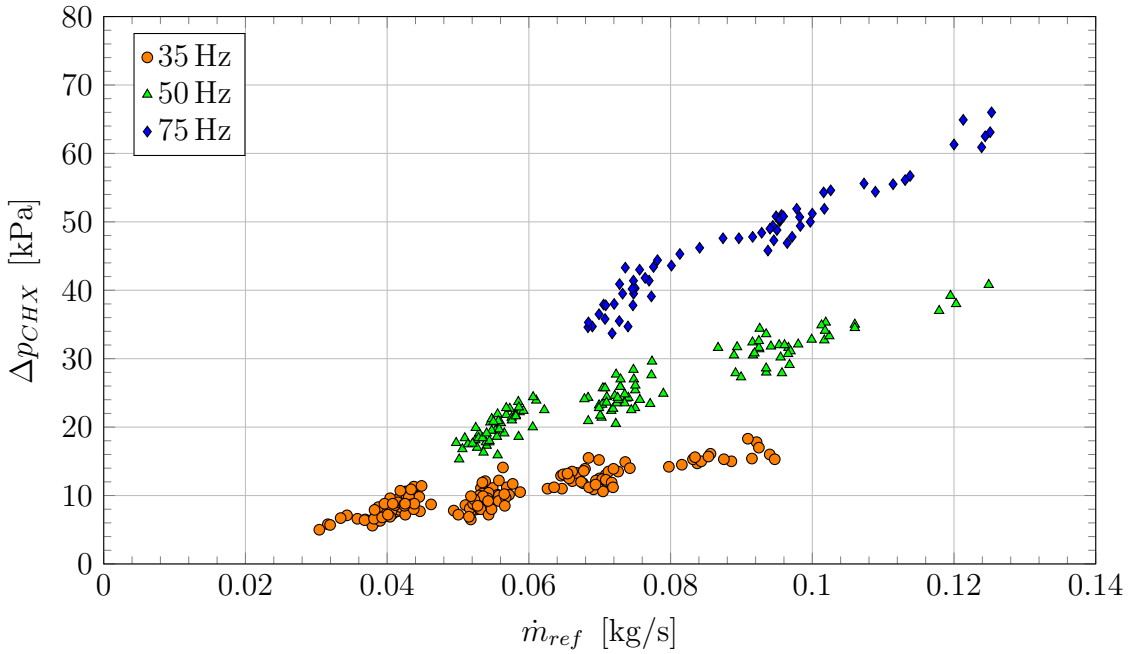

Figure 5.15: CHX pressure drop as a function of the massflow and the compressor speed

The basic premise for the installation of the compressor heat exchanger has been the provision of additional suction gas superheat outside of the evaporator regarding the avoidance of a wet compression in order to keep the superheat in the evaporator as low as possible. The obtained experimental data discussed above reveal several effects of the CHX on compressor and cycle efficiency. The first aspect is that the recovered waste heat increases the heating capacity of the heat pump on the high pressure side similar to the internal heat exchanger discussed in Section 3.2.4. With the higher entry enthalpy and the additional pressure drop the positive effect of an increased heating capacity might be balanced out by an increased compressor work as a consequence of an increased slope of isentropes with increasing enthalpy in combination with a higher pressure ratio due to the lower suction gas pressure (see also Section 3.2.4). Nevertheless in the standard air cooled compressor configuration the compressor motor waste heat is transferred entirely to the surrounding. Experimentally however, a clear comparison on the influence of CHX on cycle efficiency has not been carried out since no second air cooled compressor has been at disposal and furthermore the focus has lied on the overall characterization of a butane high temperature heat pump in terms of efficiency and heating capacity. By simulation the potential of a pressure drop reduction in terms of efficiency will be discussed in Chapter 6. As a main result, data showed that up to 24 % of the inverter output power has been recovered with CHX decreasing with the refrigerant massflow due to the limited heat transfer area. Finally, the obtained experimental results have again been utilized to characterize the CHX for the simulation models described in Chapter 6.

5.5 Basic and Superheater Cycle

The basic cycle configuration states a standard single stage heat pump cycle utilizing a high pressure receiver and a subcooler as already described in Chapters 3 and 4. The superheater equalls basically an evaporator area extension within the basic cycle configuration and thus shall be discussed together in this section. Figure 5.16 shows the combined layout including sensor positions and refrigerant states according to Chapter 4 and the corresponding t/h state diagram. Depending on the considered cycle configuration the respective shut off valves are operated (e.g. basic cycle: V7 is open, V8 and V9 are closed). Starting at state 1, the superheated refrigerant enters the compressor and is compressed leaving at condensation pressure level (state 2). The transported compressor oil is separated in the oil separator where heat is transferred to the surrounding. Furthermore energy is transported with the separated lubricant back to the compressor. Hence the refrigerant leaves the oil separator with state 3 with a lower enthalpy and temperature before entering the condenser. Within the condenser the refrigerant condenses until a saturated liquid state is reached in the high pressure receiver (state 4r) and further subcooled in the subcooler until state 6 is reached (equals approx. state 4). The expansion follows in the EXV into the two phase region (state 7).In the evaporator (and superheater), the refrigerant is evaporated (and superheated) until state 8. Depending on the basic or superheater configuration, the refrigerant enters either directly the compressor heat exchanger or the superheater followed by the compressor (state 9). Within the compressor heat exchanger, the already superheated fluid is further heated until state 1 is reached again. Depending on the cycle configuration either source temperature 1 (superheater) or 2 (basic) has been controlled in respect to the desired setpoint value.

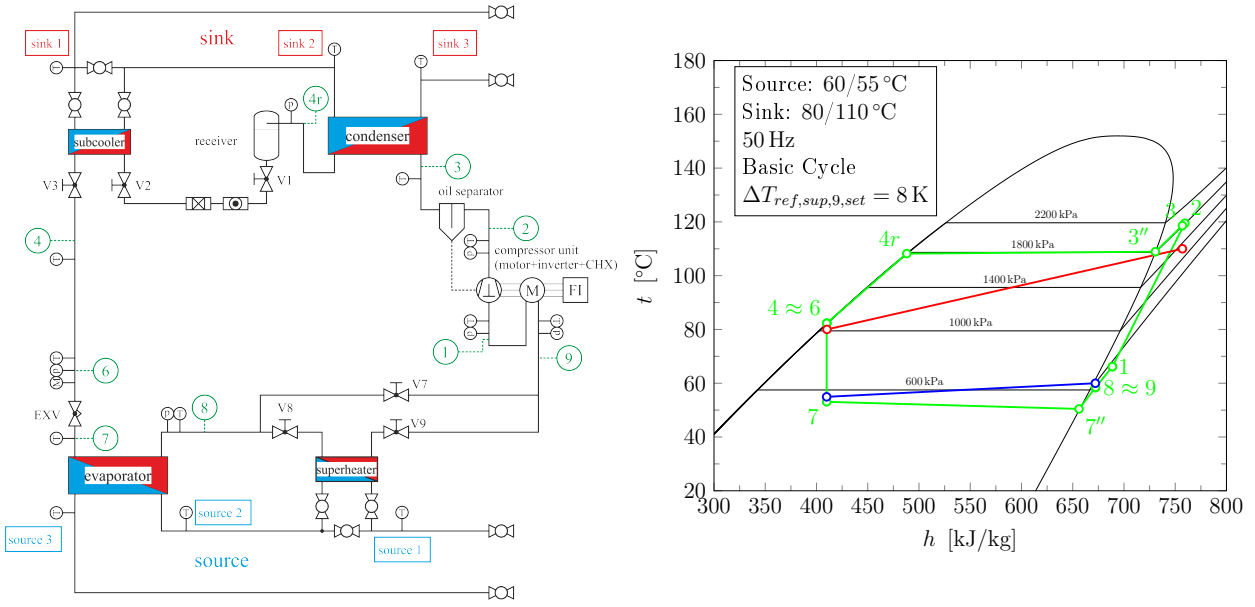

Figure 5.16: Combined cycle layout of the basic and superheater configuration including sensor positions and refrigerant states (left) and corresponding t/h diagram of the Basic cycle obtained from experiment with sink and source temperatures indicated (right)

In order to evaluate the high temperature heat pump prototype, source and sink boundary conditions as well as the compressor frequency has been varied as described in Section 5.1. As a result, maps for different quantities have been derived as a function of the condensation temperature with source side temperatures and the compressor frequency as parameters. These quantities are described in the following sections.

5.5.1 Capacities and Compressor Consumption of the Basic Cycle

The heating capacity in combination with the temperature boundary conditions on source and sink side are important selection criteria not only for high temperature heat pumps but heat pumps in general. The required electrical compressor consumption determines the necessary power supply and in combination with the heating capacity, the efficiency and in the end the operating costs. The resulting heating capacity $\dot{Q}_{w,H}$ as the product of measured water volume flow, density, specific heat capacity and temperature difference across the condenser (see Section 3.2.1 and Figure 5.16) is depicted in Figure 5.17 as a function of the condensation temperature ($= t''_{ref,3}$, see Figure 5.16), source temperatures and compressor speed as parameters. As described in Section 5.3.2, a superheat setpoint of 8 K at sensor position 9 has been defined and the basic cycle configuration selected. With the developed high temperature heat pump a maximum heating capacity of approximately 46.5 kW can be provided with source temperatures of 70/65 °C and sink temperatures of 70/100 °C with a compressor frequency of 75 Hz. A heating capacity of approx. 34 kW can be achieved with source temperatures of 60/55 °C, sink temperatures of 80/110 °C and a compressor speed of 75 Hz. As stated in Section 5.4.3 the high load operation point with source temperatures of 80/75 °C has had to be omitted due to winding head temperature issues. The combined measurement uncertainty according to Equation 5.1 is depicted with error bars and lies within a range of ±0.42 kW and ±0.82 kW (approx. ±2.3 %). The heating capacity decreases with increasing sink temperature level and increases clearly with increasing source temperature level and compressor speed.

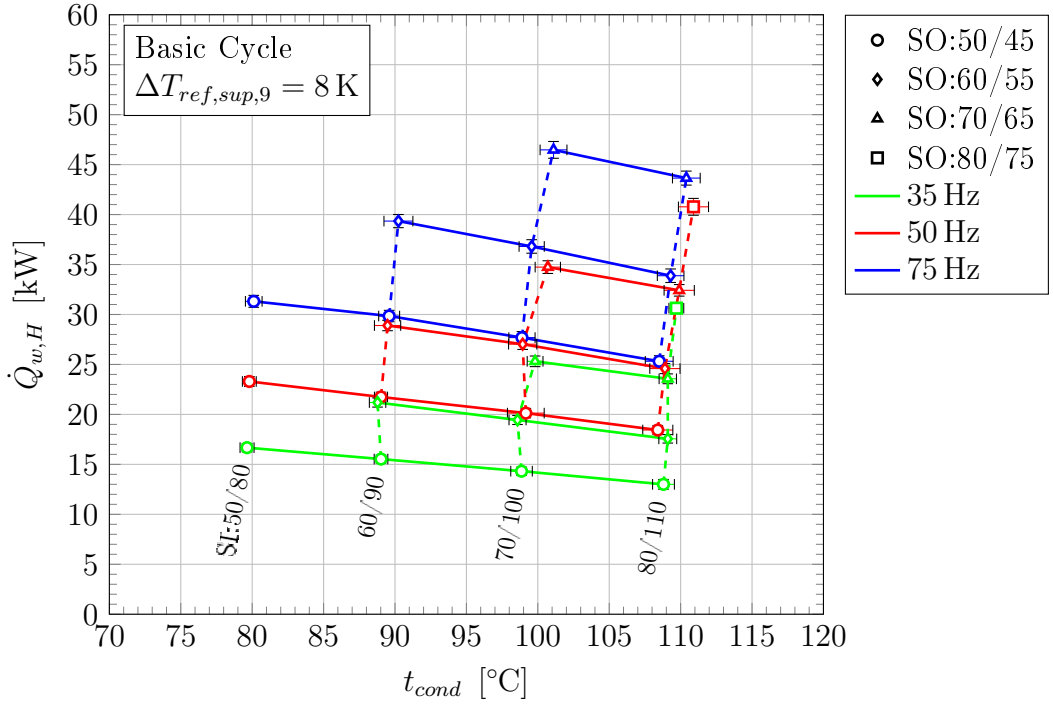

Figure 5.17: Experimental results of heating capacity for the basic cycle as a function of condensation temperature with source temperatures and compressor speed as parameters

An identical behaviour can be observed for the evaporator capacity $\dot{Q}_{w,source}$ determined with source side massflow and temperatures based on Section 3.2.1 as displayed in Figure 5.18. The highest evaporator capacity with approx. 38 kW has been applied at a source temperature level of 70/65 °C, sink temperatures of 70/100 °C and a compressor frequency of 75 Hz.

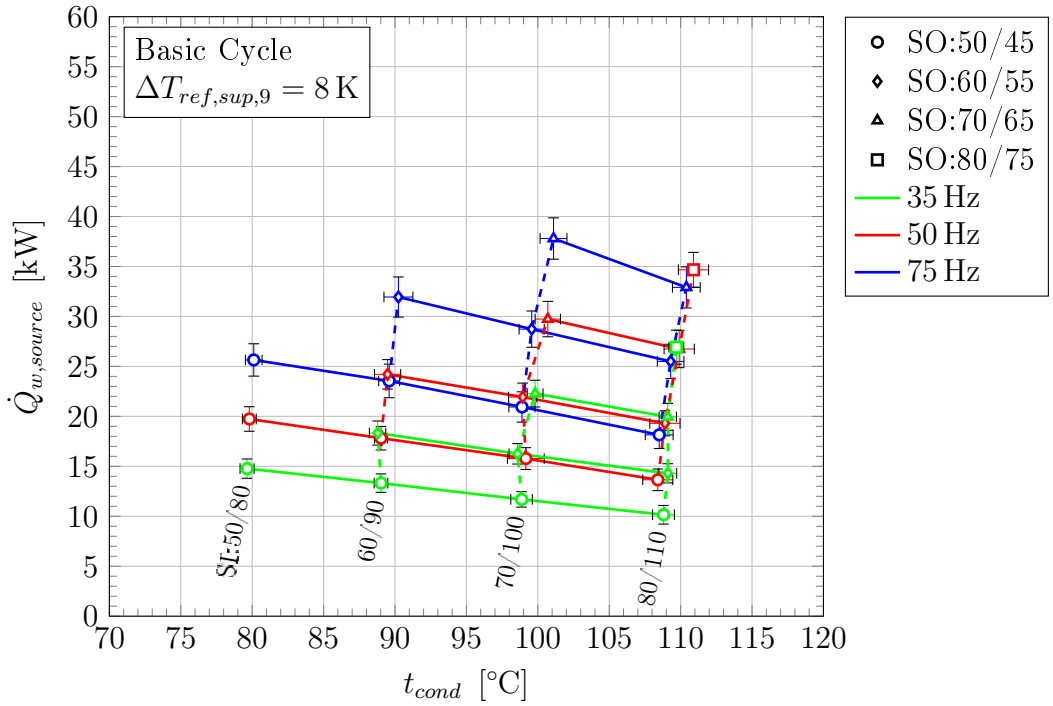

Figure 5.18: Experimental results of evaporator capacity for the basic cycle as a function of condensation temperature with source temperatures and compressor speed as parameters

The measurement uncertainty has been determined analogously to the heating capacity however is increased due to the significantly lower source side temperature difference with a identical absolute uncertainty for the temperature sensors (compare to Section 5.2). The total uncertainty for the source side heating capacity ranges between approx. ±0.7 kW and ±2 kW. The increase in pressure ratio and thus a decrease in volumetric efficiency which effects the refrigerant massflow (see Sections 5.4.2 and 5.5.3) contributes to the decrease in heating and evaporator capacity with increasing condensation temperature level. The more dominant reason however, is a decrease in usable enthalpy difference due to the decrease of phase change enthalpy for increasing condensation temperatures for both, the heating and evaporator capacity as depicted in the experimentally obtained t/h diagrams of Figure 5.19 with dashed lines indicating the source and sink temperature levels. The only limitation of the subcooler outlet enthalpy (state 4) states the inlet temperature of the heat sink, since the utilized subcooler and condenser provide sufficient heat transfer area which is indicated by small pinch point temperature differences. The superheat caused by the CHX increases with increasing condensation temperature and thus required compression work (state 9 to 1). The consequence is a reduced suction gas density further reducing refrigerant massflow and hence heating capacity. Although this effect is small since density changes are rather small along an isobaric line in the superheated vapour region.

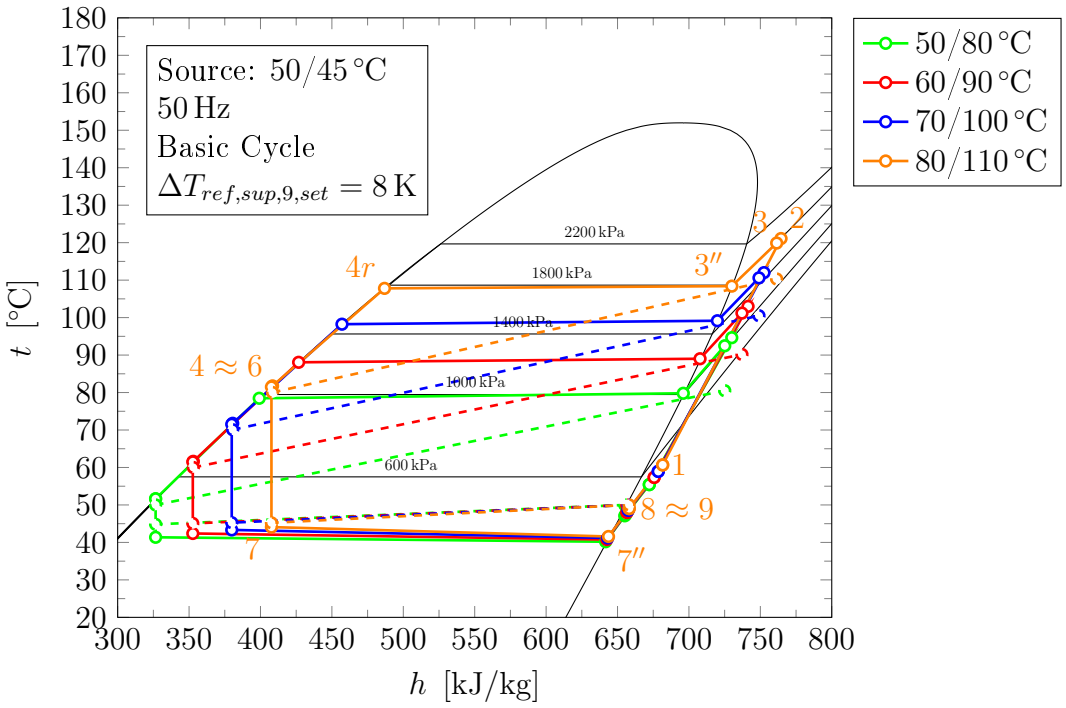

Figure 5.19: Experimentally derived t/h diagram for the basic cycle configuration, a compressor speed of 50 Hz, source temperatures of 50/45 °C and a varying sink temperature level

The increase in heating and evaporator capacity with increasing source temperature level is a result of increased refrigerant massflow caused by an increased evaporation temperature ($= t''_{ref,7}$, see Figure 5.16) and thus suction gas density. Corresponding t/h diagrams are displayed in Figure 5.20 for a compressor speed of 50 Hz, a sink temperature level of 80/110 °C and varying source temperature levels. The dashed lines are again indicating the source and sink temperature levels. The increased massflow with rising evaporation temperature increases pressure drops across the components. Especially the significant pressure drop of the CHX (see Figure 5.15) reduces the suction gas density working against the massflow

increase with increasing evaporation temperature. The increase in pressure ratio caused by pressure drops on the low and high pressure side results in a decreased volumetric efficiency. The superheat within the CHX (state 9 to 1) decreases significantly with increasing evaporation temperature due to the limited CHX heat transfer area and driving temperature difference as described in Section 5.4.3. This is beneficial in terms of a higher suction gas density however the usable compressor waste heat decreases which has a negative effect on heating capacity.

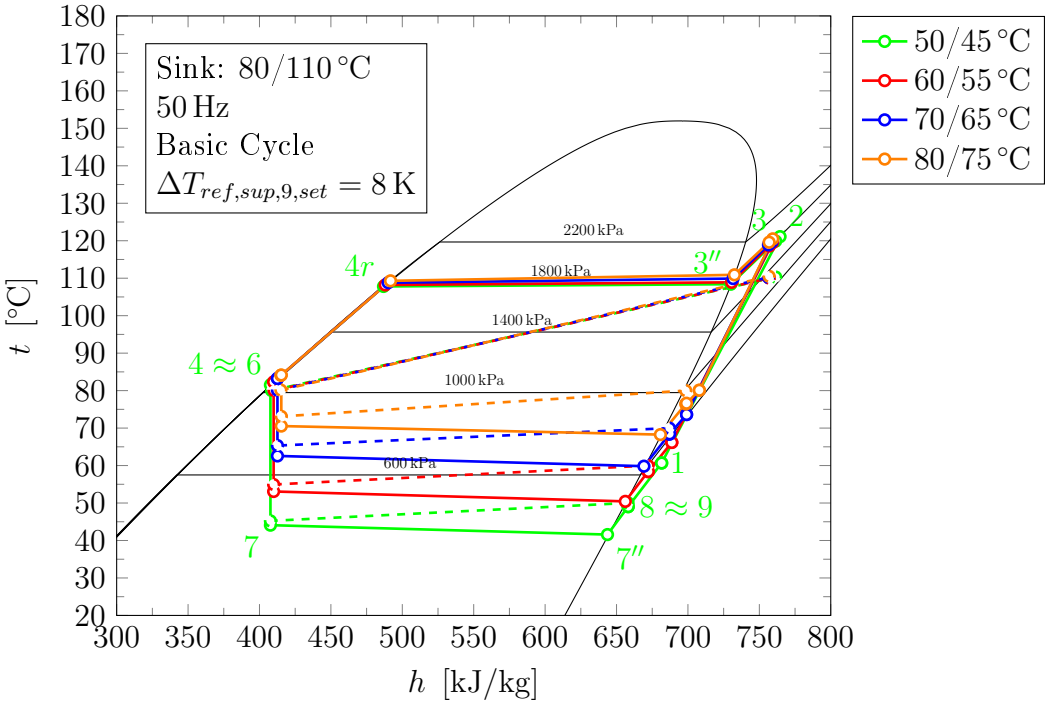

Figure 5.20: Experimentally derived t/h diagram for the basic cycle configuration, a compressor speed of 50 Hz, sink temperatures of 80/110 °C and a varying source temperature level

The influence of evaporation and condensation temperature as well as compressor speed on the electrical consumption of the compressor is depicted in Figure 5.21 for the basic cycle configuration. The maximum compressor consumption within the investigated field of operation has been obtained to approx. 11.6 kW for a source temperature level of 70/65 °C, sink temperature of 80/110 °C and a compressor speed of 75 Hz. The minimum required compressor consumption has been recorded to approx. 3 kW for a compressor speed of 35 Hz, source and sink temperatures of 70/65 °C and 50/80 °C, respectively. The compressor consumption increases with increasing condensation temperature and thus pressure ratio as already discussed in Section 5.4.1. The increased refrigerant mass flow due to a rising source temperature level and the increase in compressor volume flow (speed) further increase the electrical compressor consumption. The compressor power proportionally increases with the suction gas density and the compressor volume flow (i.e. speed) as depicted in Figure 5.21 and described with Equation 3.50.

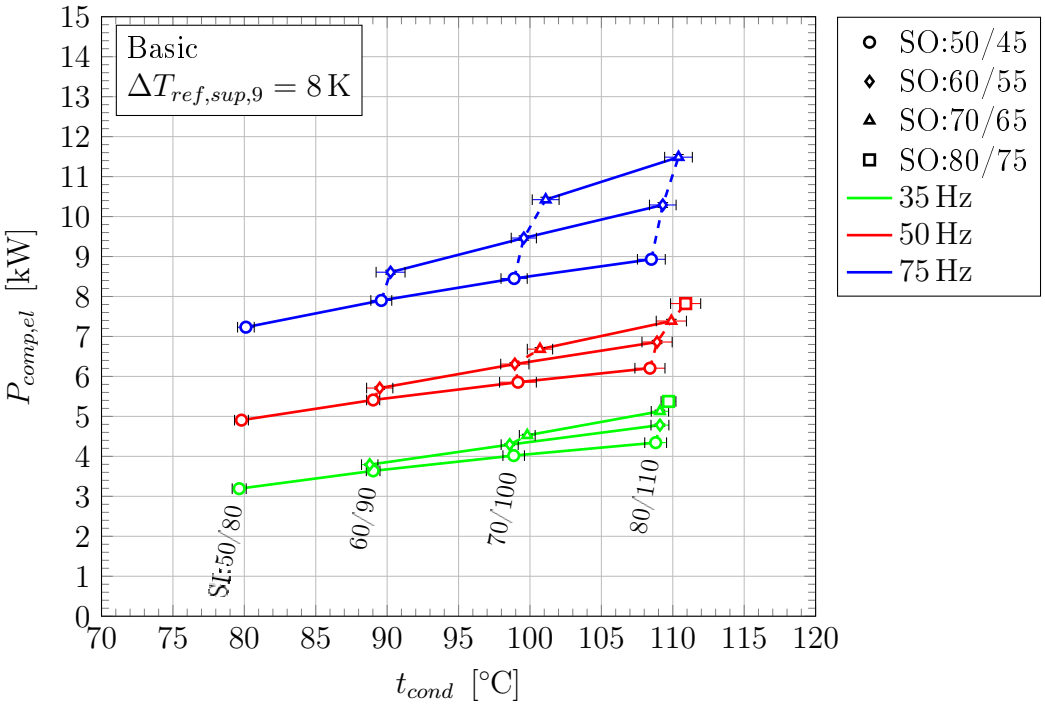

Figure 5.21: Experimental results of electrical compressor consumption for the basic cycle as a function of condensation temperature with source temperatures and compressor speed as parameters

The electrical compressor consumption is of course significantly affected by the compressor efficiencies. The overall isentropic efficiency slightly increases with increasing pressure ratio and evaporation temperature as a consequence of the combination of isentropic and mechanical efficiency characteristics described in 5.4.2. This increase lies in a range of 0.04 percentage points. The overall isentropic efficiency of the compressor however decreases slightly within a range of approx. 0.05 percentage points with increasing compressor frequency.

5.5.2 Efficiency of the Basic Cycle

The efficiency in terms of COP has been derived based on the heating capacity and the electrical compressor consumption described in the previous section. The Coefficient of Performance states an important quantity for the selection and economic application of high temperature heat pumps in industry. For the present investigated heat pump, Figure 5.22 shows the results of the heating COP as a function of the condensation temperature with the source temperature level and the compressor frequency as parameters. The cycle configuration and superheat setpoint corresponds to the previous section. The following Coefficient of Performance for the heating application $COP_{w,H}$ has been calculated according to Equation 3.8 of Section 3.1.3. When comparing the results for the heating capacity and compressor consumption with Figure 5.22 it becomes clear that the efficiency decreases strongly with increasing condensation temperature due to decreased heating capacity and an increasing compressor power. For a constant sink temperature level and an increasing source temperature level the compressor power increases, however weaker due to the decreasing compression ratio, than the increase in heating capacity thus resulting in a COP increase. The maximum COP within the investigated field of operation has been found to 5.7 for a source temperature level of 80/75 °C, sink temperatures of 80/110 °C and a compressor frequency of 35 Hz. The lowest efficiency of 2.8 is achieved in the operation point with the highest temperature lift and a frequency of 75 Hz. The total propagated uncertainty for the

$COP_{w,H}$ ranges between ±0.07 and ±0.13 (approx. 2.4 % in each case) and is indicated with error bars in Figure 5.22.

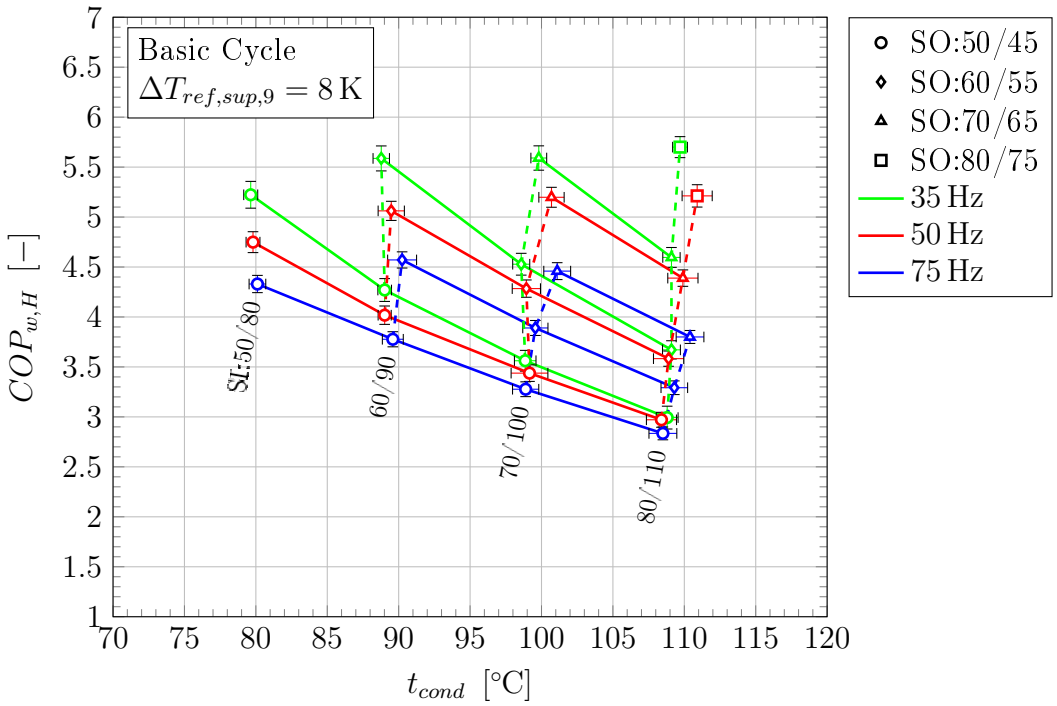

Figure 5.22: Experimental results of the heating COP for the basic cycle as a function of condensation temperature with source temperatures and compressor speed as parameters

In addition to the temperature lift, the compressor speed and in consequence the refrigerant massflow has a significant influence on the overall cycle efficiency. As depicted in Figure 5.22 above, the COP significantly decreases with increasing compressor frequency and furthermore it becomes stronger with increasing source temperature level, thus evaporation temperature and finally refrigerant massflow. In order to elucidate the consequences of an increased refrigerant massflow on cycle irreversibilities, Figure 5.23 depicts the comparisons of three t/h diagrams for a source and sink temperature level of 70/65 °C and 80/110 °C respectively with varying compressor frequencies. The strong influence of the compressor speed on the refrigerant cycle can be clearly observed with change of the compression process. The internal isentropic efficiency decreases significantly and thus the overall compressor efficiency due to an increase of process irreversibilities as discussed in Section 5.4.1 . With nearly identical inlet states (state 1) the compression process changes to higher outlet temperatures and enthalpies (state 2) with increasing compressor frequencies resulting in a higher internal compression work (compare to Figure 5.7) as depicted in Figure 5.23. This additional enthalpy difference can actually be utilized in the condenser to increase the heating capacity. The rise of the enthalpy change induced on the refrigerant ($w_{comp,ref,i} = \Delta h_{ref,1,2}$) however is stronger than the resulting increase of specific heating capacity ($q_H = \Delta h_{ref,3,4}$) leading to an effective reduction of the cycle efficiency. Since the internal isentropic efficiency increases with a rising pressure ratio (see Figure 5.10a) the difference between COP of different frequencies decreases with increasing condensation temperature as shown in Figure 5.22.

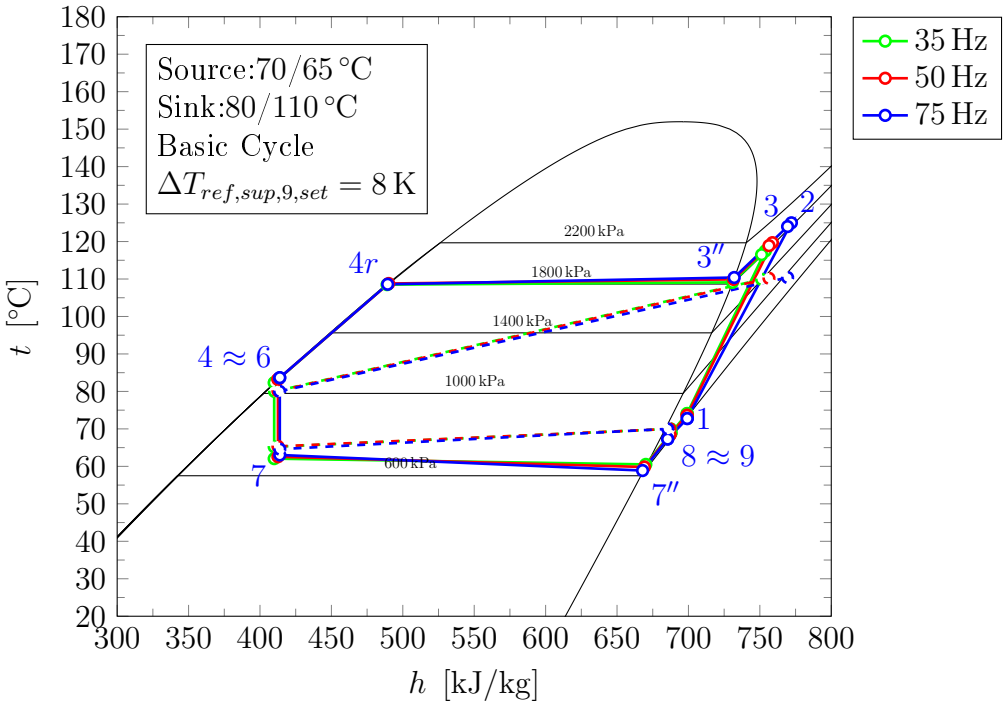

Figure 5.23: Experimentally derived t/h diagram for the basic cycle configuration, source temperatures of 70/65 °C, sink temperatures of 80/110 °C and a varying compressor frequency

Not only compression irreversibilities are causing the efficiency degradation with increasing compressor speed but other effects such as increased pressure drops and temperature differences within heat exchangers which are not as clearly visible in Figure 5.23 but still noticeable. For example the increased pressure drop on the suction side (different states 7″) and the pressure drop due to the CHX (states 9 to 1) along with increased suction and discharge valve pressure drops are further increasing the pressure ratio of the compression and thus specific compression work. Finally, due to the increased heating and evaporator capacities higher temperature differences across the condenser and the evaporator are required for the given heat transfer area and coefficients leading to an increased condensation (compare to Figure 5.22) and decreased evaporation temperature (see different states 3″ and 7″). As a consequence the temperature lift increases and thus the pressure ratio which again increases compression work for increasing compressor frequencies. In conclusion, with an increasing refrigerant massflow and thus heating capacity caused either by an increase of suction gas density (evaporation temperature) and/or compressor speed, cycle irreversibilities increase significantly. This leads to reduction in COP in a range between 0.7 (Source 50/45 °C, Sink 80/110 °C/50 Hz) and 22 % (Source 70/65 °C, Sink 70/100 °C/75 Hz) with values of 35 Hz as basis.

5.5.3 Parameters of the Basic Cycle

Further cycle parameters have been investigated in order to fully characterize the high temperature heat pump prototype. A selection of these quantities is given in Figure 5.24 as a function of the condensation temperature with the source temperature level and the compressor speed as parameter. At first the evaporation temperature in combination with the refrigerant massflow as depicted in Figures 5.24a and 5.24b. Interestingly the evaporation temperature slightly increases with increasing condensation temperature for a certain source temperature level and compressor speed. The reason can be deduced by considering the state diagrams of Figure 5.19 and the decreasing evaporator capacity with increasing con-

densation temperature depicted in Figure 5.18. The decreasing evaporator capacity results in lower pinch point temperature differences between source and refrigerant temperatures at the resulting heat transfer coefficient in combination with evaporator area (see Figure 5.19) thus the evaporation temperature slightly increases (approx. 1 K). With a rise in compressor speed the evaporation temperature however decreases as a consequence of increased required temperature differences for the increased capacity to be transferred and increasing pressure drops in the evaporator. In contradiction to the increasing evaporation temperature with condensation temperature level stands a marginal decrease in refrigerant massflow as depicted in Figure 5.24b as a result of the decreasing volumetric efficiency with increasing pressure ratio (see Section 5.4.2). The increase of evaporation temperature is hence weaker than the decrease in volumetric efficiency resulting in a decrease in refrigerant massflow with increasing condensation temperature.

A very important quantity especially for high temperature heat pumps with lubricated compressors states the compressor outlet temperature ($t_{ref,2}$). As described in Chapter 4, the allowed compressor outlet temperature regarding the utilized lubricant to avoid degradation and/or decomposition is approx. 140 °C. The maximum observed compressor outlet temperature for the basic cycle configuration given in Figure 5.24c can be found at approx. 125 °C for a compressor speed of 75 Hz remains in a safe distance from the given threshold. This can also be considered as an advantage of overhanging working fluids in high temperature applications that the compressor outlet superheat is limited due to the proximity of the compressor outlet state to the two phase region. This of course, depends on the internal isentropic efficiency which is a function of the compressor speed. With increasing compressor speed the compression process irreversibilities are increasing causing the compressor outlet temperature to rise. The increase in compressor outlet temperatures between 35 and 75 Hz ranges between 5 to 8 K. The compressor outlet temperature increases with increasing condensation temperature nearly linear. The evaporation temperature shows basically no influence on the compressor outlet temperature (see Figure 5.24c). The refrigerant subcooling after the high pressure receiver can have a strong influence on cycle efficiency and heating capacity (see Section 3.2.3) which will be discussed in further detail in Chapter 6. Nevertheless the experimental subcooling results shall be discussed briefly. The degree of subcooling at state 4 ($\Delta T_{sub,ref,4}$) is defined as the temperature difference between state $4r$ ($t_{ref,4r} = t_{sat,ref,4r}(p_{ref,4r})$) and 4 (see also Figure 5.16). Figure 5.24d shows the resulting subcooling as a function of the condensation temperature with the source temperature level and compressor speed as parameter. The subcooling lies within an range of 25 and 27.8 for a sink temperature difference of 30 K and decreases with increasing compressor speed since pinch point temperature differences increase due to the increasing heating capacity. A similar trend can be observed for the subcooling dependency on an increasing evaporation temperature which is in turn again a increase in refrigerant massflow an thus an increase in capacity of the subcooler. The influence of the condensation temperature appears to be of lesser importance. For the given heat exchanger area and heat transfer coefficient the subcooler outlet temperature is only limited to the sink inlet temperature and the resulting pinch point temperature difference and thus states the optimum value according to Equation 3.27 of Section 3.2.3. However since only small differences in subcooling occur with changing parameters, the significant measurement uncertainties have to be taken into account in this interpretation (up to 0.25 K, see Section 5.2).

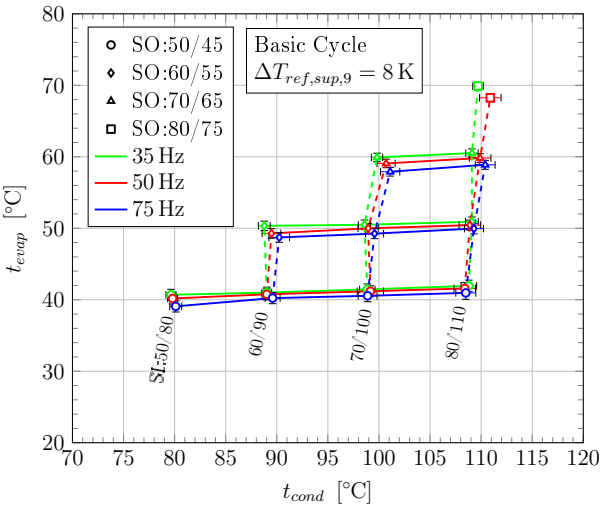

(a) Evaporation temperature

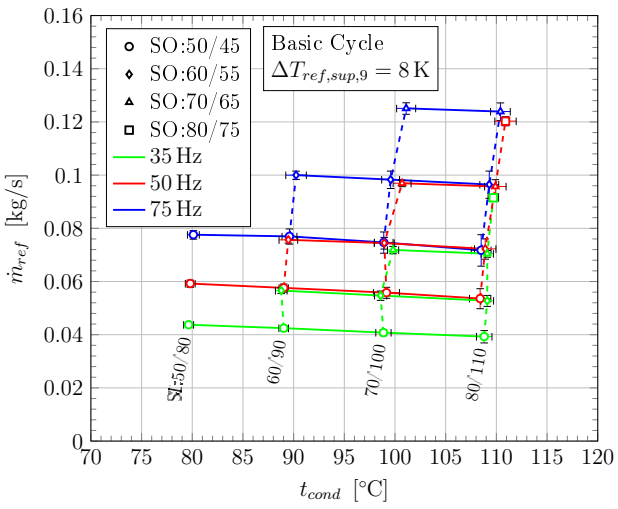

(b) Refrigerant massflow

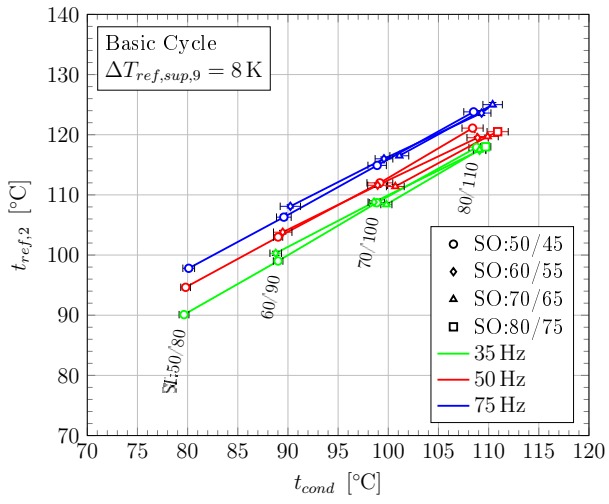

(c) Compressor outlet temperature

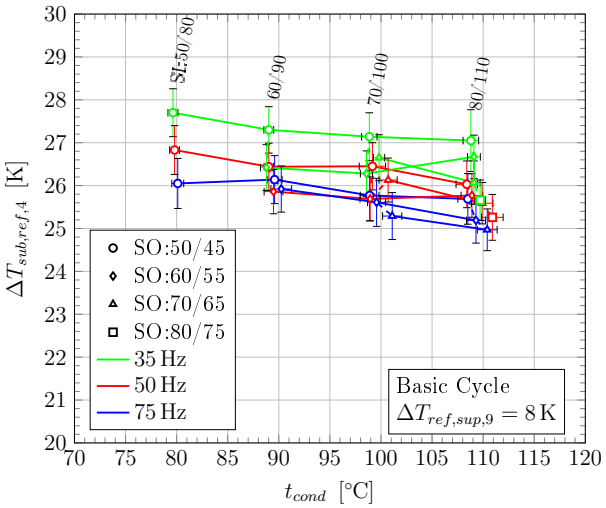

(d) Degree of subcooling between state 4r and 4

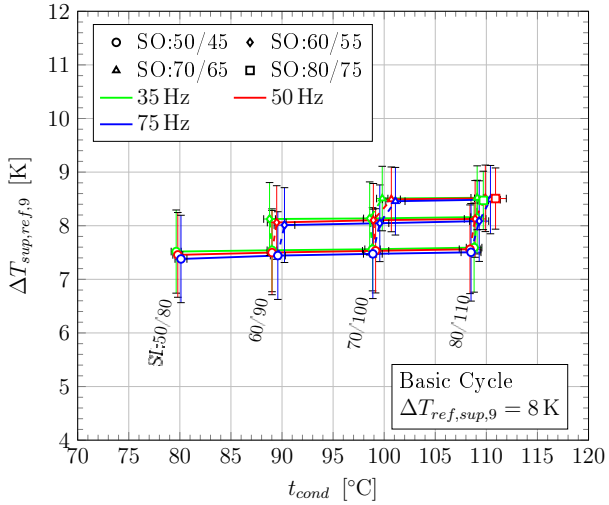

(e) Degree of Superheat at state 9

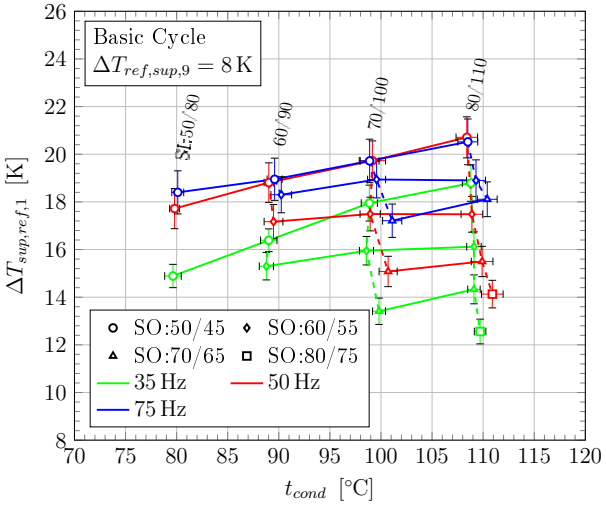

(f) Total degree of superheat at compressor inlet

Figure 5.24: Experimental results of different parameters for the basic cycle configuration as a function of the condensation temperature with the source temperature level and compressor speed as parameter

Finally, the EXV control superheat at state 9 ($\Delta T_{sup,ref,9}$) and the total superheat at the compressor inlet state 1 ($\Delta T_{sup,ref,1}$) are especially of interest regarding the avoidance of a wet compression concerning the required superheat defined in Section 3.7. The superheat is generally defined as the temperature difference of the temperature at the considered sensor location and the saturation temperature corresponding to the pressure at this location (see Section 3.2.2). In Figure 5.24e, the resulting superheat at state 9 can be observed as a function of the condensation temperature and the source temperature level and the compressor frequency. Although the superheat set point has been defined identically in all operation points, the results show an increase with increasing evaporation temperature level. However as clearly visible, the corresponding measurement uncertainties have to be considered since the deviations are within 1 K. The obtained superheat results are in a range between 7.5 to 8.4 K and have been therefore found to be acceptable.

The total superheat at state 1 depicted in Figure 5.24e ranges between approx. 12.5 and 20.8 K and lies therefore in any source sink temperature combination above the theoretically required superheat derived in Chapter 3 (see Figure 3.19). In fact every investigated operation point lies within save distance to the required superheat threshold as consequence of the minimum stable evaporator superheat of 8 K and the additional superheat in the CHX. The evaporator superheat could have been further decreased however has been limited due to stability reasons. The total superheat increases with increasing condensation temperature as a result of increasing compression work with pressure ratio for a certain source temperature level. The refrigerant mass flow in this case remains more or less constant (see Figure 5.24b) therefore superheat increases. For an increased evaporation temperature level at constant sink temperatures the resulting superheat decreases due to the fact that compressor power does not increase proportionally to the massflow since the pressure ratio and thus compression work decreases. Furthermore, as shown in Section 5.4.3, the fraction of recovered waste heat decreases with increasing massflow and thus evaporation temperature. With increasing compressor speed, massflow and compressor power increases and as a result CHX-capacity and thus superheat increases. For a compressor speed of 75 Hz the superheat remains at the same level of 50 Hz as a consequence of the limited heat transfer area in combination with high compressor loads as described in Section 5.4.3.

5.5.4 Influence of the Superheater

The superheater is basically an evaporator area extension, especially interesting in cases when a high degree of superheat in the evaporator is necessary. Since the combination of CHX and evaporator provides sufficient superheat in order to avoid a wet compression under the circumstance of cycle stability, the superheater might not be necessary in this regard. Nevertheless, as outlined in Section 5.3.2, the superheater contributes to stability improvement since the evaporation is shifted into the evaporator. The application of the superheater and thus the increase of the total evaporator area from 1.94 to 3.96 m^2 results in an increase of evaporation temperature for each investigated operation point as depicted exemplary for a compressor frequency of 50 Hz in Figure 5.25a as a function of the condensation temperature with the source temperature level as parameter. The increase of the evaporation temperature throughout the investigated points ranges between 1.36 and 2.14 K, decreases with increasing condensation temperature and tends to increase with increasing evaporation temperature. However these tendencies are lying in a range of 0.03 to 0.37 K and thus well below or in close vicinity to the measurement uncertainty and have therefore to be considered only as indicators. Nevertheless, these characteristics appear logical since the positive effect of the superheater increases with rising evaporator capacity. At lower evaporator capacities the given heat transfer area is sufficient and the resulting pinch point temperature differences

are already low (see also Figures 5.19 and 5.20 in Section 5.5.1). With increasing evaporation temperature the suction gas density and as a result, the refrigerant massflow increases and as a consequence the heating capacity for the superheater configuration as depicted in Figures 5.25b and 5.25c. The absolute increase in heating capacity for the superheater cycle follows the same tendencies as the evaporation temperature described above and lies between 0.56 and 1.6 kW. The relative improvement in this regard ranges between 1.8 and 6 % (Basic Cycle as basis). The electrical compressor consumption remains nearly constant since the effects of increasing mass flow and decreasing pressure due to a rising evaporation temperature are counteracting. As a result the COP improves for the superheater cycle between 0.1 and 0.28 and in relative numbers between 0.75 and 6 %.

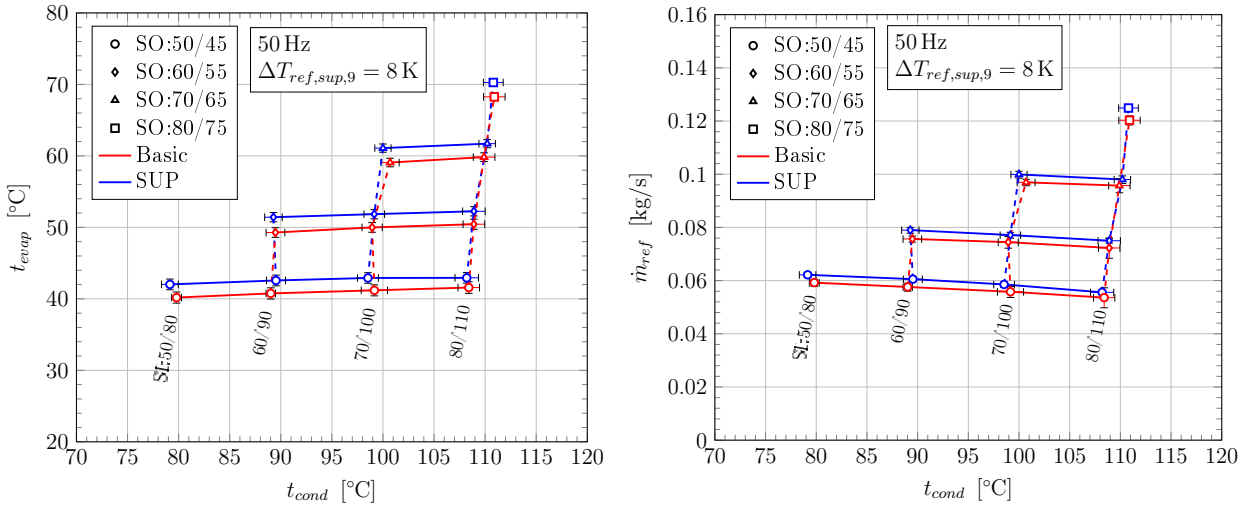

(a) Evaporation temperature

(b) Refrigerant massflow

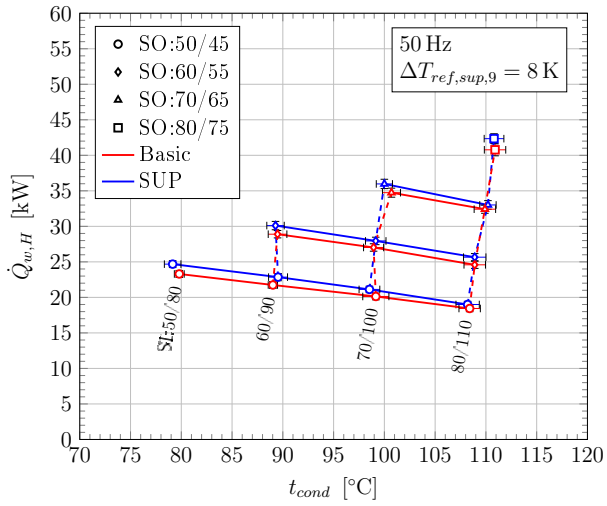

(c) Heating capacity

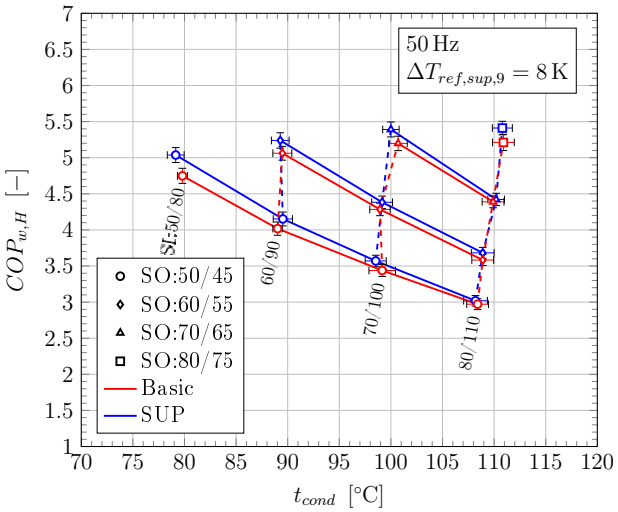

(d) Coefficient of Performance

Figure 5.25: Influence of the superheater application on evaporation temperature, refrigerant massflow, heating capacity and COP as a function of the condensation temperature with the source temperature level as parameter and a compressor frequency of 50 Hz

The improvement in cycle efficiency furthermore increases with decreasing compressor speed and generally with refrigerant massflow. In low capacity cases (low frequency and low evaporation temperature) the increase in refrigerant massflow and thus heating capacity increase for given source and sink temperature levels can be fully utilized since the given condenser area is sufficient for these cases. In higher capacity cases the transferable condenser capac-

ity is already limited by the available heat exchanger area. With an increase in refrigerant massflow and the limited heat transfer area, the high pressure increases and weakens the positive effect of the superheater which can already be observed in Figures 5.20 and 5.23. In comparison to 50 Hz, the improvement of the superheater cycle in terms of efficiency for 35 Hz lies above in the investigated field of operation with relative values between 1.2 and 6.4 %. For the 75 Hz case, the efficiency improvement remains lower with relative values between 0.9 and 2.6 %.

5.6 Internal Heat Exchanger Cycle

The main premise of utilizing an internal heat exchanger for the investigated R600 high temperature heat pump prototype has been, to provide sufficient superheat decoupled from the heat source in order to avoid wet compression and to avoid compromising cycle efficiency with a high degree of superheat in the evaporator (see also Sections 3.2.2, 3.7 and 5.7). Furthermore, as outlined in Section 3.2.4, an increase in cycle efficiency can be possible due to the application of an internal heat exchanger. The utilized experimental IHX cycle layout (left) and a corresponding experimentally obtained t/h state diagram (right) with indicated source and sink temperatures are depicted in Figure 5.26. It shall again be noted that the IHX has been realized as parallel flow heat exchanger (red dashed lines, compare to Chapter 4). The heat pump process remains in a large part identical to the basic cycle described in Section 5.5. The difference persists in an additional subcooling effect from state 4 to state 6 at the outlet of the subcooler. The heat is transferred from the high pressure side to the low pressure side and results in a temperature increase of the gaseous refrigerant from state 8 to state 9 and therefore the refrigerant is further superheated. For the presented results, the IHX 3 way valve (VIHX) has been set to 100 % in any case, meaning that the flow path leads entirely across the IHX.

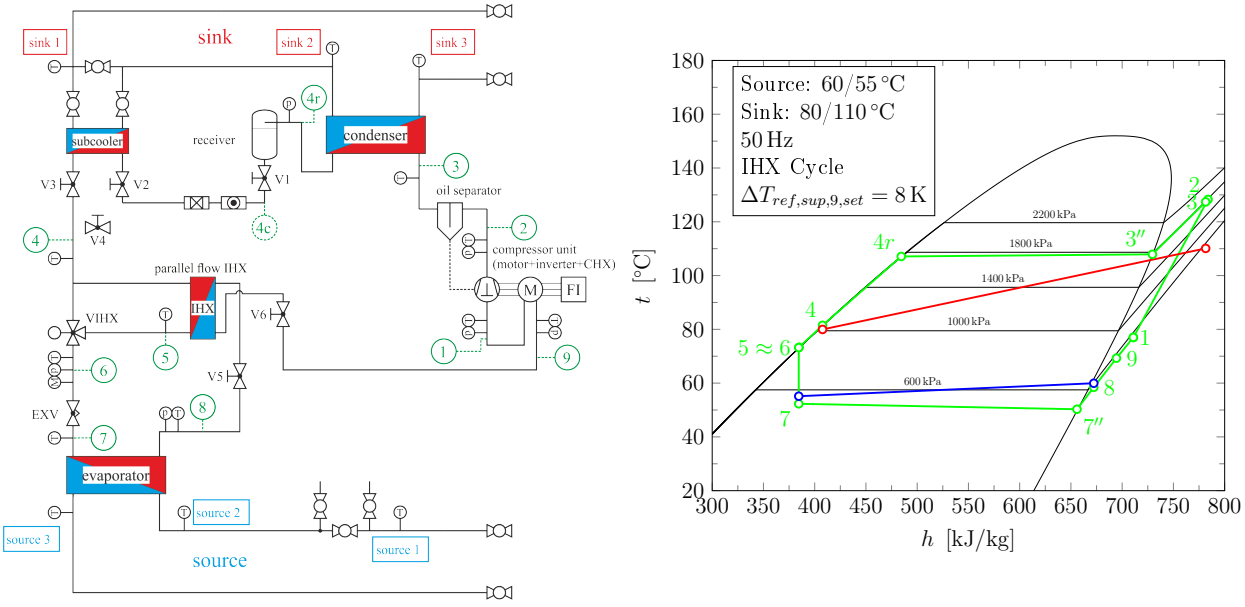

Figure 5.26: Cycle layout of the IHX configuration including sensor positions and refrigerant states (left) and corresponding t/h state diagram obtained from experiment with indicated source and sink temperatures (right)

The superheat heat set point has been again defined to 8 K, however the sensor position has been changed to state 8 in order to keep the evaporator superheat constant for all investigated

cycle configurations for comparison reasons. The results for the IHX Cycle in the following sections are presented in a more compact way since basic characteristics of the heat pump process remain identical to the basic cycle. For these similarities it will be referred to the respective Basic Cycle sections, different aspects and effects of the internal heat exchangers will be explained in detail. A detailed cycle comparison will be presented in Section 5.8.

5.6.1 Capacities, Compressor Consumption and Efficiency of the IHX Cycle

The heating and evaporator capacity characteristics naturally remain identical to the basic cycle with decreasing values for an increasing condensation temperature due to decreasing enthalpy differences across the condenser and evaporator as depicted in Figures 5.27a and 5.27b (see also Figure 5.19). With increasing evaporation temperature and compressor speed (i.e. volume flow) and thus refrigerant massflow, heating and evaporator capacity increases. The heating capacity of the IHX cycle reaches a maximum of 46.8 kW within the investigated field of operation at a source and sink temperature level of 70/65 °C and 70/100 °C respectively and a compressor speed of 75 Hz. The minimum heating capacity results to 13.7 kW for a source temperature level of 50/45 °C, a sink temperature level of 80/110 °C and a frequency of 35 Hz. The evaporator capacity ranges within the field of operation between 11.2 and 37.6 kW for the same operation points. The electrical compressor consumption depicted in Figure 5.27c shows a similar behaviour compared to the basic cycle since the characteristics of the determining parameters such as pressure ratio and refrigerant massflow basicylly do not change. The highest required compressor power among the investigated operation points results to 11.5 kW for a compressor frequency of 75 Hz, a source temperature level of 70/65 °C and sink temperatures of 80/110 °C. The lowest obtained value for the compressor power remains at 3.2 kW for the lowest investigated temperature lift and a compressor frequency of 35 Hz. Similar, the general characteristics of the cycle efficiency remain identical to the Basic Cycle (see Section 5.5.2) decreasing significantly with increasing temperature lift and compressor speed. As depicted in Figure 5.27d the efficiency results range between 3 and 5.7 with the corresponding operation points 50/45 °C-80/110 °C-75 Hz and 80/75 °C-80/110 °C-35 Hz respectively. A new parameter in terms of capacities in the IHX Cycle states the IHX capacity. The IHX capacity is calculated based on the fundamentals described in Chapter 3 as the product of refrigerant massflow and enthalpy difference between state 8 and 9. Since the massflow on the high and low pressure side (states 4 to 6 and 8 to 9, respectively, see Figure 5.26) is identical, the enthalpy differences remain identical.

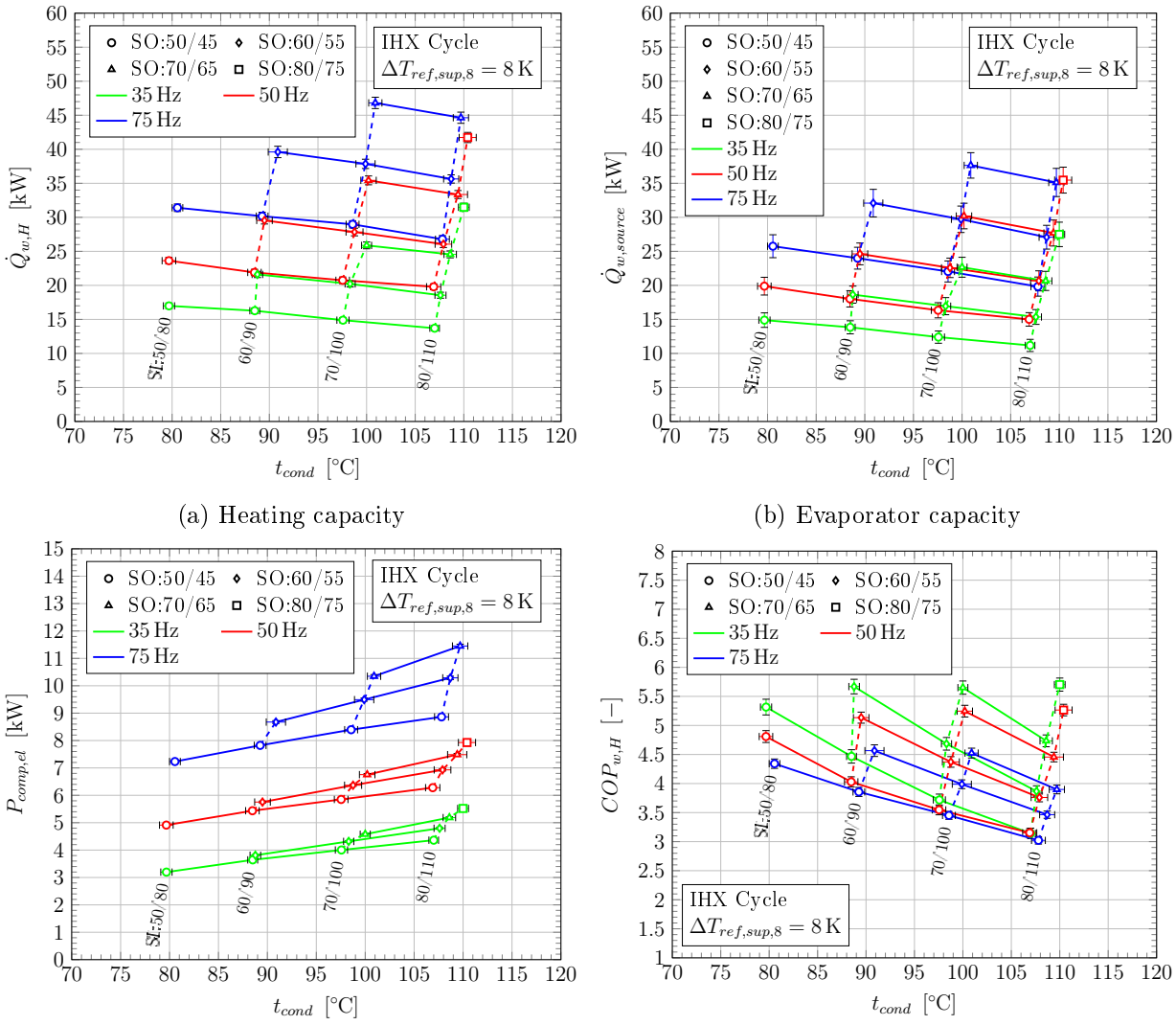

(a) Heating capacity

(b) Evaporator capacity

(c) Compressor consumption

(d) Coefficient of Performance

Figure 5.27: Experimental results of main capacities, compressor consumption and efficiency as a function of the condensation temperature with the source temperature level and compressor frequency as parameter

The experimental results regarding IHX capacity ($\dot{Q}_{ref,IHX,LP}$, calculated at the low pressure side) are displayed in Figure 5.28 as a function of the condensation temperature with the source temperature level and the compressor speed as parameter. For a given source temperature level the IHX capacity increases with increasing condensation temperature since the driving temperature difference increases significantly and vice versa for an increasing evaporation temperature (see Figures 5.28 and 5.29). Since the enthalpy difference remains independent from the refrigerant massflow to the greatest extend (of course the massflow has an influence on the heat tansfer coefficient however has been found to be negligible, compare to Figures 5.30a and 5.30d), the compressor speed serves as factor and defines the slope of the IHX capacity characteristics. With increasing massflow clearly, the IHX capacity increases. The obtained experimental results for the IHX heating capacity range between 0.09 and 2.1 kW for operation points 50/45 °C-50/80 °C-35 Hz and 50/45 °C-80/110 °C-75 Hz respectively.

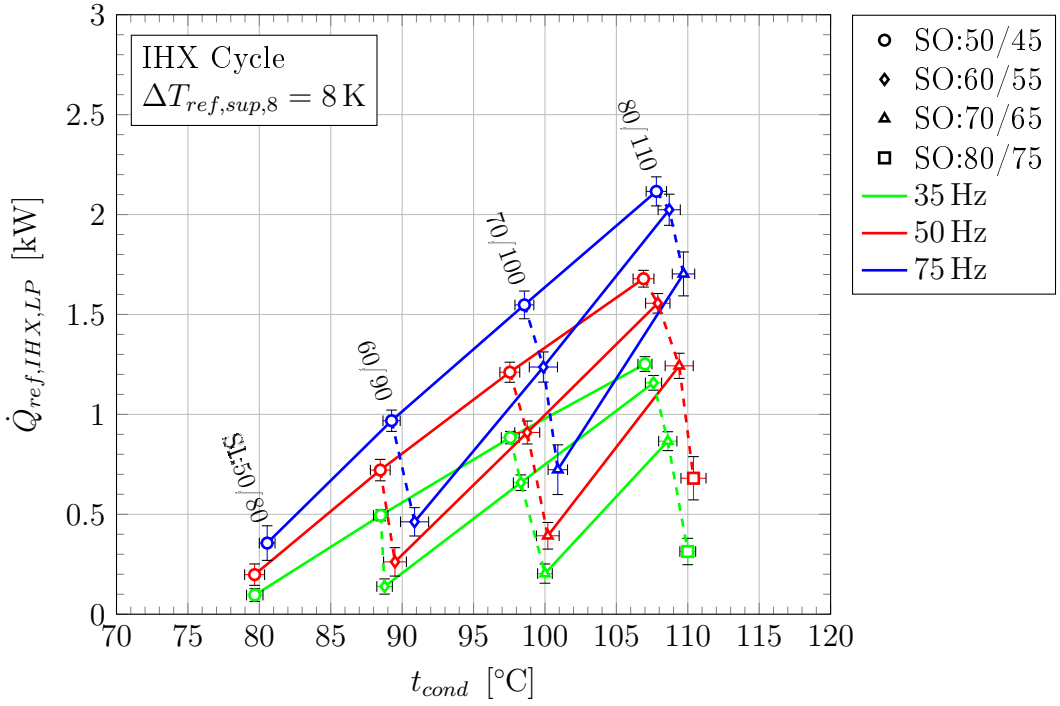

Figure 5.28: Experimental results of the IHX capacity as a function of condensation temperature with source temperatures and compressor speed as parameters

As a consequence of the IHX application, the additional raise of the suction inlet enthalpy (state 1) results in an increased condenser inlet enthalpy and hence a higher refrigerant enthalpy difference across the condenser and the subcooler which can be observed in the t/h state diagram depicted in Figure 5.29 for a compressor frequency of 50 Hz, a source temperature level of 50/45 °C and varying sink temperatures.

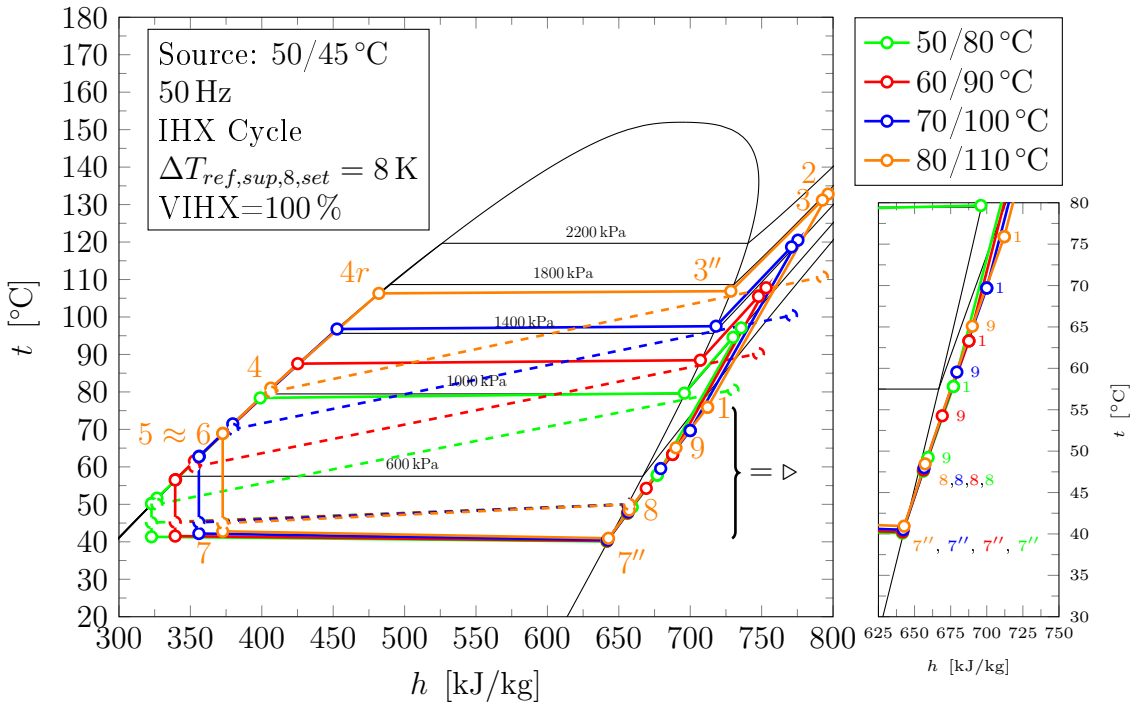

Figure 5.29: Experimentally derived t/h diagram for the basic cycle configuration, a compressor speed of 50 Hz, source temperatures of 50/45 °C and a varying sink temperature level

The temperature difference between the subcooler outlet on the refrigerant side (state 4) and the sink inlet is determined by heat transfer and heat exchanger area. This is accordingly true for the evaporator outlet on the refrigerant side (state 8) and the source inlet. Therefore, in cases when source inlet and sink inlet temperatures are identical, the temperature difference between state 4 and 8 ranges between 4 and 6.7 K and thus results in low IHX capacities as shown in Figure 5.28 above. The decrease in enthalpy difference across the evaporator (state 7 to 8) is reduced compared to the basic cycle due to the decrease of evaporator inlet enthalpy (state 7) as a result of the additional IHX subcooling.

5.6.2 Parameters of the IHX Cycle

A general effect of the internal heat exchanger on the thermodynamic cycle is the increase in suction gas superheat. Figure 5.30a shows the superheat at state 9 ($\Delta T_{sup,ref,9}$) calculated according to Section 3.2.2 as a function of the condensation temperature, with the source temperature level and compressor frequency as parameter. It shall be noted that the experimental results of $\Delta T_{sup,ref,9}$ are containing the controlled evaporator superheat ($\Delta T_{sup,ref,8}$). In this regard it can be observed that the superheat for cases with identical sink and source inlet temperatures remain low in a range from 8.6 to 12 K which equals 0.6 to 4 K above the evaporator superheat setpoint of 8 K. The characteristic of the IHX outlet superheat follows basically the IHX capacity characteristic (see Section 5.6.1) with increasing values for an increasing temperature difference between high and low pressure side. However since the enthalpy differences are to the greatest extend identical on each heat exchanger side (loss free heat transfer assumed, see Chapter 3, Equation 3.11) and nearly independent of the refrigerant massflow, the superheat values show basically no change with increasing compressor frequency (at approximately identical pressure levels). The results for the degree of superheat at state 9 (IHX low pressure outlet) are ranging between 8.6 and 24.4 K in the investigated field of operation. The experimental results regarding the total suction gas superheat at the compressor inlet ($\Delta T_{sup,ref,1}$) are depicted in Figure 5.30b showing the superimposed behaviour of the IHX and CHX. The suction gas temperature at state 1 is additionally increased by the recovered waste heat of the compressor motor leading to high superheat values above 35 K. The total superheat basically increases with increasing compressor frequency. However, as already discussed in Section 5.4.3, the given heat transfer area of the CHX limits the recoverable waste heat and thus the resulting superheat. A significant consequence of the strongly increased suction gas superheat is a corresponding increase of the compressor outlet temperature. Figure 5.30c shows the respective results of the measured compressor outlet temperatures.

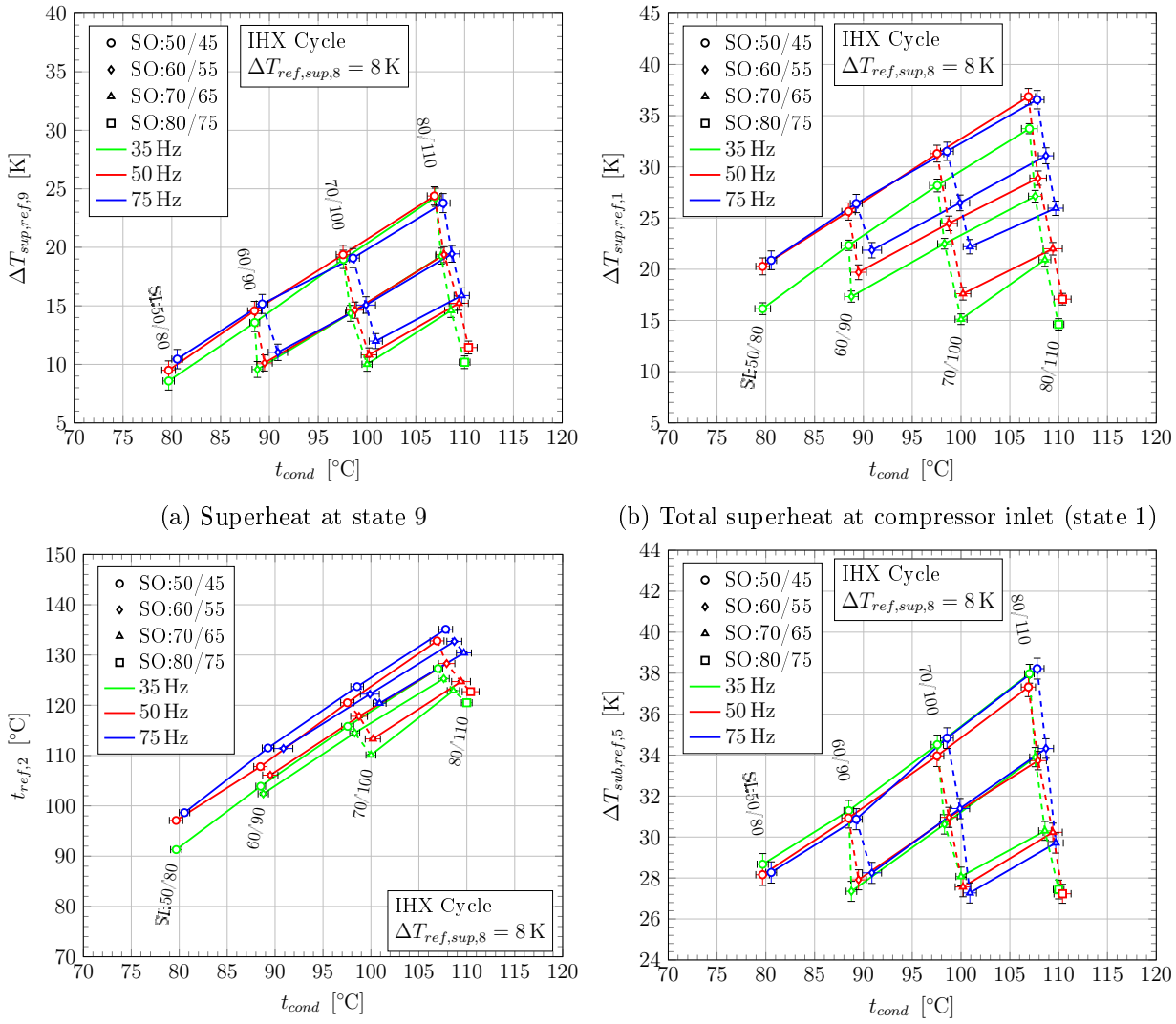

(a) Superheat at state 9

(b) Total superheat at compressor inlet (state 1)

(c) Compressor outlet temperature

(d) Total subcooling at state 5

Figure 5.30: Experimental results of superheat and subcooling parameter as well as compressor outlet temperature as a function of the condensation temperature with the source temperature level and compressor frequency as parameter

The compressor outlet temperature naturally increases with rising condensation temperature and decreases with increasing evaporation temperature following the superheat characteristic of the IHX. Furthermore the increase in compressor outlet temperature can again be observed as a result of the decreasing internal isentropic compressor efficiency as discussed in Section 5.4.2. The resulting compressor outlet temperatures are close to the compressor oil threshold of 140 °C with values between 91.3 and 135 °C. The total subcool at state 5 is calculated as the temperature difference between state 4*r* and 5 (see Chapter 3) and is depicted in Figure 5.30d. The subcool characteristic corresponds to the superheat results of displayed in Figure 5.30a as basically independent of the refrigerant massflow and decreasing with decreasing heat pump temperature lift. The resulting values are containing the degree of subcool caused by the subcooler and range between 27.2 and 38.2 K.

5.7 Influence of Evaporator Superheat (w/o IHX)

Evaporator superheat in combination with a certain source side temperature difference can have a strong influence on heating capacity and cycle efficiency. Especially in high tem-

perature heat pump applications using overhanging working fluids such as R600, R245fa or R1336mzz-Z, the required superheat to avoid a wet compression might reach values up to 35 K (see Section 3.7). Depending on the source side temperature difference, a high superheat in the evaporator can have significant negative effects on cycle efficiency and heating capacity. Therefore a superheat decoupled from the heat source can be provided by other sources such as compressor waste and/or an internal heat exchanger in order to keep evaporator superheat in an appropriate range. As already discussed in Chapter 3 the lowest possible superheat is generally considered to be favourable in order to utilize high phase change heat transfer coefficients across the largest part of evaporator heat transfer area and an increased temperature difference in the superheating section. Further effects such as superheat stability however can set a lower boundary to the realizable degree of superheat for a certain heat pump system (see Section 5.3.2).

In order to elucidate the effect of a changing degree of superheat on the investigated high temperature heat pump prototype, the superheat set point has been varied from 18 to 2 K for a source temperature level of 60/55 °C, a sink temperature level of 80/110 °C and a compressor frequency of 50 Hz. This operation point has been investigated for the Basic and the Superheater Cycle. Additionally for the Superheater Cycle, a source temperature difference of 10 K with a source inlet temperature of 60 °C and otherwise identical operation conditions has been investigated for comparison. The source and sink side temperature differences have been maintained by operating the respective metering valves and/or changing the pump speed. The recording interval of a steady operation point has been set to 10 min. The presented values are the temporal average of the recorded data. An important note regarding the following results is concerning of course the stability of low superheat setpoints as discussed in Section 5.3.2 where the temporal results of the superheat signal have been presented. Since the superheat setpoint is varied below the defined stability limit of 8 K, superheat oscillations occur as depicted in Figures 5.4 and 5.5. The amplitude of the oscillation however have been found to be in an acceptable range in order to discuss basic effects of the performed variations. As an indicator in this regard, the temporal standard deviation of the superheat signal is included in the given error margins according to Section 5.2. With an increasing EXV valve opening the flow resistance across the valve decreases. As a consequence the suction gas density has to increase to maintain massflow continuity and thus evaporation (pressure) temperature rises. Due to the increase in evaporation temperature, the degree of superheat decreases hence the driving temperature difference in the superheating section increases. Furthermore with increasing evaporation pressure the average vapour quality in the evaporator decrease and hence the liquid fraction of the refrigerant increases. As a result larger heat exchanger area is occupied with liquid refrigerant where boiling processes can take place, which increases the overall heat transfer coefficient of the evaporator. A further effect of the increased refrigerant density is the accumulation of more refrigerant mass in the evaporator. The corresponding experimental results regarding the evaporation temperature and the refrigerant massflow as a function of the resulting superheat at state 9 and the above described operation points are depicted in Figure 5.31. It shall again be noted that the source temperature difference have been held constant throughout the superheat variation. The evaporation temperature and refrigerant massflow range between approx. 43 and 53 °C as well as 0.055 and 0.08 kg/s. The results for the superheater configuration in combination with a source temperature difference of 5 K lie generally higher than the basic cycle due to the increased overall heat exchanger area as outlined in Section 5.5.4.

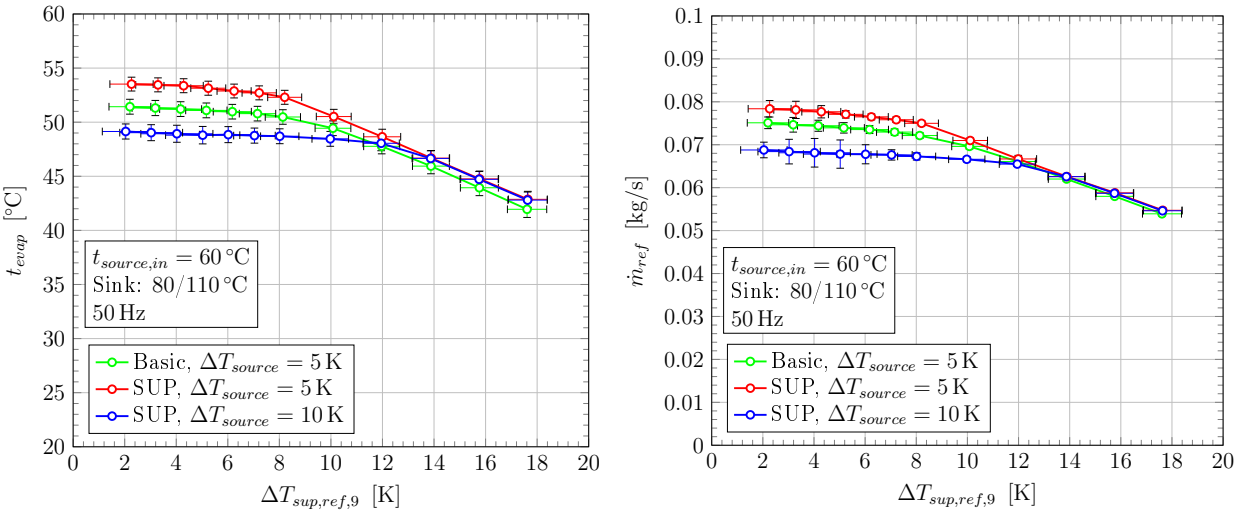

(a) Evaporation temperature

(b) Refrigerant massflow

Figure 5.31: Evaporation temperature and refrigerant massflow as a function of the superheat at state 9 for the basic and the superheater configuration, a source inlet temperature of 60 °C, source temperature differences of 5 and 10 K, a sink temperature level of 80/110 °C and a compressor frequency of 50 Hz

The most interesting aspect of the above described characteristics however is the strong change in its gradient with a decreasing degree of superheat forming nearly a plateau beneath a certain superheat threshold which is dependent on the source side temperature difference. This threshold can be found for a source side temperature difference of 5 and 10 K at a superheat of approx. 8 and 12 K, respectively, appearing to be independent of the cycle configuration. At this transition point as depicted in Figure 5.32a, the determining pinch point temperature difference shifts from the source inlet to the outlet (see also Section 3.2.2, $\Delta T_{pp,source,in}$ and $\Delta T_{pp,source,out}$) as depicted in Figure 5.32a for the basic configuration. The source outlet temperature ($t_{source,3}$, see Figure 4.4) then states the upper boundary for the evaporation temperature (evaporator pressure drops have to be considered). Hence in the plateau region, the evaporation temperature is determined by heat transfer of the evaporator. The slight decrease of the source outlet temperature difference ($t_{source,3} - t_{ref,7}$) is likely a result of the increasing heat transfer area occupied by two phase refrigerant and a rising driving temperature difference in the superheating section with decreasing degree of superheat. The corresponding $t/\dot{Q}$ diagram of the evaporator for selected superheat set points based on the refrigerant side capacity and the basic cycle can be found in Figure 5.32b. For high superheat set points and the resulting lower refrigerant massflow and thus evaporator capacity sufficient heat transfer area remains for the single phase heat transfer to increase resulting degree of superheat. For low superheat set points, the EXV opening follows the same characteristic as the evaporation temperature of Figure 5.31a as depicted in Figure 5.32a. A small change of the EXV opening results in a high variation of the resulting superheat below the transition point discussed above (see Figure 5.32). With the remaining heat transfer area and the strongly decreased driving temperature difference in combination with a low heat transfer coefficient of the gaseous flow, apparently small changes in evaporation pressure, temperature and massflow have a high impact on the resulting superheat as can be observed in Figure 5.32b for example between 6 and 2 Ksuperheat.

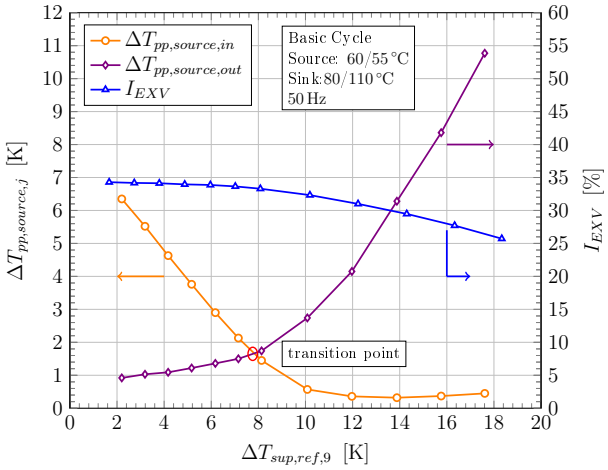

(a) temperature differences at source inlet and outlet, EXV opening

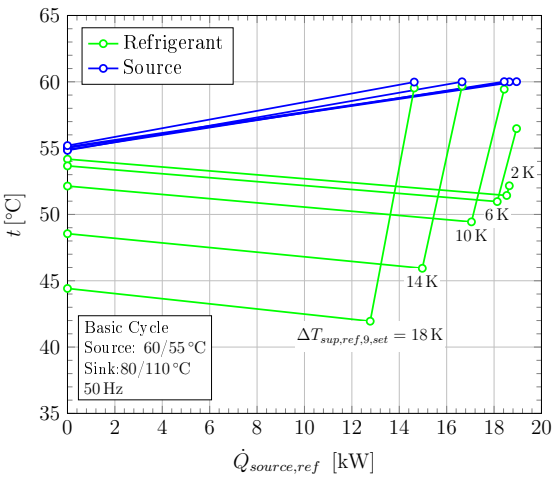

(b) $t/\dot{Q}$ diagram of the evaporator

Figure 5.32: Characteristics of the temperature differences at source inlet and outlet ($\Delta T_{pp,source,in}$ and $\Delta T_{pp,source,out}$ respectively) of the evaporator and EXV opening (I_{EXV}) with selected $t/\dot{Q}$ diagrams for the basic configuration for a source inlet temperature of 60 °C, source temperature differences of 5 K, a sink temperature level of 80/110 °C and a compressor frequency of 50 Hz)

As a consequence of the superheat decrease, the evaporator capacity increases due to massflow increase as already displayed in Figure 5.32b and clearly follows the evaporation temperature and massflow characteristics as depicted in Figure 5.33a. The evaporator capacity increases up to 29 and 32 % of the basic and superheater cycle with a source temperature difference of 5 K in a superheat range between 18 K and the transition point ($\approx$ 8 K, compare to Figure 5.32a). For a source temperature difference of 10 K, the evaporator capacity increases up to 17 % in a superheat range between 18 K and the transition point ($\approx$ 12 K, not depicted). Below the transition point, the evaporator capacity decreases slightly due to the decrease in enthalpy difference ($\Delta h_{ref,7,9}$) across the evaporator as depicted in Figure 5.33b, since the inlet enthalpy remains constant, determined by the high pressure side. The relative change of the evaporator capacity below the superheat transition point results to approx. -1.1 % and -3.5 % for the superheater configuration with a source temperature difference of 5 and 10 K respectively. The decreasing specific evaporator capacity with declining evaporator superheat causes a decrease in specific heating capacity as displayed in Figure 5.33b since compressor inlet state and thus the outlet state is shifted to lower enthalpies. The slightly increasing refrigerant massflow below the superheat transition point cannot compensate this decline in enthalpy difference and thus the heating capacity and finally the COP decreases, especially for a source temperature difference of 10 K as displayed in Figure 5.34b. The relative change in heating capacity and COP below the transition point results to -0.5 and -2.3 % respectively for the basic cycle and the superheater cycle with a source temperature difference of 10 K respectively. Since the decrease of evaporator and heating capacity below the transition point remains very low, measurement uncertainties have to be taken into account regarding the above made statements. However, as described in Chapter 3, the simulation results exhibit a similar behaviour independently of uncertainties, thus indicating that the decrease of heating and evaporator capacity below the transition point has also a theoretical background.

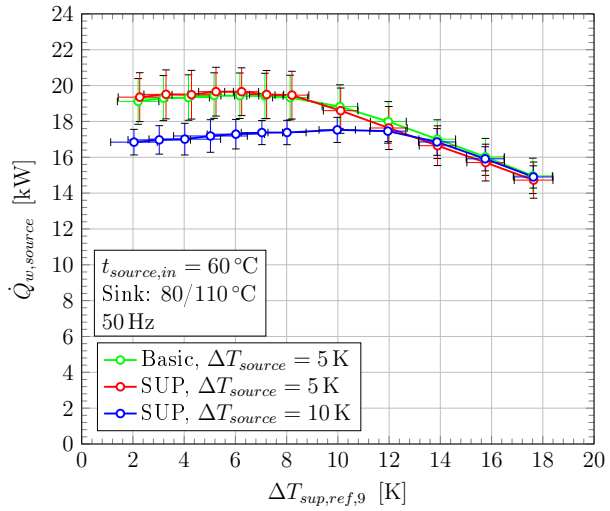

(a) Evaporator capacity

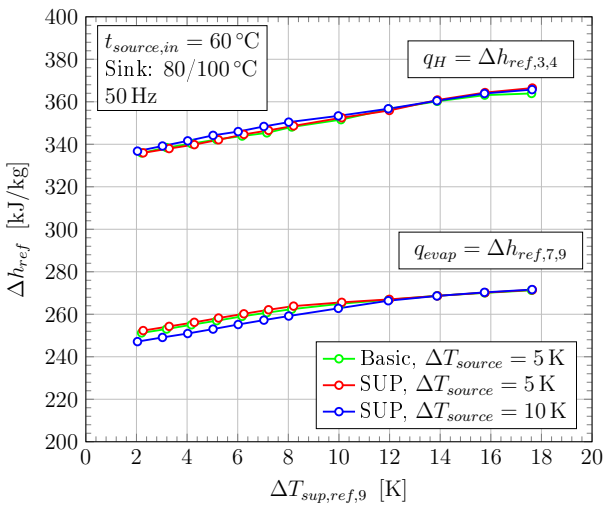

(b) Specific heating and evaporator capacity

Figure 5.33: Evaporator capacity and specific heating and evaporator capacity as a function of the superheat at state 9 for the basic and the superheater configuration, a source inlet temperature of 60 °C, source temperature differences of 5 and 10 K, a sink temperature level of 80/110 °C and a compressor frequency of 50 Hz

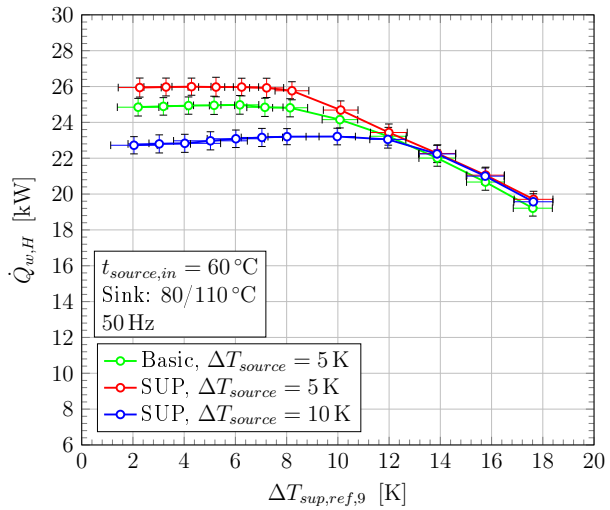

(a) Heating capacity

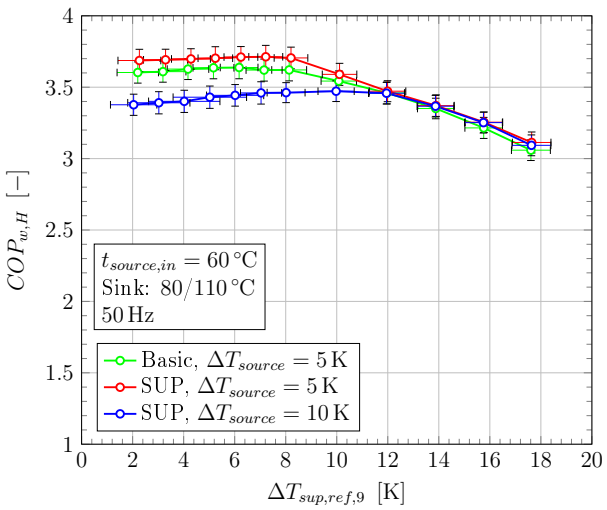

(b) Coefficient of performance

Figure 5.34: Heating capacity and Coefficient of Performance as a function of the superheat at state 9 for the basic and the superheater configuration, a source inlet temperature of 60 °C, source temperature differences of 5 and 10 K, a sink temperature level of 80/110 °C and a compressor frequency of 50 Hz

The above presented results indicate that a minimum possible superheat might not be the optimum in terms of heating capacity and cycle efficiency. The optimum degree of superheat is more a function of the source side temperature difference with further influences of evaporator pressure drop and heat transfer area (pinch point temperature difference) which corresponds to the correlation by e.g. Pitarch et al. (2018) in the context of an optimum degree of subcooling (see Chapter 3). The influence of an additional evaporator area realized by the application of the superheater shows similar behavior as the basic cycle deviating only in an absolute increase of evaporation temperature and it's consequences as already discussed in

Section 5.5.4. In conclusion, the lower boundary in terms of evaporator superheat regarding operational stability might therefore not be a critical parameter given the above presented results. In order to gain more information regarding an optimum superheat set point as a function of different source and sink temperature differences, compressor frequencies and the use of an internal heat exchanger, a comprehensive parameter study has been carried out with the validated heat pump simulation model and will be discussed in Chapter 6.

5.8 Cycle Comparison and Carnot Efficiency

A comparison of the investigated cycle configurations especially in terms of heating capacity and cycle efficiency is an important aspect for future industrial applications in order to decrease operational costs. Therefore selected parameters for all investigated cycle layouts are compared and analysed in this section. Based on the obtained results the corresponding Carnot efficiency has been derived to provide the possibility to compare the investigated prototype to the state of the art in high temperature heat pumps. For the following analysis, the discussed results for the IHX and Superheater configurations have been normalized by Basic cycle data in order to show the relative deviation between the different cases. In terms of state diagrams, absolute values have been utilized for comparison. As an example in this regard, the t/h diagram of all three cycle configuration for a compressor speed of 50 Hz, a source and sink temperature level of 50/45 °C and 80/110 °C respectively, is depicted in Figure 5.35.

The first point that stands out in the t/h diagram is the outlet state of the evaporator (state 8*est*) with a vapour quality well below saturation. This point is a result of the evaporation process shifted into the superheater for the considered operation and superheat set point (compare to Sections 5.3.2 and 5.5.4). The outlet state has therefore been estimated via the source side capacity between source temperature 2 and 3 (see Section 5.5) since a direct determination based on pressure and temperature is not possible within the two phase region. Figure 5.35 shows once more the effects of the different cycle modifications described in the respective Sections above in comparison to the Basic cycle. The superheater increases the evaporation temperature due to an increase in evaporator area compared to the Basic and IHX cycle however has nearly no other effect on the thermodynamic heat pump process. In contradiction to the IHX cycle, which increases the specific evaporator and in turn an increase in specific heating capacity due to the additional subcooling and superheating effect. An interesting effect of the IHX application can be observed if condensation temperatures between cycle configurations are compared. In fact, due to the increase of the driving temperature difference in the desuperheating section (section 3 to 3″) the area distribution in terms of heat transfer coefficient might change slightly in favor for the condensing section. Thus the area with a significantly larger condensing heat transfer coefficient increases, allowing a lower driving temperature difference in this section and hence a lower condensation temperature. The deviation for the 50 Hz case however lies in a range between 0.09 K which is clearly below the measurement uncertainty and 1.6 K for the highest investigated temperature lift. The effect furthermore decreases with decreasing temperature lift since the decline in IHX capacity as outlined in Section 5.6.1 and increasing compressor frequency.

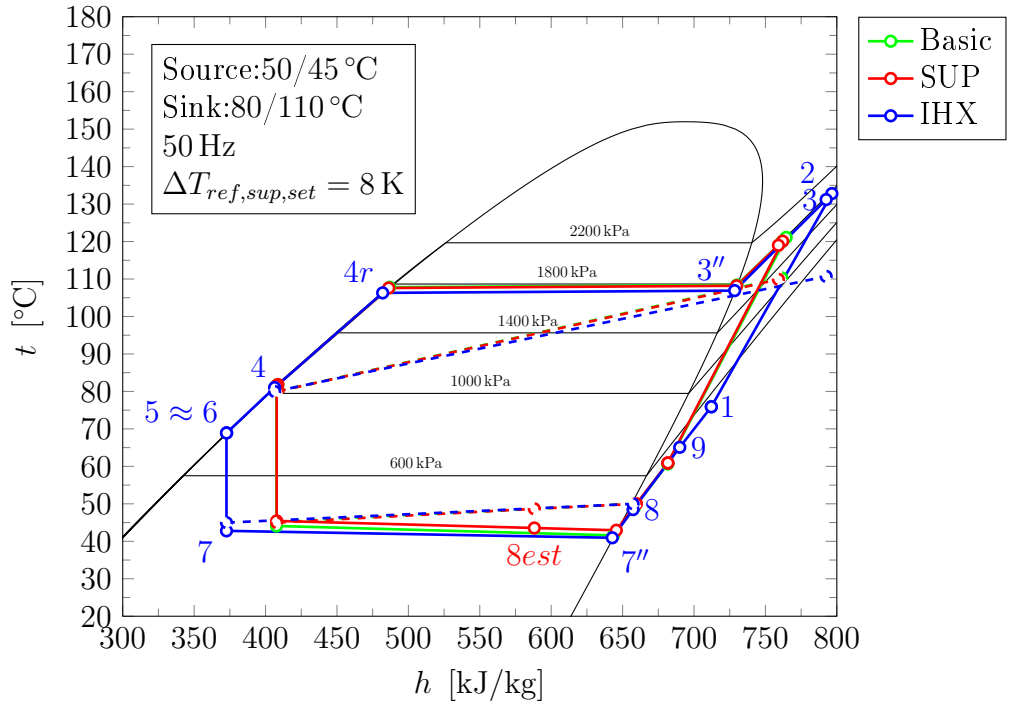

Figure 5.35: Experimentally derived t/h diagram for the three investigated cycle configurations, a compressor speed of 50 Hz, source temperatures of 50/45 °C and sink temperatures of 80/110 °C

The normalized values regarding evaporator capacity ($\dot{Q}_{w,source}$), heating capacity ($\dot{Q}_{w,H}$) and the cycle efficiency for the heating application ($COP_{w,H}$) are depicted in Figure 5.36 for the IHX and Superheater cycle as a function of the condensation temperature, source temperature level and compressor frequency. As displayed in Figure 5.36a for the IHX cycle, the normalized evaporator capacity clearly increases with increasing condensation temperature for a certain source side temperature level and frequency up to 10 %compared to Basic cycle since inlet enthalpy decreases with a constant superheat set point and a slightly decreasing refrigerant massflow. The positive effect of course increases with increasing temperature lift as outlined above. The influence of the compressor frequency however is not as distinct. While at 35 Hz the increase in evaporator capacity appears nearly linear for a source temperature level of 50/45, results of 50 and 75 Hz however show a more exponential increase for the same source level. In this regard, effects like increasing pressure drops and pinch point temperature differences with increasing compressor speed are influencing the results in terms of compressor efficiencies, heat transfer and suction gas density. Furthermore, also measurement uncertainties have to be considered in some cases since differences are certainly very low. In comparison the Superheater Cycle shows in tendency an opposite trend compared to the IHX cycle as shown in Figure 5.36b. With increasing condensation temperature the normalized evaporator capacity decreases from approx. 1.04 to 1 (50 Hz). Values below 1 might well be a result of measurement uncertainties of the evaporator capacity as outlined in Section 5.5.2. The heating capacity for the IHX cycle follows basically the characteristic of the evaporator capacity which can be observed in Figure 5.36c as a result of the increased condenser inlet enthalpy (see Section 5.6.1). A maximum improvement of approx. 7.3 % has been obtained. In contradiction to the IHX cycle, the heating capacity improvement of the Superheater Cycle decreases more clearly with compressor frequency and source temperature level as a result of a limited condenser heat transfer area. The maximum improvement in this case has been found to be approx. 8.1 % for a compressor frequency of 35 Hz.

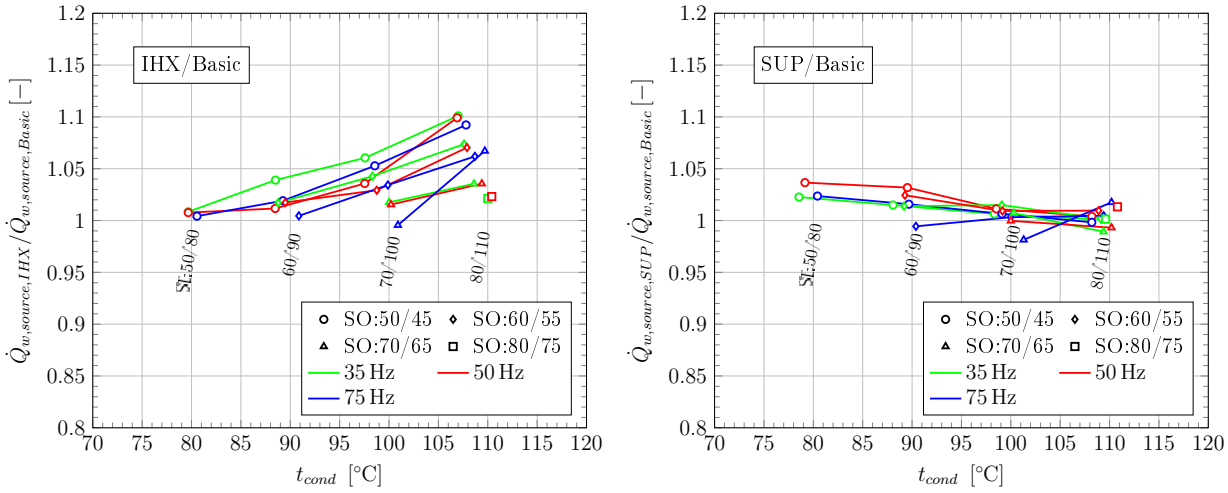

(a) Normalized evaporator capacity, IHX cycle

(b) Normalized evaporator capacity, SUP cycle

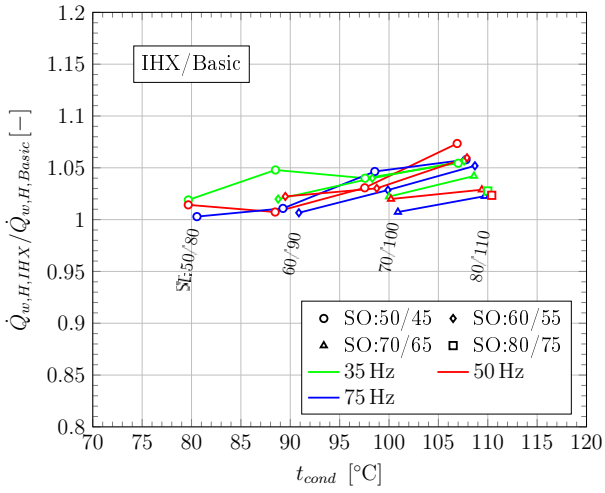

(c) Normalized heating capacity, IHX cycle

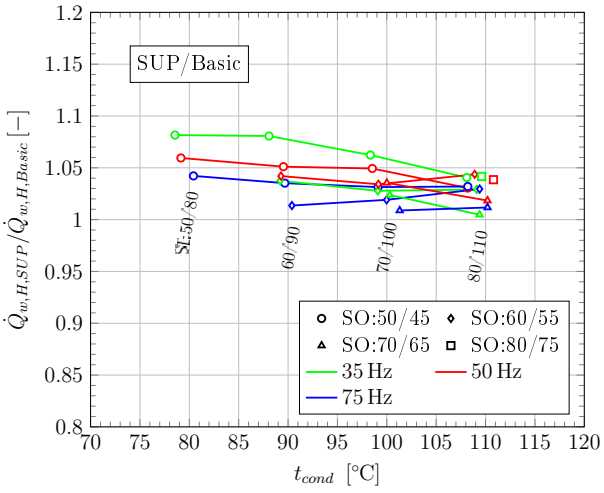

(d) Normalized heating capacity, SUP cycle

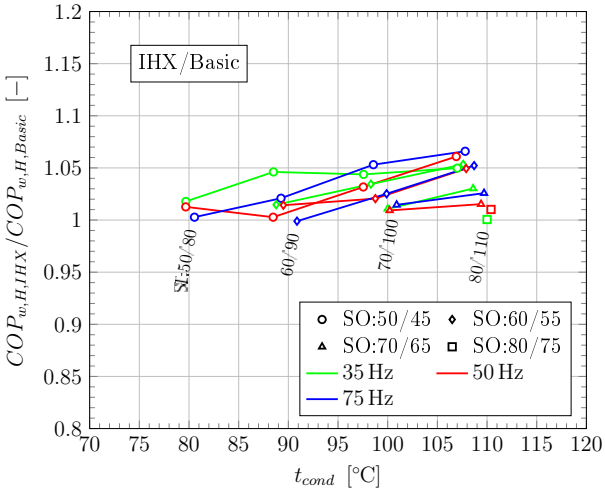

(e) Normalized COP, IHX cycle

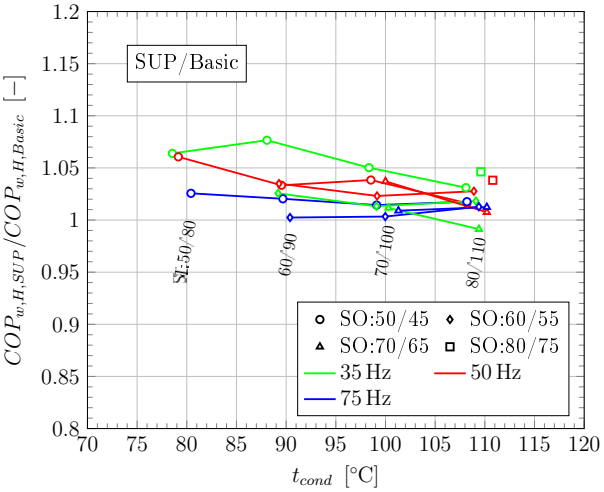

(f) Normalized COP, SUP cycle

Figure 5.36: Normalized capacities and efficiencies for the IHX and Superheater cycle compared to the Basic cycle as a function of condensation temperature, source temperature level and compressor frequency

The efficiency improvement in both cases follow the characteristics of the respective normalized heating capacity since the electrical compressor consumption remains nearly constant using the IHX (only marginal influence on compressor work and suction gas density) and the Superheater cycle (counteraction of increasing massflow and decreasing pressure ratio). As a result the IHX cycle shows a maximum improvement of approx. 6.6 % and the Superheater cycle of approx. 7.6 % as depicted in Figures 5.36e and 5.36f respectively. Clearly the Superheater cycle states basically only a heat transfer area increase which has to be carried out also for the condenser in order to increase cycle efficiency across the entire field of operation. Nevertheless an increase of cycle stability has been obtained as described in Section 5.3.2. The improvement potential of the internal heat exchanger is also strongly dependent of the operational boundary conditions of the high temperature heat pump which has to be considered for future heat pump design. The most important aspect considering the internal heat exchanger is the strongly increased compressor outlet temperature compared to the Basic Cycle (up to 135 °C, see Sections 5.5 and 5.6). This might be critical for compressor lubrication or sealing material in combination with a high superheat stability threshold and a high superheat due to the compressor motor as it is the case in the present prototype (total superheat up to 38 K, IHX).

In order to compare the different cycle configurations and operation points to the ideal cycle, the Carnot COP has been evaluated according to Chapter 3. The calculation of the $COP_{C,h}$ is based on the source outlet temperature ($= T_C$) and the sink outlet temperature ($= T_H$). The ratio between the actual COP and the Carnot COP defines the Carnot efficiency $\nu_{Ca,H}$ of the investigated heat pump as given in Equation 5.3 (see Section 3.1.1).

$$\nu_{Ca,H} = \frac{COP_{w,H}}{COP_{C,h}} \tag{5.3}$$

Furthermore, considering the temperature glide of heat source and sink the Lorenz efficiency ($COP_{Lo,H}$) might be more appropriate for comparison as stated for example by Arpagaus et al. (2018b). The Lorenz efficiency is defined by Equation 5.4 as follows (see also Chen et al., 2002a).

$$COP_{Lo,H} = \frac{T_{m,sink}}{T_{m,sink} - T_{m,source}} \tag{5.4}$$

With the thermodynamic mean temperature ($T_{m,j}$ in K) following Equation based on Bach et al. (1966) and Maurer (2016).

$$T_{m,j} = \frac{T_{j,in} - T_{j,out}}{\ln \frac{T_{j,in}}{T_{j,out}}} \tag{5.5}$$

The index j denotes *source* or *sink* respectively. Consequently a Lorenz efficiency factor ($\nu_{Lo,H}$) can be defined analogously to Equation 5.3. Figure 5.37 shows the corresponding results of the actual, Carnot and Lorenz COP and the obtained Carnot and Lorenz efficiency factors ($\nu_{Ca,H}$ and $\nu_{Lo,H}$) as a function of the temperature lift, compressor speed and cycle configuration. The Carnot COP in the considered field of operation ranges between approx. 6 and 11 for temperature lifts ($t_{sink,3} - t_{source,3}$, compare to Chapter 4) of 35 an 65 K respectively. For comparison, the efficiency of the heat pump prototype results to approx. 6 and 3.1 for the same temperature lifts. Figure 5.37a shows clearly that the main influence on the COP is stated by the compressor frequency. With increasing frequency and thus refrigerant cycle irreversibilities increase.

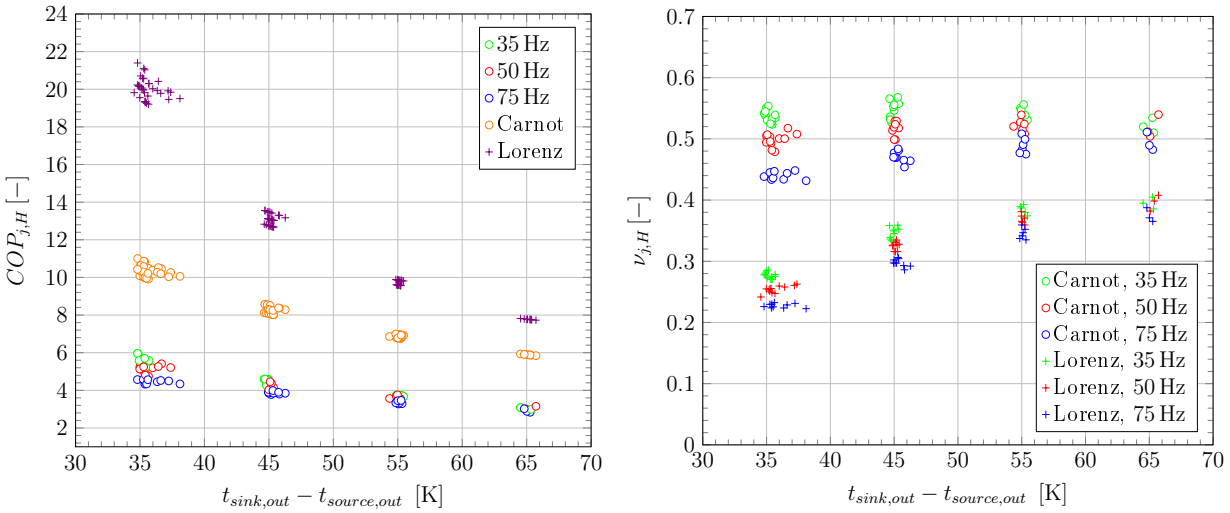

(a) Actual, Carnot and Lorenz COP

(b) Carnot efficiency

Figure 5.37: COP, Carnot and Lorenz efficiency as a function of temperature lift, compressor speed and cycle configuration

This has of course consequences for the obtained Carnot efficiency as depicted in Figure 5.37b showing the same dependency on compressor speed. Based on the given Carnot cycle efficiency and temperature lift definition a Carnot efficiency of up to 53 % can be achieved at low compressor speeds. The Carnot efficiency for a compressor frequency of 75 Hz ranges between 42 and approx. 50 % increasing with increasing temperature lift. The characteristic of the Carnot efficiency resembles strongly to the overall isentropic efficiency of the compressor which increases with increasing pressure ratio and thus temperature lift and decreases with increasing compressor speed confirming the compressor to have a dominant influence on cycle efficiencies and irreversibilities. A similar trend can be observed for the obtained Lorenz efficiency factor however significantly lower due to the mean thermodynamic temperature approach. The Lorenz efficiency factors are ranging between approx. 21 and 41 % increasing with increasing temperature lift and decreasing compressor frequency.

5.9 Additional Remarks

With the presented high temperature heat pump prototype, heating capacities between approx. 13 and 47 kW can be provided with a COP greater 3 for a temperature lift of up to 65 K (between sink and source outlet). It has been experimentally shown that a sink outlet temperature of 110 °C can be provided with source inlet temperatures in a range of 50 to 80 °C. High potential in refrigerant charge reduction remains due to the complex piping in order to realize different cycle configurations. In this regard also mass migration problems have occured resulting in long start up periods. In the development process of the heat pump, the provision of sufficient superheat to avoid a wet compression, decoupled from the heat source (outside of the evaporator, see Chapter 3) has been considered to be a major aspect in the prototype design. Thus measures like an internal heat exchanger have been taken into account. In the end, the provided superheat in certain IHX operation points can be counter productive resulting in high compressor outlet temperatures. In combination with the recovered motor waste heat and the isentropic efficiency of the compressor, an evaporator superheat of 8 K has been found to be clearly sufficient to avoid a wet compression throughout all experimental tests. The investigated R600 high temperature heat pump prototype exhibits Carnot efficiencies in a range between 42 and 53 % which lies in a range

with currently available high temperature heat pumps (see Arpagaus et al., 2018b). The developed high temperature heat pump prototype consists of readily available components and indicates, with a total operation time greater than 300 h, to be the basis for a reliable high temperature heat pump technology for future applications in industrial waste heat recovery.

6 SIMULATION MODEL

In order to investigate a variety of operation conditions exceeding the capabilities of the test rig, to describe optimizing potential and provide results for economic estimations, a simulation model has been set up based on the developed high temperature heat pump prototype. In the present chapter, methodologies, simplifications and results regarding the simulation models are outlined.

6.1 Basic Methodology and Assumptions

The Basic and the IHX cycle have been derived theoretically for the simulation model since the superheater states only an extension of evaporator area and therefore provides no further insight in terms of cycle behaviour. The developed cycle models are based on the investigated heat pump prototype in terms of layout and main components. The theoretical background has already been outlined in Chapter 3. The heat exchanger models such as evaporator, condenser and IHX are following the ε/NTU method as described in Section 3.2.1. The compressor is described as defined in Section 3.3 as a combination of volumetric, isentropic and mechanical efficiency. The cycle models have then be implemented in the software package Engineering Equation Solver (EES) v.9.901 (F-Chart, 2016). The utilized software provides a comprehensive fluid data base with thermophysical property functions and transport properties. In order to provide quick results with a fair agreement to the obtained experimental data a set of simplifications and assumptions have been defined as follows:

- Industrial heat pumps are not expected to operate highly dynamic, therefore only a steady state model has been considered.
- The outlet state of the condenser has been considered to be saturated liquid in any operation point. This implies an appropriately charged system regardless of the operation point and thus a distinct liquid level in the high pressure receiver (see Section 3.5). In high load operation points this might not always be the case in reality if refrigerant charge amount is initially to high.
- The ε/NTU method implies constant refrigerant properties such as specific heat and heat transfer coefficients along the flow path. Therefore overall heat transfer coefficients for the corresponding heat exchanger sections such as evaporation, condensation and single phase have been applied to describe the heat transfer. Transport and thermophysical properties have been defined at mean temperatures and pressures of the respective fluid (see also Sections 3.2.1 and 6.2).
- All plate heat exchangers have been assumed to be of the chevron (herringbone) type since they are very common (Shah and Sekulic, 2003) and no detailed information on plate pattern and corrugation shape has been available (see Chapter 4 and Section 6.2). Furthermore, the corrugation angle is assumed to be identical for each plate (see Figure 6.1).
- All heat transfer and flow phenomena have been simplified to zero dimensional considerations.
- Pressure drops have only been considered for heat exchangers including the CHX. Pressure drops of auxiliary components (e.g. oil separator), measurement equipment and piping have been neglected.

- The expansion valve has been simply modeled by an isenthalpic change of state.
- The compressor has been modeled based on experimentally derived efficiency characteristics as a function of the pressure ratio.
- All heat losses to the surrounding have been neglected except the compressor heat losses which are accounted for in the efficiency approach.
- In the simulation studies only the Basic and the IHX cycle have been considered since the Superheater only states an area extension of the evaporator.
- In contradiction to the experimental set up, the IHX has been modeled as a counter flow heat exchanger for the final simulation studies (see Sections 6.6, 6.7 and 6.8) in order to estimate the potential of an increased effectiveness compared to the parallel flow arrangement. The model validation has been carried out with the original parallel flow arrangement. A brief simulation study compares both flow types in 6.5.
- As source and sink medium, water at a pressure of 250 kPa has been selected. The refrigerant has been selected to be *n*-Butane (R600). The plate material is stainless steel based on the heat exchanger specification as given in Chapter 4. All thermophysical properties have been obtained via property functions implemented in the EES software package.

The resulting simulation model requires only the source and sink temperatures (inlet and outlet), the evaporator superheat and the compressor frequency as input parameters. A parameter study has been carried out varying the source inlet and sink outlet temperatures ($t_{source,1}$, $t_{sink,3}$, compare to Figure 4.4) and temperature differences (ΔT_{source},ΔT_{sink}), the evaporator superheat ($\Delta T_{sup,evap}$) and the compressor frequency (f) to further investigate the influence on heating capacity and cycle efficiency. The applied boundary conditions are collected in Table 6.1.

Table 6.1: Boundary conditions of the simulation studies

Cycle	f	$t_{source,1}$	$t_{sink,3}$	ΔT_{source}	ΔT_{sink}	$\Delta T_{sup,evap}$
	[Hz]	[°C]	[°C]	[K]	[K]	[K]
Basic	35	50	80	5	10	2 to 18
IHX	50	60	90	10	20	
	75	70	100	15	30	
		80	110	20		

The source and sink temperature range has been selected corresponding to the investigated experimental field of operation as discussed in Chapter 5. The source and sink temperature difference has then been varied in order to account for different source and sink heat capacity rates (see Chapter 3) for each cycle configuration, operation point, compressor frequency and evaporator superheat set point. The superheat set point has been changed within a range between 2 and 18 K with a stepsize of 1 K in order to investigate the interaction with different source temperature differences which has been observed during the experimental tests (see Chapter 5). Furthermore the optimizing potential in terms of pressure drops and frequency inverter will be discussed.

6.2 Heat Transfer and Pressure Drop

In order to provide appropriate overall heat transfer coefficients for each heat exchanger several correlations based on the dimensionless Nusselt-, Reynolds- and Prandtl-Numbers have been obtained from literature. The focus of this literature research has been set on compact brazed plate heat exchangers corresponding to the investigated heat pump prototype (see Chapter 4). In order to validate beforehand the obtained Nusselt correlations, each heat exchanger has been separately modeled within the EES software package according to the assumptions above and Chapter 3. In the next step, experimental data regarding the respective refrigerant massflow, refrigerant inlet and outlet states and in cases of the evaporator, condenser and subcooler, the source and sink states, have been provided as input parameters. The obtained simulation results are including the overall heat transfer coefficient for each heat exchanger section (e.i. desuperheating, condensation, subcooling, evaporation, superheating). Based on experimental data, the ($UA_{phx,ht,j,exp}$, see Section 6.4) value has been estimated using the LMTD-Method for the evaporator and condenser (see Equation 3.14). The subcooler and the IHX have been evaluated identically, however the overall heat transfer coefficient $U_{hx,j,exp}$ is directly accessible since no phase transition point occurs within these heat exchangers. The obtained simulation results have then been compared to the experimentally derived heat transfer coefficients (and $UA_{phx,ht,j,exp}$ values) to get an indication of the correlation applicability. The overall heat transfer coefficient U_{phx} has been modeled based on two consecutive channels of the considered plate heat exchanger. Figure 6.1 displays the corresponding basic assumption of one dimensional heat transfer including forced convection the high and low temperature side (α_{HT} and α_{LT} respectively) and heat conduction through the plate (λ_p). Furthermore fundamental geometry parameters such as plate height and width ($H_{phx,p}$, $W_{phx,p}$), the angle of the chevron pattern $\psi_{phx,p}$ and the amplitude of the corrugation profile ($a_{phx,p}$), important for the utilized heat transfer coefficient correlations described in Sections 6.2.2 and 6.2.1 are depicted. However, as outlined above, detailed information on shape and angle of the corrugation pattern has not been available from the manufacturer. Nevertheless global parameters such as corrugation amplitude ($a_{phx,p}$), plate basic geometry (height and width), number of plates ($n_{phx,p}$), effective heat transfer area ($A_{phx,ht}$) or area enlargement factor (Φ_{phx}) have been either obtained directly from manufacturer data or derived based on this data (see Chapter 4 and Appendix A.2). Φ_{phx} defines the area enlargement factor caused by the corrugation pattern and is defined by Equation 6.1 as the ratio between projected plate area contributing (cover and back plate are not considered hence $(n_{phx,p} - 2)$) to the heat transfer and effective heat transfer area $A_{phx,p,ht}$ (compare to Figure 6.1). The effective heat transfer area of the condenser has been obtained from manufacturer design data (see Appendix A.2).

$$\Phi_{phx} = \frac{A_{phx,p,ht}}{(H_{phx,p,ht} \cdot W_{phx,p}) \cdot (n_{phx,p} - 2)} \tag{6.1}$$

A further important parameter for the application of the following correlations is the specific massflow per unit area G_{phx} defined by Equation 6.2 as the ratio of refrigerant massflow and the area A_j of the considered flow channel cross section.

$$G_{phx} = \frac{\dot{m}_{ref}}{A_j} \tag{6.2}$$

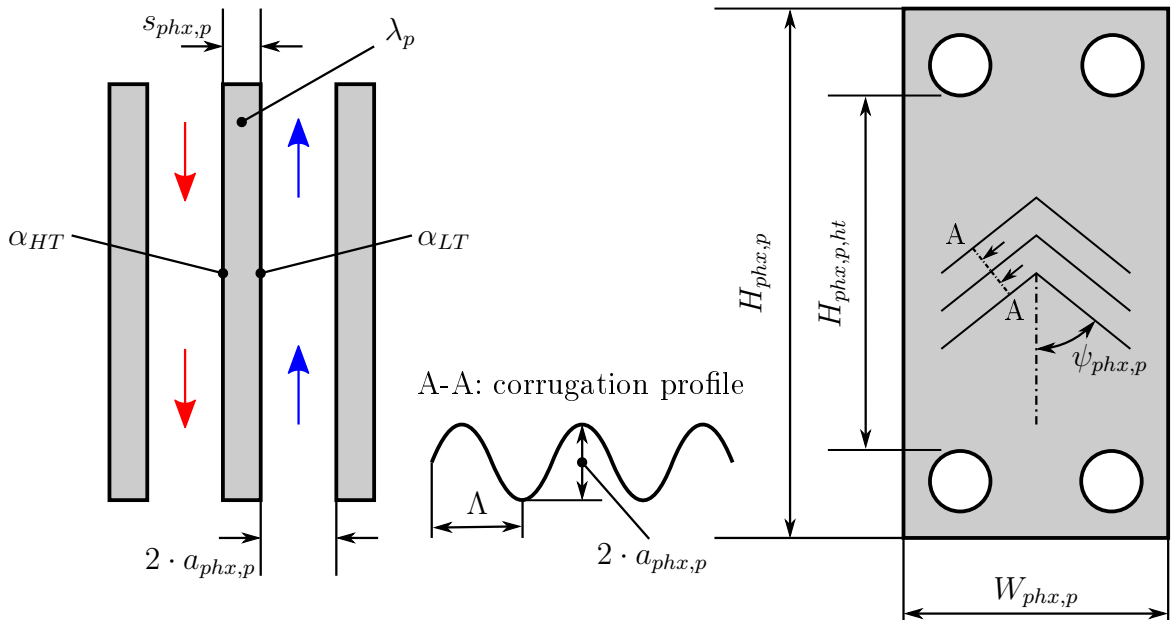

Figure 6.1: Basic assumption of one dimensional transfer and geometry parameters for heat transfer modeling of the utilized plate heat exchangers partially based on Martin (1996) and Longo et al. (2014)

Mathematically, the heat transfer problem reduces finally to a one dimensional heat transport through a plate which can be found in many textbooks such as Shah and Sekulic (2003). Equation 6.3 describes the overall heat transfer coefficient U_{phx} as a function of convection (α) and conduction (λ_p) heat transfer resistances corresponding to Figure 6.1.

$$U_{phx} = \frac{1}{\frac{1}{\alpha_{HT}} + \frac{s_{phx}}{\lambda_p} + \frac{1}{\alpha_{LT}}} \tag{6.3}$$

The entire pressure drop of the considered heat exchangers (Δp_{phx}) has been modeled based on Shah and Sekulic (2003) (see also Longo et al., 2014) considering the pressure drop of ports and manifolds ($\Delta p_{phx,port}$), the pressure change caused by acceleration and deceleration (momentum, $\Delta p_{phx,M}$), the change in static pressure ($\Delta p_{phx,stat}$) and of course the frictional pressure drop ($\Delta p_{phx,fr}$) as given in Equation 6.4.

$$\Delta p_{phx} = \Delta p_{phx,port} + \Delta p_{phx,M} \pm \Delta p_{phx,stat} + \Delta p_{phx,fr} \tag{6.4}$$

The port and manifold pressure drop combined has been derived empirically by Shah and Sekulic (2003) and can be written with Equation 6.5 as a function of the specific massflow per unit area (with $A = \dot{A}_{phx,port}$) and the inlet density $\rho_{phx,port,in}$ of the considered heat exchanger.

$$\Delta p_{phx,port} = \frac{1.5 \cdot G^2_{phx,port}}{2 \cdot \rho_{phx,port,in}} \tag{6.5}$$

The change in momentum along the flow path due to density changes can be described for a single phase flow according to Shah and Sekulic (2003) with Equation 6.5 where $G_{phx,ch}$ denotes the specific massflow of the heat exchanger channel and the respective inlet and outlet densities ($\rho_{phx,in}$, $\rho_{phx,out}$). Since density changes for a single flow are generally low (especially with liquids), the momentum effect has no strong influence on the total pressure drop.

$$\Delta p_{phx,M} = \left(\frac{1}{\rho_{phx,out}} - \frac{1}{\rho_{phx,in}} \right) \cdot G^2_{phx,ch} \tag{6.6}$$

With the heat exchanger channel area defined as follows (see Figure 6.1).

$$A_{phx,ch} = 2 \cdot a_{phx,p} \cdot W_{phx,p} \tag{6.7}$$

Equation 6.6 changes considering a two phase flow based on a homogenous equilibrium approach utilized by Longo et al. (2014) as described in Equation 6.8 where $x_{phx,in}$ and $x_{phx,out}$ are denoting the inlet and outlet vapour quality respectively. The saturated vapour and liquid density is described by $\rho_{sat,vap}$ and $\rho_{sat,liq}$.

$$\Delta p_{phx,M} = (x_{phx,in} - x_{phx,out}) \cdot \left(\frac{1}{\rho_{sat,vap}} - \frac{1}{\rho_{sat,liq}} \right) \cdot G_{phx,ch}^2 \tag{6.8}$$

The static (or gravity) pressure change between the respective sensor positions is positive if the fluid flow coincides with the direction of gravity and negative if otherwise.The static pressure change is then defined by the mean density within the plate heat exchanger $\rho_{phx,m}$, the gravitational constant g and the respective length ($\gamma_{phx,j} \cdot H_{phx,p,ht}$) of the considered heat exchanger section as given by Equation 6.9 .

$$\Delta p_{phx,stat} = \rho_{phx,m} \cdot g \cdot \gamma_{phx,j} \cdot H_{phx,p,ht} \tag{6.9}$$

The area factor $\gamma_{phx,j} \leq 1$ describes the ratio between the actual area occupied either by a single or two phase fluid and the entire heat exchanger area (e.g. desuperheating and condensation section in the condenser, see Chapter 3) and accounts for the liquid level in the considered heat exchanger. As a simplification the two phase regions have been considered to be fully liquid. gravitational effect of the gasous sections have been neglected. For heat exchangers with only a single phase heat transfer such as the subcooler, $\gamma_{phx,sub}$ equals one. For a single phase flow, the mean density $\rho_{phx,m}$ is estimated based on average fluid states across the heat exchanger. The two phase approach uses the homogenous equilibrium model according to Longo et al. (2014) to estimate the mean density with Equation 6.10 based on the mean vapor quality $x_{phx,m}$ as well as the saturated liquid and vapor density.

$$\rho_{phx,m} = \left(\frac{x_m}{\rho_{sat,vap}} + \frac{1 - x_m}{\rho_{sat,liq}} \right)^{-1} \tag{6.10}$$

The remaining frictional pressure drop follows the well known general expression for a single resistance ($\xi_{phx,p}$) pressure drop yielding Equation 6.11. The mean density is again defined according to single or two phase flow as described above.

$$\Delta p_{phx,fr} = \xi_{phx} \cdot \frac{G_{phx,ch}^2}{2 \cdot \rho_m} \tag{6.11}$$

Since geometry information regarding the internal pattern of the heat exchangers has been scarce and significant deviations from experimental data has been observed in the course of this thesis, a certain methodology has been conducted in order to properly describe the heat transfer coefficient and the frictional pressure drop. The utilized heat transfer and pressure drop correlations and the respective methodology shall therefore be discussed in the following sections.

6.2.1 Single Phase Heat Transfer and Pressure Drop

The single phase heat transfer coefficient $\alpha_{phx,sp}$ has been defined according to Martin (2006) especially derived for chevron type plate heat exchangers (see also Martin, 1996) which is

based on the analogy of pressure drop and heat transfer comparable to the definition of turbulent internal flow in a tube by Gnielinski (2006). The respective Nusselt correlation can then be written with Equation 6.12 as follows.

$$Nu = c_q \cdot Pr^{1/3} \cdot \left(\frac{\mu_m}{\mu_{m,wall}}\right)^{1/6} \cdot \left[\xi_{phx} \cdot Re^2 \cdot \sin\left(2\psi_{phx,p}\right)\right]^q \tag{6.12}$$

Where μ_m defines the dynamic viscosity (wall=at wall temperature). c_q and q are fitting parameters discussed later in this section. The friction pressure drop factor ξ has been derived by Martin (1996) as a function of the chevron angle $\psi_{phx,p}$ for crossing corrugation patterns ($0 \leq \psi_{phx} \leq 90°$) and the Reynolds number (Re) following Equation 6.13.

$$\frac{1}{\sqrt{\xi}} = \frac{\cos\psi_{phx,p}}{\sqrt{b \cdot \tan\psi_{phx,p} + c \cdot \sin\psi_{phx,p} + \xi_0\left(Re\right) / \cos\psi_{phx,p}}} + \frac{1 - \cos\psi_{phx,p}}{\sqrt{\xi_1\left(Re\right)}} \tag{6.13}$$

The factors b and c are defined to 0.18 and 0.36 respectively. In general the friction factors ξ_0 and ξ_1 are describing the boundary cases of 0 (straight channel flow) and 90° (wavy channel flow). A detailed description regarding these friction factors can be found in Martin (2006) and Appendix A.5. The corresponding Nusselt- (Nu), Prandtl-(Pr) and Reynolds numbers (Re) are defined as follows:

$$Nu = \frac{\alpha \cdot d_h}{\lambda_m}$$

$$Pr = \frac{\mu_m \cdot c_{p,m}}{\lambda_m}$$

$$Re = \frac{\rho_m \cdot w \cdot d_h}{\mu_m}$$

Where w denotes the flow velocity within one channel ($n_{ch,i}$ = Number of channels per fluid) calculated by Equation 6.14 (see also Figure 6.1).

$$w = \frac{\dot{m}}{\rho_m \cdot n_{ch,i} \cdot W_{phx,p} \cdot 2 \cdot a_{phx,p}} \tag{6.14}$$

Finally, the corresponding hydraulic diameter of the flow channel in a plate heat exchanger is defined by the corrugation amplitude and the resulting area enlargement factor (Φ_{phx}) as given in Equation 6.15.

$$d_h = \frac{4 \cdot a_{phx,p}}{\Phi_{phx}} \tag{6.15}$$

The single phase frictional pressure drop in Equation 6.11 can then be calculated with the following definition of the overall friction factor ξ_{phx} as a combination of Equation 6.13 and the ratio between effective heat exchanger section length ($\gamma_{phx,j} \cdot H_{phx,p,ht}$, see Section 6.2) and the hydraulic diameter d_h.

$$\xi_{phx} = \xi \cdot \frac{\gamma_{phx,j} \cdot H_{phx,p,ht}}{d_h} \tag{6.16}$$

Sole single phase heat transfer especially occurs in the subcooler and internal heat exchanger. Based on the selected Nusselt correlation in combination with Equation 6.3, the overall heat

transfer coefficient $U_{phx,j}$ has been calculated using experimental input data to define the inlet states of the refrigerant and the water side. Additionally, the overall heat transfer coefficient derived from experimental data $U_{phx,j,exp}$ has been estimated using the LMTD-Method, heating capacity and the respective heat exchanger area as described in Chapter 3. The simulation results for the subcooler using different single phase Nusselt correlations according to Gnielinski (2006), Longo (2012), Dittus-Boelter (obtained from Shah and Sekulic, 2003) and of course Martin (1996) compared to the experimentally obtained overall heat transfer coefficient are depicted in Figure 6.2. In this context, a corrugation angle of 60 has been assumed for the correlation of Martin (1996). The additional Nusselt correlations are utilizing the definition of the hydraulic diameter and Reynolds Number described above. Obviously, the characteristic of the overall heat transfer coefficient shows closely a linear behaviour in dependence of the specific refrigerant massflow in the investigated range. The experimental results are ranging between approx. 1.4 and 2.4 kW/(m^2 K) for specific mass fluxes of approx. 30 to 97 kg/(m s^2). The analysed correlations accurately representing the basic trend however either strongly under or over estimating the overall heat transfer coefficient (Longo, 2012, Gnielinski, 2006 and Dittus-Boelter). The correlation by Martin (1996) exhibits an increased agreement however with an additional degree of freedom in the corrugation angle. The effect of the corrugation inclination $\psi_{phx,p}$ for the Martin correlation can be observed in Figure 6.2 on the right. As given in Equations 6.12 and 6.13, with increasing corrugation angle, the pressure drop and the heat transfer coefficient increases, providing a better prediction of the overall heat transfer coefficient for identical boundary conditions. The pinch point temperature difference of the subcooler obtained from experimental data are very small (below 1 K), hence uncertainties regarding the derived overall heat transfer coefficient $U_{phx,sub,exp}$ have to be kept in mind, while reading the presented data. A deviation in the temperature differences can have a strong impact on the obtained $U_{phx,sub,exp}$ results.

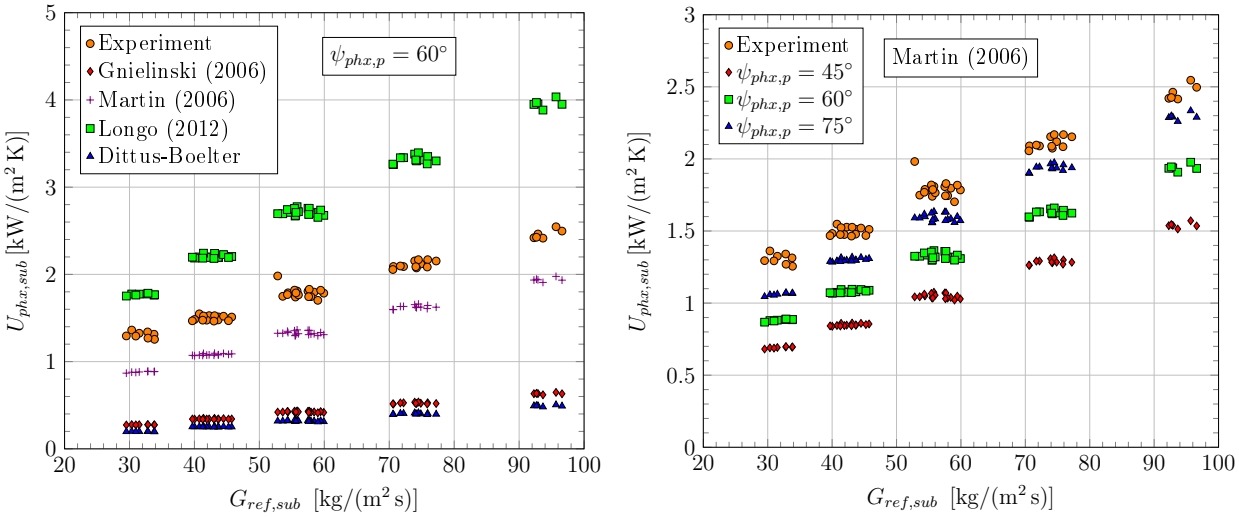

Figure 6.2: Calculated overall heat transfer coefficients according to different Nusselt correlations (left) with a corrugation angle of 60° and according to Martin (2006) as a function of the corrugation angle (right) in dependence of the specific refrigerant massflow

The obtained results depicted in Figure 6.2 have confirmed the selection of the Martin correlation regarding the heat transfer coefficient, not least because of it being especially derived for plate heat exchangers in contradiction to for example Gnielinski (2006) which is based on internal flow in a straight tube. However, as mentioned above, the uncertainty

of the plate geometry remains unsolved. Therefore, a methodology in order to estimate the corrugation inclination has been applied based on the design operation point and the performance calculation data sheet of the manufacturer (see Chapter 4). Therefore, the sum of frictional and port pressure drop ($\Delta p_{phx,fr} + \Delta p_{phx,port}$) of the refrigerant side or in case of the IHX, the high pressure side, given in the respective data sheet for the design operation point, has been utilized as an input for the heat exchanger component model leaving the corrugation angle $\psi_{phx,p}$ as a free parameter. In this regard the subcooler shows already a strongly increased agreement with experimental data as depicted in Figure 6.2, right for a corrugation angle of 75 . However the deviation has been considered still significant and has especially been observed for the IHX. Therefore, providing the design frictional pressure drop to estimate the corrugation angle can not be considered sufficient to take unknown geometry effects into account. Based on the statement of Martin (2006), that details on corrugation patterns are difficult to obtain, the fact that the empirical parameter c_q (see Equation 6.12) contains the relation of hydraulic diameter (d_h) and the wavelength of the corrugation pattern (Λ, see Figure 6.1) and therefore might have to be adjusted, the empirical parameter c_q has been altered to increase consistency with experimental results. The alteration has been carried out similar to the pressure drop adjustment using the design overall heat transfer coefficient as input parameter and design point fluid states (see Chapter 4) to determine the parameter c_q. Table 6.2 summarizes the resulting corrugation angles and c_q parameters based on the design point calculation finally used for the subcooler and IHX description.

Table 6.2: Modified parameter for the Subcooler and IHX heat transfer coefficient

	$\psi_{phx,p}$	c_q	q
	[°]	[-]	[-]
Martin (2006) (original)	-	0.122	0.374
Subcooler (modified)	75	0.128	0.374
IHX (modified)	54.7	0.052	0.374

However it has to be noted, that the adapted c_q parameter for the IHX has shown a distinct lower value than the original which indicates a significant difference in geometry than the models suggested chevron type plates. Finally, the adaption of Martin‘s Nusselt correlation using one single design point has increased the prediction ability significantly for the IHX and slightly for the subcooler as can be observed in Figure 6.3.

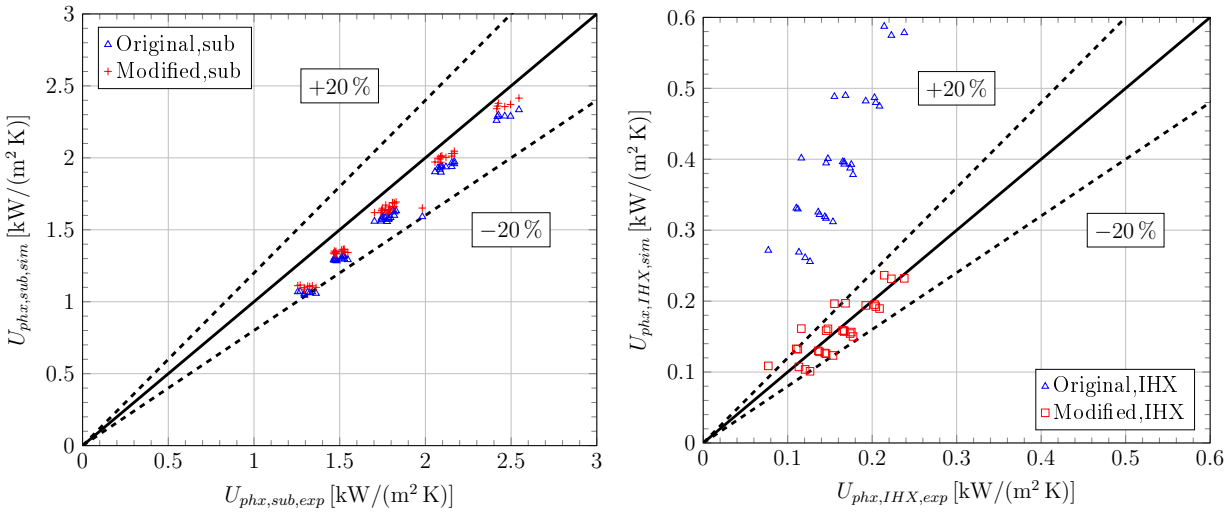

Figure 6.3: Comparison of experimental and modified overall heat transfer coefficients for the Subcooler (left) and the IHX (right) as a function of the specific massflow

The presented methodology allows a significant improvement of the Martin Correlation (Martin, 1996) for plate heat exchangers with unknown internal geometry based on, in many cases available, single operation point design data provided by the manufacturer. However, especially for the IHX, in some operation points the overall heat transfer coefficient is still overestimated significantly by up to 62 %. For the Subcooler a maximum relative deviation of −20 % has been calculated. Nevertheless an average deviation of 21 % and −9 % for the IHX and subcooler respectively has been found to be acceptable considering the complexity of heat transfer and fluid flow within corrugated plates.

6.2.2 Two Phase Heat Transfer and Pressure Drop

Generally in condensers and evaporators a combination of multi and single phase heat transfer occurs. While the single phase model has been described in the previous section the two phase approach shall be discussed at this point. Identical to the single phase heat exchangers, a condenser and evaporator model based on the ε/NTU has been set up with experimental input data in order to validate the applied heat transfer correlations. In contradiction to the single phase heat exchangers, the experimental overall heat transfer coefficient U cannot be determined directly since single and multiphase flow occur simultaneously and thus leaving the actual occupied heat transfer area for each heat exchanger section unknown (see Chapter 3). As a consequence, only the product of heat transfer coefficient and the respective heat transfer area ($UA_{hx,j}$) occupied by the corresponding phase can be experimentally estimated and utilized as validation parameter.

For the refrigerant condensation heat transfer coefficient α_{cond}, the correlation derived by Longo et al. (2015b) based on the assumption of forced convection condensation, has been utilized as described with Equation 6.17.

$$\alpha_{cond} = 1.875 \cdot \Phi_{phx} \cdot \frac{\lambda_{liq}}{d_{h,Longo}} \cdot Re_{eq}^{0.445} \cdot Pr_{liq}^{1/3} \tag{6.17}$$

The equivalent Reynolds Number considering the two phase flow Re_{eq} is based on the homogenous equilibrium model obtained from Longo et al. (2015b) and given by Equation 6.18 using the saturated liquid (sat, liq) and vapour (sat, vap) states as well as the mean vapour

quality (x_m) in the condensing section. With the assumption of a complete condensation, the mean vapour quality results to 0.5.

$$Re_{eq} = G \cdot \left[(1 - x_m) + x_m \cdot \left(\frac{\rho_{sat,liq}}{\rho_{sat,vap}} \right)^{1/2} \right] \cdot \frac{d_{h,Longo}}{\mu_{liq}} \tag{6.18}$$

The definition of the hydraulic diameter used by Longo et al. (2015b) is given in Equation 6.19

$$d_{h,Longo} = 2 \cdot a_{phx,p} \tag{6.19}$$

The single phase section (desuperheating) and the water side (sink side) in the condenser has been modeled according to Section 6.2.1. The corrugation angle has been derived by using the water side pressure drop as input parameter as described in Section 6.2.1 with the c_q parameter left to the original value given in Table 6.2. On the refrigerant side the heat transfer area of the condenser is distributed among the condensing and the desuperheating section following Equation 6.20.

$$A_{phx,ht} = A_{phx,ht,cond} + A_{phx,ht,desup} \tag{6.20}$$

The evaporator has been investigated analogously in order to verify the utilized heat transfer correlation. Longo et al. (2015a) presented a heat transfer coefficient correlation for convective boiling in brazed plate heat exchangers investigating HFC and HC refrigerants following Equation 6.21.

$$\alpha_{evap} = 0.122 \cdot \Phi_{phx} \cdot \frac{\lambda_{liq}}{d_{h,Longo}} \cdot Re_{eq}^{0.8} \cdot Pr_{liq}^{1/3} \tag{6.21}$$

The equivalent Reynolds Number and the hydraulic diameter can then be taken from Equations 6.18 and 6.19. The Prandtl Number has been already defined in Section 6.2.1. The superheating section and the water side (source side) have been modeled according to the single phase approach discussed above and in the previous section. The resulting $U \cdot A$ values have been compared to the experimentally derived UA values as depicted in Figure 6.4 left for the condensing (*cond*) and evaporating (*evap*) section with the main part lying within $\pm 20\,\%$. Similar results can be obtained for superheating and desuperheating section based on the correlation by Martin (1996) which is in tendency overestimating. The comparison of the $U \cdot A$ values combining the single and two phase heat transfer correlation for each heat exchanger section indicate a fair agreement with reality corresponding to the validation results of Longo et al. (2015a), Longo et al. (2015b) and have therefore been implemented in the simulation model. Please note the deliberate difference between $U \cdot A$ and UA. The $U \cdot A$ value is actually calculated as the product of the overall heat transfer coefficient and the corresponding heat transfer area obtained from the heat exchanger model. The UA value is results from the LMTD-method described in Chapter 3 and is derived from experimentally obtained data (capacity and temperatures).

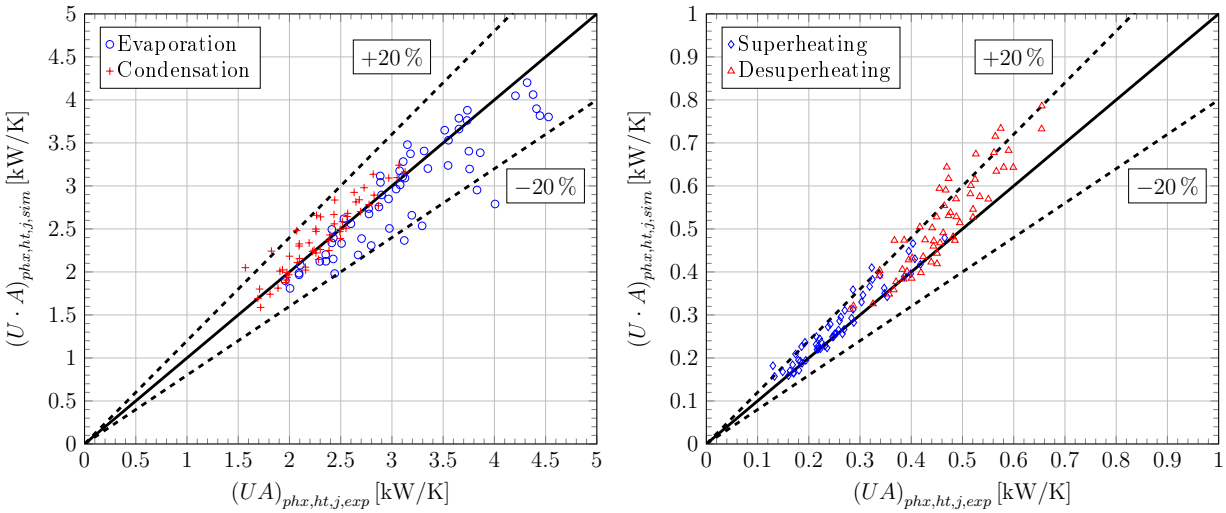

Figure 6.4: Comparison between experimentally derived and simulated $U \cdot A$ values based on correlations of Longo et al. (2015a), Longo et al. (2015b) and Martin (1996) for the condensation, evaporation and single phase heat transfer

The frictional pressure drop for the evaporating and condensing section follows Equation 6.11 representing a linear dependency on the kinetic energy per unit volume (KEV) as suggested by Longo (2010) and Longo et al. (2016) respectively.

$$KEV = G^2/2 \cdot \rho_m \tag{6.22}$$

Based on the assumption of Longo (2010) stating that every corrugation pattern and internal geometry might have a constant corresponding friction factor $\xi_{phx,fr,j}$, this friction factor has been estimated by providing the total frictional refrigerant side pressure drop obtained from design data of the manufacturer (see Chapter 4) as input parameter to the condenser and evaporator model. The single phase pressure drop in the super- and desuperheating section has been obtained from Martin's correlation (see Equation 6.13), reminding that the corrugation angle has been already defined by the water side (see Appendix A.2). Finally, the resulting friction factors for the evaporation ($\xi_{phx,fr,evap}$) and condensation section ($\xi_{phx,fr,cond}$) are given in Table 6.3.

Table 6.3: Resulting evaporation and condensation friction factors obtained from the calibrated heat exchanger models

	$\xi_{phx,fr,j}$ [-]
condensation (for $[\Delta p] = \text{kPa}$)	1.97
evaporation (for $[\Delta p] = \text{kPa}$)	0.321

The total pressure drop $\Delta p_{phx,j}$ based on Equation 6.4 has been compared to experimental data as depicted in Figure 6.5 as a function of the kinetic energy per unit volume ($[KEV] = \text{J/m}^3$) for the condenser (left) and evaporator (right), respectively. The KEV values have been derived with the density based on the homogenous equilibrium model described in Section 6.2 (see Equation 6.10). The utilized experimental pressure drop for the condenser has been estimated with the obtained pressure results of state 2 and $4r$ (see

Chapter 4 or 5). This experimental pressure drop additionally includes the oil separator which obviously contributes to the deviation from experimental results. Nevertheless a clear linear dependency of the pressure drop for the condenser and thus the desuperheating and condensation process can be confirmed.

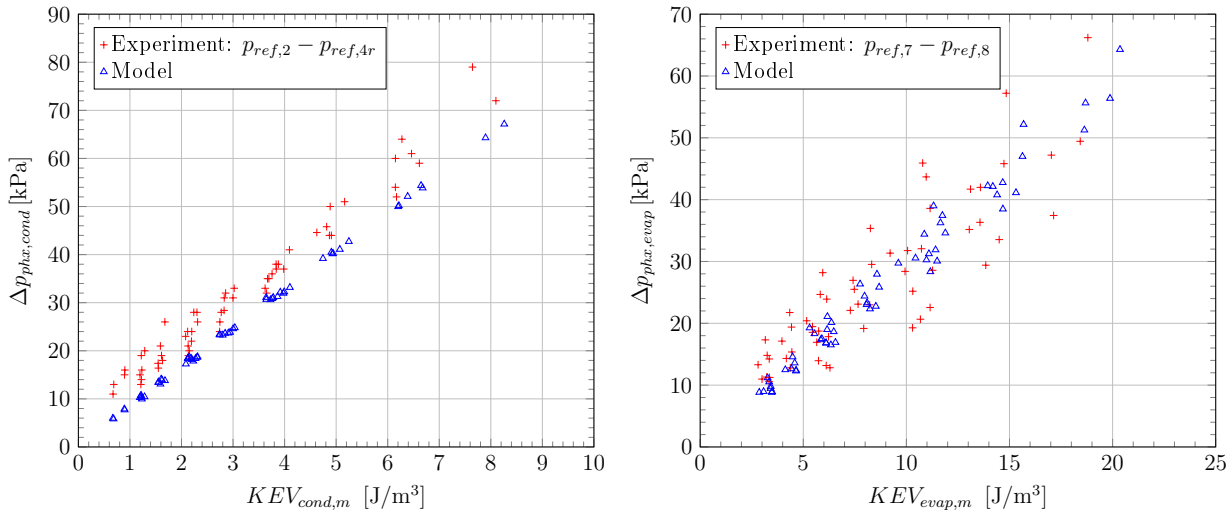

Figure 6.5: Comparison of the total experimental and simulated pressure drop as a function of the kinetic energy per unit volume of the corresponding two phase section for the condenser and evaporator

A general linear dependency can also be observed for the evaporator as depicted in Figure 6.5, right. The experimental data has been obtained from state 7 and 8 (see Figure 4.4), where sensor locations are very close to the evaporator inlet and outlet which is indicated by the same gradient of simulation and experimental results in contradiction to the condenser. The scattering of the evaporator pressure drop is a result of changing mean refrigerant qualities due to different evaporator inlet states while the condenser mean quality remains nearly constant since a complete condensation is assumed showing a fair approximation of the experimental behaviour. The utilized two phase pressure drop approach using a constant friction factor as proposed by e.g. Longo (2010) which has been calibrated with manufacturer design point based results, shows a fair agreement with experiment in a range of approx. ±20 %.

6.3 Compressor and CHX Parametrisation

The compressor parametrization follows the common efficiency approach outlined in Chapter 3. Therefore a quadratic polynomial model equation as given in Equation 6.23 as a function of the pressure ratio ($\pi_p = p_{ref,2}/p_{ref,1}$) has been utilized in order to describe internal isentropic ($\eta_{is,i}$), mechanical (η_m), volumentric (λ_{vol}) and FI efficiency (η_{FI}) based on experimental data of Chapter 5. Furthermore, where necessary, the compressor frequency has been set as parameter according to the experimental results described Chapter 5. Using a quadratic regression method, the coefficients of Equation 6.23 have been derived for a compressor frequency 35, 50 and 75 Hz based on the experimental data presented in Section 5.4.2.

$$\eta_j(f) = a_0(f) + a_1(f) \cdot \pi_p + a_1(f) \cdot \pi_p^2 \tag{6.23}$$

The internal isentropic efficiency has been approximated with a quadratic approach while the mechanical efficiency has been simplified with a linear characteristic. The volumetric

efficiency can also be described with a linear characteristic and is furthermore independent of the compressor speed while the inverter efficiency is independent of both, pressure ratio and compressor speed and thus set to a constant value of approx. 94 %. The resulting characteristics are summarized in Figure 6.6 as a function of the pressure ratio and with the compressor frequency as parameter. The corresponding polynomial coefficients can be found in Table 6.4. The characteristics are valid within a pressure ratio range of $1.8 \leq \pi_p \leq 5.4$.

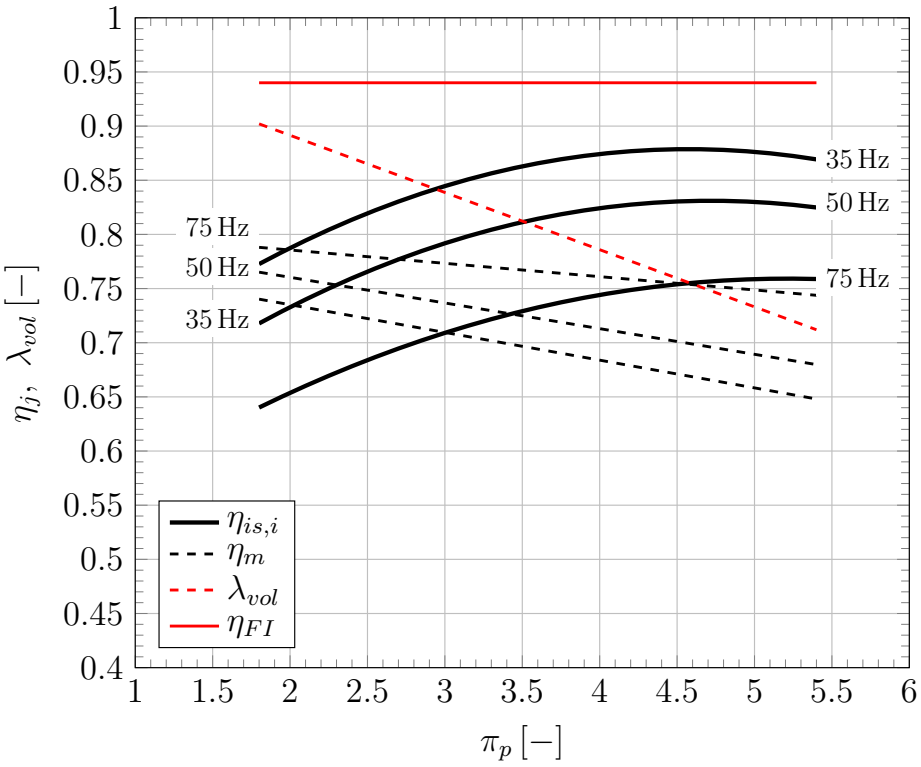

Figure 6.6: Efficiency characteristics as a function of the pressure ratio and the compressor speed utilized in the simulation model

Table 6.4: Utilized coefficients for the compressor characteristics

Efficiency	$\eta_{is,i}$			η_m			η_{FI}	λ_{vol}
Frequency	35 Hz	50 Hz	75 Hz	35 Hz	50 Hz	75 Hz	n.a.	n.a.
Coefficient	[-]	[-]	[-]	[-]	[-]	[-]	[-]	[-]
a_0	0.5902	0.535	0.4817	0.7863	0.8078	0.8102	0.94	0.9971
a_1	0.1262	0.1255	0.1064	-0.0256	-0.0237	-0.0123	0	-0.0528
a_2	-0.0138	-0.0133	-0.0102		0		0	0

The obtained efficiency characteristics combined with Equations 3.50 define the refrigerant massflow and the entire compressor electrical consumption in the heat pump simulation model. The complex geometry and heat transfer processes of the compressor heat exchanger have been simplified in order to increase the applicability of the simulation model. A more detailed approach has been presented in Moisi and Rieberer (2016) where a thermal network model of the compressor drive stator and the CHX has been developed. However significant boundary conditions such as temperature of the separating hood had to be assumed (see also Chapter 4). Furthermore the limits of the EES simulation software had been reached in terms of number of processable equations and variables. The simplified approach for

the cycle models uses again experimentally derived polynomial characteristics in order to describe the compressor motor waste heat recovered by the CHX ($\dot{Q}_{CHX}$). The compressor motor waste heat is clearly dependent on the compressor power. Therefore the ratio between the compressor power and $\dot{Q}_{CHX}$ shall be the starting point for the selected model equation. The experimental results for this ratio $r_{q,CHX}$ given in Figure 5.14, Section 5.4.3 shows the nearly exponential decrease with increasing refrigerant massflow. A further analysis has shown, that the internal compressor power $P_{comp,i}$ (see Equation 3.43) is even more suitable to form this ratio since scattering of the experimental results is reduced. The final model equation follows an exponential characteristic again obtained by regression methods from experimental data. Hence $r_{q,CHX}$ is described by Equation 6.24 as follows.

$$r_{q,CHX} = \frac{\dot{Q}_{CHX}}{P_{comp,i}} = 0.0662 \cdot \dot{m}_{ref}^{-0,457} \tag{6.24}$$

The entire pressure drop of the CHX ($[\Delta p_{m,CHX}]$ = kPa) has been estimated based on Equation 6.11 using a friction factor ξ_{CHX} estimated by experimental pressure results of state 9 and state 1 (see e.g. Section 5). The pressure drop of the CHX can then described by Equation 6.25. The density $\rho_{m,CHX}$ has been calculated with the mean pressure and temperature.

$$\Delta p_{m,CHX} = \xi_{CHX} \cdot KEV_{CHX} = 0.07456 \cdot \frac{G_{ref,m,CHX}^2}{2 \cdot \rho_{m,CHX}} \tag{6.25}$$

The corresponding characteristics of proportional factor for the recovered motor waste heat and the resulting pressure drop with the experimental basis are depicted in Figure 6.7. The model equation for $r_{q,CHX}$ remains valid within a range refrigerant massflow range of 0.28 to 0.128 kg/s. The pressure drop of the CHX as already described above follows a nearly linear characteristic.

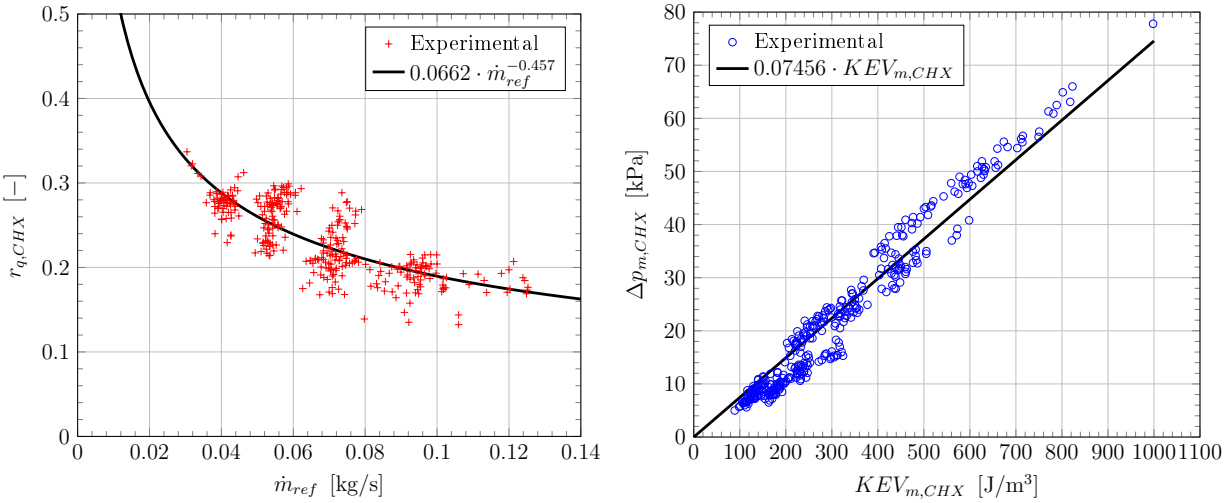

Figure 6.7: Characteristic for the ratio of internal compressor power and recovered waste heat as a function of the refrigernat massflow (left) and pressure drop characteristic as a function of KEV (right) in comparison to the experimentally obtained data.

The obtained characteristics for the compressor efficiencies and the CHX form a semi empirical approach valid within the given parameter ranges in combination with the heat transfer correlations of the heat exchangers and the property functions of different refrigerant states (see Chapter 3 and 5).

6.4 Model Validation

The developed semi empirical model has been validated against the presented experimental data of Chapter 5 based on the Basic and the IHX cycle. The Superheater cycle has been neglected since it states only a minor alteration of the Basic cycle. The measured source and sink inlet and outlet temperatures, the evaporator superheat controlled by the EXV and the compressor frequency have been applied as inputs to the simulation model in order to validate performance indicators such as heating capacity ($\dot{Q}_{w,H}$),evaporator capacity ($\dot{Q}_{w,source}$), electrical compressor consumption ($P_{el,comp}$) and efficiency ($COP_{w,H}$) as well as defining parameters such as condensation and evaporation temperatures ($t_{cond} = t''_{ref,3}$ and $t_{evap} = t''_{ref,7}$, see Section 6.1), refrigerant massflow ($\dot{m}_{ref}$) and pressure ratio ($\pi_p = p_{ref,2}/p_{ref,1}$). The comparison of experimental and simulation results regarding the cycle defining parameters are summarized in Figure 6.8. The simulation model underestimates the condensation temperature (see Figure 6.8b) within a range of -2 and 0 K as a results of overestimated heat transfer coefficients for the condensing and desuperheating section in addition to an underestimated pressure drop of the condenser (see Section 6.2.2). The evaporation temperature (see Figure 6.8b) is also generally underestimated in a range between -2 and 0 K by the simulation approach as a result of the mainly underestimated heat transfer coefficient in the evaporation section of the heat exchanger (see Section 6.2.2). The refrigerant massflow as a function of the suction gas density and thus the evaporation temperature is correspondingly predicted lower in a range of -5 to 0 % by the simulation model (see Figure 6.8c). The pressure ratio is tendentiously overpredicted up to 5 % for the Basic cycle (blue) within the entire investigated range. For the IHX cycle (red), the relative deviation of the pressure ratio can be found within a range of -5 and 5 %.

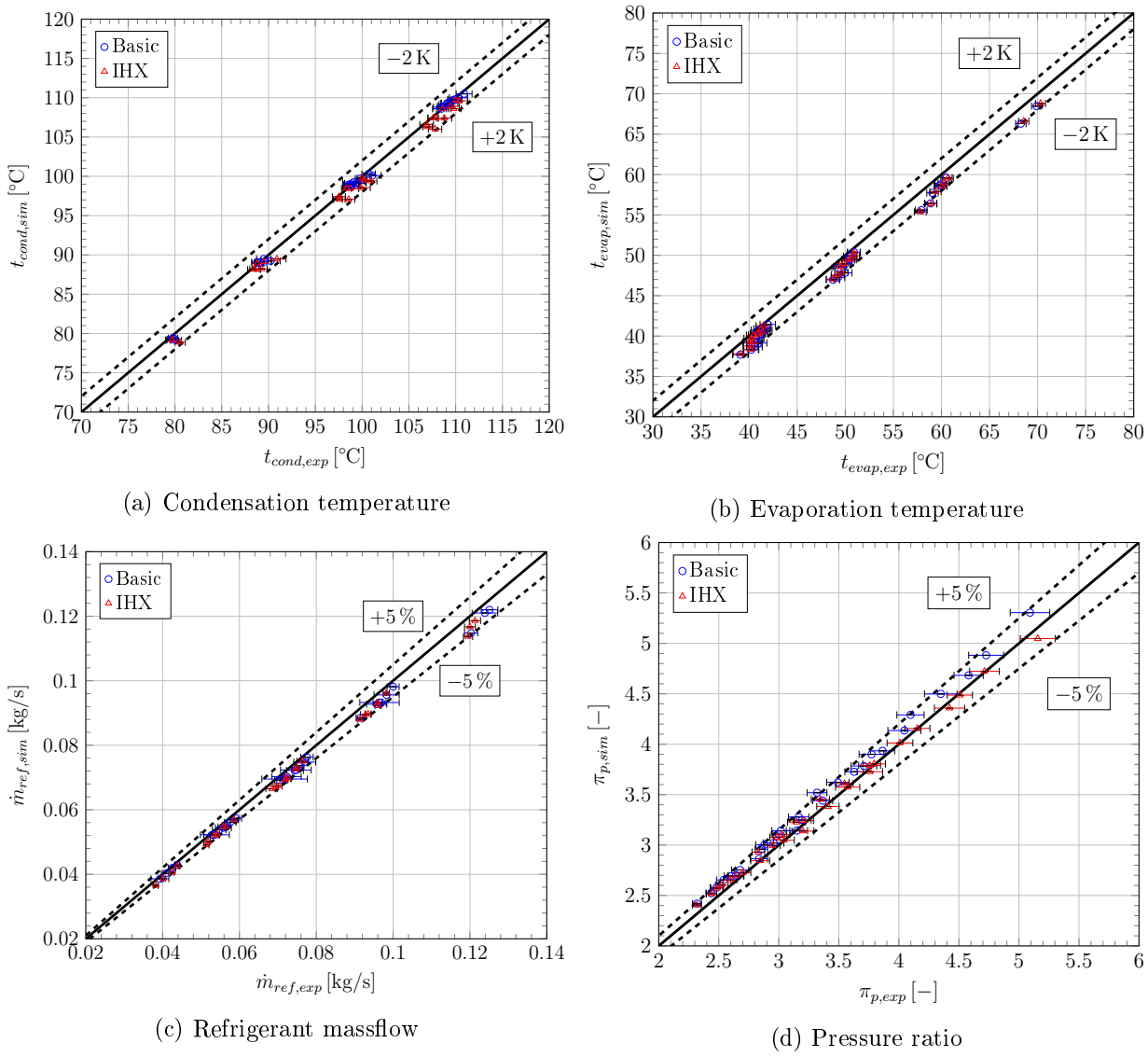

(a) Condensation temperature

(b) Evaporation temperature

(c) Refrigerant massflow

(d) Pressure ratio

Figure 6.8: Model validation regarding cycle defining parameters condensation and evaporation temperature, refrigerant massflow and pressure ratio for the Basic and IHX cycle

The comparison of experimental and simulation results regarding performance indicators are summarized in Figure 6.9. The simulated heating capacity (see Figure 6.9a) deviates within a range of −5 to 0 % from the experimental data which is the consequence of a underestimated massflow (see Figure 6.8). In addition to the refrigerant massflow, the evaporation temperature has also an influence on the evaporator capacity (decreasing enthalpy difference) and therefore predicting the simulation results lower than experimentally obtained values within a range of ±10 % (see Figure 6.9b). The electrical compressor consumption (Figure 6.9c) is overestimated by the simulation model within a range of approx. 0 and 10 %. The main reason can be found in the simplified efficiency approach utilized in the simulation model (see Section 6.3) in combination with the overestimated pressure ratio (see Figure 6.8d). A closer look on the overall isentropic efficiency validation revealed an underestimation of the simulated values compared to experimental results within a range of 0 and −10 % (see Appendix A.6) which contributes to the deviation of the compressor consumption in Figure 6.9c. Finally the simulated heat pump efficiency for the Basic and IHX cycle deviates in a range of approx. −10 to 0 % as a result of the discussed lower predicted heating capacity and the overestimated compressor consumption.

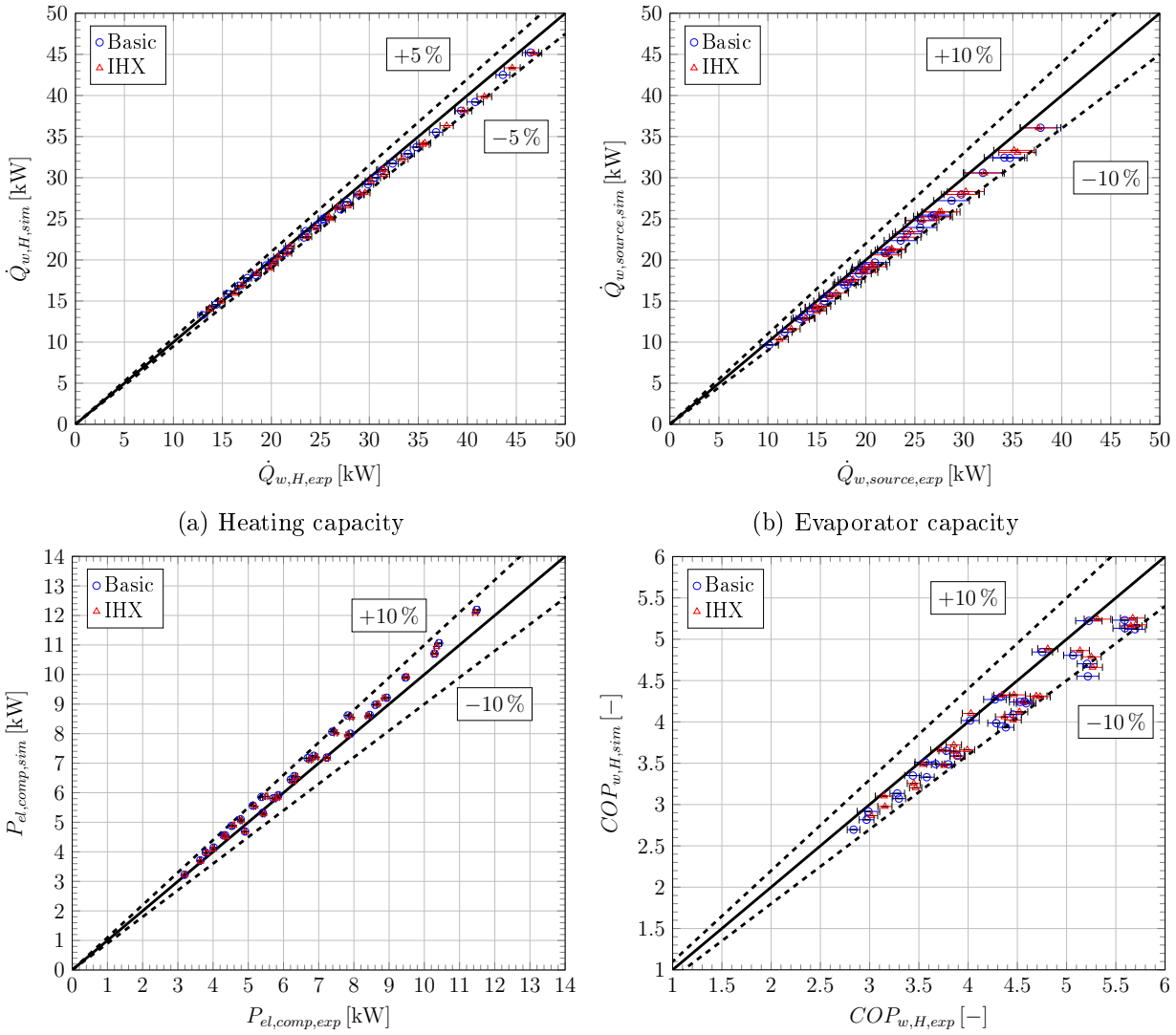

(a) Heating capacity

(b) Evaporator capacity

(c) Compressor consumption

(d) Coefficient of performance

Figure 6.9: Model validation regarding performance indicators heating capacity, evaporator capacity, compressor consumption and efficiency for the Basic and IHX cycle

In conclusion, the utilized semi empirical simulation approach delivers quick steady state results suitable for parameter studies. The heat transfer has been modeled according to classic text book approaches using overall heat transfer coefficients based on correlations found in open literature. As a result the condensation and evaporation temperature has been predicted within 2 K. Performance indicators deviate in a range of ±10 %. However, based on the above discussed model validation data, the utilized simulation approach has been found to be in fair agreement with experiment providing the possibility to make reliable statements based on obtained simulation results.

6.5 Comparison of Parallel- and Counter Flow IHX

The investigated heat temperature heat pump is equipped with a parallel flow internal heat exchanger. Generally, a counter flow arrangement exhibits a higher effectiveness (see Chapter 3 and e.g. Bergman et al., 2011) compared to the parallel flow as a result of more favourable temperature characteristics. Therefore the potential of the counter flow arrangement with the given internal heat exchanger has been analysed by means of simulation, based on the validation input data already used in the previous chapter. Figure 6.10 shows the comparison

between counter and parallel flow of effectiveness ($\varepsilon_{IHX,j}$), IHX capacity ($\dot{Q}_{IHX,j}$), heat pump heating capacity ($\dot{Q}_{w,H,j}$) and finally the COP. As stated above the effectiveness (Figure 6.10a) of the counter flow IHX increases by up to 14 % resulting in an increase of IHX capacity of approx. 10 % (Figure 6.10b). The improvement of the IHX although has no significant effect on the heating capacity and thus on the COP of the heat pump cycle. The absolute improvement for the heating capacity can be found in the second and for the COP in the third digit after the decimal point.

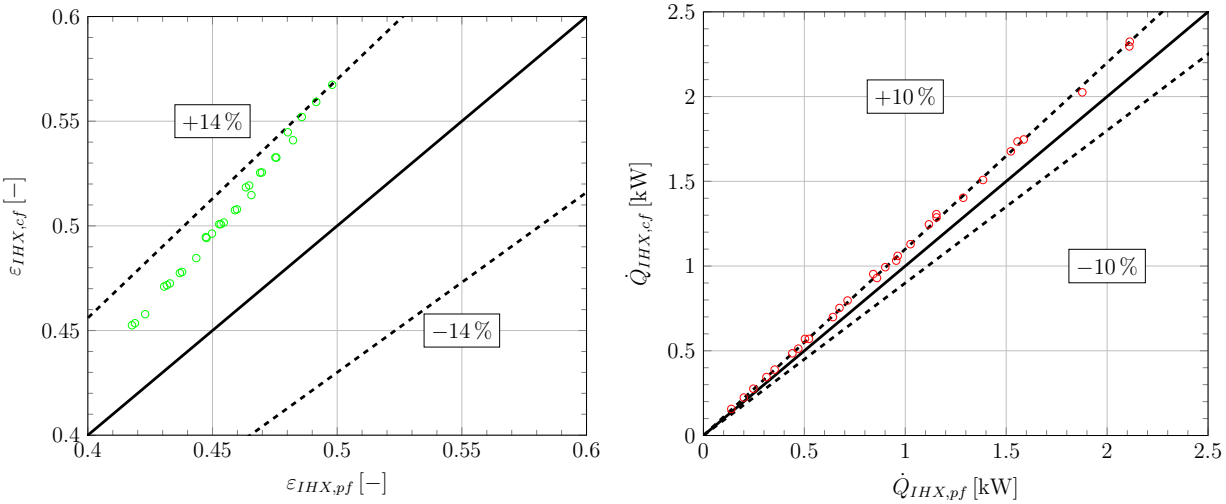

(a) IHX effectiveness

(b) IHX capacity

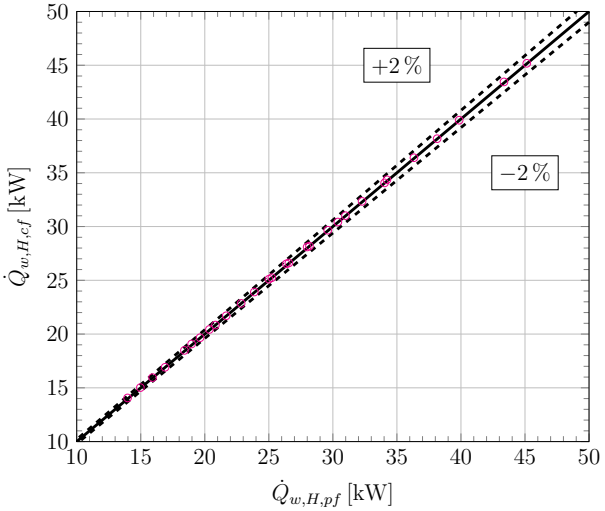

(c) Heating capacity

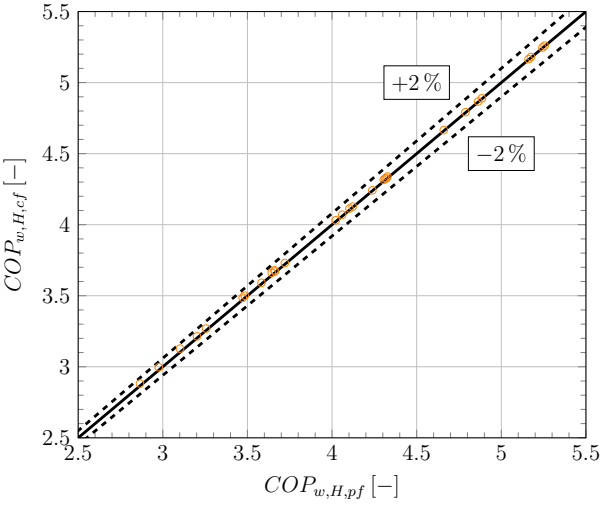

(d) Coefficient of performance

Figure 6.10: Comparison between counter and parallel flow arrangement in terms of simulated, IHX effectiveness, IHX capacity, heating capacity and COP

The rather limited influence can also be observed in the comparison of the resulting cycle states depicted in Figure 6.11 for a compressor frequency of 35 Hz (left) and 75 Hz (right). For the counter flow arrangement the superheat in state 9 increases approx. by 2 K for both compressor frequencies. The compressor outlet temperature in state 2 increases for the counter flow arrangement similarly with approx. 2 K for both compressor frequencies.

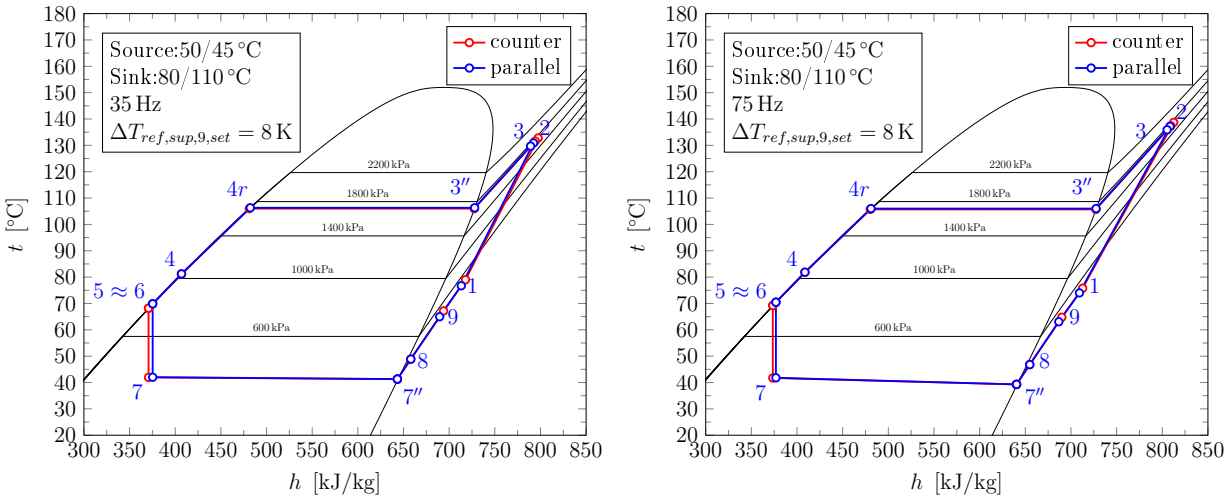

Figure 6.11: Comparison between counter and parallel flow arrangment in terms of cycle states depicted in a t/h diagram for 35 Hz and 75 Hz with a source temperature level of 50/45 °C and a sink temperature level of 80/110 °C

The presented simulation results have shown that the IHX capacity can be improved by changing to a counter flow arrangement. However the overall effect on heating capacity and COP is insignificant. Depending on the compressor lubricant, an increased compressor outlet temperature might not even be desired. Nevertheless in terms of effectiveness, the counter flow arrangement stands clearly above the parallel flow in nearly any heat exchanger application. Hence counter flow heat exchanger are most commonly utilized for heat exchanging purposes and shall therefore be applied for the simulation studies in the following sections.

6.6 Influence of Heat Sink and Source Temperature Difference

The temperature characteristics of the heat source and sink are strongly influencing the cycle efficiency and heating capacity of the investigated high temperature heat pump and heat pumps in general. In process industry different fluid streams based on varying media such as air, water or steam are utilized resulting in different temperature characteristics in the condenser and evaporator depending on the heat capacity rate of the respective fluid stream in combination with the product of heat transfer coefficient and heat transfer area of the heat exchanger ($\dot{C}$ and $U \cdot A_{hx}$ respectively, see Chapter 3). Therefore different source and sink temperature differences have been investigated with the developed simulation model in order to investigate the effects on the heat pump cycle. The parameters have been varied according to Table 6.1. The $t/\dot{Q}$ diagram for the condenser depicted in Figure 6.12 for the Basic cycle shows clearly the influence of the sink side temperature difference on the heating capacity for a given compressor speed (in this case50 Hz) and a given supply temperature of for example 110 °C. The source inlet temperature has been selected to 50 °C with a source temperature difference of 5 K. The evaporator superheat has been chosen to 8 K. For the Basic cycle depicted in Figure 6.12 left, two effects can be observed regarding changing sink temperature differences. The first aspect is clearly the increased usable enthalpy difference across the condenser and subcooler for increasing sink temperature differences, i.e. lower sink inlet temperatures. Hence, for a given refrigerant massflow (constant evaporation temperature and compressor speed), pressure ratio (nearly constant compressor consumption) and supply temperature, the heating capacity increases with increasing sink side temperature difference as depicted in Figure 6.12. Depending on the heat exchanger design and thus

heat transfer, the refrigerant temperature at the outlet of the condenser is limited by the sink inlet temperature. In the investigated case the heat transfer allows a very small pinch point temperature differences between refrigerant outlet and sink inlet within the condenser stating the optimum degree of subcooling as discussed e.g. by Pitarch et al. (2018) and presented in Chapter 3. The second aspect is the increasing condensation temperature (and thus pressure) as a result of an increased condensation section inlet temperature causing a lower driving temperature difference (see again Chapter 3). With an increasing sink side temperature difference the increased temperature difference across the condensation section allows a lower condensation temperature. Low sink side temperature differences for a given supply temperature therefore combine these two negative effects of a decreased usable enthalpy difference and an increased condensation temperature. The application of an internal heat exchanger can compensate the negative effects to a certain extend since the refrigerant side inlet temperature of the condenser and hence the enthalpy are increasing the heating capacity as depicted in Figure 6.12 on the right. The application of the IHX and the resulting increasing condenser refrigerant inlet temperature allows a lower condensation temperature compared to the Basic cycle since the driving temperature difference in the desuperheating section increases significantly which has been already observed experimentally and discussed in Section 5.8. With an increasing sink temperature difference, the positive effect of a rising driving temperature difference at the condensing section inlet on the sink side is enhanced by the increased refrigerant side temperature difference across the desuperheating section leading to a lower required condensing temperature for the IHX cycle. The condensation temperature of the Basic Cycle lies approximately 3 K above the IHX configuration for a sink side temperature difference of 30 K. Besides the positive effects of the IHX, a strong disadvantage given the significantly increased compressor outlet temperatures exists which are enhanced at low sink side temperature differences since the inlet temperature of IHX on the high pressure side is increased leading to an increased IHX capacity and thus higher compressor inlet temperatures (compare to Sections 3.2.4 and 5.6).

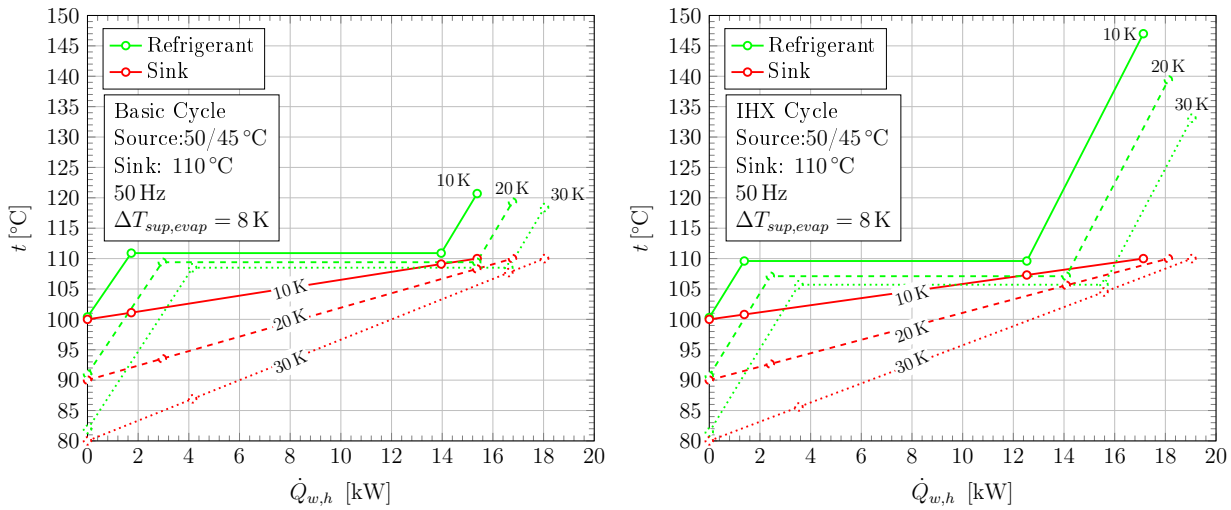

Figure 6.12: Simulated condenser $t/\dot{Q}$ diagram of the Basic and IHX Cycle for varying sink side temperature differences, a source temperature level of 50/45 °C, a compressor frequency of 50 Hz and an evaporator superheat of 8 K

The estimated compressor outlet temperatures (≈ condenser inlet) of up to 147 °C given in Figure 6.12 would not have allowed a safe operation of the investigated high temperature heat pump with the utilized compressor lubricant (see Chapter 4). As a consequence, different

compressor lubricants have to be investigated. The evaporator shows the expected behaviour of decreasing capacity for decreasing source side temperature differences and thus source side heat capacity rate as depicted in Figure 6.13 for the Basic (left) and IHX Cycle (right). The sink side temperature level has been assumed to 80/110 °C with a compressor speed of 50 Hz and a evaporator superheat of 8 K. Two effects are responsible for the decline of the evaporator capacity. The first aspect is the decreasing usable refrigerant enthalpy difference across the evaporator as a result of the constant inlet enthalpy limited by the sink inlet temperature and the decreasing evaporation temperature. The second effect is the decrease of suction gas density with decreasing evaporation pressure causing the refrigerant massflow and as a result, the evaporator and heating capacity of the heat pump to decline (see also Chapter 5). Furthermore the decreased evaporation pressure causes an increased pressure ratio and thus increased specific compressor work (see Chapters 3 and 5). Additionally, the pressure ratio also influences different compressor efficiencies as discussed in detail in Chapter 5.

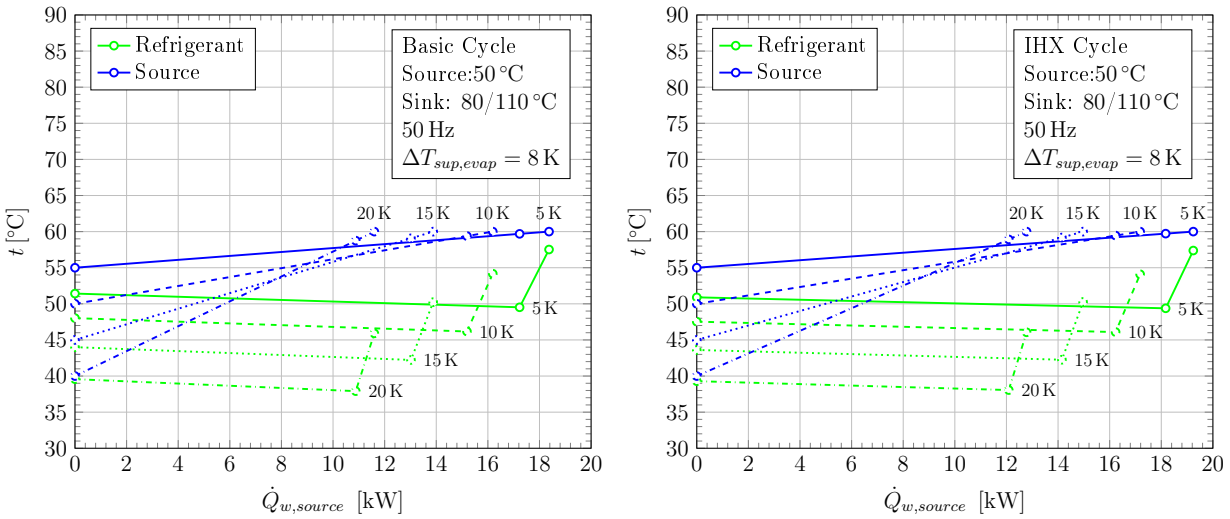

Figure 6.13: Simulated evaporator $t/\dot{Q}$ diagram of the Basic and IHX Cycle for varying source side temperature differences, a sink temperature level of 80/110 °C, a compressor frequency of 50 Hz and an evaporator superheat of 8 K

The influence of different sink side temperature differences (ΔT_{sink}) for the Basic Cycle, a given superheat ($\Delta T_{sup,evap} = 8$ K), source side temperature difference ($\Delta T_{source} = 5$ K) and compressor frequency ($f = 50$ Hz) on heat pump performance as a function of the source inlet temperature can be observed in Figure 6.14. The heat pump efficiency depicted in Figure 6.14a clearly displays the advantage of increased sink side temperature difference. For example the relative improvement between a source temperature difference of 10 and 30 K for a source temperature level of 50/45 °C and a desired supply temperature of 110 °C results approx. to 20 %. In terms of COP, an increase in sink side temperature difference by 20 K is nearly equivalent to a decrease of supply temperature by 10 K throughout the field of operation. The COP improvement is a result of the increased heating capacity, showing a relative improvement for the above discussed operation point of approx. 17 %. Regarding the heating capacity an increase of sink side temperature difference by 10 K can be considered equivalent to a decrease in supply temperature of 10 K for the given boundary conditions. The compressor consumption (see Figure 6.14c) is not as strongly affected as the heating capacity since the evaporation temperature is mainly left unaltered by the changing evap-

orator inlet enthalpy caused by different sink side temperature differences. The required compressor power clearly increases with increasing source temperature level however flattens with decreasing pressure ratio since suction gas density and compressor work follow opposing trends (see also Chapters 3 and 5). A slight decrease in compressor consumption however can be observed for higher sink side temperature differences as a consequence of the decreasing condensation temperature depicted in Figure 6.14d caused by the increased condensing section entry temperature (i.e subcooler outlet) difference as discussed above (see Figure 6.12). The condensation temperature generally increases slightly with increasing source temperature level due to the increase of heating capacity transferred across the given heat exchanger area (see also Chapter 5).

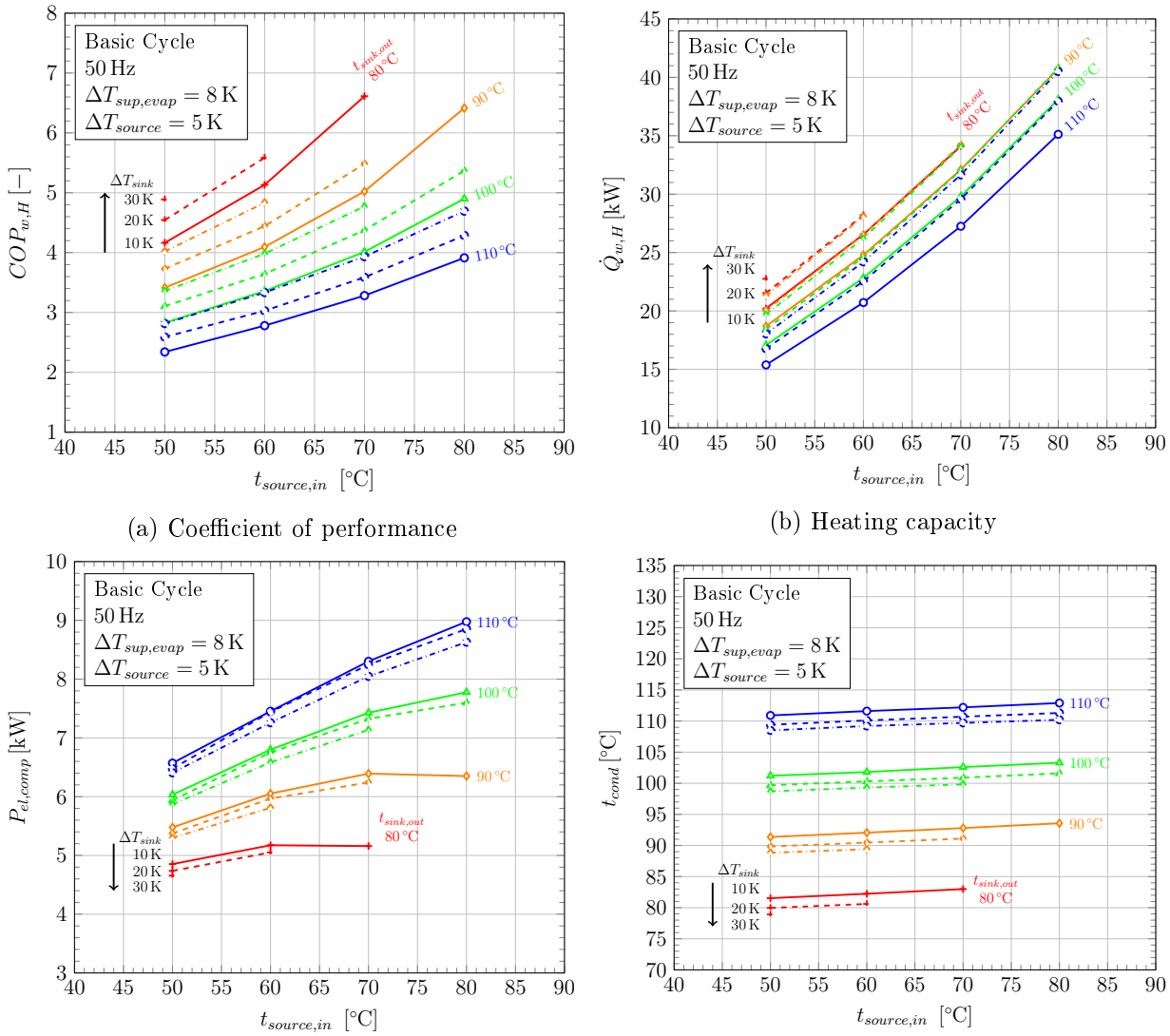

(a) Coefficient of performance

(b) Heating capacity

(c) Compressor consumption

(d) Condensation temperature

Figure 6.14: Selected simulated results of the Basic Cycle as a function of the source side inlet temperature given for a compressor frequency of 50 Hz, a source side temperature difference of 5 K and an evaporator superheat of 8 K, with the supply temperature and sink side temperature difference as parameters

The effect of a changing source side temperature difference on the evaporation temperature has been outlined above (see Figure 6.13and Chapter 5) and is strongly dependent on the superheat set point. Exemplary for the influence of the source side temperature difference,

Figure 6.15 displays the dependency of the efficiency ($COP_{w,H}$), heating capacity ($\dot{Q}_{w,H}$), compressor consumption ($P_{el,comp}$) and evaporator capacity for the Basic Cycle on the source side temperature difference (ΔT_{source}) for a source inlet temperature of 50 °C, a compressor frequency of 50 Hz, changing supply temperatures ($t_{sink,out}$) and sink side temperature differences (ΔT_{sink}). The evaporator superheat has been selected to 8 K. The evaporation temperature clearly drops with increasing source side temperature difference (depending on the evaporator superheat set point, see Section 6.7) resulting in a nearly linear decreasing cycle efficiency as depicted in Figure 6.15a for the investigated sink temperatures. The positive effect of a high sink temperature difference on COP can again be observed. The decreasing suction gas density causes the heating capacity to decrease for a given compressor frequency as given in Figure 6.15b.

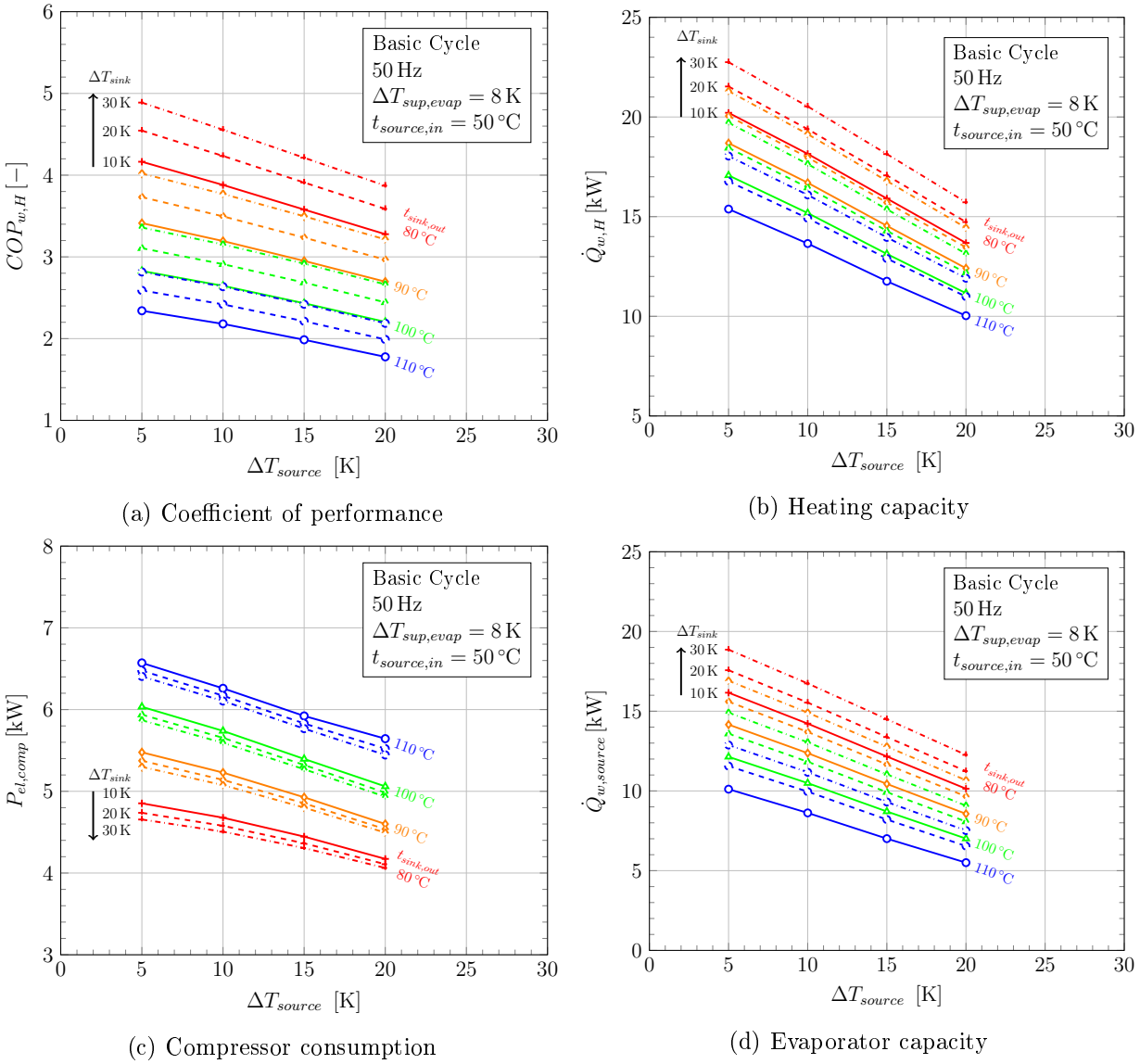

(a) Coefficient of performance

(b) Heating capacity

(c) Compressor consumption

(d) Evaporator capacity

Figure 6.15: Selected simulation results of the Basic Cycle as a function of the source side temperature difference given for a compressor frequency of 50 Hz, a source inlet temperature of 50 °C and a evaporator superheat of 8 K, with the supply temperature and sink side temperature difference as parameters

For a supply temperature of 110 °C and a sink temperature difference of 10 K the relative reduction of the heating capacity results to approx. −33 % for source temperature differences

between 5 and 20 K. The compressor consumption shows a declining behaviour since the decrease of suction gas density is more dominant than the increase in specific compressor work (see Figure 6.15c).Furthermore the volumetric efficiency decreases with increasing pressure ratio further decreasing the refrigerant massflow. The evaporator capacity depicted in Figure 6.15d of course follows the same trend, decreasing with increased source side temperature difference. Similar to the heating capacity, an increased sink side temperature difference increases the usable enthalpy difference across the evaporator thus increasing the evaporator capacity. The relative change in evaporator capacity for a sink temperature of 110 °C and a sink temperature difference of 10 K within a source temperature difference of 5 and 20 K results to approx. −50 % with a nearly constant gradient across the investigated operation points. The IHX cycle shows basically identical characteristics in terms of source and sink side temperature differences as described above. However experimental results presented in Section 5.6 and the simulation results depicted in Figure 6.12 indicate an improvement in terms of efficiency and heating capacity compared to the basic cycle. The results for the Basic and IHX cycle considering efficiency and heating capacity as a function of evaporator superheat, source and sink temperature differences are briefly discussed in the following section.

6.7 Influence of Evaporator Superheat

The obtained experimental results regarding the variation of the evaporator superheat set point has shown an impact on heat pump performance indicators (e.g. COP) in dependence on source side temperature differences. Figure 6.16 summarizes the simulation results regarding COP as a function of the evaporator superheat and the source side temperature differences for the Basic and the IHX cycle. The compressor frequency has been selected to 50 Hz with a sink side temperature difference of 30 K. As outlined in Chapter 5, the coefficient of performance increases with decreasing evaporator superheat and source side temperature difference. Low superheat in combination with a low source side temperature difference provides the maximum COP for a given compressor speed, source inlet temperature and sink temperature level. However as explained in detail in Section 5.7, the gradient of the COP characteristics decreases nearly to a plateau with a weak maximum indicated by a circle in Figure 6.16. These maximum values however are in many cases only determined by the third digit after the decimal point. Furthermore the resolution of 1 K in superheat might not provide the actual maximum which can be located in between. Nevertheless the results can give an indication of the dependency of COP maximum and superheat set point which will be further discussed in connection with Figure 6.19. As an example for the Basic cycle and a source inlet temperature of 50 °C (see Figure 6.16a), the COP characteristic is qualitatively in good agreement with experimental results discussed in Section 5.7. The COP clearly decreases with increasing source side temperature difference and increasing supply temperature. Generally, the weak COP maximum shifts to higher superheat setpoints with increasing source side temperature difference however remains constant for increasing sink outlet temperatures, in particular for a source inlet temperature of 50 °C. For increasing source inlet temperatures the evaporator superheat at COP maximum remains also nearly constant. A deviation by 1 K might be a consequence of the resolution as described above. The IHX cycle shows basically the same characteristics, the COP maxima however, are shifted generally to lower superheat setpoints compared to the Basic cycle and remain again within a distance of approx. 1 K for changing heat sink outlet temperatures. The heating capacity is affected by the driving temperature difference between high pressure and low pressure side of the internal heat exchanger.

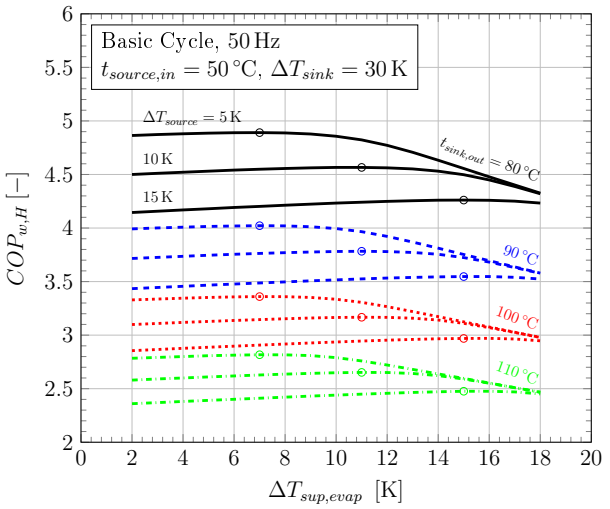

(a) Basic, $t_{source,in} = 50\,°C$

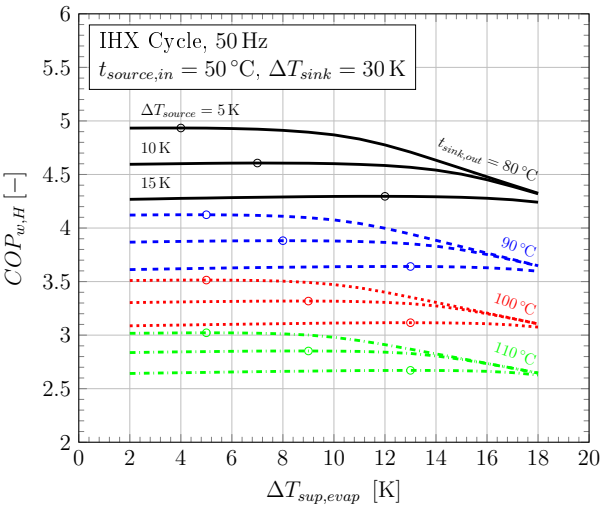

(b) IHX, $t_{source,in} = 50\,°C$

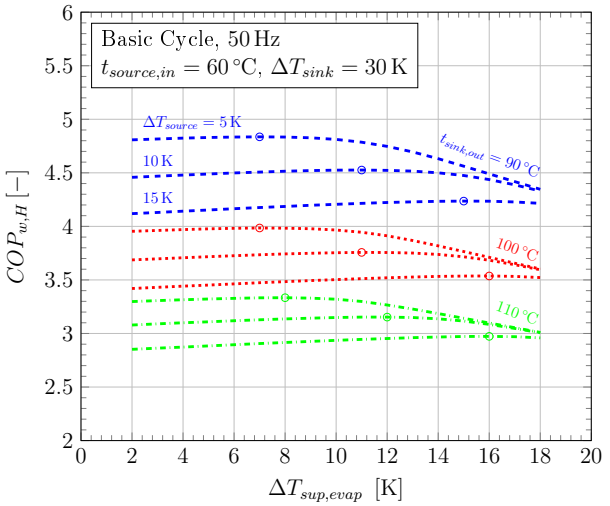

(c) Basic, $t_{source,in} = 60\,°C$

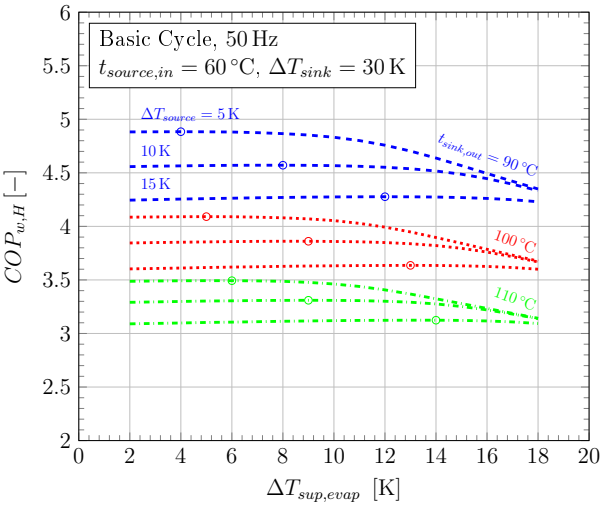

(d) IHX, $t_{source,in} = 60\,°C$

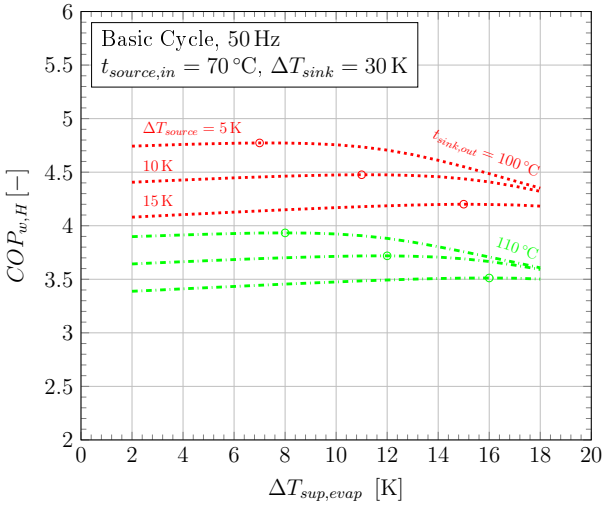

(e) Basic, $t_{source,in} = 70\,°C$

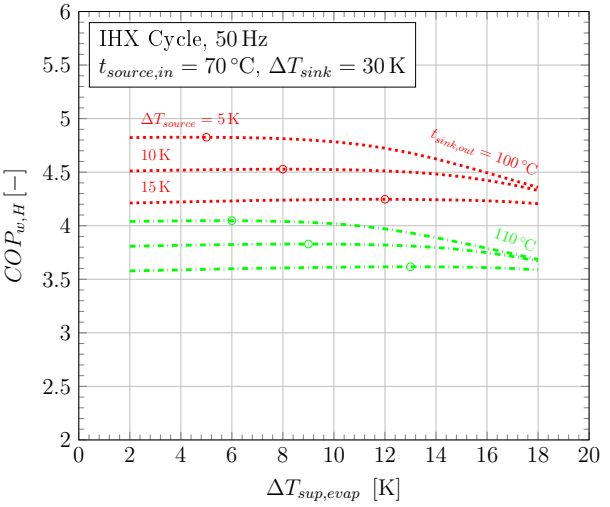

(f) IHX, $t_{source,in} = 70\,°C$

Figure 6.16: Efficiency simulation results of the Basic and IHX Cycle as a function of the evaporator superheat given for a compressor frequency of 50 Hz, a sink temperature difference of 30 K and varying source temperatures with the supply temperature and source side temperature difference as parameters

With a decreasing evaporator superheat and declining evaporation temperature caused by an increased source side temperature difference, the entry temperature of the IHX decreases. Hence the aforementioned driving temperature difference between high and low pressure side increases. With rising supply temperature this effect becomes stronger, increasing the COP compared to the Basic cycle by an approximate absolute value of 0.1 to 0.2 (compare Figures 6.16a to 6.16f). The temperature characteristics of the evaporator in the IHX cycle compared to the Basic configuration remains unaltered by different entry enthalpies of the evaporator for the same operation point as indicated in Figure 6.13 in the previous section. The COP characteristic for different superheat set points and source side temperature differences is a consequence of a changing evaporation temperature as outlined in Chapter 5. The decrease of COP below the maximum is a consequence of still slightly increasing compressor consumption due to an increasing refrigerant massflow (see Section 5.7) in combination with a slightly declining heating capacity. The heating capacity depicted in Figure 6.17 for a compressor frequency of 50 Hz and varying source inlet and sink outlet temperatures shows identical tendencies as the heat pump efficiency. With decreasing superheat the evaporation temperature rises and thus refrigerant massflow and heating capacity until the pinch point temperature difference transfers from the source inlet to the source outlet (see also Chapter 3 and Chapter 5). In this transition point the source inlet and outlet pinch point temperature differences are identical ($\Delta T_{pp,source,in} = \Delta T_{pp,source,out}$, see Figure 5.32a) at a certain superheat value ($\Delta T_{sup,evap,trans}$). It can be observed that the heating capacity optimum is again very weak with similar restrictions due to resolution as described above. However the optimum cannot be found at identical superheat values compared to the cycle efficiency but shifted to lower superheat set points for both cycle configurations. In the Basic cycle case, the optimum superheat values remain nearly constant (within ± 1 K) for increasing source side temperatures. In the IHX case the optimum shift to lower superheat values is superimposed by the IHX effect as described above. Taking a closer look on Figure 6.17 the improvement of the IHX can be observed in absolute values of the heating capacity increasing with rising heat sink supply temperatures at constant source inlet temperatures. The deviation ranges around 1 kW.

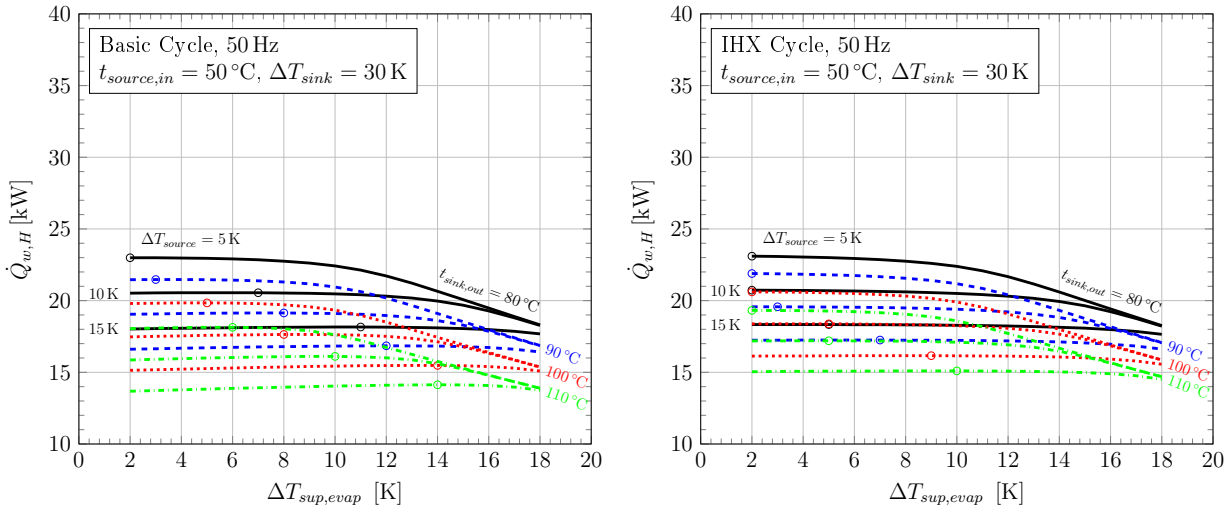

(a) Basic, $t_{source,in} = 50\,°C$

(b) IHX, $t_{source,in} = 50\,°C$

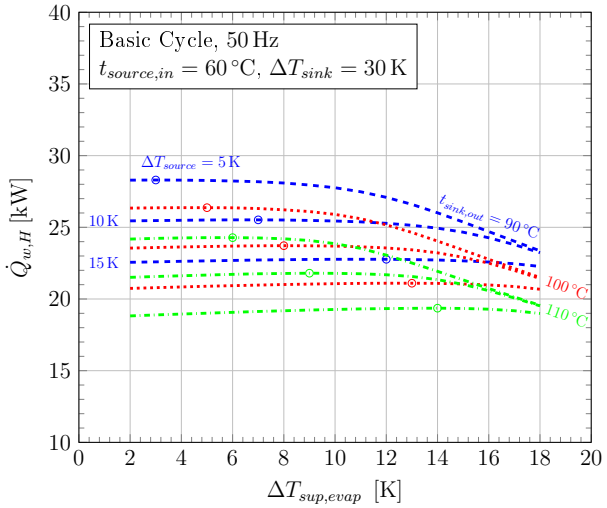

(c) Basic, $t_{source,in} = 60\,°C$

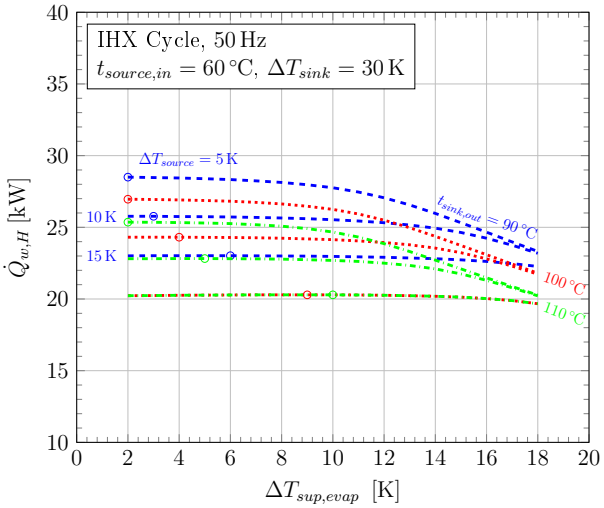

(d) IHX, $t_{source,in} = 60\,°C$

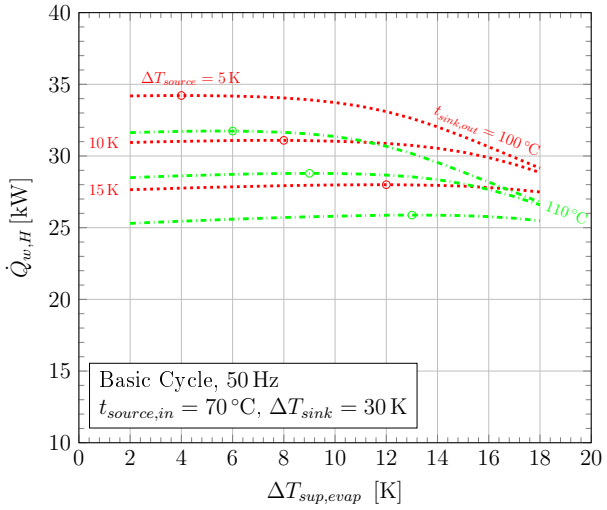

(e) Basic, $t_{source,in} = 70\,°C$

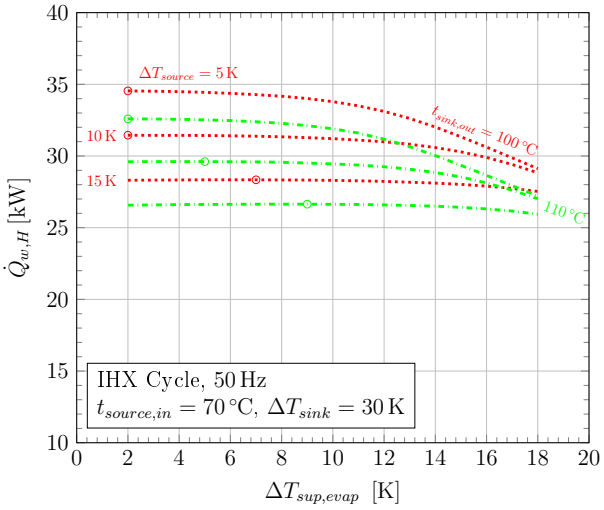

(f) IHX, $t_{source,in} = 70\,°C$

Figure 6.17: Heating capacity simulation results of the Basic and IHX Cycle as a function of the evaporator superheat given for a compressor frequency of 50 Hz, a sink temperature difference of 30 K and varying source temperatures with the supply temperature and source side temperature difference as parameters

The COP and the heating capacity curve flattens significantly with increasing source temperature difference indicating a connection between degree of superheat at the pinch point transition and source side temperature difference. Furthermore, based on the investigations of Pitarch et al. (2018) on efficiency optimum subcooling, there can be a superheat optimum following similar criteria (compare to Chapter 3). The temperature differences in the evaporator are following the relation given in Equation 6.26 and are depicted in Figure 6.19.

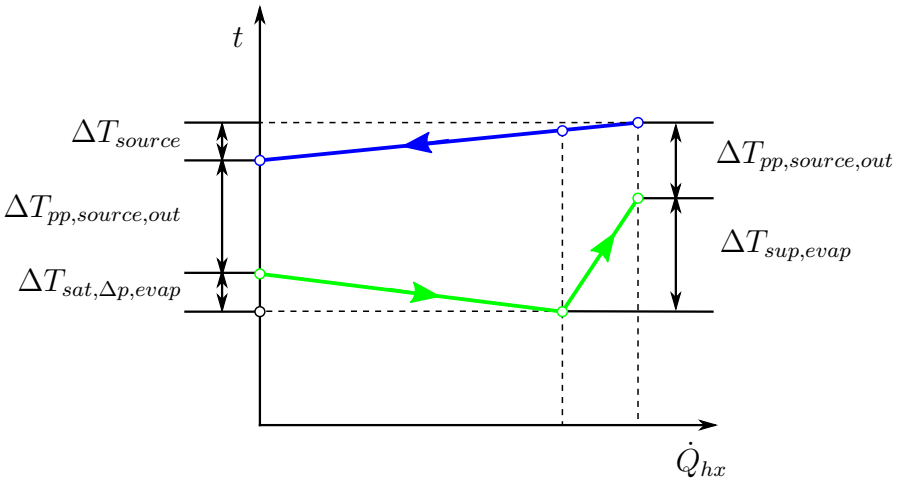

Figure 6.18: Temperature differences in the evaporator

The evaporator superheat can be calculated considering the source side temperature difference (ΔT_{source}), the pinch point temperature difference at source outlet ($\Delta T_{pp,source,out}$), the saturation temperature decrease induced by pressure drops and the pinch point temperature difference at the source inlet ($\Delta T_{pp,source,in}$)

$$\Delta T_{sup,evap} = \Delta T_{source} + \Delta T_{pp,source,out} + \Delta T_{sat,\Delta p} - \Delta T_{pp,source,in} \tag{6.26}$$

At the pinch point transition, $\Delta T_{pp,source,out}$ and $\Delta T_{pp,source,in}$ are assumed to be identical (see e.g. Pitarch et al., 2017a) thus simplfying Equation 6.26 to describe the evaporator superheat at this transition point ($\Delta T_{sup,evap,trans}$). The source side temperature difference however, shall remain constant.

$$\Delta T_{sup,evap,trans} = \Delta T_{source} + \Delta T_{sat,\Delta p,trans} \tag{6.27}$$

Pitarch et al. (2017a) and Pitarch et al. (2018) state that the optimum degree of subcooling in terms of heat pump COP for a certain operation point (i.e. sink side temperature difference) can be be found when identical pinch point temperature differences occur in the condenser. Figure 6.19a compares the approximate superheat set point where and COP optimum has been found ($\Delta T_{sup,evap,COP,opt}$)to the evaporator superheat at the transition point ($\Delta T_{sup,evap,trans}$) for the Basic cycle in the investigated field of operation. The absolute deviation between both values are remaining within $\pm 1\,\mathrm{K}$ which strongly indicates that an efficiency optimum can be reached at the a superheat value corresponding to the transition point. Considering Equation 6.27 and the results discussed above, the transition point shifts to higher values with increasing source side temperature difference. Furthermore the effect of compressor speed and thus refrigerant massflow shifts the transition point further to higher values since pressure drops increase and thus $\Delta T_{sat,\Delta p,trans}$. The correspondence between the pinch point transition point and a COP optimum however, can not be found for the IHX cycle since the refrigerant temperature a the evaporator outlet has an influence on the effect

of the IHX and thus on heating capacity. As briefly discussed above, while the transition point nearly remains identical to the Basic cycle results since temperature characteristics do not change for each investigated operation point, the approximate COP optimum shifts to lower superheat values as depicted in Figure 6.19b. Depending on compressor speed (saturation pressure drop) and source side temperature difference, the deviation between superheat at COP maximum and transition point ranges between −1 and −5 K. The approximate maximum heating capacity in terms of evaporator superheat can be found at significantly lower superheat values compared to the transition point as depicted in Figure 6.19c for the Basic cycle and Figure 6.19d for the IHX cycle.

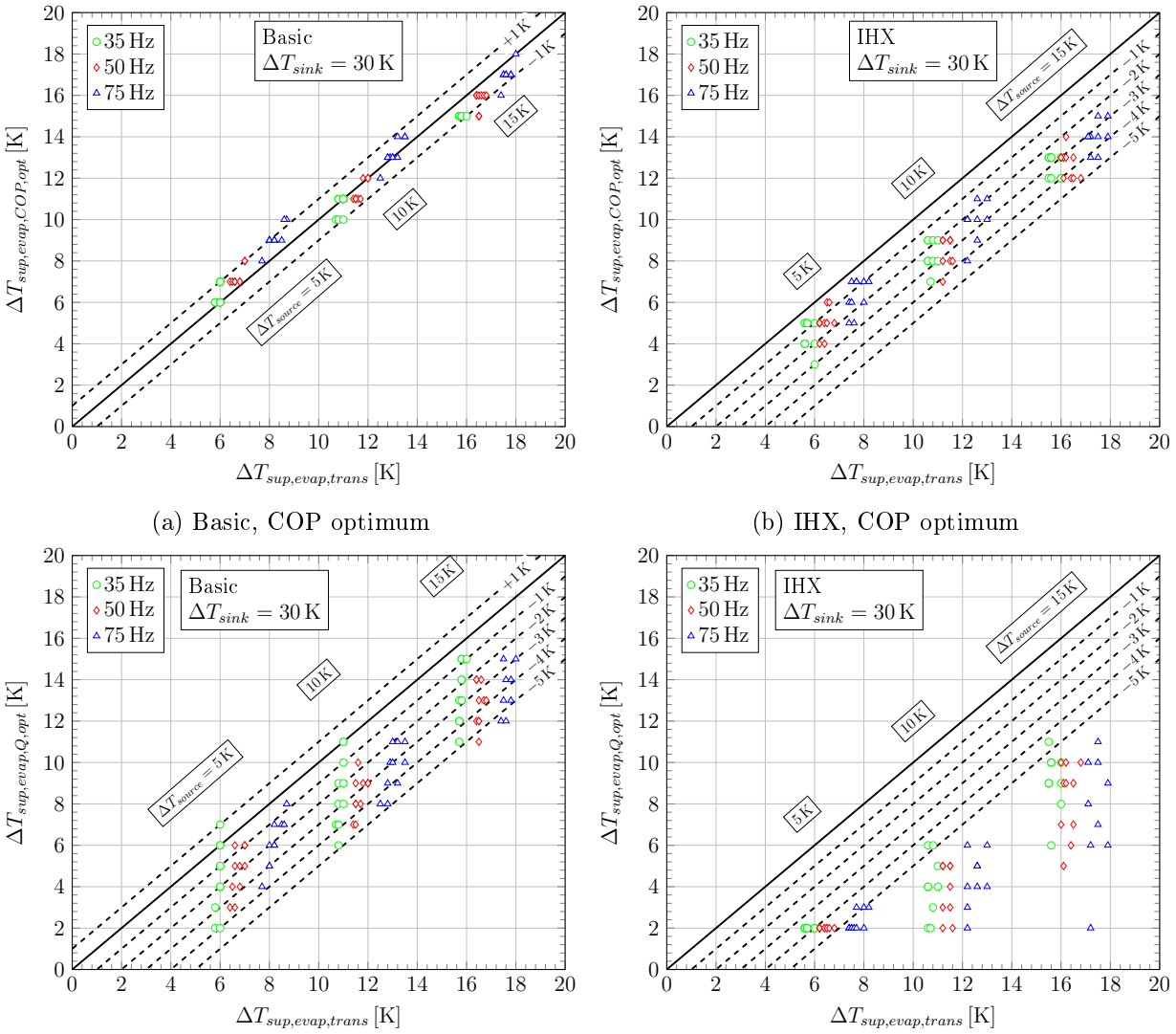

(a) Basic, COP optimum

(b) IHX, COP optimum

(c) Basic, heating capacity maximum

(d) IHX, heating capacity maximum

Figure 6.19: Comparison of evaporator superheat at COP optimum and heating capacity maximum ($\Delta T_{sup,evap,COP,opt}$ and $\Delta T_{sup,evap,Q,opt}$ respectively) to the respective superheat at the pinch point transition point ($\Delta T_{sup,evap,trans}$) for the Basic and the IHX cycle in the investigated field of operation

Furthermore it has been observed that with increasing supply temperature and thus increasing condensation temperature, the deviation decreases. However, similar to the efficiency results, the maxima are only determined by the second digit after the decimal point and might be even included in round off errors. Nevertheless, the comparison between the COP and heating capacity characteristics show clearly that at a certain superheat threshold exists,

below that, no significant improvement of cycle efficiency and heating capacity occurs. Based on the results presented in Figure 6.19a for an optimum COP and the insignificant improvement of heating capacity below the superheat at pinch point transition ($\Delta T_{sup,evap,trans}$) the optimum superheat set point ($\Delta T_{sup,evap,opt}$) can be approximately determined by Equation 6.28.

$$\Delta T_{sup,evap,opt} \approx \Delta T_{sup,evap,trans} = \Delta T_{source} + \Delta T_{sat,\Delta p,trans} \tag{6.28}$$

For practical use in heat pump design and operation, Equation 6.28 might be simplified to Equation 6.29 since pressure drops can be neglected.

$$\Delta T_{sup,evap,opt} \approx \Delta T_{source} \tag{6.29}$$

Consequently for heat sources which perform a phase change, for example a condensation of saturated vapor (see Chapter 7), the approximate optimum superheat heat set point would result to 0 according Equation 6.29 (if pressure drops and stability are not considered).

6.8 Optimizing Potential

Besides general aspects such as optimum heat sink and source temperature differences and superheat set points, further optimizing potential exist for the investigated heat pump prototype. Depending on the heat pump application in industrial waste heat recovery, thermal process might require a continuous heat supply at very distinct source and supply temperatures. Therefore it can be possible to match the requirements already in the design process in a way that no wide range capacity control becomes necessary which is provided by a frequency inverter . Therefore the FI can be omitted and hence it‘s losses avoided (see Chapter 5). The second optimizing aspect is the significant pressure drop in heat exchangers and especially in the CHX (see Chapter 5). Therefore simulation scenarios have been set up in order to simply estimate the optimizing potential of the investigated high temperature heat pump by neglecting the FI efficiency (η_{FI}) and all heat exchanger pressure drops. The calculated operation points are in accordance to Chapter 5. Furthermore only the Basic cycle has been considered since the improvement potential can be assumed nearly independent of the cycle configuration (additional pressure drops of IHX are hence neglected). The total improvement potential for the COP and the heating capacity, based on an inverter efficiency of 1 ($\eta_{FI} = 1$) and neglected pressure drops, are depicted in Figure 6.20 as a function of the condensation temperature with compressor frequency and the source temperature level as parameters. The inverter improvement potential is independent of the operation point and compressor frequency leading to a constant increase in COP in all operation points by 6 % (see Figure 6.6). The inverter however, has no influence on heating capacity since only the compressor consumption is affected. Figure 6.20 left, shows the normalized COP with an improvement ranging from approximately 7 to 20 % in the entire field of operation. The improvement potential increases with the source temperature level and compressor frequency since refrigerant massflow and thus pressure drops would increase. The COP improvement however decreases with increasing condensation temperature and thus pressure ratio and decreasing volumetric efficiency. The potential therefore decreases since refrigerant massflow decreases (see Chapter 5).

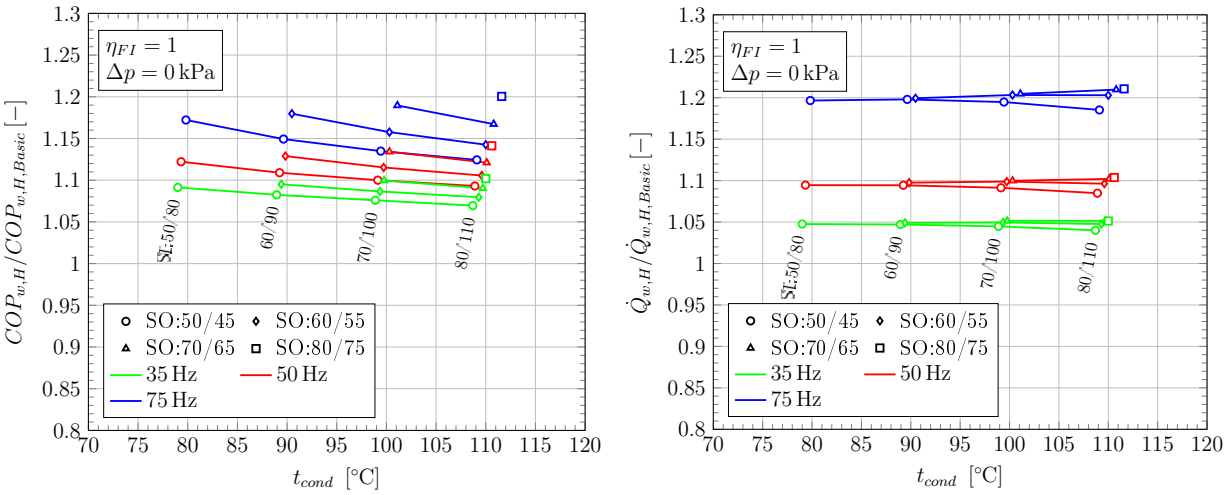

Figure 6.20: Simulated normalized efficiency (left) and heating capacity (right) based on $\eta_{FI} = 1$ and neglected pressure drops as a function of the condensation temperature with the compressor frequency and the source temperature level as parameter

The effect of the volumetric efficiency can also be clearly observed in the capacity results presented in Figure 6.20 left. The improvement potential increases up to approximately 21 % with the strongest influence being the compressor frequency. The increasing source temperature level and thus evaporation temperature has a minor impact on the improvement potential. Clearly further optimizing potential can be found regarding the compressor overall isentropic efficiency and in terms of necessary heat exchanger area and thus investment costs. Efficiency measures concerning different cycle modifications such as economizer configurations or ejectors application can further improve the thermodynamic cycle of R600 high temperature heat pumps as briefly discussed in Chapter 4. In this regard additional studies have to be carried out.

6.9 Concluding Remarks

The above presented results allow the derivation of a set of premises for an optimum design and operation of high temperature heat pumps and heat pumps in general considering different heat sink and source boundary conditions as well as control parameters. These premises can be summed up in the following enumeration and can be considered valid for the Basic and IHX cycle configuration:

- **The heat sink temperature difference shall be as high as possible:** Prerequisite for this statement is that the heat exchanger area and the heat transfer coefficient is sufficient in order to utilize refrigerant subcooling to the greatest extend (see following statement).
- **The optimum degree of subcooling follows Equation 3.27 in Chapter 3 derived by Pitarch et al. (2018):** The optimum degree of subcooling is dependent on the sink side temperature difference. A high sink side temperature difference allows to increase the usable enthalpy difference thus decreasing the compressor speed or size for a given supply temperature and heating capacity. As a result the heat pump efficiency increases.
- **The heat source temperature difference shall be as low as possible:** Theoretically the optimum case would be 0 K (e.g. phase change). With a low source

side temperature difference in combination with a certain degree of superheat (see following statement) the evaporation temperature can be increased to the greatest extend decreasing the pressure ratio and increasing refrigerant massflow and thus heating capacity as well as cycle efficiency.

- **A practical approach to the optimum superheat set point follows Equation 6.29:** The optimum superheat can be estimated with the desired source temperature difference. From an efficiency and capacity point of view, no significant improvement can be observed below this threshold. Superheat values greater than the source temperature difference can lead to a decline in heating capacity and cycle efficiency.

Especially the last statement is connected to heat pump control stability and the required superheat to avoid wet compression (see Chapters 3 and 5). Following Equation 6.29, unnecessary low superheat set point values can be avoided, hence improving control stability. If a high degree of superheat is required to avoid wet compression, the use of an internal heat exchanger might be favourable to keep the evaporation temperature as high as possible. Regarding further optimizing potential of the investigated high temperature heat pump prototype substantial efficiency and capacity improvements can be made by optimizing pressure drops and omitting the inverter. A large potential concerning pressure drop can be found for the customary built CHX (see Chapter 4) in changing heat exchanger channels from meandering to tangential flow and using cast iron manufacturing rather than a welding construction. Computational Fluid Dynamics could further improve the compressor motor waste heat recovery.

7 HEAT PUMP APPLICATION

The present chapter shall briefly outline possible application cases of the investigated high temperature heat pump using thermodynamical assessment based on the developed simulation model. An economical assessment of the investigated application cases have been presented in Moisi et al. (2018) and shall therefore not be discussed in the following sections.

7.1 Methodology

A basic thermodynamical assessment has been carried for selected application cases of the investigated R600 high temperature heat pump with the aim to show the energetic and CO_2 reduction potential. Especially in the field of food processing technologies promising application cases can be found since the main heating and cooling media are steam and water in temperature levels from 50 to130 °C which perfectly fit to the investigated high temperature heat pump. Hence a literature research has been carried out regarding thermal processes in food industries with suitable temperature levels. As a result of this literature research, three case scenarios of unit processes, where the integration of the considered heat pump system can be favorable compared to conventional heating systems (e.g. natural gas boiler), have been selected. The energetic performance of the heat pump system is calculated with the validated simulation model described in Chapter 6. The thermal processes as well as the integration of the heat pump are described in Section 7.2. Furthermore, the thermal processes are described by their characteristic temperature levels obtained from the respective literature which serve as boundary conditions for the HTHP instead of giving a detailed thermodynamic analysis of the processes themselves. However own assumptions have had to be made where no information was available. The required heating capacity for the investigated thermal processes has been adapted to the heating capacity of the HTHP prototype (around 28 kW) although in reality higher capacities might be necessary (several 100 kW). The considered unit processes are the evaporation of liquid foods (concentration), continuous sterilization of food in containers and blanching. All three processes can be basically heated by steam or water (see Fellows, 2017 or Featherstone, 2015). Both configurations have been considered for the high temperature heat pump, however for simplification, the phase change heat transfer correlations (evaporation and condensation) used for the refrigerant side, have also been used for the sink and source side. The thermodynamic assessment has been carried out for the presented high temperature heat pump and for comparison, a gas fired steam boiler.

7.1.1 Natural Gas Steam Boiler

Since the main heating medium in thermal food processing is steam, the investigated heating system to be compared is a gas fired steam boiler. The rated capacity of the gas boiler has been defined to 50 kW in order to meet the heating capacity of the investigated R600 HTHP. The energy consumption in terms of natural gas (E_{NG}) can be calculated by considering the operating hours per year (τ_{op}), the required heating capacity $\dot{Q}_{H,NG}$ and a boiler efficiency η_{NG}. The expression is given by Equation 7.1.

$$Q_{NG} = \tau_{op} \cdot \frac{\dot{Q}_{H,NG}}{\eta_{NG}} \tag{7.1}$$

The primary energy consumption for natural gas can be estimated by using primary energy factors ($f_{prim,NG}$) as given by Equation 7.2.

$$f_{prim,NG} = \frac{E_{prim,NG}}{Q_{NG}} \tag{7.2}$$

Using the primary energy consumption $E_{prim,NG}$ and the emission factor of natural gas $f_{CO_2,NG}$ yields the total CO_2 emissions ($m_{CO_2,NG}$) described by Equation 7.3.

$$m_{CO_2,NG} = Q_{NG} \cdot f_{CO_2,NG} \tag{7.3}$$

The boundary conditions and assumptions are collected in Table 7.1.

Table 7.1: Boundary conditions for the investigated gas boiler

Description	Symbol	Value	Source
rated capacity	$\dot{Q}_{H,NG}$	50 kW	own assumption
boiler efficiency	η_{NG}	0.90	own assumption
primary energy factor	$f_{prim,NG}$	1.1	OIB (2015)
emission factor	$f_{CO_2,NG}$	236 g/(kW h)	OIB (2015)

7.1.2 R600 High Temperature Heat Pump

The investigated high temperature heat pump has been discussed extensively in previous chapters. For the calculations the Basic Cycle configuration has been utilized. The primary energy use and the CO_2 emissions can be calculated analogous to the steam boiler. The only difference is that the heating capacity has to be divided by the resulting COP for the considered application case to yield the electrical power $P_{el,HP}$ and further on the total energy consumption of the heat pump as given by Equation 7.4. assuming steady state operation

$$E_{el,HP} = \tau_{op} \cdot \frac{\dot{Q}_{w,H}}{COP_{w,H}} \tag{7.4}$$

The primary energy factor and the emission factor is based on the Austrian electricity mix OIB (2015). The selected boundary conditions of the high temperature heat pump used for the application case assessment are given in Table 7.2

Table 7.2: Boundary conditions of the considered high temperature heat pump

Description	Symbol	Value	Source
rated capacity for cost calculation	$\dot{Q}_{H,HP}$	50 kW	present analysis
primary energy factor	$f_{prim,HP}$	1.92	OIB (2015)
emission factor	$f_{CO_2,HP}$	276 g/(kW h)	OIB (2015)

7.2 Application Cases

7.2.1 Food Industry: Evaporation

Evaporation processes are widely used in food processing technology to increase the solids fraction of liquid foods and also contributes to the reduction of water activity and thus to

food preservation. The basic concept for concentrating liquid foods is that heat is transferred from a heating medium (commonly steam) to the food in order to increase its temperature to the boiling point and thus evaporating water. The evaporated vapour is then separated and condensed in a condenser and the concentrated product is extracted. The evaporator is operated under partial vacuum (below atmospharic pressure) in order to decrease the boiling point of the liquid feed. This so called "single effect" evaporation is the most basic process and displayed in Figure 7.1a (Fellows, 2017).

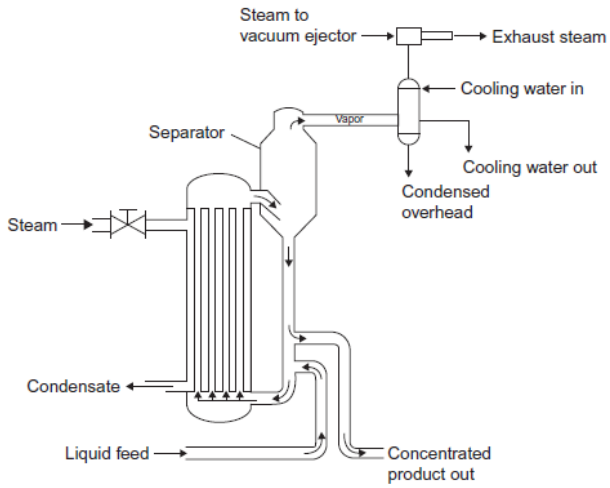

(a) single effect

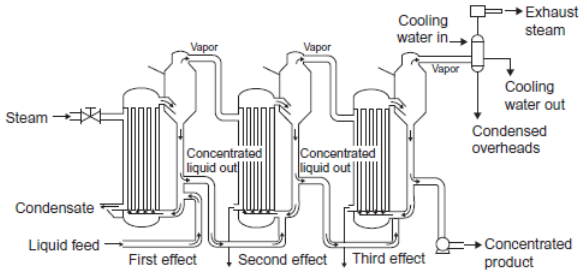

(b) multi effect

Figure 7.1: Schematics of (a) single effect evaporation system and (b) multi effect evaporator (obtained from Singh and Heldman, 2014)

Since evaporation of liquid foods is a very energy demanding process in food industry, different configurations including so called "multi effect" evaporators where the evaporated vapor of the first effect is used in the subsequent effect (see Figure 7.1b) are applied. However in order to achieve evaporation in the subsequent stages, an gradually increasing vacuum has to be maintained in the following effects to reduce the boiling temperature. The "multi effect" evaporation is applied to reduce steam and thus energy consumption however high initial cost have to be considered. The thermodynamically most efficient configuration would be stated by a "multi effect" evaporator using mechanical vapour recompression (MVR) between the stages yielding again high initial costs. Furthermore thermal vapour recompression (steam ejector) is utilized but with drawbacks in off design operation. The principle of heat transfer inside the evaporator is mainly natural convection by using falling and/or rising film shell and tube heat exchangers with a height up to 15 m and tube diameters of up to 50 mm. Also forced convection by circulating the liquid food is applied (Fellows, 2017). In any case heating steam has to be produced for the first effect of the evaporator. Commercial evaporators are operated with heating steam pressures in the range of 120 kPa to 270 kPa (105 °C to 130 °C) and evaporator pressures of 12 kPa to 30 kPa (boiling temperature of the product approx. 40 °C to 65 °C) for products like tomato and garlic paste, condensed milk, jams, concentrated soups, etc. (Fellows, 2017). Analysing the process and the required temperature levels, the application of the considered R600 high temperature heat pump can state an option to recover the heat at the condenser and supply the evaporator with hot water or saturated steam at the desired temperature. In order to evaluate the potential of the heat pump application, two test cases using hot water and saturated steam have been defined based on a "single effect" evaporator. The considered heat pump integration into the

evaporation process and the respective temperatures and mass flows are depicted in Figure 7.2.

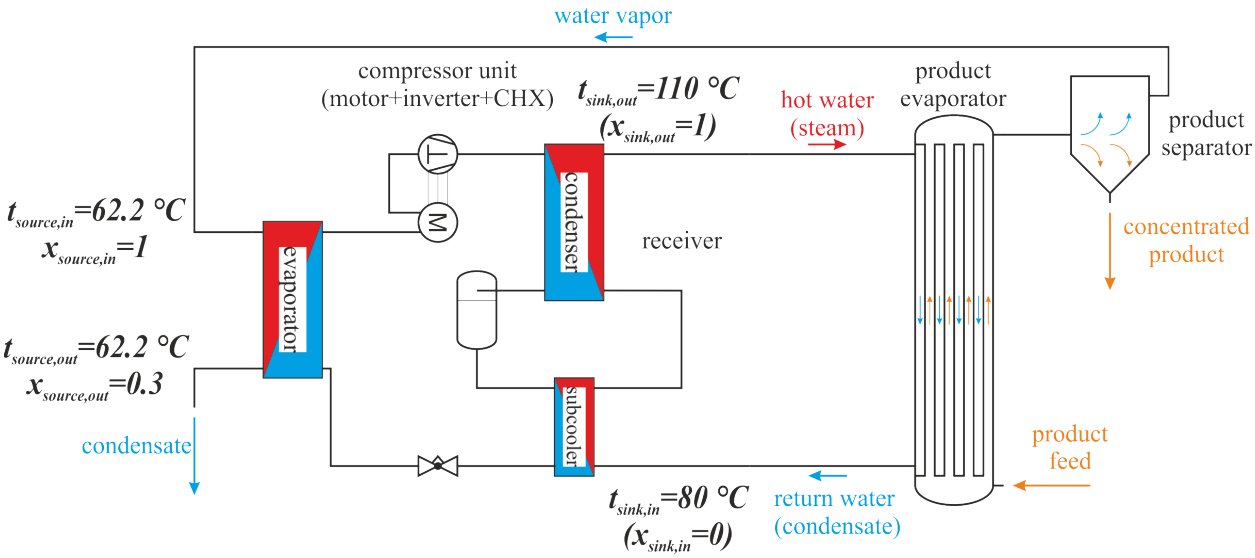

Figure 7.2: Integration of the R600 high temperature heat pump into a single effect evaporator

The temperature boundary conditions have been basically adopted from examples given in Singh and Heldman (2014), however own assumptions and adjustments have been made where no information has been available. The temperature of the supplied hot water or saturated steam has been set to 110 °C. The boiling temperature in the evaporator has been defined to 62.2 °C for example concentrating apple juice based on Singh and Heldman (2014). According to Fellows (2017), rising film evaporators require a temperature difference of at least 14 K between the heating and the evaporating medium to maintain sufficient natural convection. Therefore the return temperature of the hot water has been set to 80 °C. The return state in case of steam supply has been defined to be saturated liquid at 110 °C. The evaporated process water vapor is condensed in the evaporator of the heat pump and therefore serves as heat source for the heat pump in both cases. As already mentioned in Section 7.1 the capacity requirements for the evaporator (e.g. massflow) has been adapted to meet the heating capacity of the investigated heat pump system (see e.g. Chapter 5) in this test case. For real applications capacity upscaling might be necessary. The considered boundary conditions according to Figure 7.2 are summed up in Table 7.3.

Table 7.3: Boundary conditions for the evaporation process

Case	Description	Symbol	Value	Source
both	heating capacity	$\dot{Q}_H$	28 kW	own assumption
	source saturation temp.	$t_{source,sat}$	62.2 °C	Singh and Heldman (2014)
	source inlet quality	$x_{source,in}$	1	Singh and Heldman (2014)
	source outlet quality	$x_{source,out}$	≈ 0.3	result
	source medium	-	water vapor	Singh and Heldman (2014)
liq. water	sink inlet temp.	$t_{sink,in}$	80 °C	Fellows (2017)
	sink outlet temp.	$t_{sink,out}$	110 °C	Fellows (2017)
steam	sink saturation temp.	$t_{sink,sat}$	110 °C	based on Fellows (2017)
	sink outlet quality	$x_{sink,in}$	1	own assumption
	sink inlet quality	$x_{sink,out}$	0	own assumption

7.2.2 Food Industry: Sterilization of Canned Foods

As reported in Featherstone (2015), sterilization and pasteurization processes in food industry are essential to increase shelf life (up to one year) and decrease microbial spoilage of products due to heat treatment without using any preservatives. Depending on the product, acidity and other ingredients, different process conditions have to be met. Low-acid products (PH $>$ 4.6) for example, require sterilization temperatures in the range of 110 °C to 135 °C in order to achieve commercial sterility. In comparison for high acid foods mainly temperatures of 70 °C to 110 °C are sufficient (pasteurization).

Sterilization is a unit process in food industry and is highly used for processing foods in containers such as trays, pouches, glass jars and especially cans (Fellows, 2017). The heating medium is mainly steam however glass containers are processed in hot water since thermal shock can cause container damage. In order to understand the basic sterilization process, the batch operation in so called retorts should be considered. Figure 7.3a shows the schematic of a retort with steam, air and water connections for heating and cooling the product.

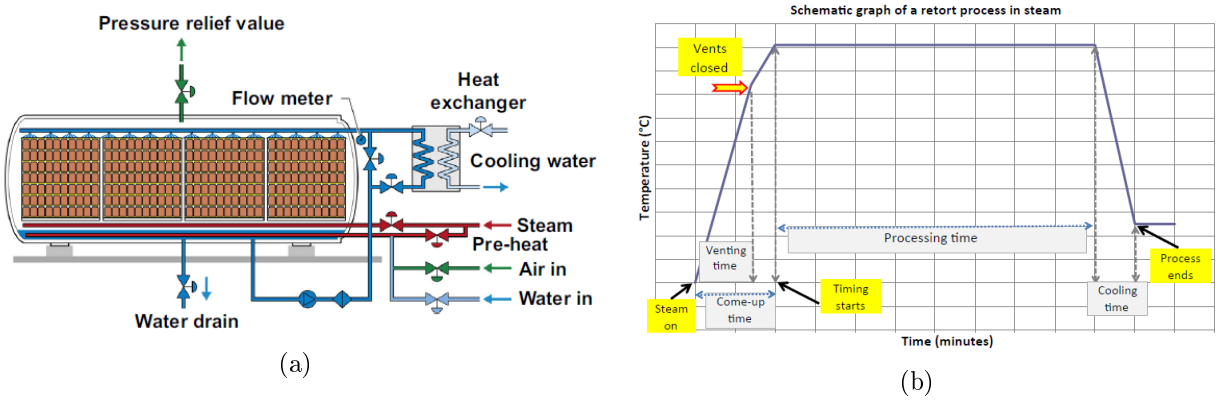

(a) (b)

Figure 7.3: (a) Schematics of a steam water spray retort and (b) basic time and temperature dependent sterilization process in batch application (obtained from Featherstone, 2015)

The temperature characteristics over time of the corresponding process is given in Figure 7.3b. Before starting the process the product has to be filled into the retort. After that air has to be vented from the retort containment which is carried out by the admittance of steam (venting process). During the venting process the temperature increases until all air is exhausted (approx. 105 °C). The vents are closed and the retort is heated to the desired temperature (approx. 121.1 °C) by the application of steam and remains at this temperature until the required process time is reached. The final step is cooling the product by water and pressurized air (pressure cooling) until the average product temperature is approx. 40 °C (see Featherstone, 2015 and Fellows, 2017). Besides the batch application continuous sterilization processes are very common in food industry since energy and time savings can be realized as well as high product quality and high capacities. Especially for canned food so called "continuous rotary pressure cooker-coolers" are applied. In this case most products are sterilized at a temperature of 121.1 °C (see Featherstone, 2015). These facilities basically consist of horizontal cylinders (so called "shells") which are connected to each other. Each shell can represent a Section in the sterilization process of Figure 7.3b. For example, in the first shell the cans are preheated and held at the required temperature and in the second shell the product is cooled down to approx. 40 °C. However venting is only necessary at start up of the pressure cooker which reduces steam consumption compared to the batch process. The product is conveyed through the shells at the perimeter of rotating drum guided by a reel which induces a spiraling motion. The filling and discharging is carried

out continuously and automatically. Figure 7.4 shows the basic setting of a rotary pressure cooker-cooler with two shells obtained from Featherstone, 2015.

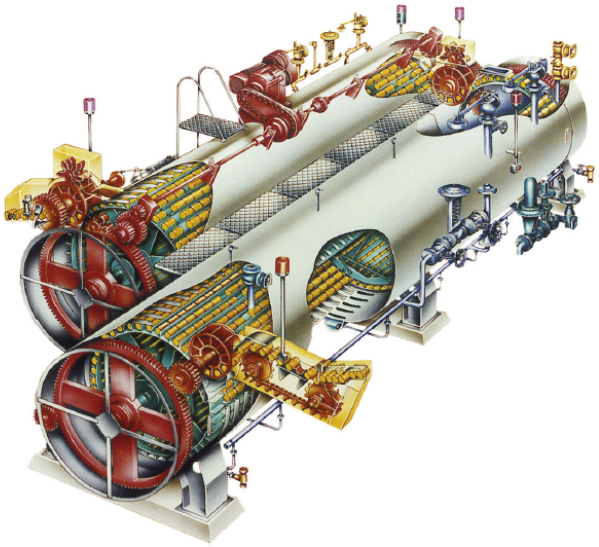

Figure 7.4: Schematics of continuous rotary pressure cooker with two shells (obtained from Featherstone, 2015)

The test case of the considered R600 high temperature heat pump shall therefore be the application in a rotary pressure cooker-cooler with two shells, the cooking and the cooling shell. Similar to Section 7.2.1, steam and hot water as heating medium have been investigated. The heat pump shall provide pressurized hot water at a temperature of 121.1 °C for the cooking shell. The outlet temperature of the returning heating water is set to be 90 °C. The application of hot water instead of steam is more suitable for glass containers as stated above. In case of saturated steam as the heating medium a saturation temperature of 121.1 °C for the cooking shell has been assumed. The outlet state of the cooking shell is assumed to be saturated liquid at the same saturation temperature. The question of the heat source however is more difficult. In the first place it would be considered obvious to utilize the waste heat of the cooling shell with direct coupling of the cooling water mass flow to the heat pump evaporator. The required heating capacity and the heat sink temperatures determine the required refrigerant mass flow which in turn defines the evaporator capacity at certain heat source inlet temperatures and water mass flow. Furthermore the required cooling capacity cannot exceed the heating capacity. The inlet temperature of the heat source along with the temperature difference across the evaporator and the suction gas superheat determine the evaporation temperature (see Chapter 6). Choosing a low cooling water mass flow results in a higher cooling shell outlet/evaporator inlet temperature which would be in fact favourable for the efficiency of the heat pump. However the low cooling water mass flow in combination with the given refrigerant mass flow results in a rather high temperature difference across the evaporator which compensates the positive effect of a high evaporator inlet temperature by lowering the evaporation temperature and decreasing the COP of the heat pump significantly. The cooling massflow results from a defined product outlet temperature ($t_{prod,out}$) of 40 °C as described above. Figure 7.5 shows simulated t/h diagrams of the direct integration (Figure 7.5a) compared to a decoupled process (Figure 7.5b).

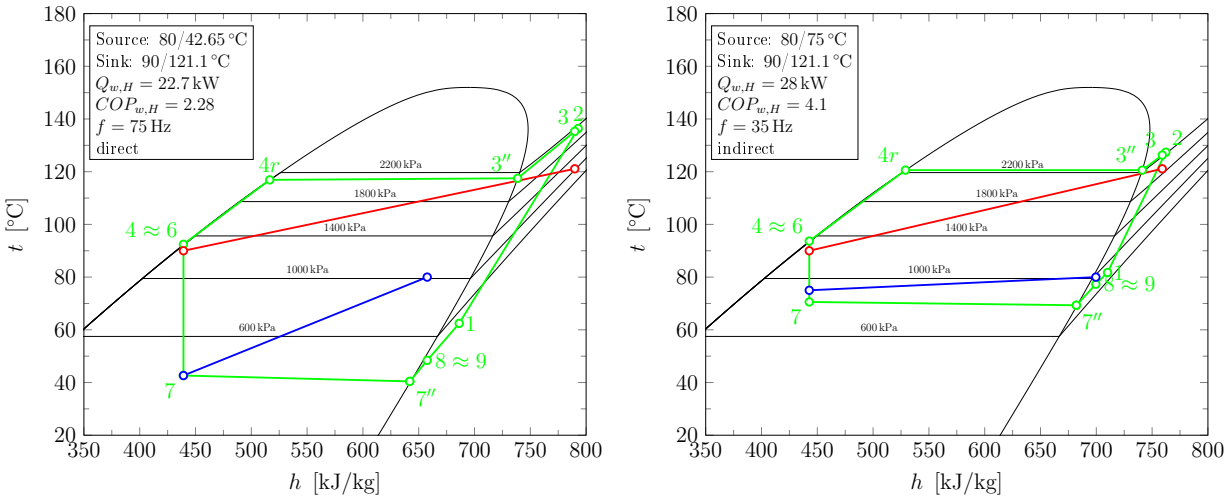

(a) direct integration

(b) indirect integration

Figure 7.5: t/h diagrams of a direct and indirect heat pump integration into the continuous sterilization process corresponding to Figure 7.6

Increasing the cooling water mass flow would reduce the temperature difference on the source side with the given refrigerant mass flow but also decreases the evaporator inlet temperature which results in a decrease of COP. The evaporation application in Section 7.2.1 shows that a direct integration can be a possibility if the source side stream undergoes a phase change (condensation) since the heat source temperature remains constant as long as no subcooling is reached. The influence of source and sink temperature differences has also been discussed in Chapter 6. Because of the disadvantages of the direct integration it has been assumed that a central waste heat storage provides a water stream with 80 °C and a temperature difference of 5 K across the evaporator as heat source for the heat pump (see Figure 7.5). Such heat storage systems can be found in food processing for example to store cooling water from batch retorts according Featherstone (2015) and Quijera et al. (2014). A schematic of the heat pump integration into the process is depicted in Figure 7.6. The required heating capacity for the process has again been adapted to the investigated heat pump (see Section 7.1), upscaling might be necessary for real application. Table 7.4 provides a summary of the considered boundary conditions in reference to Figure 7.6.

Table 7.4: Boundary conditions of the sterilization process

Cases	Description	Symbol	Value	Source
both	heating capacity	$\dot{Q}_{w,H}$	28 kW	own assumption
	source inlet temperature	$t_{source,in}$	80 °C	own assumption
	source outlet temperature	$t_{source,out}$	75 °C	own assumption
	source medium	-	liquid water	own assumption
liq. water	sink inlet temperature	$t_{sink,in}$	90 °C	Featherstone (2015)
	sink outlet temperature	$t_{sink,out}$	121.1 °C	own assumption
steam	sink saturation temperature	$t_{sink,sat}$	121.1 °C	Featherstone (2015)
	sink outlet quality	$x_{sink,in}$	0	own assumption
	sink inlet quality	$x_{sink,out}$	1	own assumption

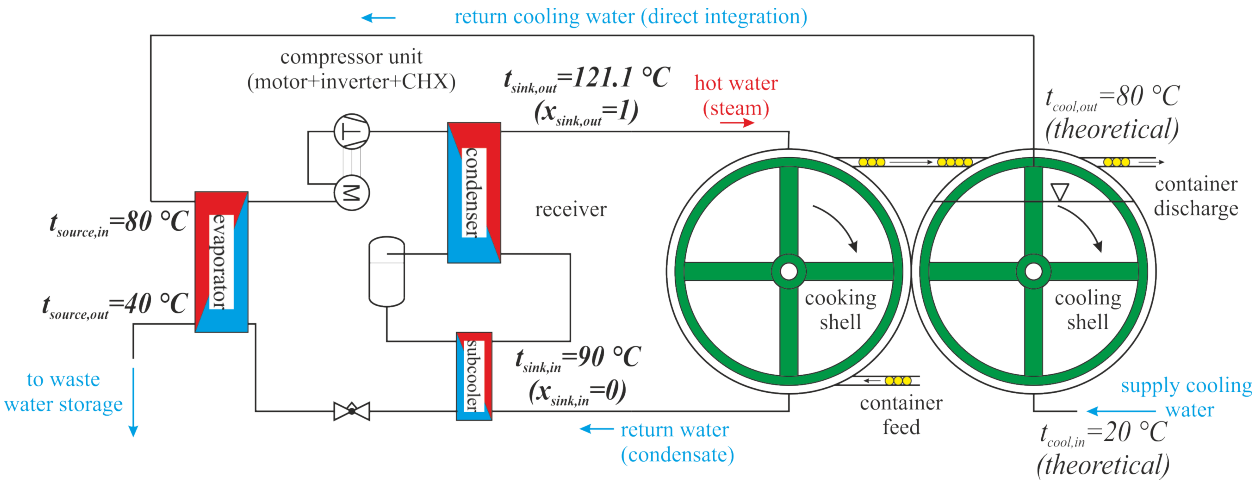

(a) Direct integration

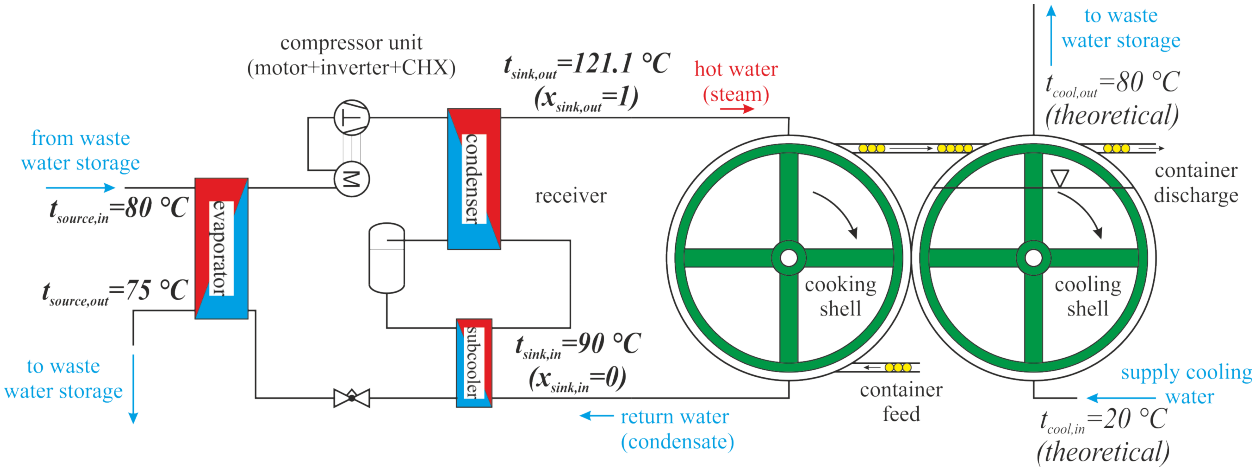

(b) Indirect integration

Figure 7.6: Integration possibilities of a R600 high temperature heat pump into a continuous sterilization process including process parameters

7.2.3 Food Industry: Blanching

Blanching is another unit process in food industry where heat is utilized in order maintain quality for further processing by inactivation of enzymatic activity and is considered a mild heat treatment. The process consists of a heating and a subsequent cooling step. In the heating step, the product (mainly fruits and vegetables) is heated rapidly to a a certain temperature mainly in the range between 70 °C to 100 °C. The heating medium can be steam or hot water. After the heating step the product is subsequently cooled down to ambient temperature by chilled water. In continuous processes the cooling water can be used for preheating the product. Figure 7.7 shows a schematic layout of a continuous steam blancher which shall be considered in this application case (see Fellows (2017)).

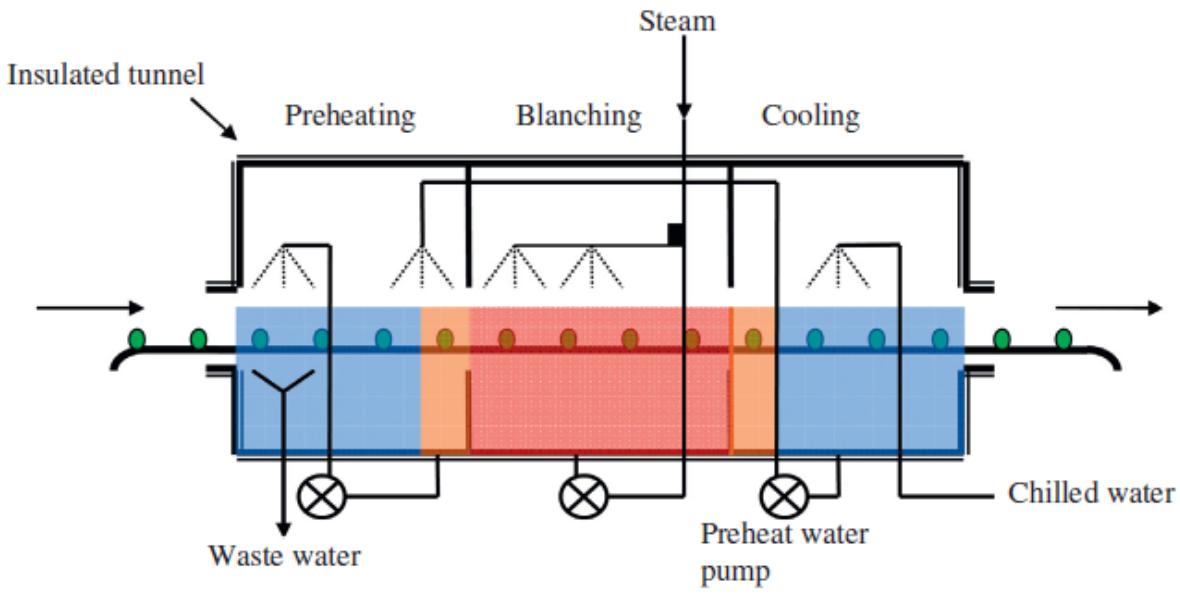

Figure 7.7: Schematics of continuous steam blancher obtained from Fellows (2017)

Similar to Section the possibility of steam and hot water as heating medium is considered. The heating temperature of the blanching Section has been set to 100 °C for saturated steam and hot water based on an example in Fellows (2017) for blanching peas. The return temperature of the blanching Section has been set to 70 °C in case of the hot water application and the return state in case of the steam application has been assumed to be saturated liquid at 100 °C. In terms of the heat source the same considerations regarding direct coupling of the cooling water apply as discussed in Section 7.2.3. Hence a central waste heat storage providing water at an evaporator inlet temperature of 60 °C and a temperature difference of 5 K across the evaporator has been assumed. The heat pump integration and the respective states and boundary conditions are shown in Figure 7.8.

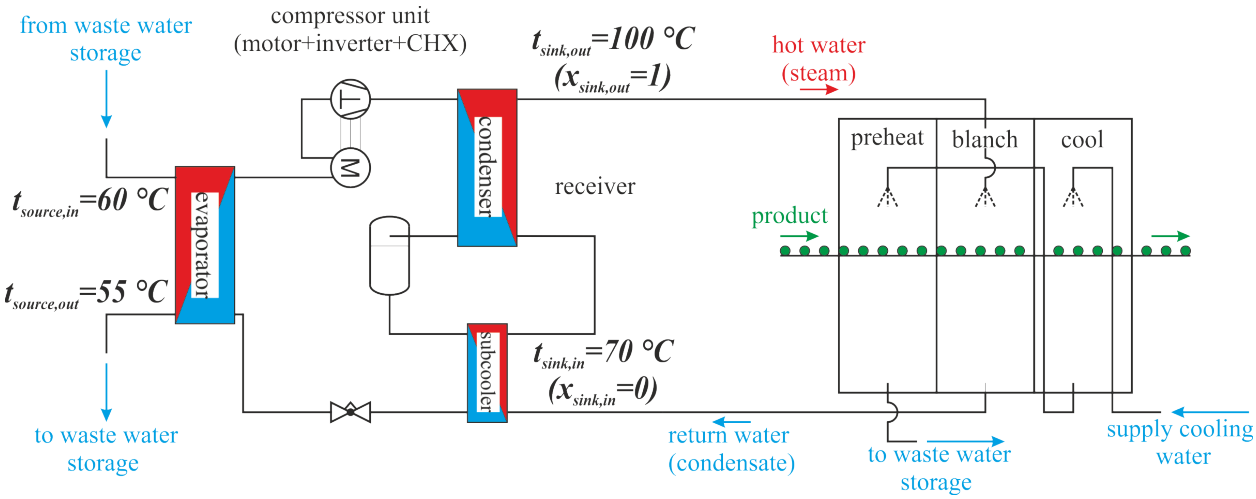

Figure 7.8: Integration and process parameters of a high temperature heat pump into the blanching process

Table 7.5 summarizes the boundary conditions for the blanching process corresponding to Figure 7.8.

Table 7.5: Boundary conditions for the blanching process

Case	Description	Symbol	Value	Source
both	heating capacity	$\dot{Q}_{w,H}$	28 kW	own assumption
	source inlet temperature	$t_{source,in}$	60 °C	own assumption
	source outlet temperature	$t_{source,out}$	55 °C	own assumption
	source medium	-	liquid water	own assumption
liq. water	sink inlet temperature	$t_{sink,in}$	70 °C	Fellows (2017)
	sink outlet temperature	$t_{sink,out}$	100 °C	own assumption
steam	sink saturation temperature	$t_{sink,sat}$	100 °C	Fellows (2017)
	sink outlet quality	$x_{sink,in}$	0	own assumption
	sink inlet quality	$x_{sink,out}$	1	own assumption

7.3 Thermodynamic Analysis

The developed simulation model described in Chapter 6 has been utilized for the simplified steady state analysis of the above described application cases. Starting with the evaporation process (see Section 7.2.1), Figure 7.9 depicts the resulting t/h diagrams with source and sink temperature characteristics indicated, for the hot water and steam supply. The both evaporation application cases perfectly reflect the influence of source and sink temperature characteristics on cycle efficiency as discussed in Chapter 6. For a given heating capacity (28 kW), the hot water supply case requires a compressor frequency of only approx. 51 Hz compared to the steam supply with a compressor speed of nearly 71 Hz (to be fair at this point this effect could be avoided if a larger compressor is used, as a result the compressor frequency would decrease and the overall isentropic efficiency increase). This is clearly a result of the difference in specific heating capacity due to the different temperature characteristics of heating liquid water compared to vaporization for a given supply temperature. The low inlet temperature of 80 °C in the water supply case and the decoupling of the condenser and the subcooler by the high pressure receiver allows a high degree of subcooling having no negative effect on the condensation temperature (see Chapter 3). In the steam supply case, the saturated liquid enters the subcooler at already 110 °C. As a result the driving temperature difference decreases significantly, increasing the condensation temperature. Hence the available enthalpy difference across the condenser and subcooler is significantly limited. The evaporation pressure remains nearly the same for both cases since source side boundary conditions do not change. With the increasing pressure ratio of the steam supply case, not only the specific compression work increases but as well the volumetric efficiency decreases (see Chapter 5). Furthermore the overall isentropic efficiency is negatively affected by the increased compressor speed (see Chapter 5). The sum of the described effects contribute to the significant decrease of COP for an identical heating capacity and supply temperature in the steam supply case ($COP_{w,H} = 3.58$) compared to the hot water case ($COP_{w,H} = 2.43$). One optimizing potential for both cases remains regarding the heat source. In combination with the constant source temperature as a result of vapour condensation, the efficiency optimum superheat would be zero according the statements provided in Section 6.9. For the present simulation, a superheat of 8 K has been selected according to the heat pump prototype.

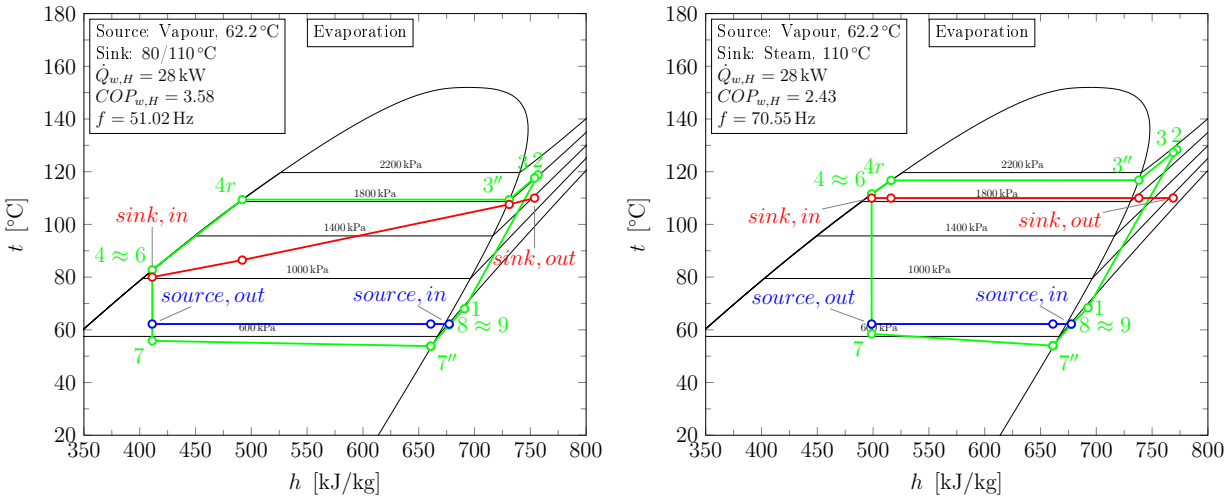

(a) hot water supply (b) steam supply

Figure 7.9: Simulated t/h diagrams of the evaporation case for hot water supply (a) and low pressure steam supply (b)

Similar results can be obtained for the sterilization cases (see Section 7.2.3) illustrated in Figure 7.10. The efficiency of the hot water supply case results to approx. 4.1. The steam supply case exhibits an efficiency of approx.2.66 for a given heating capacity of 28 kW and a supply temperature of 121.1 °C. The reason for this difference can again be found in the different sink side temperature characteristics and their consequences as outlined above. The improvement potential on the source side regarding the evaporator superheat is limited in the sterilization cases since pinch point temperature differences are already nearly equall, stating the approximate optimum point according Sections 6.7 and 6.9.

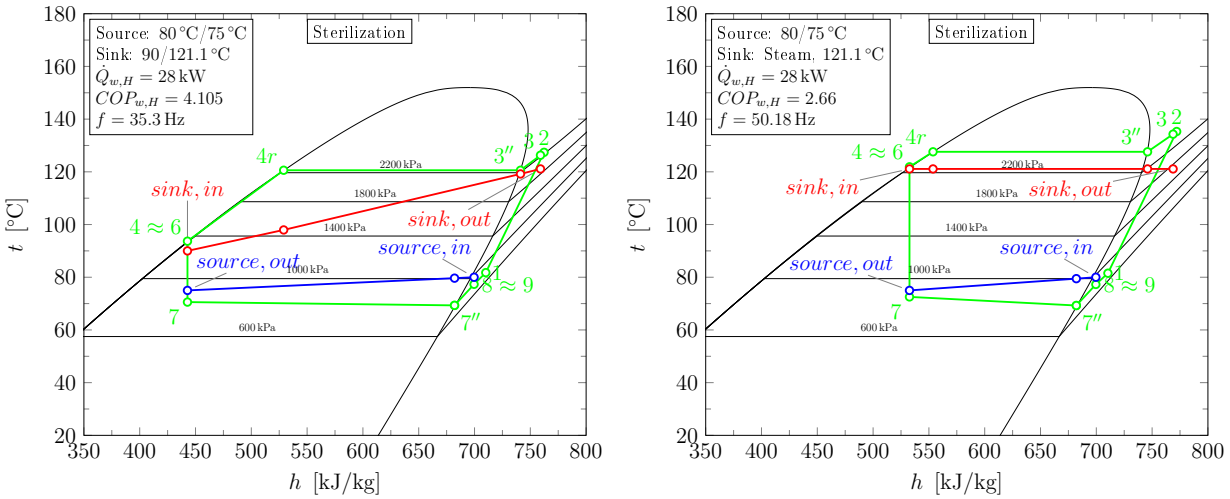

(a) hot water supply (b) steam supply

Figure 7.10: Simulated t/h diagrams of the sterilization case for hot water supply (a) and low pressure steam supply (b)

Finally, the blanching process (see Section 7.2.3) naturally shows similar qualitative results regarding the comparison of hot water supply and steam generation with efficiencies of approx. 3.9 and 2.7 as depicted in Figure 7.11. For the steam supply case, the superheat could have slightly increased since the pinch point temperature difference at the source outlet is lower than at the inlet.

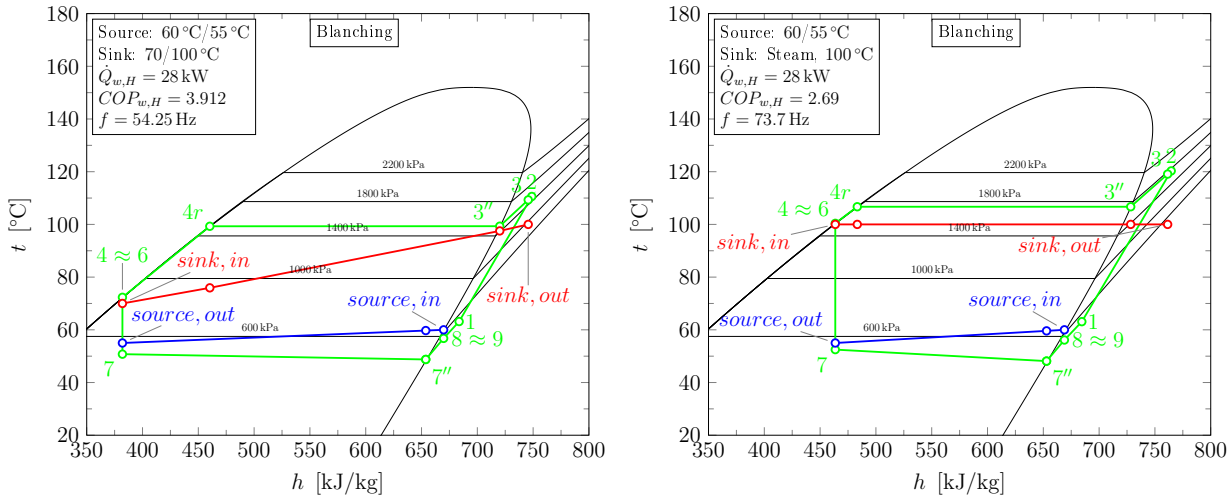

(a) hot water supply

(b) steam supply

Figure 7.11: Simulated t/h diagrams of the blanching case for hot water supply (a) and low pressure steam supply (b)

The above presented results illustrate the importance of source and sink boundary condition for the application of high temperature heat pumps or heat pumps in general. Especially in the steam supply cases, an internal heat exchanger can increase the cycle efficiency as outlined in Chapter 5, if the sink side temperature characteristics are limiting heat pump efficiency. Furthermore, as carried out by Wemmers et al. (2017), the subcooler can be decoupled from the steam supply heat sink providing hot process water increasing the cycle efficiency to levels of the hot water supply cases (see also Section 2.2). In conclusion, the results of the validated simulation model based on the assumed boundary conditions obtained from literature clearly indicate that food processing can be an important field of application for a R600 high temperature heat pump with the possibility of high operating efficiencies. The combination of cooling and heating processes using mainly water and steam as heat source and sink media in a temperature range of 20 to 130 °C is a further argument for the application in food processing industries. Clearly, the presented results are only considering unit processes in a simplified way however process integration tools such as pinch point analysis (see e.g. Arpagaus, 2018) can be utilized to optimize the heat pump integration. In terms of high capacity application (several 100 kW), Wemmers et al. (2017) has already shown the practical feasibility of a R600 high temperature heat pump (see Chapter 2). A brief look on energy consumption and CO_2 reduction potential based on the investigated application cases is outlined in the following section.

7.4 Energy Consumption and Emissions

The total primary energy consumption and CO_2 emission have been estimated based on primary energy factors and emission factors obtained from literature following Equations 7.1, 7.2 and 7.3 as described in Sections 7.1.1 and 7.1.2. Varying the time in operation per year (τ_{op}) of the heat pump and the natural gas boiler, a linear characteristic for the energy consumption and the amount of emission results as depicted in Figure 7.12. The energy consumption and thus carbon emissions are naturally corresponding to the COP results of the different application cases. The maximum primary energy consumption of the steam supply cases and very high operation times of 8000 h/a ranges from 160 (sterilization) to approx. 180 MW h/a (evaporation). In this regard, the hot water cases range from approx. 100 (sterilization) to 120 MW h/a (evaporation). In comparison, the natural gas boiler would

require approx. 270 MW h/a of primary energy for the same time in operation. Analogously, the results of the CO_2 emissions depicted in Figure 7.12, show a maximum production of carbon dioxide under the assumed boundary conditions for the steam supply cases of up to nearly 25 t/a and approx. 17 t/a for the hot water supply cases (evaporation). The natural gas boiler results are ranging up to 59 t/a. It shall again be noted, that primary energy factor and emission factor are based on the Austrian electricity mix with a generally large fraction of renewable energy sources compared to other countries.

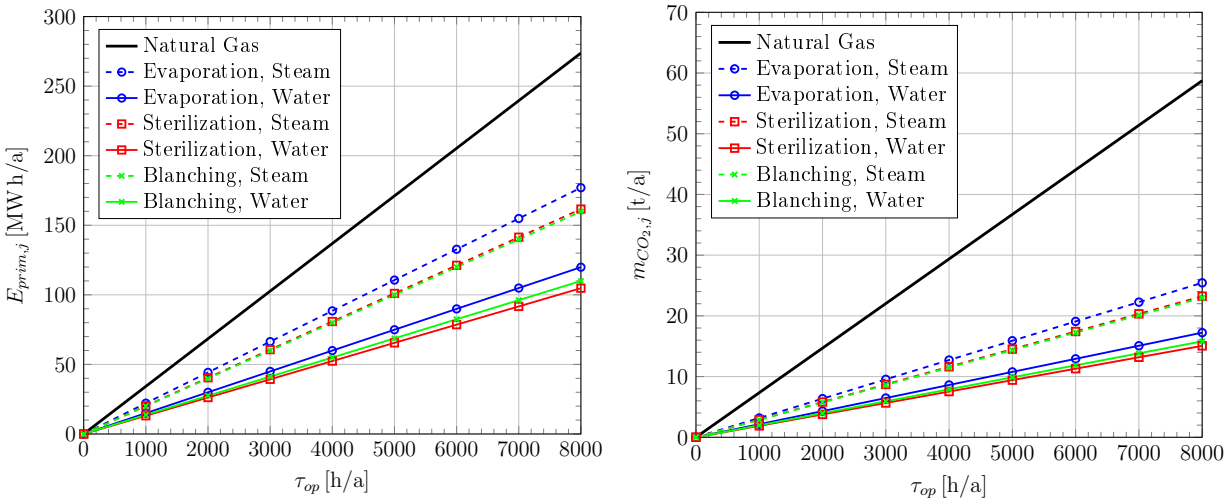

Figure 7.12: Simulation results for primary energy consumption (left) and CO_2 emissions (right) as a function of the operating hours per year for each application case and the natural gas boiler

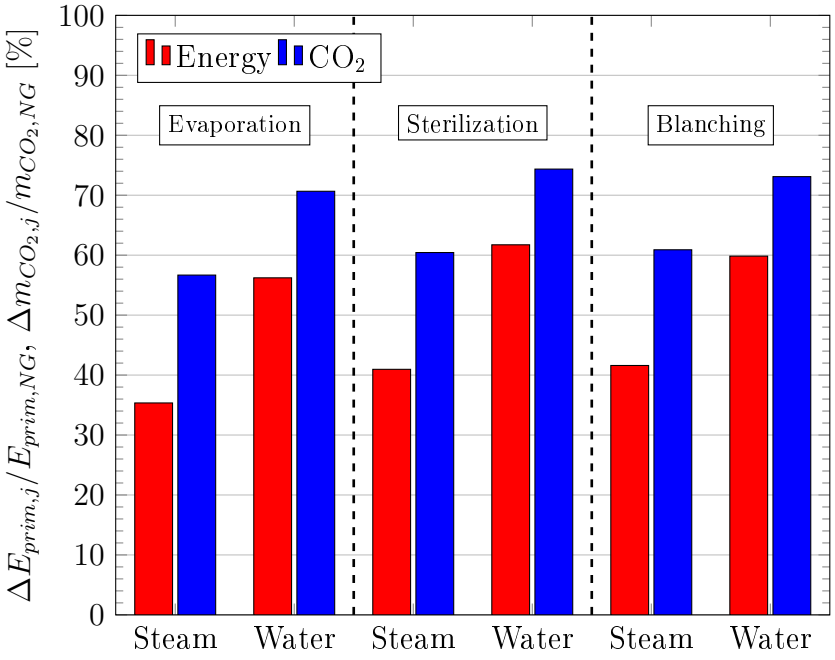

Figure 7.13: Estimated relative primary energy and CO_2 emission reduction for the investigated application cases compared to the natural gas boiler

Finally, the relative reduction of energy consumption (red) and carbon emissions (blue) for the different high temperature heat pump application cases compared to the use of a natural

gas boiler is depicted in Figure 7.13. In terms of primary energy consumption, theoretically up to 63 % can be saved for example in the water supply sterilization case. For the same application, carbon dioxide can be significantly reduced by approx. 74 %. Despite the lower cycle efficiencies, the steam supply cases still provide a reduction potential in terms energy consumption ranging from 36 % (evaporation) to approx. 42 % (sterilization). Regarding the emission reduction potential, the steam supply cases range between 56 % (evaporation) and 60 % (sterilization). The obtained estimations regarding energy consumption and carbon dioxide emissions show clearly the high potential of further decarbonization and that significant resource savings are possible applying high temperature heat pumps for process heat preparation. Additionally, the use of the natural refrigerant R600 contributes to this emission reductions. Clearly, safety aspects, process integration and most of all costs have to be considered for a broadened application of high temperature heat pumps. However as presented in Moisi et al. (2018), for a low capacity range corresponding to the investigated R600 heat pump system, dynamic payback times of up to 6 years (cases with hot water preparation, $\tau_{op} = 6000\,\mathrm{h}$) compared to a natural gas boiler might be also economically attractive. In combination with 100 % renewable electricity generation (photovoltaic, wind or hydro power), the investigated high temperature heat pump could provide nearly carbon free process heat for industrial applications.

8 SUMMARY AND OUTLOOK

The presented thesis is based on the results of the cooperative project "Hot Cycle" (FFG No.: 848892) under the cooperation of the Institute of Thermal Engineering (IWT) of TU Graz and Frigopol-Kaelteanlagen GmbH. The project had been funded by the Climate and Energy Fund and carried out within the Austrian Energy Research Program 2015. The main premise of the project has been the development of a high temperature heat pump providing supply temperatures up to 110 °C in a capacity range of up to 50 kW utilizing a separating hood compressor.

In a greater context, high temperature heat pumps can offer the possibility to reduce the fossil fuel consumption and thus carbon emissions in industrial process heat preparation in order to meet global climate goals. Additionally, the use of low GWP refrigerants shall further reduce the total global warming impact (TEWI) of a heat pump application. Consequently, a subcritical single stage high temperature heat pump prototype using *n*-Butane (R600) meeting the project requirements has been developed and experimentally analyzed.

A fundamental aspect of the cycle development has been the "overhanging" nature of the two phase region of R600. With increasing specific heat capacity at constant volume, the stronger an overhanging shape manifests. As a consequence, the compression process can enter the two phase region causing liquid droplets to form which can provoke compressor damage. Providing a sufficient superheat, the compression process remains in the superheated region. This quantity can be described as required superheat. Based on an isentropic compression approach obtained from literature, a methodology has been described in order to derive the required superheat based on a fluid property database for any known refrigerant. Detailed characteristics in this regard have been presented for R600 as a function of the evaporation temperature with the condensation temperature as parameter in a range from 0 to 120 °C. The maximum required superheat has been found to be 17.6 K for highest temperature lift of 120 K. Furthermore, different values of the internal isentropic efficiencies have been investigated, showing a shift of the required superheat maximum to lower superheat values and increasing evaporation temperatures with decreasing efficiency values. In this regard, the isentropic approach might overestimate the required superheat in real applications. However the fundamental characteristic of the isentropic compression allows the interpretation of the required superheat quantity as a fluid property detached from a real process and provides a comparable quantity to other high temperature refrigerants.

A high required superheat provided entirely in the evaporator in combination with low source side temperature differences can cause a reduction in cycle efficiency. Therefore, six cycle configuration obtained from literature in combination with three variations of superheat preparation (evaporator, internal heat exchanger and suction gas cooled compressor) have been investigated by means of simulation. As a result a two staged cycle performed best in terms of COP and heating capacity. However the strong impact of decoupling the superheat from the heat source has led to comparable efficiency results for the single stage cycle. As a consequence of a decreased complexity and acceptable efficiency results, a single stage cycle using a high pressure receiver an subsequent subcooler has been finally selected for the heat pump prototype.

The heat pump prototype has been constructed by the project partner Frigopol. Heat exchangers and valves have been designed by using partially manufacturer design software and input data from design simulations. The heat pump prototype combines a basic single stage cycle and the use of an internal heat exchanger. Furthermore a superheater can increase the evaporator area. Additionally, the commonly air cooled separating hood compressor obtained from the project partner has been adapted to a suction gas cooled compressor

by a customary built heat exchanger. As a result, it has been possible to investigate different means of superheat preparation experimentally. The different cycle configurations have been realized by operating the corresponding shut off valves. Except the compressor heat exchanger, all components of the high temperature test rig have been standard heat pump equipment and are readily available. The compressor speed has been controlled with a frequency inverter. The main control quantity has been the superheat at the inlet of the compressor. The main premise of the measurement concept has been to provide complete state diagrams and performance indicators such as efficiency, heating capacity and compressor consumption for different temperature and compressor speed boundary conditions. In order to provide source and sink inlet temperatures in a range from 50 to 80 °C appropriate source and sink hydraulics have been designed and constructed. As source and sink medium, pressurized water has been utilized.

On the source and sink side the test conditions have ranged between 50 and 80 °C with source temperature differences of 5 K and sink side temperature differences of 30 K. The compressor speed has been set to 35, 50 and 75 Hz. In the course of experimental testing it has been observed that the heat pump start might be potentially critical in terms of wet compression due to the rather high thermal mass of the compressor. However, practically compressor damage has not been observed. Superheat instabilities below a superheat set point of 8 K has been linked to MSS-Theory. As a result the superheat set point has been set to 8 K throughout the experimental analysis.

In the present thesis it has been the first time to test the separating hood compressor with a CHX configuration using R600 as refrigerant. In this regard detailed efficiency characteristics have been derived and compressor energy flux composition has been analyzed. The results have shown that especially dissipation and heat losses of the compression process are significant and increase with increasing compressor speed. The fraction of recovered compressor motor waste heat has been shown to be strongly dependent on refrigerant massflow. The capability of compressor cooling however is limited to evaporation temperatures below 80 °C for a compressor frequency of 75 Hz due to a limited heat transfer area and a maximum motor temperature.

Detailed efficiency maps have been derived in addition to refrigerant state diagrams for the Basic, IHX and Superheater cycle configuration. The results showed that supply temperatures in a range between 80 and 110 °C with achievable heating capacities between approx. 13 and 47 kW for the basic cycle configuration. In the investigated field of operation the heating COP has been found between 2.8 and 5.6 The application of the Superheater and internal heat exchanger have shown improvement in terms of efficiency and heating capacity with tendentious opposing trends. While the highest efficiency improvement for the Superheater cycle has been obtained at low compressor speeds to 7.6 % decreasing with increasing condensation temperature, the IHX improvement potential has been nearly independent of the compressor speed resulting in a maximum increase of 6.6 % compared to the basic cycle increasing with increasing temperature lift. In terms of compressor outlet temperature in combination with an already high superheat due to stability reasons, compressor cooling and the additional IHX superheat, values of 135 °C have been obtained which can be critical for the used compressor lubricant. Carnot and Lorenz efficiencies have been estimated up to 53 % for a temperature lift of 35 K and 41 % for a temperature lift of 65 K respectively. The Carnot and Lorenz characteristics have shown a close correlation to the compressor internal isentropic efficiency confirming the strong influence of the compressor on cycle irreversibilities.

Based on the obtained experimental results a semi empirical steady state heat pump simulation model utilizing efficiency characteristics and heat transfer correlations obtained from

literature has been developed. Since no information on the internal geometry of brazed plate heat exchangers have been available, a single point calibration based on manufacturer design pressure drops and heat transfer coefficients have been utilized to improve heat transfer accuracy especially for the subcooler and IHX. A model validation has shown a fair agreement with experiment for heating capacity and cycle efficiency within a range of ±5 % and in between −10 and 0 % respectively. The derived cycle model has been utilized for a simulation study varying the superheat set point, source and sink temperature differences for different operation points. The results clearly confirm that an increased sink side temperature difference provides the possibility to utilize subcooling to the greatest extend and thus increasing cycle efficiency and heating capacity. As already described in literature, the optimum degree of subcooling can be obtained if pinch point temperature differences are identical in the condenser. In this regard a similar behaviour has been been suspected for the superheat set point. As experimental and theoretically investigated in the present thesis by variing the superheat set point for different source temperature difference the obtained results strongly indicate that there is a weak efficiency optimum at identical source inlet and outlet pinch point temperature differences. This holds true for the basic cycle. The clear connection for the IHX cycle has not been found due to the changing evaporator inlet conditions as a result of the operation point dependent subcooling. As a practical result however the optimum superheat can be approximated equal to the source side temperature difference since efficiency and heating capacity do not significantly change below this threshold.

Finally, three application cases in food processing for the high temperature heat pump have been obtained from literature considering evaporation (concentration), continuous sterilization and blanching. The application case specific boundary conditions have been derived from literature combined with own assumptions where data has not been available. The supply temperatures have ranged between 100 °C (blanching), 110 °C (evaporation) and 121.1 °C (sterilization). Utilizing the developed simulation model, steam preparation and hot water supply has been investigated for each of the three cases, clearly showing that a constant sink temperature significantly decreases the cycle efficiency since subcooling can not be harnessed compared to the hot water supply with sink side temperature differences of 30 K. The comparison in terms of carbon emission reduction has been based on primary energy and emission factors obtained from literature. Compared to a natural gas boiler, theoretically up to 74 % of carbon emissions for the hot water supply and up to 61 % for the steam supply can be reduced applying the investigated high temperature heat pump for process heat preparation.

In conclusion, the present thesis contributes new theoretical aspects by providing a methodology to determine the required superheat for overhanging working fluids based on an isentropic compression process obtained from literature. The influence of the internal isentropic efficiency has been outlined and required superheat characteristics as a function of evaporation and condensation temperature have been presented in detail especially for R600 and in comparison to other overhanging refrigerants, which has only been published before to the best knowledge by the author of the present thesis. The developed high temperature heat pump states a reliable alternative to fossil fuels for process heat preparation in a temperature range up to 110 °C based on readily available components. The detailed experimental data significantly contributes to the characterization, capabilities and application of R600 high temperature heat pumps including the effect of an internal heat exchanger additional evaporator heat transfer area and the variation of evaporator superheat. The latter aspect has been shown to be significantly influenced by the source side temperature difference. Based on literature research, experimental and theoretical analysis, practical recommendations have been presented regarding subcooling and evaporator superheat in dependence of

sink and source temperature differences. Temperature and waste heat recovery characteristics of the novel compressor heat exchanger have been experimentally derived, revealing optimizing potential in pressure drops and heat transfer. Further optimizing potential of the high temperature heat pump prototype can be found in refrigerant charge and pressure drops due to complex combination of several cycle configuration.

Future applications of R600 might use the transcritical cycle increasing the possible supply temperatures and broadening the field of application. In this regard, appropriate compressor technology and equipment has to be available to sustain high pressure and temperatures. The reduction of the refrigerant charge due to the high flammability will state a challenge for the establishment of R600 high temperature heat pumps in industrial processes heat preparation. Clearly also the investment costs are a significant factor. Nevertheless, the estimation of different application cases in food industry have shown a high carbon reduction and energy savings potential. In combination with renewable electricity generation a step to nearly carbon free process heat preparation can be made using a R600 high temperature heat pump.

LITERATURE

ABB (2016). ABB Frequenzumrichter für HLK-ACH580-1, technisches Datenblatt.

Adler, B. and Mauthner, R. (2017). Rotation heat pump. In *Proceedings of 12th IEA Heat Pump Conference, Rotterdam*.

AlfaLaval (2016a). AC70X/ACH70X-Product leaflet, `https://www.alfalaval.com/globalassets/documents/microsites/heating-and-cooling-hub/pd-leaflets/ac70_product-leaflet.pdf`, (Online: 10.09.2020)).

AlfaLaval (2016b). Correspondence with Alfa Laval- Technical description and product offer, (internal communication).

AlfaLaval (2020). Homepage, `https://www.alfalaval.de/`, Online (08.05.2020).

Arpagaus, C. (2018). *Hochtemperatur-Wärmepumpen: Marktübersicht, Stand der Technik und Anwendungspotentiale*. VDE Verlag GmbH, Berlin-Offenbach.

Arpagaus, C., Bless, F., Uhlmann, M., Büchel, E., Frei, S., Schiffmann, J., and Bertsch, S. S. (2018a). High temperature heat pump using HFO and HCFO refrigerants – System design, simulation, and first experimental results. In *17th International Refrigeration and Air Conditioning Conference*, number 2199, West Lafayette. Purdue University.

Arpagaus, C., Bless, F., Uhlmann, M., Schiffmann, J., and Bertsch, S. S. (2018b). High temperature heat pumps: Market overview, state of the art, research status, refrigerants, and application potentials. *Energy*, 152:985 – 1010.

Bach, K., Grassmann, P., Göldner, R., Linge, K., Neuenschwander, A., Plank, R., and Vahl, L. (1966). Kältemaschinen-Kaltgasmaschinen und Kaltdampfmaschinen. In Plank, R., editor, *Handbuch der Kältetechnik*. Springer-Verlag GmbH, Berlin, Heidelberg.

Baehr, H. D. and Kabelac, S. (2006). *Thermodynamik*. Springer Verlag, Berlin, Heidelberg, New York, 13 edition.

Baehr, H. D. and Stephan, K. (2010). *Wärme- und Stoffübertragung*. Springer-Verlag, Berlin, Heidelberg, 7 edition.

Bamigbetan, O., Eikevik, T., Nekså, P., Bantle, M., and Schlemminger, C. (2019a). The development of a hydrocarbon high temperature heat pump for waste heat recovery. *Energy*, 173:1141 – 1153.

Bamigbetan, O., Eikevik, T. M., Nekså, P., Bantle, M., and Schlemminger, C. (2018a). Theoretical analysis of suitable fluids for high temperature heat pumps up to 125 °C heat delivery. *International Journal of Refrigeration*, 92:185 – 195.

Bamigbetan, O., Eikevik, T. M., Nekså, P., Bantle, M., and Schlemminger, C. (2019b). Experimental investigation of a prototype R-600 compressor for high temperature heat pump. *Energy*, 169:730 – 738.

Bamigbetan, O., Eikevik, T. M., Neksa, P., Bantle, M., and Schlemminger, C. (2018b). Experimental investigation of the performance of a hydrocarbon heat pump for high temperature industrial heating. In *Proceedings of the 13th IIR Gustav Lorentzen Conference On Natural Refrigerants*, Valencia, Spain. International Institute of Refrigeration.

Bergman, T. L., Lavine, A. S., Incropera, F. P., and Dewitt, D. P. (2011). *Fundamentals of Heat and Mass Transfer*. John Wiley & Sons, Inc., 7th edition.

Bertinat, M. P. (1986). Fluids for high temperature heat pumps. *International Journal of Refrigeration*, 9(1):43 – 50.

Bieler+Lang (2003). Gasmess-und Warnsysteme: Gasmesscomputer 8022, GMC8022E-Betriebs-und Montageanleitung.

Bieler+Lang (2010). Datenblatt: ExDetector HC150/HC150-K.

BIPM (2008). Evaluation of measurement data — Guide to the expression of uncertainty in measurement, JCGM 100:2008 . Online (20.04.2020), `https://www.bipm.org/utils/common/documents/jcgm/JCGM_100_2008_E.pdf`.

Bobelin, D. and Bourig, A. (2012). Experimental results of a newly developed very high temerpature industrial heat pump (140 °C) equipped with a scroll compressor and working with an new blend refrigerant. In *International Refrigeration and Air Conditioning Conference*. Paper 1299, Purdue University, West Lafayette.

Bosnjakovic, F. (1998). *Technische Thermodynamik-Teil I.* Springer-Verlag Berlin Heidelberg, 8. korrigierte Auflage.

Calm, J. M. (2008). The next generation of refrigerants – historical review, considerations, and outlook. *International Journal of Refrigeration*, 31(7):1123 – 1133.

Cao, X.-Q., Yang, W.-W., Zhou, F., and He, Y.-L. (2014). Performance analysis of different high-temperature heat pump systems for low-grade waste heat recovery. *Applied Thermal Engineering*, 71(1):291 – 300.

Chamoun, M., Rulliere, R., Haberschill, P., and Peureux, J.-L. (2014). Experimental and numerical investigations of a new high temperature heat pump for industrial heat recovery using water as refrigerant. *International Journal of Refrigeration*, 44:177 – 188.

Chen, G., Gan, Z., and Jiang, Y. (2002a). Discussion on refrigeration cycle for regenerative cryocoolers. *Cryogenics*, 42(2):133 – 139.

Chen, W., Zhijiu, C., Ruiqi, Z., and Yezheng, W. (2002b). Experimental investigation of a minimum stable superheat control system of an evaporator. *International Journal of Refrigeration*, 25(8):1137 – 1142.

Chen, Y., Deng, S., Xu, X., and Chan, M. (2008). A study on the operational stability of a refrigeration system having a variable speed compressor. *International Journal of Refrigeration*, 31(8):1368 – 1374.

Corberán, J. M., Segurado, J., Colbourne, D., and Gonzálvez, J. (2008). Review of standards for the use of hydrocarbon refrigerants in a/c, heat pump and refrigeration equipment. *International Journal of Refrigeration*, 31(4):748 – 756. Refrigeration with Ammonia and Hydrocarbons.

Danfoss (2010). Technische Broschüre-Absperrventile SVA, SVA-ST,SVA-HS, SVA-SS, `https://assets.danfoss.com/documents/DOC040786416785/DOC040786416785.pdf`, (Online: 10.09.2020)).

Domanski, P., Didion, D., and Doyle, J. (1994). Evaluation of suction-line/liquid-line heat exchange in the refrigeration cycle. *International Journal of Refrigeration*, 17(7):487 – 493.

Domanski, P. A., Brown, J. S., Heo, J., Wojtusiak, J., and McLinden, M. O. (2014). A thermodynamic analysis of refrigerants: Performance limits of the vapor compression cycle. *International Journal of Refrigeration*, 38:71 – 79.

Drexler-Schmid, G., Lauermann, M., Popovac, M., and Baumhakel, A. (2017). FFG Nr.: 843935-HighButane 2.0-Konzeption einer neuartigen Butan-Hochtemepraturwärmepumpe zur Effizienzsteigerung in industriellen Prozessen. publizierbarer Endbericht, Österreichische Forschungsförderungsgesellschaft mbH (FFG).

Eames, I. W., Milazzo, A., and Maidment, G. G. (2014). Modelling thermostatic expansion valves. *International Journal of Refrigeration*, 38:189 – 197.

E+H (2016a). Technische Information: Proline Promag 50P, 53P-Magnetisch-induktives Durchflussmesssystem.

E+H (2016b). Technische Information: Proline Promass 80F, 80M, 83F, 83M-Coriolis-Massdurchfluss-Messsystem.

Eifler, W., Schlücker, E., Spicher, U., and Will, G. (2009). *Küttner Kolbenmaschinen-Kolbenpumpen, Kolbenverdichter, Brennkraftmaschinen*. Vieweg und Teubner.

Elbel, S. and Lawrence, N. (2016). Review of recent developments in advanced ejector technology. *International Journal of Refrigeration*, 62:1 – 18.

ELTAKO (2020). Drehstromzähler DSZ12D-3x65A mit Display,MID geeicht, Online (27.05.2020), `https://www.eltako.com/fileadmin/downloads/de/_bedienung/DSZ12D_28365612-1_internet_dtsch.pdf`.

EN378 (2016). Refrigerating systems and heat pumps- safety and environmental requirements, Austrian Standard International-Standardization and Innovation.

Engie (2018). CO2-Kältemaschinen und CO2-Hochtemperaturwärmepumpen. Online (29.10.2018): https://www.engie-refrigeration.de/.

ESK (2017). ESK-Components-Product Summary, `https://www.esk-schultze.de/Katalog/ESK_Summary.pdf`, (Online: 10.09.2020).

EU (2014). Regulation (EU) No 517/2014 of the European Parliament and of the Council of 16 april 2014 on fluorinated greenhouse gases and repealing regulation (ec) no 842/2006. *Official Journal of the European Union*, 57(L150):195–229.

F-Chart (2016). Engineering Equation Solver v. 9.901. `http://www.fchartsoftware.com/ees/`.

Falkner, S. (2018). *Experimental investigation of injection cooling for water as the working fluid of high temperature heat pumps andtheoretical study of industrial drying processes*. PhD thesis, Institut für Energietechnik und Thermodynamik, TU Wien.

Featherstone, S. (2015). Volume 1: Fundamental Information on Canning. In *A Complete Course in Canning and Related Processes*. Elsevier, 14 edition.

Fellows, P. (2017). *Food Processing Technology-Principles and Practice*. Elsevier, 4 edition.

Fermi, E. (1956). *Thermodynamics*. Dover Publications Inc., New York.

Feynman, R. P., Leighton, R. B., and Sands, M. (2007). *Feynman-Vorlesungen über Physik: Mechanik, Strahlung, Wärme*, volume 1. Oldenbourg, 5 edition.

Frigomec (2012). Datasheet-Liquid Receivers, `https://www.frigomec.com/pdf/ricevitori_di_liquido/1.pdf`, (Online: 10.09.2020)).

Frigopol (2020a). Homepage, `http://www.frigopol.com/`, (Online: 20.05.2020).

Frigopol (2020b). Trennhauben-Kälte-Kompressoren, `http://www.frigopol.com/wp-content/uploads/009-MA-101-01-W2-Standardkompressoren.pdf`, (Online: 15.05.2020).

Gnielinski, V. (2006). *VDI-Wärmeatlas*, chapter G1-Durchströmte Rohre, pages 785–791. Verein Deutscher Ingenieure, VDI-Gesellschaft Verfahrenstechnik und Chemieingenieurwesen (GVC).

Granryd, E. (2001). Hydrocarbons as refrigerants — an overview. *International Journal of Refrigeration*, 24(1):15 – 24.

Grundfos (2016). Grundfos Datenheft: TP,TPD,TPE,TPED, TPE2, TPE2 D, TPE3, TPE3 D, Trockenläuferpumpen in Inlinebauweise.

Hafner, A., Försterling, S., and Banasiak, K. (2014). Multi-ejector concept for R-744 supermarket refrigeration. *International Journal of Refrigeration*, 43:1 – 13.

Hannl, D. (2015). *Absorptions/Kompressions-Wärmepumpe für Hochtemperaturanwendungen mit dem Arbeitsstoffgemisch Ammoniak/Lithiumnitrat*. PhD thesis, Institute of Thermal Engineering, TU Graz.

Harby, K. (2017). Hydrocarbons and their mixtures as alternatives to environmental unfriendly halogenated refrigerants: An updated overview. *Renewable and Sustainable Energy Reviews*, 73:1247 – 1264.

Helminger, F., Kontomaris, K., Pfaffl, J., Hartl, M., and Fleckl, T. (2016). Hochtemperatur-Wärmepumpen-Messergebnisse einer Laboranlage mit HFO-1336mzz-Z bis 160°C Kondensationstemperatur. 14. Symposium Energieinnovation, Technische Universität Graz.

Hölz, H., Mollenhauer, K., and Tschöke, H. (2007). *Dubbel-Taschenbuch für den Maschinenbau*, chapter P: Kolbenmaschinen, pages P2–P90. Springer-Verlag Berlin Heidelberg.

Hoffmann, J. (2015). *Taschenbuch der Messtechnik*. Fachbuchverlag Leipzig im Carl Hanser Verlag, 7 edition.

Huang, L., Tao, L., Tang, C., Chen, Y., Zheng, Z., Wang, G., and Tao, H. (2019). Experimental research on instability of expansion valve–dry evaporator refrigeration system. *Applied Thermal Engineering*, 162:114275.

Huelle, Z. R. (1972). The MSS line–a new approach to the hunting problem. *ASHRAE Journal*, (43-6).

Hughes, D. W., McMullan, J. T., Mawhinney, K. A., Morgan, R., and Sutcliffe, B. L. (1980). Lubricant Related Problems with Heat-Pumps. In *International Compressor Engineering Conference*, number 325, West Lafayette. Purdue University.

IPCC (2014). Climate Change 2014: Sythesis Report. Contribution of Working Groups I, II and III to the Fifth Assessment Report of the Intergovernmental Panel On Climate Change. Online (07.04.2020). Core Writing Team, R.K. Pachauri and L.A. Meyer (eds.), IPCC, Geneva, Switzerland, `https://www.ipcc.ch/site/assets/uploads/2018/02/SYR_AR5_FINAL_full.pdf`.

Kleiber, M. and Joh, R. (2006). *VDI-Wärmeatlas*, chapter D1-Berechnungsmethoden für Stoffeigenschaften, pages 139–173. Verein Deutscher Ingenieure, VDI-Gesellschaft Verfahrenstechnik und Chemieingenieurwesen (GVC).

Kondou, C. and Koyama, S. (2015). Thermodynamic assessment of high-temperature heat pumps using Low-GWP HFO refrigerants for heat recovery. *International Journal of Refrigeration*, 53:126 – 141.

Kontomaris, K. (2014). HFO-1336mzz-Z: High Temperature Chemical Stability and Use as Working Fluid in Organic Rankine Cycles. In *International Refrigeration and Air Conditioning Conference. Paper 1525.*

Kriwan (2017). Vorläufiges Datenblatt-INT280-130.

Lawrence, N. and Elbel, S. (2019). Experimental investigation on control methods and strategies for off-design operation of the transcritical R744 two-phase ejector cycle. *International Journal of Refrigeration*, 106:570 – 582.

Lemmon, E. W., Huber, M. L., and McLinden, M. O. (2013). REFPROP-Reference Fluid Thermodynamic and Transport Properties-Standard Reference Database 23, Version 9.1. National Institute of Standards and Technology.

Liang, N., Shao, S., Xu, H., and Tian, C. (2010). Instability of refrigeration system – a review. *Energy Conversion and Management*, 51(11):2169 – 2178.

Longo, G. (2012). Hydrocarbon Refrigerant Vaporization Inside a Brazed Plate Heat Exchanger. *Journal of Heat Transfer*, 134:101801.

Longo, G. A. (2010). Heat transfer and pressure drop during hydrocarbon refrigerant condensation inside a brazed plate heat exchanger. *International Journal of Refrigeration*, 33(5):944 – 953.

Longo, G. A., Mancin, S., Righetti, G., and Zilio, C. (2015a). A new model for refrigerant boiling inside Brazed Plate Heat Exchangers (BPHEs). *International Journal of Heat and Mass Transfer*, 91:144 – 149.

Longo, G. A., Mancin, S., Righetti, G., and Zilio, C. (2016). HFC404A vaporisation inside a Brazed Plate Heat Exchanger (BPHE): Comparison with the possible long-term low GWP substitutes HC290 (Propane) and HC1270 (Propylene). *Applied Thermal Engineering*, 108:1401 – 1408.

Longo, G. A., Righetti, G., and Zilio, C. (2015b). A new computational procedure for refrigerant condensation inside herringbone-type Brazed Plate Heat Exchangers. *International Journal of Heat and Mass Transfer*, 82:530 – 536.

Longo, G. A., Zilio, C., Righetti, G., and Brown, J. S. (2014). Experimental assessment of the low GWP refrigerant HFO-1234ze(Z) for high temperature heat pumps. *Experimental Thermal and Fluid Science*, 57:293 – 300.

Martin, H. (1996). A theoretical approach to predict the performance of chevron-type plate heat exchangers. *Chemical Engineering and Processing: Process Intensification*, 35(4):301 – 310.

Martin, H. (2006). *VDI-Wärmeatlas*, chapter N6-Druckverlust und Wärmeübergang in Plattenwärmeübertragern, pages 1687–1693. Verein Deutscher Ingenieure, VDI-Gesellschaft Verfahrenstechnik und Chemieingenieurwesen (GVC).

Maurer, T. (2016). *Kältetechnik fuer Ingenieure*. VDE Verlag GmbH.

Mikielewicz, D. and Wajs, J. (2019). Performance of the very high-temperature heat pump with low gwp working fluids. *Energy*, 182:460 – 470.

Mithraratne, P. and Wijeysundera, N. (2002). An experimental and numerical study of hunting in thermostatic-expansion-valve-controlled evaporators. *International Journal of Refrigeration*, 25(7):992 – 998.

Mithraratne, P., Wijeysundera, N., and Bong, T. (2000). Dynamic simulation of a thermostatically controlled counter-flow evaporator. *International Journal of Refrigeration*, 23(3):174 – 189.

Mobil (2018). Mobil Gargoyle Arctic SHC 200 Series, Product Datasheet.

Moisi, H. and Rieberer, R. (2016). Erforderliche Sauggasüberhitzung bei einer R600-Hochtemperaturwärmepumpe – Nutzung der Motorabwärme. In *Deutscher Klima- und Kältetechnischer-Verein (DKV)-Tagung, Kassel, Paper AA II.2.*

Moisi, H. and Rieberer, R. (2017). Refrigerant Selection and Cycle Development for a High Temperature Vapor Compression Heat Pump. In *Proceedings of 12th IEA Heat Pump Conference*, number O 3.4.3, Rotterdam. Internationa Energy Agency.

Moisi, H. and Rieberer, R. (2018). Experimental Analysis of a R600 High Temperature Heat Pump. In *13th IIR-Gustav Lorentzen Conference on Natural Refrigerants (GL2018)*, volume 1 of *Refrigeration Science and Technology Proceedings*, pages 553–560. International Institute of Refrigeration.

Moisi, H., Rieberer, R., and Baumhakel, A. (2018). FFG Nr.: 848892-HotCycle-Kältemittel und Kreislaufdesign für Hochtemperatur-Wärmepumpen kleiner bis mittlerer Leistung mit Trennhaubenkompressor. publizierbarer Endbericht, Österreichische Forschungsförderungsgesellschaft mbH (FFG).

Moisi, H., Rieberer, R., Verdnik, M., and Baumhakel, A. (2017). Entwicklung einer R600-Hochtemperatur-Wärmepumpe - Simulation und erste Messungen. In *Deutscher Klima- und Kältetechnischer-Verein (DKV)-Tagung, Bremen, Paper AA IV.08.*

Morrison, G. (1994). The shape of the temperature-entropy saturation boundary. *International Journal of Refrigeration*, 17(7):494 – 504.

Murthy, A. A., Subiantoro, A., Norris, S., and Fukuta, M. (2019). A review on expanders and their performance in vapour compression refrigeration systems. *International Journal of Refrigeration*, 106:427 – 446.

NI (2020a). National Instruments Homepage, LabView, Online (23.05.2020), https://www.ni.com/de-at/shop/labview/labview-details.html.

NI (2020b). NI cRIO-9072/9073/9074- User manual and specifications, Online (23.05.2020), http://www.ni.com/pdf/manuals/374639f.pdf.

Nilsson, M., Risla, H. N., and Kontomaris, K. (2017). Measured performance of a novel high temperature heat pump with HFO-1336mzz(Z) as the working fluid. In *Proceedings of 12th IEA Heat Pump Conference*, number O.3.5.3, Rotterdam. International Energy Agency.

Noack, R. (2016). Entwicklung einer Hochtemperatur-Wärmepumpe für Nutztemperaturen über 120°C. Deutscher Kälte- und Klimatechnischer Verein,Tagung, Kassel, Presentation IV 17.

Ochsner (2018). Höchstemperatur-Wärmepumpen. Online (29.10.2018): http://ochsner-energietechnik.com/hoechsttemperatur-waermepumpen/.

OIB (2015). OIB-Richtlinie 6: Energieeinsparung und Wärmeschutz, OIB-330.6-009/15, Österreichisches Institut für Bautechnik.

Palm, B. (2008). Hydrocarbons as refrigerants in small heat pump and refrigeration systems – A review. *International Journal of Refrigeration*, 31(4):552 – 563. Refrigeration with Ammonia and Hydrocarbons.

Pitarch, M., Hervas-Blasco, E., Navarro-Peris, E., Gonzálvez-Maciá, J., and Corberán, J. M. (2017a). Evaluation of optimal subcooling in subcritical heat pump systems. *International Journal of Refrigeration*, 78:18 – 31.

Pitarch, M., Navarro-Peris, E., Gonzálvez-Maciá, J., and Corberán, J. M. (2017b). Experimental study of a subcritical heat pump booster for sanitary hot water production using a subcooler in order to enhance the efficiency of the system with a natural refrigerant (R290). *International Journal of Refrigeration*, 73:226 – 234.

Pitarch, M., Navarro-Peris, E., Gonzálvez-Maciá, J., and Corberán, J. M. (2018). Experimental study of a heat pump with high subcooling in the condenser for sanitary hot water production. *Science and Technology for the Built Environment*, 24(1):105–114.

PMR (2016). PMR 160601AN22-Manufacturer offer, unpublished.

Pottker, G. and Hrnjak, P. (2015). Effect of the condenser subcooling on the performance of vapor compression systems. *International Journal of Refrigeration*, 50:156 – 164.

Quijera, J. A., Alriols, M. G., and Labidi, J. (2014). Integration of a solar thermal system in canned fish factory. *Applied Thermal Engineering*, 70(2):1062 – 1072. PRES'13 Process Integration.

Rajapaksha, L. and Suen, K. (2004). Influence of liquid receiver on the performance of reversible heat pumps using refrigerant mixtures. *International Journal of Refrigeration*, 27(1):53 – 62.

Reißner, F. (2015). *Development of a novel high temperature heat pump system*. PhD thesis, Friedrich-Alexander-University, Erlangen-Nuremberg.

Rieberer, R., Zotter, G., Hannl, D., Moser, H., Kotenko, O., Zottel, A., Fleckl, T., and Malenkovic, I. (2015). IEA Heat Pump ProgrammeAnnex 35: Anwendungsmöglichkeitenfür industrielle Wärmepumpen, Berichte aus Energie- und Umweltforschung 17/2015. Technical report, BMVIT.

Sarkar, J., Bhattacharyya, S., and Gopal, M. R. (2007). Natural refrigerant-based subcritical and transcritical cycles for high temperature heating. *International Journal of Refrigeration*, 30(1):3 – 10.

Shah, R. K. and Sekulic, D. P. (2003). *Fundamentals of Heat Exchanger Design*. John Wiley and Sons, Inc., Hoboken, New Jersey.

Shen, B. and Groll, E. A. (2005a). Review Article: A Critical Review of the Influence of Lubricants on the Heat Transfer and Pressure Drop of Refrigerants- Part 1: Lubricant Influence on Pool and Flow Boiling. *HVAC&R Research*, 11(3):341–359.

Shen, B. and Groll, E. A. (2005b). Review Article: A Critical Review of The Influence of Lubricants on the Heat Transfer and Pressure Drop of Refrigerants- Part 2: Lubricant Influence on Condensation and Pressure Drop. *HVAC&R Research*, 11(4):511–526.

Siemens (2010). Stetige Kältemittelventile M3FK..LX.. mit Magnetantrieb, PN32, Datenblatt 4722.

Siemens (2015a). ACVATIX-Stetige Kältemittelventile MVL661..-.. mit Magnetantrieb, PS45, Datenblatt 4714.

Siemens (2015b). Hauptdatenblatt: Dreiwegeventil mit Aussengewinde, PN16, VXG44..

Siemens (2016). Hauptdatenblatt: ACVATIX-Elektromotorische Stellantriebe für Ventile-SAS...

Singh, R. P. and Heldman, D. R. (2014). *Introduction to Food Engineering*. Elsevier, 5 edition.

Skreinig, M. (2016). Modellierung, Auslegung und Konstruktion einer Sauggaskühlung für einen Kältemittelkompressor. Master's thesis, Institute of Thermal Engineering, TU Graz.

Star (2016). Neatpump: Natural refrigerant heat pumps. Online (12.04.2016): http://www.star-ref.co.uk/our-products/neatpump/neatpump-brochure.aspx.

Stephan, P., Schaber, K., Stephan, K., and Mayinger, F. (2013). *Thermodynamik-Grundlagen und technische Anwendungen- Band 1: Einstoffsysteme*. Springer-Verlag Berlin Heidelberg, 19 edition.

Stouffs, P., Tazerout, M., and Wauters, P. (2001). Thermodynamic analysis of reciprocating compressors. *International Journal of Thermal Sciences*, 40(1):52 – 66.

Tamura, I., Taniguchi, H., Sasaki, H., Yoshida, R., Sekiguchi, I., and Yokogawa, M. (1997). An analytical investigation of high-temperature heat pump system with screw compressor and screw expander for power recovery. *Energy Conversion and Management*, 38(10):1007 – 1013. International Symposium on Advance Energy Conversion Systems and Related Technologies.

UN (2015). United Nations: Paris Agreement. Online (07.04.2020). https://unfccc.int/files/essential_background/convention/application/pdf/english_paris_agreement.pdf.

UNEP (1989). The Montreal Protocol on Substances that Deplete the Ozone Layer.

UNEP (2016). Amendment to the Montreal Protocol on Substances that Deplete the Ozone Layer.

Verdnik, M. (2017). Inbetriebnahme und messtechnische Analyse einer R600-Hochtemperaturwärmepumpe. Master's thesis, Institute of Thermal Engineering, TU Graz.

Wedekind, G. L. (1971). An Experimental Investigation Into the Oscillatory Motion of the Mixture-Vapor Transition Point in Horizontal Evaporating Flow. *Journal of Heat Transfer*, 93(1):47–54.

Wedekind, G. L. and Stoecker, W. F. (1968). Theoretical Model for Predicting the Transient Response of the Mixture-Vapor Transition Point in Horizontal Evaporating Flow. *Journal of Heat Transfer*, 90(1):165–174.

Wemmers, A., van Haasteren, A., Kremers, P., and van der Kamp, J. (2017). Test results R600 pilot heat pump. In *Proceedings of 12th IEA Heat Pump Conference*, number O.3.4.2, Rotterdam. International Energy Agency.

Wolf, S. (2017). *Integration von Wärmepumpen in industrielle Produktionssysteme-Potenziale und Instrumente zur Potenzialerschließung.* PhD thesis, Institut für Energiewirtschaft und rationelle Energieanwendung, University of Stuttgart.

Wolf, S., Fahl, U., Blesl, M., Voß, A., and Jakobs, R. (2014). Analyse des Potenzials von Industriewärmepumpen in Deutschland. Technical report, Institut für Energiewirtschaft und Rationelle Energieanwendung-Universität Stuttgart, Informationszentrum Wärmepumpen und Kältetechnik. Endbericht, Förderkennzeichen 0327514A.

Yang, Z., Zhuo, Y., Ercang, L., and Yuan, Z. (2014). Travelling-wave thermoacoustic high-temperature heat pump for industrial waste heat recovery. *Energy*, 77:397 – 402.

A APPENDIX

A.1 List of Refrigerants

The list of investigated working fluids presented in Table A.1 for the refrigerant selection is based on ESS v. 9.901 (F-Chart, 2016). As in 2016 the HFO refrigerant R1336mzz-Z has not been available in the mentioned software version and has therefore been analysed based on property data given in Kontomaris (2014).

Table A.1: List of investigated working fluids based on the EES v. 9.901 fluid property database

Refrigerant	crit. Temperature [°C]	Refrigerant	crit. Temperature [°C]
ACETONE	235	R11	198
ARGON	-122.5	R113	214.1
BENZENE	288.9	R114	145.7
CarbonylSulfide	105.6	R116	19.88
cis-2-butene	162.6	R12	112
CYCLOHEXANE	280.5	R123	183.7
CYCLOPENTANE	238.6	R1233zd(E)	165.6
D4	313.3	R1234yf	94.7
D5	346	R1234ze(E)	109.4
DIMETHYLETHER	127.2	R1234ze(Z)	150.1
ETHANE	32.17	R124	122.3
ETHANOL	241.6	R125	66.02
ETHYLBENZENE	344	R13	28.86
ETHYLENE	9.195	R134a	101
FC72	175.7	R13B1	67
FC87	147.9	R14	-45.65
FLUORINE	-128.7	R141B	204.2
HFE7000	164.6	R142b	137.1
HFE7100	195.3	R143a	72.7
HFE7500	261	R143m	104.8
HYDROGEN	-240	R152a	113.3
HYDROGENSULFIDE	100.2	R161	102.1
ISCEON89	70.1	R218	71.87
ISOBUTENE	144.9	R22	96.13
ISOHEXANE	224.6	R227ea	102.8
ISOPENTANE	187.2	R23	26.13
isopropanol	235.2	R236ea	139.3
KRYPTON	-63.72	R236fa	124.9
MD4M	380.1	R245fa	154
MDM	290.9	R290	96.68
METHANE	-82.59	R32	78.11
METHANOL	240.2	R365mfc	186.9
mm	245.5	R404A	72.12
M-XYLENE	343.7	R407C	86.2
n-BUTANE	152	R41	44.13
n-DECANE	344.6	R410A	71.34
n-DECANE	344.6	R423A	99.52
n-DODECANE	385	R500	105.5
NEON	-228.7	R502	82.16
NEOPENTANE	160.6	R507A	70.62
n-HEPTANE	267	R508B	13.99
n-HEXANE	234.7	R600	152
NITROGEN	-147	R600a	134.7
NITROUSOXIDE	36.37	R717	132.3
n-NONANE	321.4	R718	374
n-OCTANE	296.2	R744	30.98
n-PENTANE	196.5	RC318	115.2
n-UNDECANE	365.7	SES36	177.6
OXYGEN	-118.6	Steam	374
O-XYLENE	357.1	SULFURDIOXIDE	157.5
ParaHydrogen	-240.2	SULFURHEXAFLUORIDE	45.57
PROPYLENE	92.42	TOLUENE	318.6
p-XYLENE	343	TRANS-2-BUTENE	155.5
		XENON	16.59

A.2 Complementary Heat Exchanger Data

Table A.2: Complementary Evaporator data

Description	Symbol	Unit	Evaporator	
Manufacturer	-	-	Alfa Laval	Source
Model	-	-	AC-70X-40M	-
effective heat transfer area	$A_{phx,ht}$	$[m^2]$	1.94	AlfaLaval (2016b)
effective geometric Area ($W_{phx,p} \cdot H_{phx,p,ht} \cdot [n_{phx,p} - 2]$)	$A_{phx,geo}$	$[m^2]$	1.83	calc. based on AlfaLaval (2016b)
plate width	$W_{phx,p}$	[m]	0.111	AlfaLaval (2016b)
plate height	$H_{phx,p}$	[m]	0.526	AlfaLaval (2016b)
vertical distance between center of connections	$H_{phx,p,con}$	[m]	0.466	AlfaLaval (2016b)
effective plate height for heat transfer	$H_{phx,p,ht}$	[m]	0.433	calc. based on AlfaLaval (2016b)
heat exchanger length	$L_{phx,p}$	[m]	0.127	AlfaLaval (2016b)
plate thickness	$s_{phx,p}$	[m]	0.0004	AlfaLaval (2016b)
maximum connection diameter	$d_{phx,con,max}$	[m]	0.033	AlfaLaval (2016b)
Number of plates	$n_{phx,p}$	[-]	40	AlfaLaval (2016b)
number of channels high temperature side	$n_{phx,ch,HT}$	[-]	20	AlfaLaval (2016b)
number of channels low temperature side	$n_{phx,ch,LT}$	[-]	19	AlfaLaval (2016b)
total number of channels	$n_{phx,ch,tot}$	[-]	39	AlfaLaval (2016b)
corrugation amplitude	$a_{phx,p}$	[m]	0.0019	AlfaLaval (2016b)
corrugation angle	$\psi_{phx,p}$	[°]	68.6	calc. based on AlfaLaval (2016b)
area enlargement factor ($A_{phx,ht}/A_{phx,geo}$)	$\Phi_{phx,calc}$	[-]	1.06	calc. based on AlfaLaval (2016b)
corrugation type	-	-	Chevron	assumed
flow arrangement	-	-	counter current	AlfaLaval (2016b)
Plate material	-	-	Stainless Steel (Alloy 316)	AlfaLaval (2016b)
high temperature side medium	-	-	Water	boundary condition
low temperature side medium	-	-	R600	boundary condition

Table A.3: Complementary Condenser data

Description	Symbol	Unit	Condenser	
Manufacturer	-	-	Alfa Laval	Source
Model	-	-	CB62-40AH-F	-
effective heat transfer area	$A_{phx,ht}$	$[m^2]$	2.3	AlfaLaval (2016b)
effective geometric Area ($W_{phx,p} \cdot H_{phx,p,ht} \cdot [n_{phx,p} - 2]$)	$A_{phx,geo}$	$[m^2]$	1.9	calc. based on AlfaLaval (2016b)
plate width	$W_{phx,p}$	[m]	0.113	AlfaLaval (2016b)
plate height	$H_{phx,p}$	[m]	0.529	AlfaLaval (2016b)
vertical distance between center of connections	$H_{phx,p,con}$	[m]	0.476	AlfaLaval (2016b)
effective plate height for heat transfer	$H_{phx,p,ht}$	[m]	0.4423	calc. based on AlfaLaval (2016b)
heat exchanger length	$L_{phx,p}$	[m]	0.141	AlfaLaval (2016b)
plate thickness	$s_{phx,p}$	[m]	0.0003	AlfaLaval (2016b)
maximum connection diameter	$d_{phx,con,max}$	[m]	0.0337	AlfaLaval (2016b)
Number of plates	$n_{phx,p}$	[-]	40	AlfaLaval (2016b)
number of channels high temperature side	$n_{phx,ch,HT}$	[-]	19	AlfaLaval (2016b)
number of channels low temperature side	$n_{phx,ch,LT}$	[-]	20	AlfaLaval (2016b)
total number of channels	$n_{phx,ch,tot}$	[-]	39	AlfaLaval (2016b)
corrugation amplitude	$a_{phx,p}$	[m]	0.00168	AlfaLaval (2016b)
corrugation angle	$\psi_{phx,p}$	[°]	66.9	calc. based on AlfaLaval (2016b)
area enlargement factor ($A_{phx,ht}/A_{phx,geo}$)	$\Phi_{phx,calc}$	[-]	1.2105263 16	calc. based on AlfaLaval (2016b)
corrugation type	-	-	Chevron	assumed
flow arrangement	-	-	counter current	AlfaLaval (2016b)
Plate material	-	-	Stainless Steel (Alloy 316)	AlfaLaval (2016b)
high temperature side medium	-	-	R600	boundary condition
low temperature side medium	-	-	Water	boundary condition

Table A.4: Complementary Subcooler data

Description	Symbol	Unit	Subcooler	
Manufacturer	-	-	Alfa Laval	Source
Model	-	-	CB30-14H	-
effective heat transfer area	$A_{phx,ht}$	$[m^2]$	0.35	AlfaLaval (2016b)
effective geometric Area ($W_{phx,p} \cdot H_{phx,p,ht} \cdot [n_{phx,p} - 2]$)	$A_{phx,geo}$	$[m^2]$	0.29	calc. based on AlfaLaval (2016b)
plate width	$W_{phx,p}$	[m]	0.113	AlfaLaval (2016b)
plate height	$H_{phx,p}$	[m]	0.313	AlfaLaval (2016b)
vertical distance between center of connections	$H_{phx,p,con}$	[m]	0.25	AlfaLaval (2016b)
effective plate height for heat transfer	$H_{phx,p,ht}$	[m]	0.2163	calc. based on AlfaLaval (2016b)
heat exchanger length	$L_{phx,p}$	[m]	0.069	AlfaLaval (2016b)
plate thickness	$s_{phx,p}$	[m]	0.0004	AlfaLaval (2016b)
maximum connection diameter	$d_{phx,con,max}$	[m]	0.0337	AlfaLaval (2016b)
Number of plates	$n_{phx,p}$	[-]	14	AlfaLaval (2016b)
number of channels high temperature side	$n_{phx,ch,HT}$	[-]	6	AlfaLaval (2016b)
number of channels low temperature side	$n_{phx,ch,LT}$	[-]	7	AlfaLaval (2016b)
total number of channels	$n_{phx,ch,tot}$	[-]	13	AlfaLaval (2016b)
corrugation amplitude	$a_{phx,p}$	[m]	0.00191	AlfaLaval (2016b)
corrugation angle	$\psi_{phx,p}$	[°]	75.1	calc. based on AlfaLaval (2016b)
area enlargement factor ($A_{phx,ht}/A_{phx,geo}$)	$\Phi_{phx,calc}$	[-]	1.206896552	calc. based on AlfaLaval (2016b)
corrugation type	-	-	Chevron	assumed
flow arrangement	-	-	counter current	AlfaLaval (2016b)
Plate material	-	-	Stainless Steel (Alloy 316)	AlfaLaval (2016b)
high temperature side medium	-	-	R600	boundary condition
low temperature side medium	-	-	Water	boundary condition

Table A.5: Complementary Superheater data

Description	Symbol	Unit	Superheater	
Manufacturer	-	-	Alfa Laval	Source
Model	-	-	CB110-20L	-
effective heat transfer area	$A_{phx,ht}$	$[m^2]$	2.02	AlfaLaval (2016b)
effective geometric Area ($W_{phx,p} \cdot H_{phx,p,ht} \cdot [n_{phx,p} - 2]$)	$A_{phx,geo}$	$[m^2]$	1.58	calc. based on AlfaLaval (2016b)
plate width	$W_{phx,p}$	[m]	0.191	AlfaLaval (2016b)
plate height	$H_{phx,p}$	[m]	0.616	AlfaLaval (2016b)
vertical distance between center of connections	$H_{phx,p,con}$	[m]	0.519	AlfaLaval (2016b)
effective plate height for heat transfer	$H_{phx,p,ht}$	[m]	0.4587	calc. based on AlfaLaval (2016b)
heat exchanger length	$L_{phx,p}$	[m]	0.139	AlfaLaval (2016b)
plate thickness	$s_{phx,p}$	[m]	0.0004	AlfaLaval (2016b)
maximum connection diameter	$d_{phx,con,max}$	[m]	0.0603	AlfaLaval (2016b)
Number of plates	$n_{phx,p}$	[-]	20	AlfaLaval (2016b)
number of channels high temperature side	$n_{phx,ch,HT}$	[-]	9	AlfaLaval (2016b)
number of channels low temperature side	$n_{phx,ch,LT}$	[-]	10	AlfaLaval (2016b)
total number of channels	$n_{phx,ch,tot}$	[-]	19	AlfaLaval (2016b)
corrugation amplitude	$a_{phx,p}$	[m]	0.00216	AlfaLaval (2016b)
corrugation angle	$\psi_{phx,p}$	[°]	60	calc. based on AlfaLaval (2016b)
area enlargement factor ($A_{phx,ht}/A_{phx,geo}$)	$\Phi_{phx,calc}$	[-]	1.278481013	calc. based on AlfaLaval (2016b)
corrugation type	-	-	Chevron	assumed
flow arrangement	-	-	counter current	AlfaLaval (2016b)
Plate material	-	-	Stainless Steel (Alloy 316)	AlfaLaval (2016b)
high temperature side medium	-	-	Water	boundary condition
low temperature side medium	-	-	R600	boundary condition

Table A.6: Complementary IHX data

Description	Symbol	Unit	IHX	
Manufacturer	-	-	Alfa Laval	Source
Model	-	-	CB30-30L-F	-
effective heat transfer area	$A_{phx,ht}$	$[m^2]$	0.81	AlfaLaval (2016b)
effective geometric Area ($W_{phx,p} \cdot H_{phx,p,ht} \cdot [n_{phx,p} - 2]$)	$A_{phx,geo}$	$[m^2]$	0.69	calc. based on AlfaLaval (2016b)
plate width	$W_{phx,p}$	[m]	0.113	AlfaLaval (2016b)
plate height	$H_{phx,p}$	[m]	0.313	AlfaLaval (2016b)
vertical distance between center of connections	$H_{phx,p,con}$	[m]	0.25	AlfaLaval (2016b)
effective plate height for heat transfer	$H_{phx,p,ht}$	[m]	0.217	calc. based on AlfaLaval (2016b)
heat exchanger length	$L_{phx,p}$	[m]	0.106	AlfaLaval (2016b)
plate thickness	$s_{phx,p}$	[m]	0.0004	AlfaLaval (2016b)
maximum connection diameter	$d_{phx,con,max}$	[m]	0.033	AlfaLaval (2016b)
Number of plates	$n_{phx,p}$	[-]	30	AlfaLaval (2016b)
number of channels high temperature side	$n_{phx,ch,HT}$	[-]	14	AlfaLaval (2016b)
number of channels low temperature side	$n_{phx,ch,LT}$	[-]	15	AlfaLaval (2016b)
total number of channels	$n_{phx,ch,tot}$	[-]	29	AlfaLaval (2016b)
corrugation amplitude	$a_{phx,p}$	[m]	0.00191	AlfaLaval (2016b)
corrugation angle	$\psi_{phx,p}$	[°]	54.7	calc. based on AlfaLaval (2016b)
area enlargement factor ($A_{phx,ht}/A_{phx,geo}$)	$\Phi_{phx,calc}$	[-]	1.173913043	calc. based on AlfaLaval (2016b)
corrugation type	-	-	Chevron	assumed
flow arrangement	-	-	counter current	AlfaLaval (2016b)
Plate material	-	-	Stainless Steel (Alloy 316)	AlfaLaval (2016b)
high temperature side medium	-	-	R600 (liquid)	boundary condition
low temperature side medium	-	-	R600 (vapour)	boundary condition

A.3 Sensor and Control Signals

The following tables have been obtained from Verdnik (2017), translated and modified.

Table A.7: Refrigerant correlated sensor and control signals

Refrigerant Circuit				
Quantity	Sensor type	Symbol	Unit	Module/Connector
Temperature ref. state 1	Pt100	$t_{ref,1}$	°C	Mod6 / RTD0
Temperature ref. state 2		$t_{ref,2}$	°C	Mod6 / RTD1
Temperature ref. state 3	Type T	$t_{ref,3}$	°C	Mod8 / TC6
Temperature ref. state 4		$t_{ref,4}$	°C	Mod8 / TC5
Temperature ref. state 5		$t_{ref,5}$	°C	Mod6 / RTD2
Temperature ref. state 6		$t_{ref,6}$	°C	Mod6 / RTD3
Temperature ref. state 7	Pt100	$t_{ref,7}$	°C	Mod7 / RTD0
Temperature ref. state 8		$t_{ref,8}$	°C	Mod7 / RTD1
Temperature ref. state 9		$t_{ref,9}$	°C	Mod7 / RTD2
Ambient pressure (absolute)		p_{amb}	bar	Mod2 / AI 7
Pressure ref. state 1 (relative)		$p_{ref,1}$	bar	Mod2 / AI8
Pressure ref. state 2 (relative)		$p_{ref,2}$	bar	Mod2 / AI9
Pressure ref. state 4r (relative)	strain gauge	$p_{ref,4r}$	bar	Mod2 / AI12
Pressure ref. state 6 (relative)		$p_{ref,6}$	bar	Mod2 / AI11
Pressure ref. state 8 (relative)		$p_{ref,8}$	bar	Mod2 / AI10
Pressure ref. state 9 (relative)		$p_{ref,9}$	bar	Mod2 / AI13
Refrigerant massflow	coriolis	$\dot{m}_{ref}$	kg/s	Mod2 / AI0
EXV position response	-	I_{EXV}	%	Mod2 / AI2
Refrigerant concentration	catalytic combustion	q_{R600}	% of LFL	Mod2 / AI1

Table A.8: Compressor correlated sensor and control signals

Compressor				
Quantity	Sensor Type	Symbol	Unit	Module/Connector
Total energy consumption	impulse counter	$W_{comp,el}$	J	Mod1 / DI6
Inverter output power	integrated	P_{FI}	W	Mod2 / AI3
Inverter output frequency		f	Hz	Mod5 / AI3
Winding head temperature	Pt1000	$t_{EM,wh}$	°C	Mod2 / AI6
Stator temperature 1	Type T	$t_{sf,Fe,1}$	°C	Mod8 / TC12
Stator temperature 2	Type T	$t_{sf,Fe,2}$	°C	Mod8 / TC13

Table A.9: Source and sink hydraulics correlated sensor and control signals

Source and sink hydraulics				
Quantity	Sensor Type	Symbol	Unit	Module/Connector
Temperature superheater inlet	Type T	$t_{source,1}$	°C	Mod8 / TC3
Temperature evaporator inlet		$t_{source,2}$	°C	Mod8 / TC2
Temperature evaporator outlet		$t_{source,3}$	°C	Mod8 / TC4
Temperature subcooler inlet		$t_{sink,1}$	°C	Mod8 / TC7
Temperature condenser inlet		$t_{sink,2}$	°C	Mod8 / TC0
Temperature condenser outlet		$t_{sink,3}$	°C	Mod8 / TC1
Source volume flow	MID	$\dot{V}_{source}$	dm^3/s	Mod2 / AI5
Sink volume flow		$\dot{V}_{sink}$	dm^3/s	Mod2 / AI4
Source valve position response	integrated	I_{source}	%	Mod5 / AI2
Sink valve position response		I_{sink}	%	Mod5 / AI1

Table A.10: Control signals of the heat pump test rig

Signal	Module/Connector
Refrigerant circuit	
EXV control	Mod3 / AO0
EXV closing	Mod1 / DO4
VHIX control	Mod3 / AO1
Compressor unit	
Compressor on	Mod1 / DO3
Frequency	Mod3 / AO2
Source and sink hydraulics	
Source mixing valve control	Mod4 / AO2
Sink mixing valve control	Mod4 / AO1
Pump source infrastructure	Mod1 / DO6
Pump sink infrastructure	Mod1 / DO5

A.4 Experimental Data

The listed experimental data in the following tables are the basis for the performance and parameter maps presented in Sections 5.5 and 5.6.

Table A.11: Experimental data of refrigerant temperatures for a compressor frequency of 35 Hz

No.	Comment	f_{set}	$t_{source,in,set}$	$t_{sink,in,set}$	$t_{ref,1}$	$t_{ref,2}$	$t_{ref,3}$	$t_{ref,4}$	$t_{ref,5}$	$t_{ref,6}$	$t_{ref,7}$	$t_{ref,8}$	$t_{ref,9}$
-	-	[°C]	[°C]	[°C]	[°C]	[°C]	[°C]	[°C]	[°C]	[°C]	[°C]	[°C]	[°C]
1		35	50	50	57.54	91.56	90.37	51.24	50.29	51.54	43.59	43.21	49.87
2		35	50	60	59.18	100.8	99.43	61.29	56.78	61.45	44.05	43.39	50.07
3		35	50	70	60.29	110.1	108.6	71.4	62.48	71.35	44.28	43.4	50.2
4		35	50	80	60.98	118.2	116.7	81.33	66.87	80.95	44.44	47.37	50.25
5		35	60	60	66.59	101	100.4	61.65	55.81	61.73	53.02	52.6	59.8
6	Superheater	35	60	70	66.46	108.4	107.5	71.73	60.93	71.61	53.35	52.6	59.86
7		35	60	80	67.36	117.6	116.5	81.85	67.57	81.58	53.66	54.29	59.98
8		35	70	70	72.96	108.2	106.9	72.56	55.34	72.42	62.53	61.91	69.61
9		35	70	80	74.13	117	115.7	82.63	62.89	82.36	62.94	64.43	69.72
10		35	80	80	83.11	118.5	117.8	83.15	70.03	83.15	72.84	72.12	79.55
11		35	50	50	54.99	90.1	88.3	51.15	40.62	51.01	41.73	47.84	48.36
12		35	50	60	56.81	99.01	97.37	61.13	48.05	60.84	42.29	48.53	48.74
13		35	50	70	58.63	108.7	107.1	71.19	56.54	70.8	42.79	48.96	49.05
14		35	50	80	60.13	117.9	116.5	81.33	64.67	80.8	43.49	49.46	49.56
15		35	60	60	64.89	100.3	99.22	61.58	56.86	61.74	51.5	58.38	58.38
16	Basic	35	60	70	65.8	108.8	107.7	71.69	62.34	71.67	51.95	58.58	58.61
17		35	60	80	66.36	117.4	116.2	81.9	67.06	81.61	52.53	58.92	59.05
18		35	70	70	72.44	108.4	107.4	72.29	61.97	72.29	61.1	67.93	68.26
19		35	70	80	74.1	117.5	116.5	82.4	68.95	82.3	62.06	68.82	68.97
20		35	80	80	81.55	118	117.1	83.13	70.09	83.15	71.26	77.65	78.3
21		35	50	50	56.29	91.3	89.3	51.23	50.27	50.19	41.85	48.4	49.55
22		35	50	60	62.88	103.9	101.8	61.15	56.67	56.61	42.45	48.98	54.93
23		35	50	70	68.58	115.8	113.1	71.09	62.52	62.39	42.25	48.81	60.05
24		35	50	80	74.47	127.3	124.6	81.08	68.69	68.48	42.7	49.07	65.75
25		35	60	60	66.84	102.4	101.1	61.64	60.6	60.57	51.54	58.72	59.87
26	IHX	35	60	70	72.33	114.5	112.9	71.68	67.06	66.96	51.9	58.98	64.91
27		35	60	80	77.19	125.3	123.3	81.68	73.26	73.1	52.16	59.06	70.06
28		35	70	70	74.25	110.1	109.1	72.45	71.13	71.01	61.3	68.75	70.04
29		35	70	80	80.65	122.9	122	82.22	77.67	77.58	61.88	69.18	75.07
30		35	80	80	83.88	120.5	119.7	83.04	81.62	81.5	71.48	78.77	80.27

Table A.12: Experimental data of source and sink temperatures for a compressor frequency of 35 Hz

No.	Comment	$t_{sink,1}$	$t_{sink,2}$	$t_{sink,3}$	$t_{source,1}$	$t_{source,2}$	$t_{source,3}$
-	-	[°C]	[°C]	[°C]	[°C]	[°C]	[°C]
1	Superheater	50.01	55.09	79.85	50.01	47.89	44.87
2		59.99	65.36	89.65	50.01	48.46	45.01
3		70	75.94	100.1	49.99	49.32	45.21
4		80.02	86.46	109.8	50.01	50.05	45.28
5		60	65.37	90.43	60.01	59.3	55.29
6		70	75.8	100.1	59.98	59.69	55.16
7		79.99	86.4	110.4	60	60.02	55.13
8		70.01	76.45	100.4	70.05	70.02	65.35
9		79.99	86.83	110	69.99	70.07	65.3
10		79.97	86.41	109.9	80	79.55	75.09
11	Basic	50.01	55.44	80.43	49.86	50.01	44.99
12		59.99	65.67	90.1	49.85	50	45.3
13		69.98	76.11	100.2	49.84	49.98	44.98
14		80.03	86.74	110.3	50	50.13	44.96
15		60.01	65.35	89.91	59.85	60	54.99
16		70	75.9	99.8	59.85	60	54.8
17		80	86.78	110.3	59.84	60.01	54.85
18		70	76.02	100.3	69.82	70	64.6
19		79.98	86.37	109.9	69.81	70	65.21
20		80.01	86.51	110	79.79	80	74.63
21	IHX	50.01	55.49	80.6	49.87	50.01	45.18
22		60	65.47	90.41	49.85	49.99	45.05
23		69.99	75.64	100.1	49.87	50	45.14
24		80.04	85.84	110.5	49.89	50.02	45.24
25		60.01	65.35	90.03	59.86	60.02	55.13
26		70.01	75.7	100.4	59.81	59.98	55.11
27		80.01	85.97	110.3	59.85	60	55.15
28		70.04	76.22	100.7	69.8	69.99	65.03
29		80.01	85.82	110.3	69.84	70.01	65.3
30		80.01	86.21	110.4	79.79	80.01	75.11

Table A.13: Experimental data of absolute refrigerant and ambient pressures for a compressor frequency of 35 Hz

No.	Comment	$p_{abs,ref,1}$	$p_{abs,ref,2}$	$p_{ref,4r}$	$p_{abs,ref,8}$	$p_{abs,ref,8}$	$p_{abs,ref,6}$	p_{amb}
-	-	[bar]	[bar]	[bar]	[bar]	[bar]	[bar]	[bar]
1		3.95	9.812	9.625	9.621	4.074	4.037	0.9634
2		3.981	12.01	11.86	11.85	4.1	4.058	0.9636
3		3.999	14.77	14.63	14.63	4.096	4.071	0.9637
4		4.008	17.81	17.68	17.68	4.092	4.077	0.964
5		5.072	12.3	12.08	12.07	5.229	5.177	0.973
6	Superheater	5.088	14.99	14.8	14.79	5.229	5.185	0.9727
7		5.128	18.16	18.01	17.99	5.238	5.2	0.9724
8		6.424	15.35	15.07	15.03	6.635	6.564	0.967
9		6.461	18.26	18.04	18	6.641	6.58	0.967
10		8.158	18.31	17.98	17.88	8.4	8.311	0.9664
11		3.802	10.05	9.876	9.873	3.866	3.882	0.9634
12		3.836	12.25	12.1	12.11	3.898	3.921	0.9634
13		3.864	14.93	14.77	14.78	3.948	3.952	0.9635
14		3.936	18.03	17.9	17.91	4.002	4.004	0.9637
15		4.914	12.19	12	11.98	5.01	4.999	0.9647
16	Basic	4.948	14.85	14.67	14.65	5.03	5.028	0.9645
17		4.998	18.13	17.97	17.95	5.085	5.083	0.9642
18		6.242	15.21	14.95	14.91	6.379	6.354	0.9652
19		6.358	18.15	17.93	17.89	6.474	6.464	0.9658
20		7.916	18.36	18.04	17.95	8.084	8.07	0.966
21		3.807	10.06	9.896	9.89	3.886	3.895	0.9857
22		3.85	12.12	11.99	11.99	3.945	3.938	0.9857
23		3.835	14.55	14.4	14.39	3.926	3.907	0.9712
24		3.871	17.45	17.34	17.33	3.953	3.95	0.9715
25		4.904	12.19	11.98	11.97	5.041	5.006	0.9719
26	IHX	4.946	14.77	14.58	14.56	5.074	5.038	0.9718
27		4.973	17.64	17.5	17.48	5.081	5.072	0.9718
28		6.258	15.27	15.03	14.98	6.429	6.397	0.9719
29		6.349	17.97	17.77	17.72	6.497	6.465	0.9815
30		7.965	18.46	18.13	18.04	8.16	8.119	0.9815

Table A.14: Experimental data of remaining quantities for a compressor frequency of 35 Hz

No.	Comment	$\dot{m}_{ref}$	$\dot{V}_{source}$	$\dot{V}_{sink}$	$P_{comp,FI}$	$t_{sf,Fe,2}$	$t_{sf,Fe,1}$	$t_{EM,wh}$	I_{EXV}	τ_{rec}	$P_{comp,el}$
-	-	[kg/s]	[dm^3/s]	[dm^3/s]	[W]	[°C]	[°C]	[°C]	[%]	[s]	[W]
1		0.0462	0.1486	0.7102	2992	62.88	65	90.61	30.85	1251	3244
2		0.04463	0.1399	0.6534	3451	65.53	67.48	96.65	27.76	1275	3651
3		0.04256	0.1257	0.595	3848	67.21	69.03	100.2	24.99	1275	4065
4		0.04041	0.1133	0.5197	4159	68.27	70.02	102.3	22.15	1283	4384
5		0.05877	0.1787	0.9555	3637	72.44	75.08	106	33.76	1285	3837
6	Superheater	0.05672	0.1647	0.83	4123	72.05	74.67	104.9	29.95	1275	4355
7		0.05432	0.1484	0.7129	4581	73.41	76.03	108.6	27.06	1312	4833
8		0.07425	0.212	1.162	4340	77.92	80.72	109.8	35.72	1280	4582
9		0.07169	0.1973	1.024	4923	79.38	82.29	115.2	32.73	1274	5196
10		0.0947	0.2659	1.343	5063	87.8	91.19	127.1	43.39	1279	5350
11		0.04375	0.1348	0.7109	3010	60.74	62.65	86.97	26.15	1208	3192
12		0.04246	0.1275	0.6844	3439	63.42	65.16	92.69	23.61	1212	3637
13		0.04079	0.1178	0.5646	3800	65.94	67.48	97.62	21.58	1215	4019
14		0.03929	0.1071	0.474	4109	68.04	69.23	101.2	19.93	1218	4343
15		0.0566	0.1752	0.8886	3589	70.42	72.98	101.9	32.6	1321	3793
16	Basic	0.05473	0.1621	0.757	4066	71.81	74.13	105.4	29.22	1243	4294
17		0.05277	0.1447	0.6726	4523	72.57	74.92	107.2	26.23	1227	4782
18		0.07187	0.2076	1.005	4298	76.94	80.2	109.4	36.08	1303	4527
19		0.07046	0.1964	1.015	4852	79.18	82.57	115.7	33.14	1290	5127
20		0.09148	0.2549	1.228	5084	85.83	89.23	122.9	41.44	1232	5374
21		0.04384	0.1365	0.7444	3017	62.03	64.06	88.7	26.75	1317	3196
22		0.04253	0.1322	0.6768	3441	69.43	71.5	99.32	24.38	767.8	3643
23		0.04011	0.1229	0.6157	3780	75.71	77.85	107.3	21.6	616.8	4004
24		0.03822	0.1126	0.5659	4124	81.88	84.15	114.5	19.34	649.5	4362
25		0.05653	0.1779	0.9257	3612	72.79	75.75	105.9	32.9	621.5	3811
26	IHX	0.05425	0.1656	0.8446	4091	78.8	81.81	114	29.16	705.5	4317
27		0.05183	0.1529	0.7663	4542	83.82	86.77	119.8	25.98	628.9	4797
28		0.07194	0.2098	1.112	4338	78.97	82.33	112.5	36.24	720.2	4579
29		0.06941	0.2024	1.067	4890	85.87	89.53	124.5	33.09	651.2	5186
30		0.09138	0.2587	1.372	5202	88.41	91.86	127.9	41.02	653.5	5520

Table A.15: Experimental data of refrigerant temperatures for a compressor frequency of 50 Hz

No.	Comment	f_{set}	$t_{source,in,set}$	$t_{sink,in,set}$	$t_{ref,1}$	$t_{ref,2}$	$t_{ref,3}$	$t_{ref,4}$	$t_{ref,5}$	$t_{ref,6}$	$t_{ref,7}$	$t_{ref,8}$	$t_{ref,9}$
-	-	[°C]	[°C]	[°C]	[°C]	[°C]	[°C]	[°C]	[°C]	[°C]	[°C]	[°C]	[°C]
1		50	50	50	56.76	94.37	93.08	51.67	49.38	51.87	43.34	42.62	48.85
2		50	50	60	58.31	102.7	101.5	61.8	53.68	61.78	44.34	43.17	49.49
3		50	50	70	59.69	111.2	110	71.76	60	71.61	45.07	43.49	49.86
4		50	50	80	60.91	120.1	119	81.84	66.86	81.54	45.44	43.55	49.98
5	Superheater	50	60	60	65.57	103.5	102.8	62.08	56.89	62.25	52.89	52.03	58.77
6		50	60	70	66.64	111.8	111	72.2	62.65	72.28	53.84	52.44	59.27
7		50	60	80	67.94	120.4	119.7	82.38	67.31	82.28	54.72	52.84	59.8
8		50	70	70	73.4	111.3	110.2	73.02	61.5	73.13	62.76	61.61	68.75
9		50	70	80	74.06	119.5	118	83.38	65.38	83.33	63.96	62.2	69.47
10		50	80	80	81.06	120.5	119.6	83.99	69.6	84.04	72.24	70.8	77.88
11		50	50	50	55.43	94.64	92.48	51.64	41.46	51.64	41.37	47.1	47.35
12		50	50	60	57.35	103	101.2	61.64	48.73	61.5	42.39	47.98	48.03
13		50	50	70	58.95	112	110.6	71.79	56.91	71.54	43.34	48.59	48.6
14		50	50	80	60.68	121.1	119.9	81.77	66.51	81.5	44.09	49.01	49.05
15	Basic	50	60	60	64.42	103.8	103	62.19	58.01	62.42	51.05	57.17	57.23
16		50	60	70	65.56	111.6	110.7	72.18	63.33	72.26	52.22	57.94	57.95
17		50	60	80	66.17	119.5	118.6	82.4	67.94	82.29	53.08	58.35	58.42
18		50	70	70	72.08	111.4	110.4	73.08	62.64	73.16	61.12	67.27	67.55
19		50	70	80	73.62	119.7	118.9	83.23	69.2	83.23	62.57	68.35	68.46
20		50	80	80	80.1	120.5	119.6	84.08	70.45	84.17	70.54	76.43	76.63
21		50	50	50	57.81	97.09	94.57	51.65	50.24	50.18	41.33	47.57	49.24
22		50	50	60	63.31	107.8	105.5	61.59	56.61	56.51	41.53	47.72	54.27
23		50	50	70	69.7	120.5	118.7	71.48	62.84	62.73	42.21	48	59.55
24		50	50	80	75.9	132.8	131.2	81.03	68.96	68.9	42.79	48.46	65.09
25	IHX	50	60	60	66.64	106.1	105.5	61.55	60.17	60.17	50.92	57.52	59.15
26		50	60	70	71.94	117.8	117.1	71.44	66.69	66.65	51.57	57.9	64.02
27		50	60	80	76.99	128.3	127.4	81.49	73.32	73.21	52.31	58.43	69.28
28		50	70	70	74.38	113.3	112.5	72.78	71.14	71.06	60.99	67.9	69.71
29		50	70	80	79.7	124.7	123.7	82.92	78.08	77.96	62.01	68.54	74.75
30		50	80	80	82.94	122.7	121.8	83.74	81.56	81.45	70.47	77.05	79.52

Table A.16: Experimental data of source and sink temperatures for a compressor frequency of 50 Hz

No.	Comment	$t_{sink,1}$	$t_{sink,2}$	$t_{sink,3}$	$t_{source,1}$	$t_{source,2}$	$t_{source,3}$
-	-	[°C]	[°C]	[°C]	[°C]	[°C]	[°C]
1	Superheater	50.01	54.86	79.94	50	47.44	44.67
2		60.04	65.4	90.6	50	48.23	45.24
3		70	75.45	99.84	50	48.84	45.48
4		80.01	85.94	109.9	50	48.66	45
5		60	64.92	89.83	60	58.36	54.84
6		69.98	75.41	100	60	58.63	54.95
7		80	85.97	110.2	59.99	59.39	55.31
8		69.99	75.76	99.79	70	68.74	64.73
9		79.99	86.62	110.2	70.01	69.39	65.21
10		79.99	86.42	110.3	80	78.15	73.63
11	Basic	50	55.19	80.49	49.85	50	44.83
12		60	65.36	90.17	49.85	50	45.07
13		70.07	75.86	100.5	49.84	49.99	45.27
14		80.02	86.07	110.3	49.88	50.02	45.23
15		60.19	65.13	90.11	59.83	60	54.76
16		70.03	75.38	99.81	59.83	60	54.88
17		80.01	86.07	110	59.82	59.99	54.94
18		70.21	75.88	100.6	69.81	70	64.61
19		80.1	86.33	110.2	69.81	69.99	65.33
20		80.13	86.67	110.5	79.78	80	73.12
21	IHX	50.01	55.1	80.53	49.86	50.01	45.11
22		60.03	65.16	90.23	49.85	50	45.23
23		70.03	75.07	100.4	49.86	50	45.19
24		79.99	83.88	110.7	49.84	50	44.98
25		59.98	63.82	90.1	59.83	59.99	55.12
26		70.03	73.64	100.2	59.81	59.99	55.01
27		79.96	83.92	110.1	59.78	59.95	55.13
28		70	75.41	100.2	69.83	70.04	64.92
29		80.02	85.8	110.4	69.81	70.01	65.31
30		80.01	86.07	110.1	79.77	79.99	73.68

Table A.17: Experimental data of absolute refrigerant and ambient pressures for a compressor frequency of 50 Hz

No.	Comment	$p_{abs,ref,1}$	$p_{abs,ref,2}$	$p_{ref,4r}$	$p_{abs,ref,8}$	$p_{abs,ref,8}$	$p_{abs,ref,6}$	p_{amb}
-	-	[bar]	[bar]	[bar]	[bar]	[bar]	[bar]	[bar]
1	Superheater	3.707	9.941	9.62	9.609	4.011	3.932	0.9632
2		3.797	12.38	12.1	12.1	4.072	3.997	0.963
3		3.85	14.83	14.57	14.57	4.11	4.036	0.9627
4		3.889	17.85	17.65	17.64	4.113	4.048	0.9624
5		4.799	12.32	11.93	11.89	5.153	5.048	0.9731
6		4.876	15.01	14.68	14.63	5.21	5.11	0.9735
7		4.949	18.09	17.81	17.78	5.264	5.177	0.9735
8		6.101	15.27	14.79	14.72	6.564	6.429	0.9669
9		6.22	18.51	18.11	18.03	6.664	6.541	0.9669
10		7.583	18.72	18.16	18.01	8.152	7.991	0.9666
11	Basic	3.556	10.08	9.796	9.79	3.811	3.78	0.9667
12		3.639	12.25	12.01	12.02	3.873	3.849	0.9669
13		3.71	15.01	14.75	14.75	3.919	3.907	0.967
14		3.789	17.91	17.71	17.72	3.962	3.952	0.967
15		4.619	12.37	12.01	11.98	4.874	4.859	0.967
16		4.722	14.95	14.64	14.6	4.965	4.947	0.967
17		4.799	18.1	17.84	17.81	5.024	5.004	0.9671
18		5.936	15.47	15.03	14.95	6.249	6.247	0.9668
19		6.105	18.42	18.05	17.97	6.367	6.384	0.9665
20		7.378	18.75	18.23	18.08	7.783	7.758	0.967
21	IHX	3.536	10.06	9.78	9.757	3.803	3.765	0.9693
22		3.552	12.11	11.88	11.87	3.817	3.761	0.9693
23		3.627	14.54	14.33	14.33	3.846	3.811	0.9694
24		3.692	17.4	17.21	17.21	3.892	3.867	0.9694
25		4.581	12.37	12.02	11.99	4.895	4.842	0.9697
26		4.645	14.9	14.58	14.55	4.942	4.888	0.9696
27		4.723	17.74	17.46	17.44	5.003	4.956	0.9695
28		5.903	15.32	14.88	14.81	6.297	6.223	0.9699
29		6.04	18.25	17.88	17.81	6.395	6.32	0.9699
30		7.358	18.58	18.04	17.91	7.838	7.75	0.9698

Table A.18: Experimental data of remaining quantities for a compressor frequency of 50 Hz

No.	Comment	$\dot{m}_{ref}$	$\dot{V}_{source}$	$\dot{V}_{sink}$	$P_{comp,FI}$	$t_{sf,Fe,2}$	$t_{sf,Fe,1}$	$t_{EM,wh}$	I_{EXV}	τ_{rec}	$P_{comp,el}$
-	-	[kg/s]	[dm^3/s]	[dm^3/s]	[W]	[°C]	[°C]	[°C]	[%]	[s]	[W]
1	Superheater	0.06218	0.2028	0.9277	4689	64	66.96	99.98	37.35	1275	4900
2		0.06055	0.185	0.9327	5284	66.48	69.31	105.4	33.17	1267	5505
3		0.05855	0.1759	0.8518	5678	68.57	71.15	109.5	30.36	1274	5916
4		0.05559	0.1587	0.6626	6046	70.46	72.79	113	27.85	1269	6294
5		0.07898	0.2496	1.165	5530	72.54	75.86	114.2	41.55	1265	5748
6		0.07712	0.231	1.064	6126	73.98	77.27	117.8	37.29	1289	6377
7		0.07499	0.2123	1.009	6688	75.93	79.11	122.8	33.93	1445	6968
8		0.09991	0.3	1.374	6402	79.2	83.14	122.8	46.42	1294	6673
9		0.09801	0.2726	1.348	7173	79.91	83.95	124.7	41.18	1285	7466
10		0.1249	0.3493	1.348	7505	86.3	90.46	132.6	51.79	1272	7826
11	Basic	0.05923	0.188	0.9222	4716	63.6	66.41	100.4	33.34	1255	4906
12		0.0576	0.1782	0.8727	5221	66.42	68.91	106	30.42	1351	5411
13		0.05581	0.1644	0.807	5642	68.7	70.87	110	28.01	1334	5855
14		0.0536	0.152	0.689	5972	71.2	72.98	114.1	26.36	1366	6206
15		0.07566	0.2388	1.12	5492	71.56	74.65	113.1	40.18	1375	5709
16		0.07445	0.2255	1.039	6069	73.1	76.22	116.7	36.7	1355	6309
17		0.07227	0.2046	0.9266	6600	73.89	77.42	118.5	33.21	1536	6861
18		0.09694	0.2846	1.343	6424	77.65	81.58	120	44.58	1341	6683
19		0.09572	0.2687	1.397	7098	79.59	83.6	125.5	41.16	1411	7386
20		0.1203	0.3357	1.232	7508	85.21	89.59	132.3	50.07	1339	7823
21	IHX	0.05859	0.1903	0.98	4702	66.49	69.29	104.5	33.59	656.5	4913
22		0.05569	0.1792	0.9119	5198	72.42	75.18	111.5	29.85	689.3	5437
23		0.05345	0.1695	0.8199	5613	79.81	82.54	121.2	27.13	648.1	5849
24		0.05139	0.1612	0.7224	6016	86.28	89.04	129.2	24.94	631.8	6279
25		0.07503	0.2424	1.225	5516	74.45	77.88	117.3	39.27	678.2	5754
26		0.07253	0.2291	1.1	6083	80.2	83.72	125.1	35.26	626.9	6368
27		0.07034	0.2157	1.041	6618	85.24	88.99	131	31.94	606.3	6929
28		0.09608	0.2918	1.436	6437	80.46	84.22	123.6	44.12	649.7	6755
29		0.0935	0.2744	1.435	7125	86.08	89.93	131.9	40.23	803.2	7485
30		0.1195	0.3465	1.374	7525	88.59	92.66	136.2	49.55	604.5	7927

Table A.19: Experimental data of refrigerant temperatures for a compressor frequency of 75 Hz

No.	Comment	f_{set}	$t_{source,in,set}$	$t_{sink,in,set}$	$t_{ref,1}$	$t_{ref,2}$	$t_{ref,3}$	$t_{ref,4}$	$t_{ref,5}$	$t_{ref,6}$	$t_{ref,7}$	$t_{ref,8}$	$t_{ref,9}$
-	-	[°C]	[°C]	[°C]	[°C]	[°C]	[°C]	[°C]	[°C]	[°C]	[°C]	[°C]	[°C]
1		75	50	50	53.47	97.34	95.71	52.11	41.36	52.18	43.27	41.96	47.65
2		75	50	60	55.46	106.3	105.1	62.1	48.29	62.07	44.67	42.62	48.42
3		75	50	70	56.99	114.8	113.8	72.16	55.82	72.03	45.66	42.94	48.77
4		75	50	80	58.74	123.5	122.6	82.3	68.25	82.2	46.64	43.23	49.12
5		75	60	60	62.54	107.4	106.4	62.55	52.67	62.69	52.85	51.25	57.3
6	Superheater	75	60	70	64.04	115.1	114.1	72.77	58.32	72.77	54.56	52.07	58.21
7		75	60	80	65.77	123.6	122.6	82.98	65.13	82.89	55.96	52.67	58.97
8		75	70	70	71.8	117.5	116.4	73.41	61.59	73.53	61.97	59.91	67.38
9		75	70	80	73.75	125.5	124.5	83.65	67.9	83.68	63.93	60.94	68.46
10		75	80	80	79.8	125.7	124.5	84.39	69.04	84.41	71.3	68.68	77.12
11		75	50	50	52.67	97.8	96.27	51.94	41.31	51.91	41.2	45.24	46.07
12		75	50	60	54.52	106.3	105.3	61.95	48.14	61.83	42.84	46.97	47.11
13		75	50	70	56.21	114.9	113.9	71.95	55.96	71.76	44.03	47.63	47.65
14		75	50	80	57.93	123.8	122.9	81.99	64.12	81.72	45.03	48.13	48.16
15	Basic	75	60	60	62.42	108.1	107.2	61.89	56.27	62.07	51.31	56.38	56.38
16		75	60	70	63.79	116	115.2	72.19	61.53	72.27	52.72	57	56.96
17		75	60	80	64.7	123.6	122.8	82.87	65.9	82.76	54.2	57.42	57.68
18		75	70	70	70.57	116.5	115.4	73.39	61.69	73.49	61.1	66.21	66.2
19		75	70	80	72.76	125	124	83.63	68.11	83.68	63.04	67.33	67.28
20		75	50	50	54.94	98.64	96.81	52.09	50.24	50.15	41.08	46.56	48.8
21		75	50	60	61.26	111.5	110.2	61.89	57	56.87	41.95	47.65	54.07
22		75	50	70	67.21	123.7	122.7	70.66	62.66	62.55	42.78	47.66	58.55
23		75	50	80	73.08	135.1	134	80.27	68.87	68.76	43.37	48.04	63.76
24	IHX	75	60	60	65.43	111.4	110.6	62.02	60.3	60.32	50.99	56.74	58.86
25		75	60	70	70.72	122.2	121.4	71.53	66.8	66.75	51.99	57.3	63.52
26		75	60	80	76	132.7	131.9	81.24	73.29	73.22	52.74	57.68	68.32
27		75	70	70	74.5	120.4	119.4	73.13	70.98	70.87	60.24	66.26	68.88
28		75	70	80	79.85	130.4	129.4	83.32	78.15	78.08	61.92	67.42	73.99

Table A.20: Experimental data of source and sink temperatures for a compressor frequency of 75 Hz

No.	Comment	$t_{sink,1}$	$t_{sink,2}$	$t_{sink,3}$	$t_{source,1}$	$t_{source,2}$	$t_{source,3}$
-	-	[°C]	[°C]	[°C]	[°C]	[°C]	[°C]
1	Superheater	50.02	54.78	80.22	50	48	44.81
2		60.02	64.9	90.28	50	48.49	45.29
3		70	75.26	100.3	50	48.55	45.19
4		80.01	85.55	110	49.99	48.45	44.99
5		60	64.71	89.87	59.99	58.23	54.61
6		69.99	75.24	100.1	60	58.69	55.15
7		80.01	85.74	110.2	60	59.02	55.35
8		69.99	75.38	100.5	70	68.08	63.27
9		80.03	85.82	110.3	70	68.67	64.03
10		80.01	85.93	110	80	77.78	71.9
11	Basic	50.01	54.62	80.23	49.85	50	44.85
12		60.01	64.72	90.4	49.85	50	45.22
13		70.02	74.89	100.2	49.86	50.01	45.15
14		80.01	85.18	110.4	49.88	50.02	45.13
15		60	63.65	89.75	59.82	60	54.95
16		69.99	74.3	99.84	59.83	60	54.77
17		80	85.68	110.3	59.83	60	54.97
18		70.01	75.37	100.3	69.8	70	63.96
19		80.01	85.87	110.4	69.81	70	64.59
20	IHX	50.06	54.82	80.44	49.84	49.99	44.93
21		60.03	64.54	90.54	49.85	50	45.19
22		69.98	71.86	100.2	49.85	50	45.2
23		79.99	81.02	110.1	49.88	50.02	45.29
24		60.3	63.62	90.54	59.84	60.01	54.93
25		70.11	72.92	100.4	59.83	60	55.09
26		79.98	82.56	110.2	59.83	60	54.94
27		69.99	74.98	100.1	69.82	70.01	63.49
28		79.97	85.27	110.1	69.83	70.02	64.35

Table A.21: Experimental data of absolute refrigerant and ambient pressures for a compressor frequency of 75 Hz

No.	Comment	$p_{abs,ref,1}$	$p_{abs,ref,2}$	$p_{ref,4r}$	$p_{abs,ref,8}$	$p_{abs,ref,8}$	$p_{abs,ref,6}$	p_{amb}
-	-	[bar]	[bar]	[bar]	[bar]	[bar]	[bar]	[bar]
1	Superheater	3.358	10.22	9.731	9.687	3.963	3.811	0.9737
2		3.452	12.42	12	11.98	4.042	3.888	0.9736
3		3.533	15	14.65	14.62	4.066	3.924	0.9736
4		3.612	17.86	17.57	17.53	4.071	3.959	0.9622
5		4.322	12.6	11.95	11.89	5.051	4.868	0.9735
6		4.459	15.26	14.71	14.65	5.175	4.978	0.9735
7		4.573	18.24	17.8	17.74	5.26	5.073	0.9735
8		5.414	15.64	14.87	14.75	6.3	6.074	0.9668
9		5.608	18.53	17.91	17.78	6.449	6.233	0.9667
10		6.708	18.83	17.97	17.8	7.791	7.486	0.9659
11	Basic	3.221	10.15	9.692	9.665	3.695	3.655	0.9693
12		3.343	12.4	12.02	12.01	3.816	3.757	0.9691
13		3.433	14.93	14.6	14.59	3.851	3.811	0.9689
14		3.525	17.95	17.67	17.67	3.894	3.862	0.9688
15		4.247	12.56	11.95	11.88	4.803	4.759	0.9685
16		4.333	15.13	14.62	14.55	4.87	4.827	0.9686
17		4.445	18.21	17.8	17.75	4.961	4.914	0.9688
18		5.416	15.6	14.88	14.75	6.072	6.047	0.9684
19		5.597	18.57	17.98	17.84	6.219	6.206	0.9683
20	IHX	3.202	10.25	9.804	9.759	3.701	3.62	0.9763
21		3.275	12.31	11.96	11.93	3.81	3.677	0.9763
22		3.356	14.84	14.53	14.51	3.811	3.736	0.9763
23		3.436	17.72	17.48	17.47	3.848	3.789	0.9764
24		4.184	12.73	12.13	12.07	4.802	4.691	0.9763
25		4.261	15.23	14.73	14.66	4.866	4.769	0.9762
26		4.34	18.03	17.65	17.59	4.914	4.824	0.9763
27		5.272	15.54	14.75	14.65	6.056	5.921	0.9696
28		5.49	18.37	17.73	17.63	6.226	6.103	0.9695

Table A.22: Experimental data of remaining quantities for a compressor frequency of 75 Hz

No.	Comment	$\dot{m}_{ref}$	$\dot{V}_{source}$	$\dot{V}_{sink}$	$P_{comp,FI}$	$t_{sf,Fe,2}$	$t_{sf,Fe,1}$	$t_{EM,wh}$	I_{EXV}	τ_{rec}	$P_{comp,el}$
-	-	[kg/s]	[dm^3/s]	[dm^3/s]	[W]	[°C]	[°C]	[°C]	[%]	[s]	[W]
1		0.08131	0.2657	1.223	7081	60.61	64.08	102.6	41.77	1271	7349
2		0.08012	0.2525	1.227	7733	63.4	66.68	110.1	37.84	1265	8017
3		0.07729	0.2341	1.06	8283	65.78	68.84	116.2	34.7	1295	8590
4		0.07399	0.2178	0.8742	8726	68.23	70.99	121.3	33.93	1283	9057
5		0.1026	0.3302	1.431	8386	69.47	73.47	120.3	48.64	1286	8704
6	Superheater	0.1017	0.3093	1.442	9260	71.45	75.51	127.2	43.86	1276	9610
7		0.09972	0.2884	1.338	10086	74.12	78.17	136.3	40.49	1291	10463
8		0.1253	0.3826	1.341	10048	78.73	83.29	139.9	53.87	1268	10421
9		0.1244	0.3645	1.365	11071	81.65	86.38	152.2	49.47	1294	11481
10		0.153	0.4493	1.299	12018	86.92	92.32	160.9	59.94	737.4	12430
11		0.07759	0.2548	1.201	6972	60.74	63.68	103.4	40.33	1227	7232
12		0.07697	0.2428	1.19	7612	63.1	65.87	109.3	37.11	1258	7901
13		0.07469	0.2282	1.04	8140	65.63	68.18	115.5	34.33	1287	8450
14		0.07175	0.2083	0.8962	8600	68.33	70.58	121.6	31.83	1277	8931
15	Basic	0.1	0.3269	1.534	8276	69.84	73.43	122.1	48.59	1337	8608
16		0.09831	0.3063	1.333	9111	72.29	75.77	130	43.95	1360	9463
17		0.09646	0.2797	1.231	9916	73.56	77.23	134.9	39.96	1261	10290
18		0.1251	0.381	1.524	10029	77.51	82.07	139.6	53.48	1289	10423
19		0.1239	0.3587	1.536	11085	80.85	85.44	152.7	49.11	1375	11486
20		0.07641	0.2541	1.23	6920	61.89	65.08	102.6	38.94	672.4	7233
21		0.07458	0.2443	1.206	7486	68.97	72.07	114.1	35.55	604.2	7823
22		0.07204	0.238	1.111	8042	76.01	78.93	126	32.52	716.6	8395
23		0.0684	0.2219	1.012	8478	82.41	85.33	134.7	29.6	605.6	8863
24	IHX	0.09822	0.3237	1.532	8310	73.03	76.48	126.1	46.74	670.2	8675
25		0.09594	0.3108	1.465	9109	78.91	82.5	136.8	41.89	839.6	9493
26		0.09286	0.2949	1.298	9877	84.69	88.5	147.6	37.65	608.8	10289
27		0.1213	0.3859	1.404	9904	81.96	86.25	146.8	51.92	666.6	10347
28		0.12	0.3696	1.508	10978	87.7	92.32	159.6	46.77	627.8	11451

A.5 Friction Factors according to Martin (2006)

The friction factors ξ_0 and ξ_1 found in Equation 6.13 of Section 6.2.1 are a function of the Reynolds number Re and the corrugation angle $\psi_{phx,p}$. For the boundary case of $\psi_{phx,p} = 0°$ two different flow regimes are distinguished for ξ_0 as given in Equations A.1 and A.2:

$Re < 2000$ (laminar):

$$\xi_0(Re) = \frac{B_0}{Re} \tag{A.1}$$

with $B_0 \approx 64$.

$Re > 2000$ (turbulent):

$$\xi_0(Re) = (1.8 \log Re - 1.5)^{-2} \tag{A.2}$$

For the second boundary case of $\psi_{phx,p} = 90°$ the friction factor $\xi_1(Re)$ is determined by Equation A.3 as follows:

$$\xi_1(Re) = a \cdot \xi_{1,0}(Re) \tag{A.3}$$

with $a = 3.8$. For $\xi_{1,0}(Re)$ once again a laminar and turbulent flow regime can be defined yielding Equations A.4 and A.5.

$Re < 2000$ (laminar):

$$\xi_{1,0}(Re) = \frac{B_1}{Re} + C_1 \tag{A.4}$$

$Re \geq 2000$ (turbulent):

$$\xi_{1,0}(Re) = \frac{K_1}{Re^n} \tag{A.5}$$

with $B_1 = 597$, $C_1 = 3.85$, $K_1 = 39$ and $n = 0.289$.

A.6 Validation Results of the Overall Isentropic Efficiency

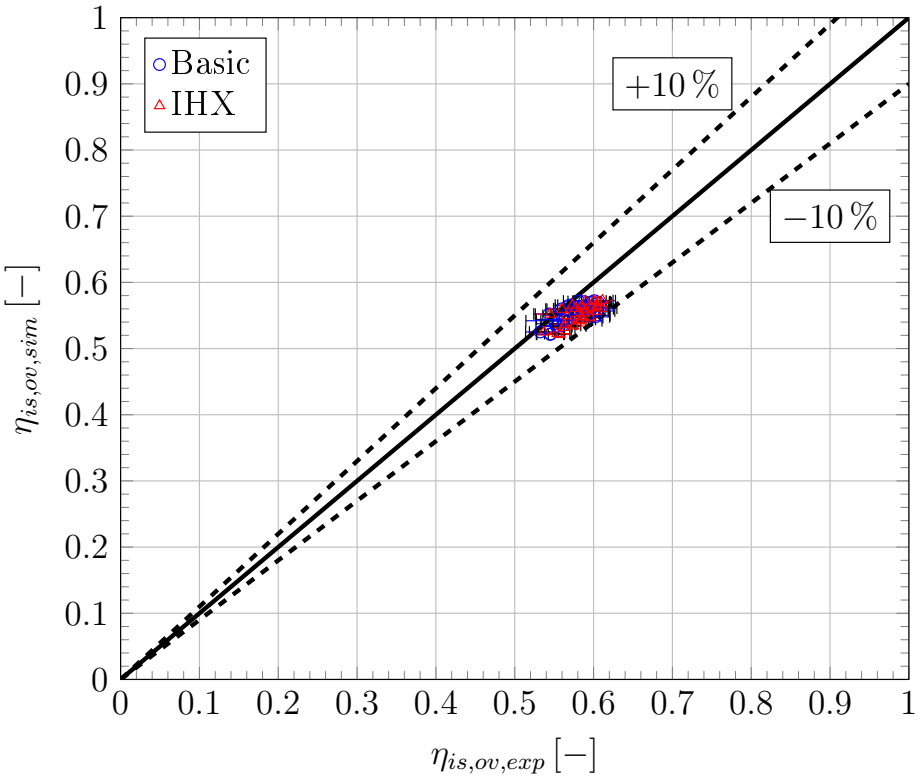

Figure A.1: Model validation regarding the overall isentropic efficiency for the Basic and IHX cycle